Synthesis of TiO_2 Nanoparticles by Spray-Lyophilization Process.

Characterization and Optimization of Properties of Photocatalytic Water Purification and Gas Sensing Applications

Doctor of Philosophy (PhD)

PIERRE MWINDO KIBASOMBA

(Student No 35974087)

Department of Physics, University of South Africa

SUPERVISORS:

1. PROF MALIK MAAZA, UNISA & iThemba LABS
2. PROF SIMON M. DHLAMINI, PHYSICS DEPARTMENT (UNISA)
3. Prof. BONEX MWAKIKUNGA, CSIR PRETORIA

Declaration

I hereby declare that this thesis entitled “Optimization of **TiO_2** Properties using Lyophilization Process for Photocatalytic, Anti-bacteria and Sensing Applications” is the results of my Ph.D. research and that it has not been submitted elsewhere for the award of the PhD degree in Physics.

Signature: 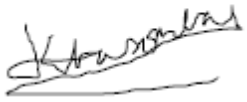

Name: Pierre M Kibasomba

Date: 2021-03-28

Acknowledgment

My sincere gratitude to:

1. The NRF and CSIR for the funding,
2. For the promoting role and supervision: Prof. Malik Maaza, Prof Simon Dhlamini, Prof Bonex Mwakikunga
3. For the unconditional love, My wife, Safi Anne Kankisingi and my children: David, Daniel, Mbilizi and Gloria Sakina
4. For the precious advise, My elder brother, Prof Roger Man-Byemba Kibasomba
5. For his sacrificial financial support, my younger brother, Dominique Igilima Kibasomba
6. For moral support, my sisters Dodo Kibasomba Elisabeth Lusange Kibasomba and their respective husbands, Moses Vita Mboma and Andrien Mukulumanya Kaningini

Dedication

To my late mother,

Georgine Takubungo Sakina

List of publications and presentations

1. **Pierre M. Kibasomba**, Simon Dhlamini, Malik Maaza, Chuan-Pu Liu, Mohamd M. Rashad, Diaa A. Rayan, Bonex W. Mwakikunga, Strain and grain size of TiO_2 nanoparticles from TEM, Raman spectroscopy and, XRD: The revisiting of the William-Hall plot method, Results in Physics 9 (2018) 629 - 635

2. G. R. Hearne, J. Zhao, A. M. Dawe, V. Pischedda, M. Maaza, M.K. Nieuwodt, **P. Kibasomba**, O. Nemraoui, J. D. Commins, M.J. Witcomb, Effect of grain size on structural transitions in anatase TiO2: A Raman spectroscopy study at high pressure (Physical Rev. B 70, 134102 (2004)

PREFACE

The synthesis of the titania nanoparticles was done and its main features were optimized by the lyophilization process. These features included the dispersion (size and size distribution), structure (phase) and, shape (morphology). The approach considered minimization of energy at the nucleation level. Principally, for selected photocatalytic applications in water purification and gas sensing, we ensured optimization of the critical properties of **TiO_2** NPS via a proper selection of Titanium bearing precursors of high purity, meticulous preparation of solutions/formulations and, processing conditions leading to the final titania product of high quality. By investigation, we singled out , pH, the concentration of solutions, nature of precursors, annealing temperature and time (duration) as the parameters that control crystallographic structures, dispersion, morphology (shape), BET surface area, vibrational, mechanical (strain/stress), gas sensitivity and selectivity, photocatalytic and antibacterial activities.

The originality of this Ph.D. work is based on full control of features of metal oxides nanoparticles (NPS) and scale-up capabilities determination of the lyophilization process, in particular for the **TiO_2** NPS. Indeed, being among the earliest, our research that started in 2001, has revealed that the Spray-lyophilization processing is extensively used for production and long shelf-life storage of high-quality nest café and baby milk formula, and numerous pharmaceuticals can equally be used for the production of high-performance **TiO_2** nanoparticles.

In chapter 4 of the thesis, we present experiments and results obtained using a lyophilization optimization strategy. First, the minimization of energy during the nucleation and crystallization is shown by XRD, TEM, and RAMAN Spectroscopy and the low (100 – 400°C) temperature decomposition of amorphous lyophilized products as per results of TGA / DSC, the phase transitions from amorphous to single-phase nanostructured (1-50nm) **TiO_2** particles,

Secondly, we discuss research results obtained using thermal analyses, TGA/DTA and DSC (Differential Scanning Calorimetry), X-ray Diffraction (XRD), TEM / HTREM, EDS,

BET, RAMAN spectroscopy, and UV-Vis spectroscopy. We summarize and recommend the lyophilization optimization strategy for crystallographic, shape, and surface (BET, surface-to-volume ratio), optical and mechanical properties' control.

Finally, we argue that optimization by lyophilization is a strategy of minimization of energy of phase transformation, in particular crystallization, depending on solution concentration, pH of a solution, the freezing and drying (both primary and secondary) temperatures, and the nature of Titanium-bearing precursor. We, therefore, include the argument based on the evidence gathered experimentally that the optimized-lyophilized **TiO_2** NPS is indeed an excellent material for a gas sensor, organic pollutants photo-decontaminant, and antibiotics in drinking water.

ABSTRACT

Monodisperse titanium dioxide (TiO_2) nanoparticles were synthesized by a novel freeze-drying process herein called *lyophilization.* The process of lyophilization is described in detail. The materials were characterized by scanning electron microscopy SEM) including energy dispersive x-ray spectroscopy (EDXS), high resolution transmission electron microscopy (HRTEM), x-ray diffraction (XRD), Raman spectroscopy and UV-Vis-IR spectrophotometry. The TiO2 nanoparticles have narrow size distribution, mono-disperse, strained with most of the characteristics showing presence of the four phases of TiO2 thus: anatase, brookite, rutile with each lyophilization process producing its own phase mostly controlled by pH and precursor concentration and anneal/calcining temperatures. With specific reference to HRTEM, Raman spectroscopy results and XRD, it was found that the Scherrer equation, the Williamson-Hall method and others of similar nature were not enough to explain the strain and the grain sizes of these particles. Therefore the Williamson-Hall method was revised to properly explain the new results. The obtained TiO_2 nanoparticles were used in three applications: (1) gas sensing (2) degradation of organic water-borne pollutants using methylene blue as an indicator (3) anti-bacterial activity.

TABLE OF CONTENTS

TABLE OF FIGURES

LIST OF TABLES

CHAPTER 1: INTRODUCTION TO TITANIA MATERIAL AND LYOPHILIZATION METHODS

This chapter starts with background information, followed by the statement, and Nano-technological rationale justifying the use of the lyophilization method and the study of titanium dioxide nanoparticles (NPS) before it outlines the aims and objectives of the thesis work relative to the lyophilization method as an optimization technique of critical properties, characterization techniques used; and applications of TiO_2 nanoparticles including gas sensing and photo-catalysts for water purification processes. It ends with an outline of what will be covered in the thesis itself.

1.1. A brief background on Titanium Dioxide

The synthesis and optimization of TiO_2 nanoparticles are derived from the Nanoscience and Nanotechnology endeavor, which is respectively the meticulous scrutiny and use of extremely tiny structures or objects, measuring between 1 – 100nm, to solve problems that we encounter in a bid to satisfy human needs. The definition is the paraphrase of the idea elaborated by Richard Feynman, the earliest physicist who shaped the field of nanoscience and nanotechnology.

Since then, the study of Titanium dioxide (TiO_2) nanoparticles (NPS), in particular, has extensively been conducted by many material-scientists, covering innumerable applications. According to Aruna (12), the applications include catalysts and supports, ceramics, inorganic membranes, gas sensing, water purification, and solar energy conversion. TiO_2 can let light pass through in the visible region and absorbs light in the ultraviolet region of the solar spectrum, quite an attractive characteristic for filter application [3].

Nanoscience and Nanotechnology of TiO_2 NPS usability in aqueous media have been mainly driven by the study of insolubility, non-toxicity, chemical stability, powerful color (whiteness) and degradation of organic substances. These features have now almost been established along with high photocatalytic activity [2]. Non-toxic substances result from the oxidation of many organic contaminants of water, particularly alcohols, in the presence of TiO_2 NPS. It is believed that the use of molecular oxygen as the ultimate

oxidant makes the photocatalytic process the cheapest [2]. Also, the chemical stability of the TiO_2 NPS is better in most photocatalytic processes.

Many more interests in nano-crystalline form and its application as a semiconductor material is the cost-effective dye solar-cells, making it a material of great scientific and technological importance. Moreover, the effectiveness of TiO_2 nanomaterials in degrading or absorbing water pollutants has been demonstrated and reported by many authors. The properties, especially, the surface properties, strongly influenced by the size, crystal structure, and morphology have been widely investigated and believed to affect the dispersion properties; on the other hand, the correlation between photo-degradation or absorption of pollutants and the degree of dispersion of TiO_2 nanoparticles has also been established. Nevertheless, decontamination processes and toxicity become difficult because of nanoparticles' dispersive properties impact on delivery and transport efficiency [52].

Still, a lot of research has been intensified to answer several questions related to the control of these properties using the synthesis route, Sol-gel in particular, and in some cases the use of surfactant molecules for the control of properties, especially the dispersion. So, an effort to explain or establish the mechanism to find a way to exploit fully the potential and to enhance the efficiency of the TiO_2 in the various applications is on-going. Some of the known techniques of enhancement are doping TiO_2 with metals, for example, Ag, or surfactants. However, the use of surfactants raises health concerns, an additional problem for applications such as water quality [52]. The author argues that toxicity originates from "incomplete degradation" of "nonylphenol (NPE) compounds" from "sewerage treatment" and their presence implies the presence of "other NPE degradation by-products" in the "aquatic environment". So, surfactants, in particular, "Nonylphenol and "its "ethoxylates", in short NPE, are toxic substances, not recommended for applications of our interest, especially water purification.

Moreover, the nature of TiO_2 particles has also been studied by several researchers trying to understand the influence of size and temperature on a succession of its three phases during the formation of NPS. Banfield [9] argues a low-temperature formation of "ultrafine **TiO_2** particles, in its "anatase, "rutile and "brookite phases; in particular, he

argues reasons anatase phase can be "synthesized at ultrafine sizes, the possibility of manipulating the succession of "phase "transformations from "composition, microstructure, qualities considering the influence of "phase-transformation". He found that, though in macrocrystalline form, "rutile is more thermo-dynamically stable than "anatase, maybe "brookite, but for "particle size diameter under 14nm, the phases' succession changes, anatase becomes more stable than rutile. So, we assume that if we gain a detailed understanding of the formation of TiO_2 NPS from low temperatures to higher ones up to 900 degrees then we will be able to optimize accordingly TiO_2 material behavior for the various applications.

1.2. Introduction to Lyophilization Technique of synthesis

Lyophilization is also known as freeze-drying. This is a synthesis technique chosen for this study. Although the details of this process will be covered in the literature review in Chapter 2, lyophilization involves liquid precursors sprayed into a cold zone such as liquid nitrogen while subjecting the whole system to vacuum conditions thereby initiating the ultimate drying of the so-produce rather amorphous material.

The lyophilization process has been considered the best storing nano-technological tool for conserving for a long period and chemically stable liquid formulations into solid forms [5]. Also, in monitoring the release of toxic gases from environmental processes, a gas sensing material that is chemically stable for a long period is critically needed.

In our view, we lay the necessity to address the following points as the required strategies justifying the use of the spray-lyophilisation process and the adequacy of characterizing techniques in line with the **TiO_2** nanoparticles made.

- **Improving the gas sensitivity / response of bulk-based metal oxides gas sensors by optimal synthesis conditions**

Because of their size, morphology and, structure, bulk material-based metal oxides sensors 'performance is de facto showing the decline in gas sensing properties, that is to say, they are now becoming lowly-sensitive, lowly-selective and respond with lesser speed. Bulk-size material is the material whose ratio between the size of the largest

lump or particle and the smallest lump is less than or equal to 2.5. Whereas, continuum-bulk material is the material of which ratio is greater than 2.5. The growing interest in bulk material-based gas sensors is because of the advantage that is offered, the reversibility of interaction between the gas with the surface of the sensing material, but also the varying conductivity in the material due to the reaction. Detecting this reaction is made easier by simply measuring the variation in capacitance, work function, mass, typical optical feature, or conductivity of Metal oxide-gas sensors, in particular semiconductors, which are extensively utilized in environmental (air, water) and safety control of gases. Improvement in the Metal Oxides gas sensing properties can be achieved considering nanostructures, defined as materials whose structural elements — clusters, crystallites, or molecules—have dimensions in the 1 to 100 nm range [3], morphology, and doping. The first aim of this work is to test the gas sensing properties of spray-lyophilized TiO_2 Nanoparticles exposed to NO_2, CH_4, NH_3, and CO gases. It was hypothesized that non-doped and optimized density surface states TiO_2 nanostructures will be more effective gas sensing materials.

- **Improving mono-dispersity of metal oxide particles and finding a synthesis technique, alternative to additive surfactant for making mono-disperse (narrow size distribution), non-toxic anti-bacterial material to curb the growing public health issues due to resistance to known antibiotics of waterborne strains**

Furthermore, the size, morphology, and structure of metal oxides are important factors in alternative remediation of antibiotic-resistant strains, a growing public health problem nowadays [6]. However, assessment of toxicity among many Metal Oxide Nanoparticles has been conducted using many models, especially in vitro dosimetry models. Because of tremendous antimicrobial effects on Streptococcus, coating brackets with Copper Oxides (CuO), Zinc Oxides (ZnO), and Zinc Copper Oxides (Zn-CuO) is a typical use of metal oxides. Nevertheless, confirmed minimal toxicity in human cell lines in the case of TiO_2 NPS has been revealed by several toxicological studies that included CuO and ZnO NPS, to cite these few most popular antibacterial metal oxides [10]. It was then hypothesized that by using Spray-lyophilization, we will be able to synthesize TiO_2 NPS

of a specific size, size distribution, structure, and morphology, alternative antibiotics with minimal or tolerable toxicity to human cells would be generated for water purification.

- **Improving the effectiveness of surface cleaning by making highly pure and uniformly composed nanomaterials**

Qualitative nanoparticle characterization has been found a highly important analytical surface approach in the determination of composition, confirmation of occurrence of reaction, and effectiveness of surface cleaning state of contaminants [11]. Quantitatively, X-ray photoelectron spectroscopy (XPS) is said to be an accurate way of determining the ultimate constituents in the structure in terms of parts per thousand, PPTH, which is the symbolic expression derived from experiment, a condition produced by chemistry and condition related to electrons of the constituents in a material [12]. Accordingly, the XPS spectra are constructed as a beam of X-rays is shed on the material at the same time the kinetic energy plus the number of electrons slipping away from surface confinement deep down more or less 10nm within the layer of material are recorded.

- **Preserving the most critical nanomaterial performance surface attributes (states) by synthesis method.**

Because of its higher resolution, thousands of times compared to light microscopy, Transmission Electron Microscopy is the imaging technique widely used to provide fine details at nanoscales such as size, size distribution, morphology (a geometric shape), and surface characteristics. These are “performance defining attributes” which are important in gas sensing and photocatalytic water purification as mentioned .earlier. Particularly, the importance of Transmission Electron Microscopy (TEM) is found, in combination with the Dynamic Light Scattering (DLS) and Static Light Scattering (SLS), in the determination of the primary size of NPS in the study of dispersion in solution, which is critical in the study of toxicity. In principle, the TEM technique creates an image by contrast that is generated by amplitude and phase shifts in the transmitted beam. The contrast depends on the sample thickness and the nature of the sample

material. The length of the electron means path in the scattered beam is inversely proportional to the weight of atoms in the sample material.

- **Preserving the intrinsic geometric and electronic structure of nanoparticles**

The importance of the Small Angle X-ray (SAX) is found in the vast characterization of material in various forms including crystalline, even amorphous semiconductors, in bulk or nanoscale forms. More interestingly, it allows obtaining “geometric” and “electronic structure” of a particular element within the nanoparticle. The underlying principle is that “data” is generated when photon energy of the “crystalline monochromator” capable of “exciting the “core” electrons is adjusted to a specific “edge” equivalent to a given principal quantum number (n).

- **Synthesizing at low temperature each TiO_2 polymorph (single Phased and crystalline anatase, rutile, and brookite), minimizing distortion of lattice parameters, tracing phase transitions at low temperature, conserving size, and minimizing strain broadening**

The mere application, at the low temperature (< 400ºC), of the X-ray Diffraction (XRD), serves in identifying the phase, evaluating the quality of the crystal, defining crystal structure, and measuring the crystal size. Samples are analyzed by XRD for eventual presence of multiple phases, presence of lattice strain, clustering of grains in a certain orientation as properties are affected because of anisotropic condition, particularly the texture. Unlike measurements at low-temperatures, the combination of the XRD patterns with in-situ high-temperature experiments is necessary to obtain ‘temperature-dependent phase transformation, ‘the thermal changes of structural parameters, and ‘changes of the ‘real structure [129].

1.3. Problem Statement and Nano-scientific and Nano-technological Rationale

Looking at the information at hand, we found that there is the need for researching further the key properties of the Titania which make it a material of choice in the gas sensing, photo-catalytic activity, and anti-bacterial activity to resolve the issue of antibiotic resistance to a good number of strains in drinking water currently being used.

As we believe the optimum functionality of TiO_2 nanoparticles and the efficiency of the TiO_2-based gas sensors, antibacterial activity and, photocatalytic activity for organic water contaminants, require a good understanding based on the five fundamental characteristics namely: structural (phase stability), vibrational, morphological, electrical, optical, and thermal stability. The lyophilization process is the best nanotechnology to produce monodisperse nanoparticles and to conserve nanoparticles' surface properties.

The thesis work considers a set of key fundamental questions, of which the answers are believed to enlighten the scientific and technological world to the benefits of control of size (mono-dispersity), structure (phase) and, morphology (shape) and their effects on gas sensing, photocatalytic, and antibacterial properties of titanium dioxide nanoparticles (TiO_2 NPS) for water purification. The states of the surface of the nanoparticles are delicately affected by the synthesis conditions, in turn causing a deteriorated performance concerning these applications. Subsequently, the control and understanding of the fundamental characteristics are critical. In this work, we analyze data obtained by the synthesis of TiO_2 NPS in advanced materials and nanoscale laboratory of the Wits University (2000-2004) by lyophilization method and selected characterization techniques. Additional information has been obtained by further experiments on the as-synthesized TiO2 nanoparticles samples that were conducted at iThemba LABS and the CSIR LABS in 2016. Fundamentally, the effects of thus obtained TiO_2 and the answers to the questions that follow are the pivot of the thesis:

- Why the lyophilization processing method?
- Do the lyophilized titanium dioxide nanoparticles have the necessary properties suitable for gas sensors, antibacterial and photocatalytic activities in the degradation of organic water contaminants?
- Can the TiO_2 properties be improved (enhanced) by controlling factors that affect the performance of gas sensors, antibacterial and photocatalytic degradation of organic materials (water purification) processes?

1.4. Aims and Objectives

The thesis work is meant to:

- To synthesize a series of TiO_2 nanoparticles by lyophilization technique.
- To optimize the lyophilization technique for critical properties of TiO_2 nanoparticles and their applications as alternative gas sensing and photocatalytic-water purification materials. We here refer to the synthesis of TiO_2 NPS in advanced materials and nanoscale laboratory of the Wits University (2000- 2004) by lyophilization technique, and the effects of thus obtained TiO_2 nanoparticles;
- To probe the intrinsic effects of the lyophilization synthesis method, mechanisms of conservation of TiO_2 NPS surface properties as a function of synthesis parameters. We consider the correlation surface properties and synthesis conditions to be the pivot of most of the investigations on the properties of TiO_2 nanoparticles tailored by lyophilization. In line with a point, the research attempts to answer questions such as why lyophilization processing method? Do the lyophilized titanium dioxide nanoparticles have the necessary properties suitable for gas sensors, antibacterial and photocatalytic activities in the degradation of organic water contaminants? Can the TiO_2 properties be improved (enhanced) by controlling factors that affect the performance of gas sensors, antibacterial and photocatalytic activities in the degradation of organic water contaminants using only lyophilization processing technique, in other words avoiding the addition of surfactants?
- To study the control of size, size distribution, structure (phase diagram), and shape of TiO_2 NPS that have been synthesized by lyophilization.
- To conduct a comparative properties characterization study of the Spray-lyophilized TiO_2 NPS.
- To conduct the Modelling of titanium isopropoxide and the $TiCl_3$ precursors for TiO_2 NPS synthesis.
- Finally, to correlate experimental characteristics of as-synthesized TiO_2 NPS to gas sensing (sensitivity to NO_2, CH_4, NH_3, and CO) and photocatalytic-water purification (anti-bacterial activity and degradation of organic contaminants) properties.

1.5. Chapters outline

We focus on the Spray-lyophilisation synthesis method, the optimization technique of critical properties of thus synthesized TiO_2 nanoparticles and their applications as alternative gas sensors, photo-catalysts in the degradation of waterborne organic and anti-bacteriological (strains) materials.

Firstly, following chapter 1 and chapter 2 are devoted to the introduction and background of properties on TiO_2 nanoparticles (literature review) respectively. We define the physical concept of freeze-drying, then we study its application as a process in the control of size, size distribution, structure (phase diagram), and shape of TiO_2 nanoparticles (NPS). The term “Spray-Lyophilization” technique referred to in this work is an adapted version of freeze-drying with an additional step, chemical solution-spraying step that precedes the freezing and drying processes. Chapter 3 is an overview of the Spray-Lyophilization principles and background. Chapter 4 deals with experiments, results, and discussions. These include synthesis and optimization studying particularly the synthesis parameters such as the pH, concentration, annealing temperature, and duration of decomposition. The optimization strategy is based on coupling the test results of the DTA / DSC and decomposition temperatures of the lyophilized products. The experiments also investigate strains, X-rays studies, and the Williamson-Hall modified method. By a series of experiments, we characterize the properties of the spray-lyophilized TiO_2 nanoparticles, including structural (phase), size and size distribution, geometrical morphology (shape), electronic properties (a measurement of the bandgap, E_g). Another series of experiments consists of investigating water purification and gas sensing-related applications of the Titania lyophilized nanoparticles. These are photo activities, antimicrobial and gas sensing responses (sensitivity and selectivity) investigations. The results of the discussions are summarized in the modeling of titanium isopropoxide and the $TiCl_3$-TiO_2 precursors. Finally, in Chapter 5, the conclusions and recommendations finalize the Ph.D. thesis.

Chapter 2: LITERATURE REVIEW

2.1. Synthesis methods:

Numerous fundamental studies have been done by many material scientists to explain the lyophilization or freeze-drying technique. Figure 1 represents the phase diagram illustrating the concept of Lyophilization for pure water in solid state, ice. The tripple point lies at the intersection of the liquid state (L), the gaseous state (G) and solid state (S). According to Baheti, Ankit et al. (2010), the coordinates of the triple point T in the case of lyophilization of ice, are given by temperature 0.01°C and pressure 0.00603 atm. As shown in the figure 1, the black arrow indicates the lyophilization taking place about the 'triple point, preventing the liquid-gas transition which occurs in a usual drying process shown by the yellow arrow.

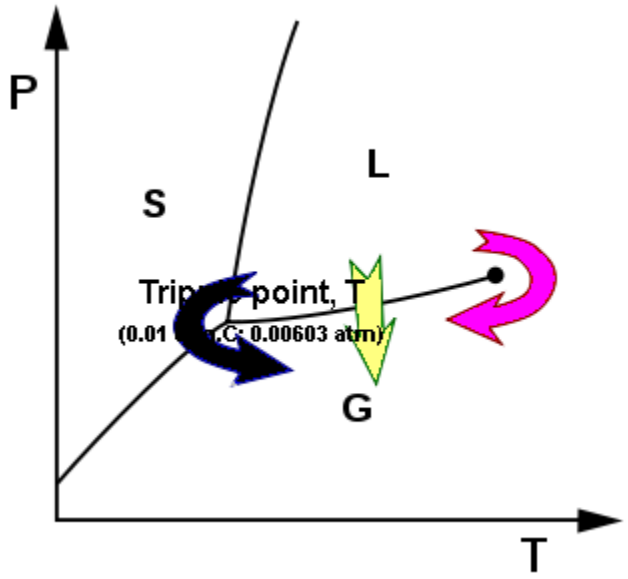

Figure 1: The Diagram for a typical lyophilization process based on the phase change of ice.

. The lyophilization process is a phenomenon that could be explained based on the difference in the amount of ‘water vapor contained in the ‘solid material and the pressure in the surrounding. It takes place at a slow pace with the molecular kinetic energy, and at the pressure in that condition. The speeding of the process requires the vacuum (pressure close to zero atm) and a ‘high-speed pump to cause the direct transformation of the solid phase to the gaseous state, avoiding the passage to the liquid phase. Explained in terms of the endothermic reaction that absorbs energy from its surrounding, the transition from solid substance to liquid, ‘partial or complete collapse of the structure or ‘shape, is due to ‘excessive absorption of energy [124].

Apart from vapor forming from frozen water, lyophilization includes other physic-chemical mechanisms such as: mollifying and structuring mixed-shapeless substances, aspect change, the disintegration of weaker bonds of solvated states; sometimes, the formation of transitional states occurs. The final stage is crucial because the separation between the solute and its dissolving substance takes place and the latter is eliminated. Among many advantages of lyophilization, the preservation of micro-characteristics namely shape and disambiguation of chemical characteristics are kept the same.

2.2. TiO_2 properties:

2.2.1. Bulk TiO_2 properties and Phase diagram

In this paragraph, we present a brief overview of the important TiO_2 structures, which have been described based on unit cell dimensions a, b, c and α, β, and γ, where a, b, c are lattice parameters and α, β, γ inter-axial angles. Also, structures are described as units built from polyhedral to visualize structural differences, and it is very convenient to describe a structure in terms of the coordination polyhedral around the cations, and how these polyhedral are linked together, sharing corners, edges, or faces. This is important so long as differences in structure play a deterministic role in the definition of relationships between structure and physical, and or chemical properties [1]. In other words, a given structure and a specific size determine distinct properties and specific functionality.

2.2.2. Crystalline structure (Phases):

Firstly, it is useful to define the term “phase”, which will be frequently used here. Porter [16] defines "phase being": "a section of a material having uniform "properties" and "composition" visibly dissimilar compared to the best part of the material. So, the boundary by surfaces across which the properties change discontinuously. TiO_2 is a polymorph, a material in the solid phase that has different structures at different temperatures. It could be regarded, hypothetically, as a single component system, containing a molecule/compound that does not dissociate over the range of temperature of interest.

In the present situation, each phase of TiO_2 contains different species of atoms or ions, Ti^{+4} and O^{-2}.

The Figure 2 below is a representation of each of the two types of the unit cell of the Titania. These are namely: “tetragonal” and “orthorhombic”. At standard atmospheric conditions of pressure (1 atm) and temperature (25º), the Titania could have one of the two structures namely: anatase (tetragonal), rutile (tetragonal) and brookite (orthorhombic).

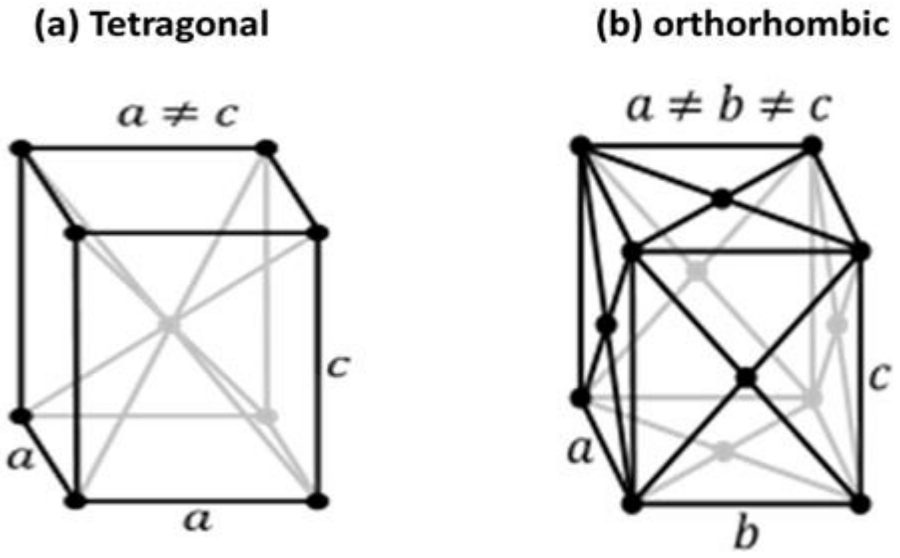

Figure 2. The two TiO_2 types of unit cell-cell

To these natural polymorphs are added high-pressure phases namely: **Columbite α-PbO_2** (orthorhombic) and **baddeleyite** (monoclinic), and orthorhombic structure of **cotunite** type, which is one of the hardest polycrystalline materials known. The rutile phase is the most stable and the most common[8], anatase and brookite are metastable phases, whereas brookite is the rarest of the three. Dewhurst and Lowther have suggested **Fluorite** structure, so far identified only theoretically as a high-pressure phase of Titania synthesized.

2.2.2.1. Description of the crystal structure:

Firstly, the TiO_2 crystal structure is described in terms of lattice parameters a, b, c, and inter-axial angles α, β, γ. The table includes calculated properties[15] such as B is the bulk modulus in GPa and E_f is the formation of energy in the eV/TiO_2 unit.

Secondly, anatase, rutile, and brookite structures could be viewed as a network of coordinated TiO_6 octahedral. These TiO6 octahedral are interconnected differently for each phase, leading to different structures and symmetries[11]. The unit cells are shown in figure 3. Dielbol [12] calls them “building “blocks. He has compared anatase structure to rutile based on “unit cells”, composed of titanium (Ti) atoms around which are arranged "six" oxygen(O) atoms as depicted in the (figure 2) He found out the similarity of structures having "two" "bonds" amid titanium and oxygen atoms and the piled-up of octahedral create a "three-fold" "coordinated" "oxygen" "atoms". The difference in that, while the "bond" "angle" is far greater, maybe, lesser than 90 degrees in the case of "anatase", in "rutile" the octahedral are tailed to another, and piled-up following "long axis" in a sequence of 90 deg. He further argues that considering Ti-O “phase diagram” possessing a great number of "stable phases" having different "crystal structures", he then concluded that the "reduction" of "bulk" TiO_2 would not be difficult. As a result, he says that clear "single" "crystals" would be colored, maybe become "dark blue".

The octahedral are less dense in anatase than in rutile Anatase contains two formula units (six atoms) per primitive cell.

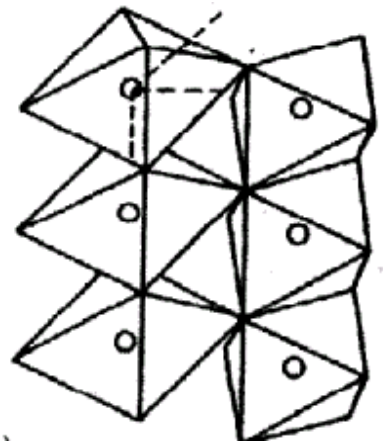

Figure 3. The [TiO_6] octahedral structure in primitive cell.

The Figure 3 above shows parts of columns of [TiO_6] octahedral showing a metal (Ti) atom surrounded by six atoms (oxygen) situated at the corners of the octahedron and Octahedral being linked together via corners, edges, and faces.

However, the overall differences in the three polymorphs of TiO_2 can be visualized in the figure 4. These structure models are in agreement with the suggestions of Thompson T.L and Yates Jr T. (2006) and Stepanov A.L, Xiao X. and Ren F. (January 2013).

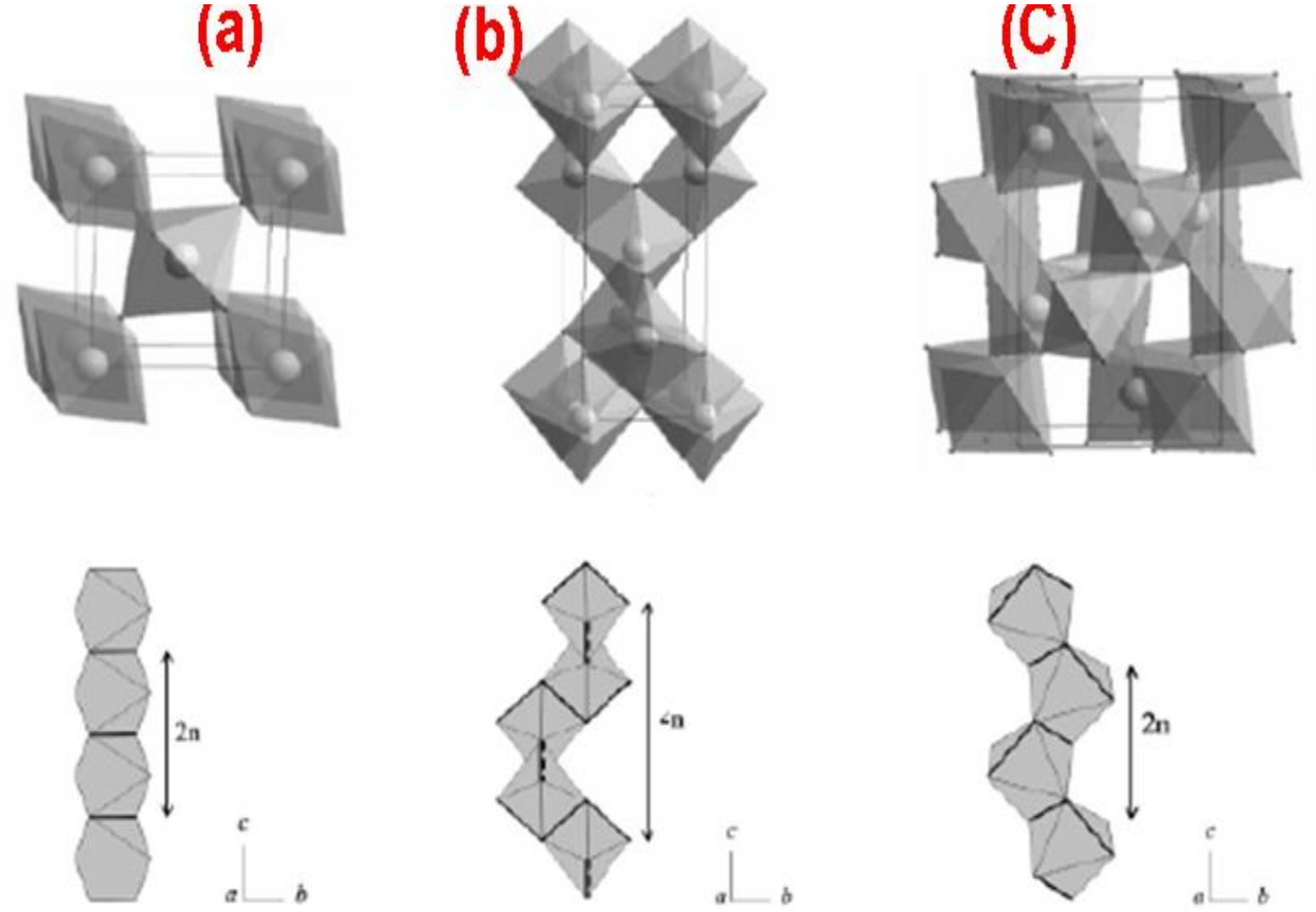
(a)
(b)
(C)
2n
4n
2n
c
a
b
c
a
b
c
a
b

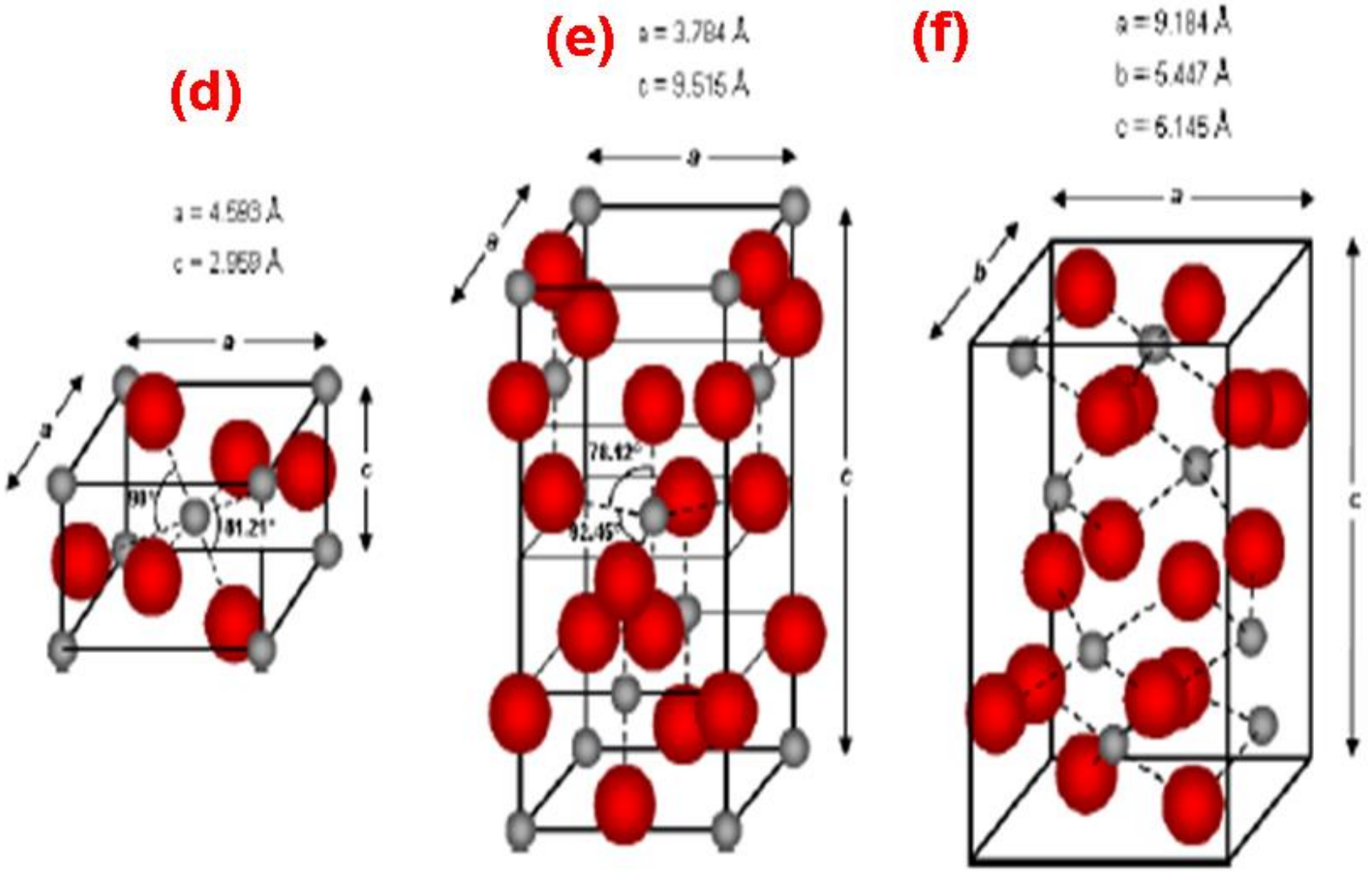

Figure 4: The TiO_2 configuration of rutile (a) & (d), anatase (b) & (e), brookite (c) & (f)

2.2.3. Electrical and optical properties:

Many authors such as Grant [15] have recently reviewed the electrical and optical properties of titanium dioxide. . Several experiments were carried out and the results were reported on electrical and electronic properties of the TiO_2 [125]. . . R. Asahi et al. have also reported in another study the electronic and optical properties of anatase **TiO_2** [115]. . In this section, the literature quoted is meant to give a background for the study conducted on the electronic transport phenomenon in TiO_2.

2.2.3.1. Electrical properties

Generally, oxides are classified as either insulating materials or semi-conductors[24]. Titanium dioxide does not make an exception to the rule. As it will be shown in the following lines, intrinsic or stoichiometric TiO_2 is an insulating material, whereas non-stoichiometric TiO_2 is of n-type semiconductor. The ability difference between an insulator and a semiconductor to conduct electricity is explained adequately in the band theory of solids. Accordingly, insulators have a gap between occupied and empty levels, so that electronic conduction is impossible in the ground state. Whereas, in a semiconductor such as silicon or germanium, the valence band is filled, but the separation energy or band gap between the filled valence and the nearest conduction band is small, compared to the large bandgap in the insulator material such as diamond, glass or rubber. At room temperature, thermal energy possessed by electrons is sufficient to promote some electrons to the conduction band, and a small degree of electrical conductivity is observed.

Titanium dioxide, in particular, in its intrinsic or stoichiometric form, is considered a poor insulating material (d^o insulator). It shows some degree of semi-conduction. Its intrinsic semi-conduction arises from the thermal excitation of electrons and holes across the bandgap.

Like most transition metal oxides, the bandgap is sufficiently large that intrinsic carriers are usually swamped by those introduced by defects and impurities [26]. It shows other properties expected of insulators such as:

- No optical absorptions at energies less than the bandgap,
- Are diamagnetic with no unpaired electrons,

- They are susceptible to loss of oxygen, which gives rise to semiconducting properties.

2.2.3.1. Optical properties

Cox describes the optical absorption of TiO_2 (rutile) as being characterized by the production of free carriers, corresponding to true band-gap transition without a strongly bound exciton being formed. At lower temperatures, a more complex structure is shown. A small exciton peak about 4meV below the main edge at 3.035eV, and the edge itself has a second exciton line superimposed (1s and 2p). Very small binding energies are expected because of the high dielectric constant. Higher-resolution spectra measured in two polarizations at 1.6K indicate some dichroism at the edge, lower energy, and the lower-energy features being observed only with the electric vector of the radiation polarized perpendicularly to the c axis.

2.2.4. Phase transformations:

Besides the thermal expansion coefficient, it is necessary to take into account changes in dimensions that occur at different points of transformation when there are many polymorphic forms, such as the case of TiO_2. The melting point, as well as the points of transition for the TiO_2 polymorphs is given in the table. These transitions are sometimes accompanied by modifications of structure and other properties.

Phase changes induced in TiO_2, a single component system, as said earlier, by changes in temperatures at a fixed pressure, say 1 atm, are of polymorphic transformations type. In such transformations, different crystal structures are found to be stable over different temperature ranges - Here, stability should be understood as “no tendency to change under the thermal influence”.

Many material scientists agree on the transformation process from anatase or brookite to rutile. [10]. Anatase and brookite polymorphs were found to be metastable from ambient temperature up to ~ 700◦C, and are converted to rutile when heated to temperatures between 700ºC and 920◦C [17]. On the other hand, Zhang has disputed the claim by Ye et al. that brookite transforms to anatase or vice versa, and then transforms to rutile. Nevertheless, admitted the possibility of reversibility of transformation between anatase and brookite at lower temperatures (below350◦C).

The enthalpies [10] of transformations are –3.26 and –0.71 respectively. Transformation enthalpies of anatase-to-rutile and brookite -to-rutile indicate that the thermodynamic phase stability for the three polymorphs is: rutile > brookite > anatase. Therefore, it was then established that anatase transforms directly to rutile /or brookite before it transforms to rutile.

Phase changes induced in a material could also be studied concerning applied pressure (P) at any given temperature (T). Different from the previous consideration, whereby the equilibrium temperatures at a specific pressure of 1 atm, here we consider other pressures, higher than 1atm, at which the equilibrium temperatures will differ. Clausius-Clapeyron equation[19] is applicable in our case. Therefore, these changes corresponding to a definite point on the equilibrium curve would be related as per equation:

$$\frac{dP}{dT} = \frac{\Delta S}{\Delta V} \qquad \text{eq.1}$$

Where, ΔS is the change in entropy, ΔV is the change in volume of the same quantity of substance as it undergoes a phase transformation from phase 1 to phase 2.

Furthermore, the study of phase transformation requires the determination of the equation of state to find the bulk modulus, B_o. The values of the latter indicate the degree of compressibility of the material. The higher the value of B_o, the less compressible it is and the harder the material is believed to be. Arlt [104] determined experimentally the equation of state of anatase TiO_2, using single crystal as well as polycrystalline material. For each phase, pressure-volume had been described as per equation of state. [105].

Still, from the work of many authors, it can be shown that the TiO_2 phase transformation could take a different route depending on the starting material, either anatase or rutile. When anatase is used as a starting material, the sequence of transformations with increasing pressure seems to follow either route1 or route 2 model such that:

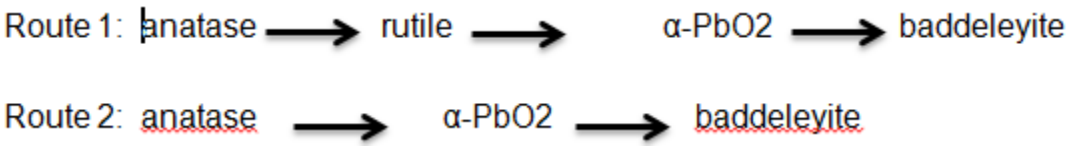

In their study, the single-crystal anatase tetragonal transformed into the orthorhombic between 13 GPa and 17 GPa. These results were also obtained by Larec and Desgreniers [23]. But, they were found to be 258 GPa for the α-PbO_2 phase and 290 GPa for the baddeleyite phase (ZrO_2). Whereas, Sato reported the formation of baddeleyite above 12 GPa. When he conducted a similar high-pressure study of anatase TiO_2 up to 49 GPa. Only two phase transitions were observed: columbite (orthorhombic α-PbO_2) and baddeleyite (ZrO_2) structures. Baddeleyite, in contrast, was found to be much harder than the rutile structure.

Haines found phase-transitions: columbite-orthorhombic (α-PbO_2) and baddeleyite (ZrO_2); bulk modulus, Bo: 59 GPa (anatase) and 98 GPa (α-PbO_2); comparative compressibility of rutile was four times greater than that of anatase ; and double that of α-PbO_2; preservation of phase-transition up to 12 GPa when rutile is compressed from room-temperature; at 15 GPa baddeleyite-phase starts forming and phase-transition is completed at 20 GPa, and null phase-transition observed till 60 GPa-compression is reached.

The Oxygen over Titanium ratio, also known as bulk effect, also affect the pahase diagram.

Looking at data gathered by Samsonov [24], it can be seen that the titanium–oxygen phase diagram is very rich with many stable phases with a variety of crystal structures, and consequently Diebold [12] has also shown that these intrinsic defects result in n-type doping and high conductivity.

Despite the similarity in electronic structure, anatase and rutile show different electrical and optical properties [6]. For example, the donor level is very shallow and the nature of the exciton states is self-trapped in anatase, whereas that of rutile is free, anatase has a large bandgap [13] of 3.2 eV, whereas rutile has a bandgap of 3.0 eV.

The non-stoichiometry problem is, as said earlier, is inherent to TiO_2, particularly at high temperatures. In practice, semiconducting behavior is characteristic of defective or non-stoichiometric oxides. These include reduced d^o compounds such as TiO_{2-x}. Tunstall et al. And Hill et al., have demonstrated that many transition metal oxides, including TiO_2, show the phenomenon of non-stoichiometry, where elements are not present in simple integral proportions. The latter is associated with defects due to the high concentration of oxygen vacancies in the case of non-stoichiometric TiO_2, making it a semiconductor. Kofstad has shown the dependence of the value of x in TiO_{x-2} as a function of the reciprocal absolute temperature and oxygen pressure. Furthermore Jarzebski has consistently demonstrated that this type of defect in TiO_2 depends on the temperature of thermal treatment. But the question becomes: how does it resemble known semiconductors, such as elemental semiconductors, silicon, and germanium?

According to Grant, "the imperfections in non-stoichiometric TiO_2 are oxygen vacancies possibly associated with Ti^{3+} ions. These centers would act as doubly charged donors giving rise to two observable activation energies in the electrical resistivity and the optical absorption". Also, in the case of reduced TiO_2, electrical conduction is done by 3d electrons.

Diebold's finding [12] that TiO_2 is the n-type semiconductor since it could be reduced easily at high temperatures. This agrees with what Grant said, it can then be stated that, in the case of reduced TiO_2, electrical conduction is done by 3d electrons.

2.2.5. Electronic transport:

Electronic transport in the semiconductor TiO_2 is characterized by parameters such as electrical conductivity, Hall Effect and, Seebeck (thermoelectric power). The Wilson and Somerfield model is usually used to interpret these properties. The model assumes spherical symmetry of energy surfaces and introduces parameters such as bandgap energy E_g, scalar effective masses of electrons (m_e^*) and holes (m_h^*), mobility of electrons μ_e and holes μ_h, concentrations of donors [D] and acceptors [A] and, ionization energies of donors E_d and acceptors E_a .

Temperature dependence of electrical conductivity and Hall Effect properties have been investigated in rutile by Becker and Hosler. The effect of annealing at various temperatures and various oxygen pressures resulted in the conductivity of 10^{-6} to 10^{2} Ohm^{-1} cm^{-1}. The hall mobility was shown to be independent of the concentration of current carriers and amounted to 0.2 cm^2/Vs at room temperature, activation energy (4 to 8) x 10^{-2} eV. Anisotropy and its temperature dependence, like those of other electrical properties, were observed by many other authors, namely Bogomolov, Shavkunov and Zhuze, and Cronemeyer. Also, Frederikse measured the room temperature (300^{o}K) resistivity value of 0.1 to 10 Ω.cm, an effective mass of 12 to 32 $m_{o,}$ on rutile single crystal samples.

Cox describes the optical absorption of TiO_2 (rutile) as being characterized by the production of free carriers, corresponding to true band-gap transition without a strongly bound exciton being formed. At lower temperatures, a more complex structure is shown. A small exciton peak about 4meV below the main edge at 3.035eV, and the edge itself has a second exciton line superimposed (1s and 2p). Very small binding energies are expected because of the high dielectric constant. Higher-resolution spectra measured in two polarizations at 1.6K indicate some dichroism at the edge, lower energy, and the lower-energy features being observed only with the electric vector of the radiation polarized perpendicularly to the c axis.

2.2.6. Photocatalytic properties:

TiO_2 is well known for its ability to degrade photo-catalytically a wide range of substances including organic materials and particularly cyanides. Uniheidelbelberg says that the effect of illumination (UV light) of "photo-catalyst increases the "rate" of "chemical "reaction" because of the decrease of the "activation "energy. Following the chemisorption of surfaces, the particles present are prepared consequently for speedy participation, most likely fragmentation type of reaction.

The basic idea of the photocatalytic activity of TiO_2 was discovered by Fujitsuma and Honda. By inserting a TiO_2 electrode in a bucket of water, connecting it electrically with a Pt counter electrode, and shining light (UV), they dissociated water into oxygen and hydrogen. To extend the absorption in the visible light spectrum,

Graetzelincreased the surface to volume ratios using highly porous 20 nm TiO_2 nanoparticles and the dye.

Let's notice that the large surface-to-volume ratio (small-sized particles) influenced significantly the photocatalytic activity. Another factor influencing the photocatalytic activity of the TiO_2 is the phase (structure). It has been shown that among the three phases of TiO_2 namely, anatase, rutile, and brookite, anatase is the best photocatalyst.

San-Gi. describes a multi-step reaction giving an account of the development of the H_2 production in the degradation process of cyanides, facilitated by the action of the TiO_2 photocatalyst.[126] as follows:

(i) The illumination of TiO_2 by ultraviolet irradiation results in the creation of electron-hole pair (h+, e-) at the surface of the TiO_2 as per reaction step:

$$TiO_2(e,h) + h\upsilon \longrightarrow h^+ + e^-$$

(ii) dissociation of water:

$$2H_2O \longrightarrow 2H^+ + 2OH^-$$

(iii) production of H_2 molecule

$$2e^- + H^+ \longrightarrow H_2$$

(iv) formation of hydroxyl radical

$$2h^+ + 2OH^- \longrightarrow 2OH^-$$

(v) oxidation of CN^- ion by hydroxyl radical and formation of harmless ion OCN^-

$$2OH^{\bullet} + CN^- \rightarrow OCN^- + 2H_2O$$

2.2.7. Gas sensing properties

The sensitivity of the large band-gap semiconductors-based sensors depends on the conductivity of the surface of sensors, which is influenced by the nature of the adsorbents, the number of electrons released as a result of chemical interactions

between the surface atoms and molecules, and the adsorbent. This statement is drawn from the theory of chemical sensing of large bandgaps such as SnO_2(3.5 eV), TiO_2 (3.0 eV), ZnO(3.2 eV), Fe_2O_3 (2.2 eV), etc semiconductors, which states that atoms and molecules interact with the semiconductor surfaces influencing their conductivity and surface potentials. According to Seiyama and Taguchi, “semiconductor "oxides make better gas "sensing" materials than "organic as well as "elemental semiconductors ones. Furthermore, they argue that "detection of the reducing gases is based on the "increase of the semiconductor's conductance.

The sensitivity of the sensor is dependent upon the fact that: "oxidation of organic matter in presence results in a decrease of "oxygen "ions together with free-electrons, consequently, the rise of conductivity. By contrast, a decrease of conductivity emanates from "conduction "electrons being attenuated because of unstable "adsorption of "electron "acceptors. However, the selectivity of the sensor is dependent upon the effect in adsorption or reaction different substances have at the metal oxide surface; the differences in the extent of the effect define the selectivity of the sensor.

2.2.8 Anti-bacterial properties:

Piskin lists "antimicrobial capabilities in various fields using M-oxides such as titanium dioxide. These include industrial environment utilities: "food, "synthetic clothing, "health "care, "packaging, "medical items, and non-industrial, day-to-day employed by people, catalysts namely: "sunscreens, "cosmetics, pharmaceuticals, and fuel. Also, Verdier has shown that the TiO_2 nanoparticles either used alone or in coatings, do have the anti-bacterial effect on E.coli bacteria [127].

CHAPTER 3: PRINCIPLES OF LYOPHILIZATION

Underlying the principles of the lyophilization Process, they are an overview of basic rules to be followed at each step for a successful product. The points listed below are further discussed considering the synthesis of ceramic compounds by the spray-lyophilization method. The latter method is used as materials properties optimizing tool for photocatalytic applications (in particular water purification). The properties include: highly porous, high surface properties (surface area, mono-dispersity i.e. narrow size distribution), etc.

The points that are covered are:

1. Define the Spray-lyophilization process as per prospective application.
2. Outline of the lyophilization process
3. Freeze-dryer equipment. (freeze-dryer)
4. Properties of Lyophilized materials
5. Principles for Aqueous synthesis (pH~7) of TiO_2 nanoparticles (powders)

3.1. Definition of lyophilization:

Each process, considered either a single or multi-step one, has its requirements. So does each Freeze-drying of the product or formulation. For instance, consider the environmental cleaning process, by evaporating volatile compounds in aqueous dissolutions of compounds that could lead to the drying of oil spills; eventually, the process will produce a non-porous cake of residues. But because the porosity in the dried product is lacking, and yet a key element, the process will not be defined as lyophilization or freeze-drying process. However, a more universally accepted definition by the scientific world is required, mainly because of the porosity of the dried product, and ability to resorb the solvent, the feature is known as “lyophilic”, Rey L.R, (1976) at the International Symposium of freezing Drying; being the first to use the word lyophilization by equating it to freeze-drying and suggested several steps generally adopted till today. According to Jennings, the proper definition of lyophilization for aqueous and non-aqueous products is a stabilizing process comprising firstly by the freezing step of the substance; secondly, the double minimization of the solvent, first by sublimation (primary drying) followed by

desorption (secondary drying). The cutoff limit of the minimization of the solvent is the value whereby no biological growth or chemical reactions is expected to happen.

However, John Barley (SP Scientific) focusing on the drying method by sublimation and the removal of bound water molecules by lyophilization process defines in these terms:: “ freeze-drying is the removal of ice or other solvents from material through the process of sublimation and the removal of bound water molecules through the process of desorption”.

Based on merged-definition Jennings T.A-Barley J., we develop the following outline of lyophilization focusing on formulations stabilization principles, and principles based on the removal of free and bound water from formulations.

3.2. The Outline of Lyophilization Process

What follows is a glimpse of the lyophilization process and the freeze-dryer, presenting basic steps and describing the equipment (freeze-dryer). The atomization process is included as an essential step for producing fine powders of desired sizes ranging from nanoscale to microscale.

3.2.1. The formulation

Defining a formulation, (physical chemistry term), means making a sample of matter in which substances in different phases are in equilibrium. The solvent is one of the phases that should be removed to enhance the stability of the formulation. The other phases are the substances that would be stabilized. Generally, these could comprise lyophilized samples such as biological, diagnostic (in vivo and in vitro), pharmaceutical, and veterinary products. Apart from their active components, these formulations could include stabilizing substances in the liquid phase. .

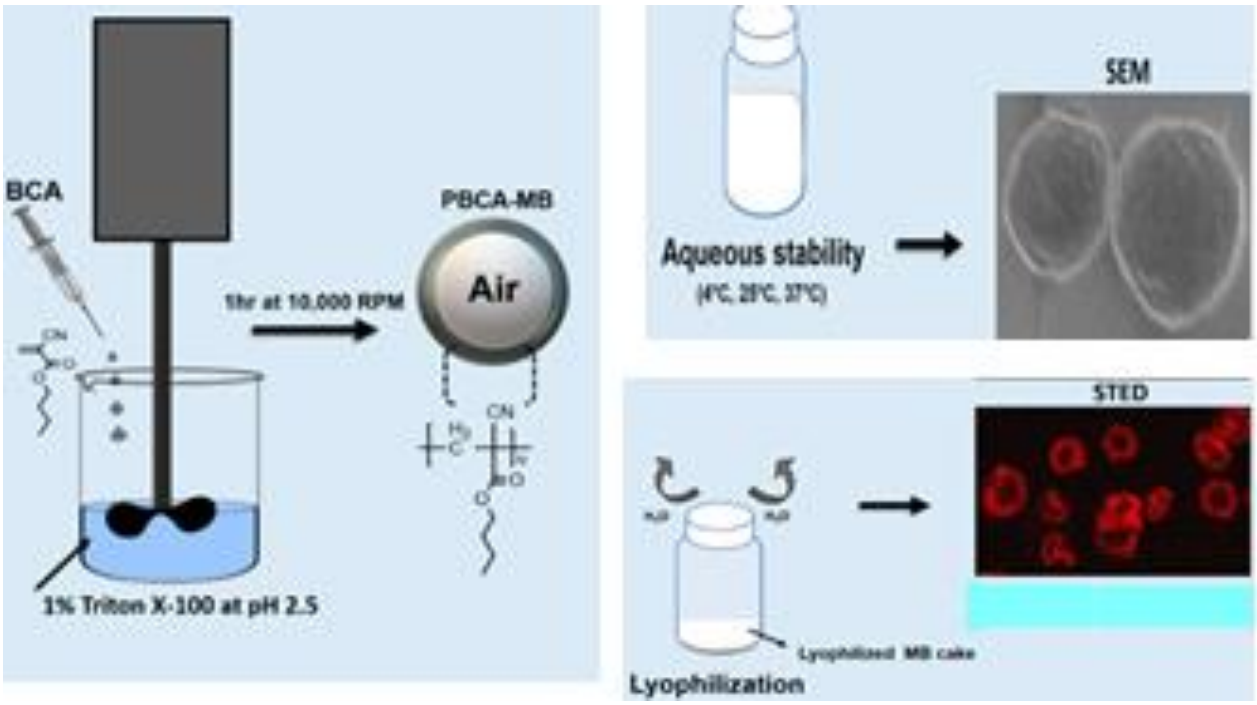

Figure 5: The preparation and 20 weeks–traced physical changes of stabilized aqueous Poly (n-butyl cyanoacrylate microbubbles formulations and its lyophilized cake produced

The Figure above is a modified image showing the preparation and 20 weeks–traced physical changes of stabilized aqueous Poly (n-butyl cyanoacrylate microbubbles formulations and its lyophilized cake produced. It also shows the SEM and STED micrographs of the stabilized and lyophilized formulations [128]

3.2.2. The atomization:

By atomizing bulk liquids or formulations, the process breaks it into tiny particles, also said small droplets. Sometimes it is called the spraying method, whereby the bulk liquids are broken into small droplets under the effect of high-speed gas/air / inert gas/fluids with centrifugal forces. The atomization process is the most known method of producing powders of various particle sizes, ranging from nanoscale to microscale, depending on the size of the nozzle. The figure below shows a uniform, round-shaped spraying pattern for medium to large-sized drops.

(a)

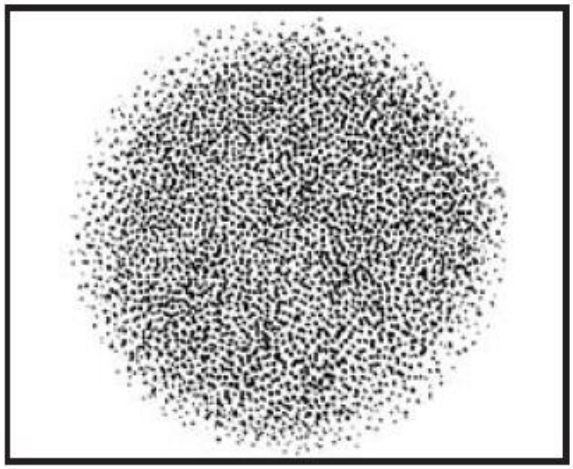

(b)

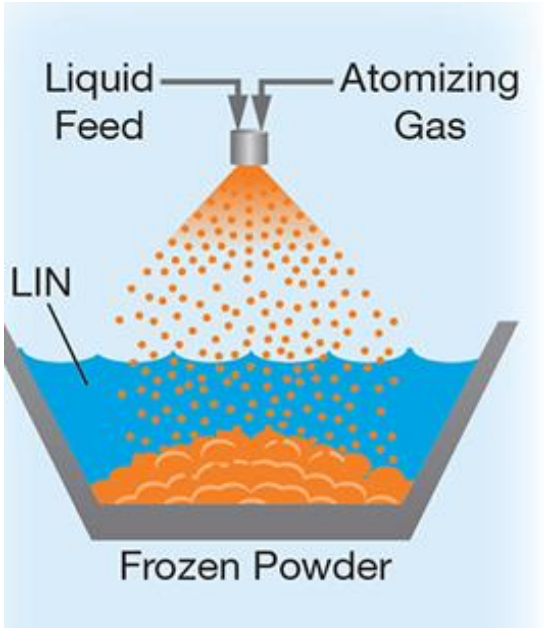

(C)

Figure 6. The Schematic diagram of the atomization process

The atomization includes the following steps:

(a) The formulation is sprayed using the nozzle under pressurized gas/air, (b) the homogeneous (uniform) particle distribution, (C) formation of powder as the droplets

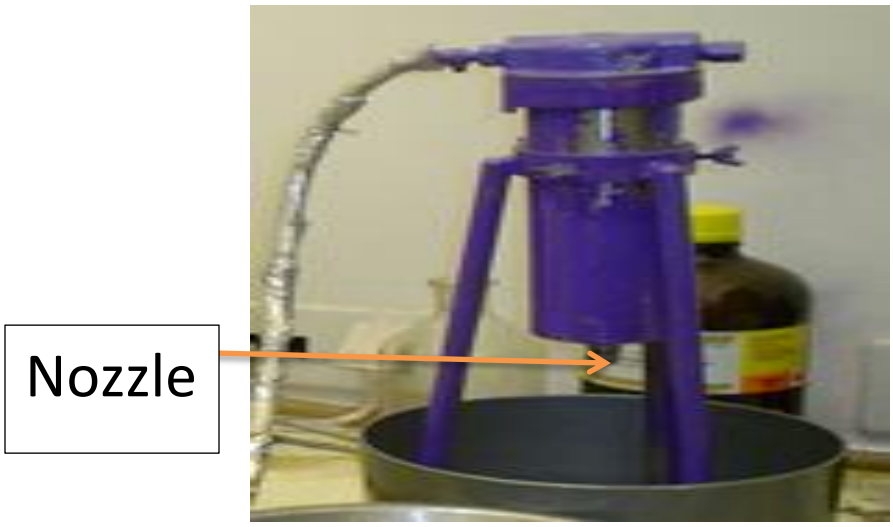

Figure 7. The picture of the atomizing apparatus

The SNOW Technology elaborates the principle of atomization –freezing as follows: By applying high pressure (compressed gas), it atomizes the formulation in fine droplets. In that, when the formulation reaches the "snow-gun", due to the high pressurized gas/air, the nozzle splits it into droplets. If the released droplets are released in a cold medium such as liquid Nitrogen (-196°C), they are frozen and crystallize informing "snow-like" powders, the so-called snowflakes.

3.2.3. Freezing

By freezing, it separates the solvent, water in the case of aqueous formulations, from the solutes, the ice crystals are formed and the solutes are confined in the gaps between ice crystals. Total freezing requires temperature depending largely on the nature of the solvent and other components of the formulation. Thermal properties of the latter and its ability to freeze-dry in a reasonable period could be affected.

3.2.4. Primary Drying

Frozen formulations obtained at atmospheric pressure are now placed in the freeze-dryer, whereby the pressure has been reduced to vacuum and heat being applied to the formulations triggering sublimation of the ice crystals. As the sublimation process continues, solvent vapors are generated and the ice-gas gap recedes through the cake. By totally removing all the water/solvent as well as other volatile components

and all ice crystals are gone from the formulations, the primary drying cycle has been completed. As a result, the volume of cake is comparable to that of the frozen matrix **i.e.** the space in the cake was once filled with solvent, it has now become porous.

3.2.5. Secondary Drying

Even when the primary drying is done, a certain amount of water should be present due to adsorption on the surface of the cake. The build-up of moisture is a function of temperature and the kind of components of the cake. The degree of moisture could be estimated much higher than 5% up to 10% in terms of the weight ratio of the dried cake. As a result, the targeted stability in the final product will be impaired with such high moisture percentage. Therefore, to meet the targeted stability, it is required that the amount of moisture content in the cake be reduced further using desorption while ensuring the volume of interstitial cake remains intact. In the final analysis, the secondary drying is completed through desorption of the remaining water by raising the temperature of the cake and lowering the partial pressure of water in the freeze-dryer. The secondary drying is also the final stage of lyophilization.

Figure 8 below, shows the evolution of freeze-dried samples of bovine pericardium at 2.23 Pa and 1.5°C. The light-region, that contrasts the dark region, is the amount of water (solvent) that diminishes with increasing time, from region (A) 8min, region(B)15min and, region (C).

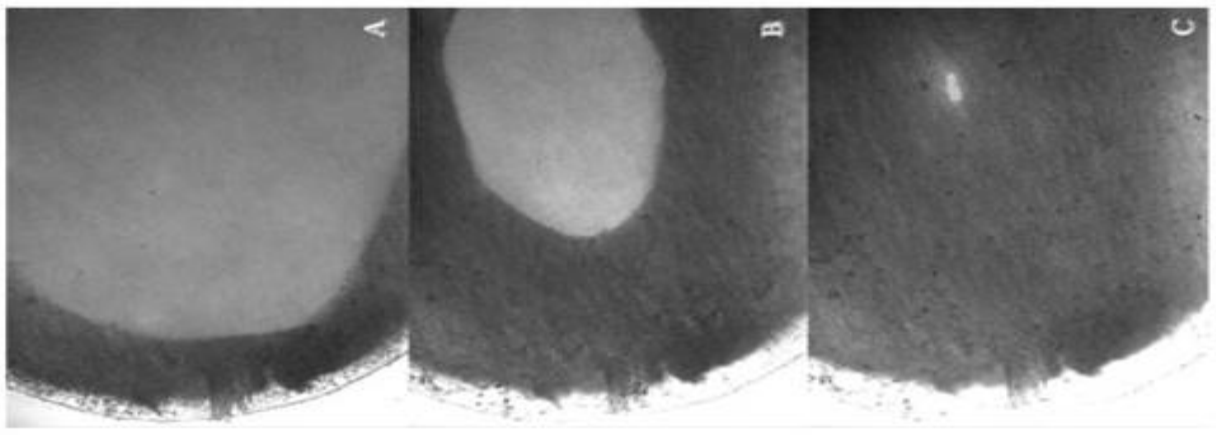

Figure 8. Evolution of freeze-dried sample of the bovine pericardium

In he the figure above, the light area shows depletion of a certain amount of water (solvent) with increasing freezing-drying time: region (A) after 8min, region (B) after15min, an

3.2.6. Airtight sealed environment:

The lyophilized product is kept safe from any external influences (temperature, moisture, etc.). The tight closure is achieved by the stoppering mechanism for as long as the product can be permanently removed from the freeze dryer.

3.2.7. Freeze-Drying Equipment (Freeze-Dryer)

Figure 9. CHRIST 2000 Freeze-Dryer, 40L, and minimal temp. (-55C)

Describing the freeze-dryer consists of some key components associated with major functions. The figure (S. Von Graberg, 2011) is an illustration of the freeze dryer showing the main components.

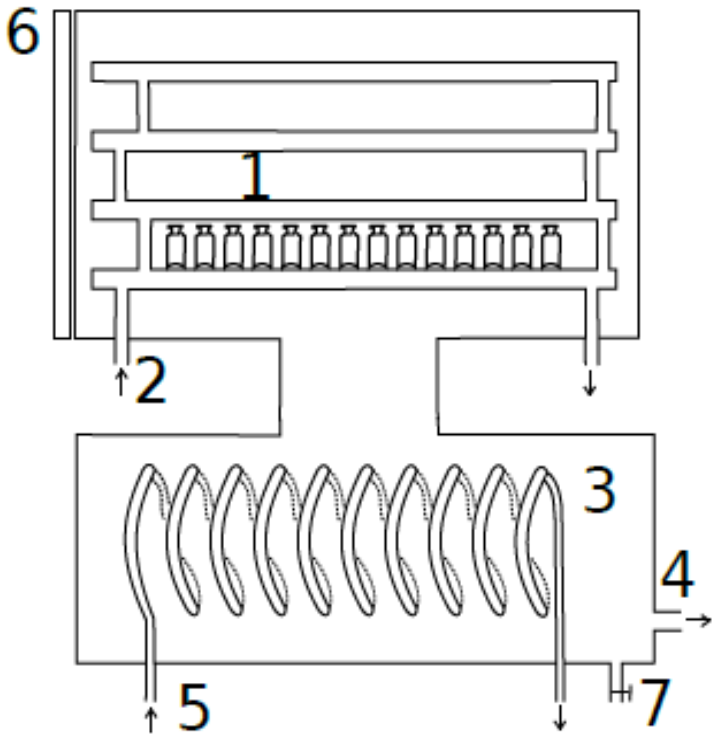

Figure 10: Freeze-Dryer; 1- Drying chamber; 2- Inlet for heat transfer; 3-condenser; 4-vacuum pump connection; 5-Inlet for condenser; 6: freeze-dryer door; 7-drain for water from the condenser

3.2.7.1. The Freeze-Drying Chamber*:*

Each Individual step of the lyophilization requires a safe environment for the product and adequate temperatures as well as pressures. These requirements are met through the freeze-drying chamber. The main parts of the chamber include: metal vessel, hinged door, usable and unusable shelves, the hydraulic ram system, pressure gauge, thermal insulation, the condenser surfaces, trays, and the vacuum pumping system. While the product is loaded on the usable shelf, the unusable shelves serve for shielding from radiation for the upper shelf. Heat transfer fluid flows through the hallowed shelves (serpentine). The heat-transfer fluid can either be chilled or heated to provide the required energy for the primary and secondary drying processes.

3.2.7.2. *The condenser Chamber:*

Describing the condenser chamber serves to contain the condenser surfaces that degas water vapor of remaining gases from the drying chamber.

The effectiveness of the condenser plates depending on their operating temperatures, it should maintain the temperature at minimum at 20°C below the product temperature during the primary drying process. Whereas, the chilling of the shelves of the dryer by a heat-transfer fluid as it expands directly, will refrigerate the condenser surfaces as a whole.

3.2.7.3. The vacuum pumping system

The required pressures to drive the primary and secondary drying are provided by the combined action of the vacuum pumping and the condenser systems. There exist oil-lubricated vacuum pumps and non-lubricated mechanical pumps. Non-condensable gases passing through the condenser are compressed by the vacuum pump and discharge the gases in the environment.

3.3. PROPERTIES OF LYOPHILIZED MATERIALS

Here are the main physical properties of the lyophilized products/formulations:

Stability: Lyophilization process will not be justified if it were not for its capability to enhance the stability of the formulation. The latter is defined as slowing down the kinetic clock for the deterioration or decline of the potency of the active component. There exists an acceptable range (110% to 90%) of potency or activity values whereby the product is said to be stable. The expiring date is determined as the length of time the totality of the lyophilized formulation maintains its potency limits.

Determining the stability of the lyophilized product applies two techniques namely: accelerated stability and long-term (real-time) studies.

3.3.1. The long-Term or Real-Time Stability method:

The temperature and humidity for storage of the lyophilized formulations are chosen the same conditions of temperature and humidity for long and real-time stability studies. At

chosen and regular time intervals, the potency or activity of samples is tested. This testing could last for years and the results used to determine a window of the period for the stability of the dried product, and the corresponding expiration date being allocated to that series of samples.

3.3.2. The accelerated Stability method

Keeping the dried product in the controlled condition of humidity (say, 50%), at fixed or elevated temperature (say 40°C), accelerates the rate of the kinetic clock. Then at chosen regular intervals of time samples of dried formulations are removed and tested for potency or activity. The stability measure of the dried period is determined by no variation in the distribution of potency during the period of investigation.

The method of accelerated stability testing is only valid in diagnosing the thermal instability in a series of dried formulations. Unlike the long-term method, it cannot be used to determine the overall stability of the product or be used to determine the expiration date. However, this method finds its application in the correlation of the results with the stability of the product as specified from a long-term approach.

3.3.3. The physical properties (appearance) of the lyophilized formulations:

To different extents, each step of the lyophilization, freezing, the primary drying, affects the appearance of a lyophilized product. The uniform cake structure is a result of the ice structure that is formed during the freezing process. Uniformity characteristic is also known as the ideal structure (sponge-like) that is caused by primary drying resulting in inequality between cake volume and the volume of the frozen matrix. However, a poor primary drying process could create a heterogeneous condition, whereby the product matrix is not a completely frozen structure (amorphous), with the worst heterogeneous appearance being the partial collapse of the cake structure.

3.3.3.1. Free water:

The formation of ice-product can be accompanied by the production of so-called “free water”. The latter is either water that has crystallized during the freezing process or water from a solution with other elements constituting the formulation. Achieving the

desired product stability, the free water is required to be cut down by desorption to a ratio amount inferior to 1% of its weight over the final dried product.

3.3.3.1. Bound water

While free water participates in the formation of either ice-matrix or the solid solution that contains the solutes, bound water instead is that water that builds up the stability of the active constituent of the lyophilized formulation. Explaining further the idea of bound water, this is that amount of water that maintains the so-called “folding configuration “of a protein molecule, and if it were taken out, the protein would lose its configuration but also would stop functioning. In principle, for a successful lyophilization process, the amount of free water must be cut down, but not the amount of bound water, which is an integral part of the active constituent of the formulation.

3.3.3.2. Reconstitution

Restoring lyophilized formulations to initial conditions, a specified amount of diluent (water in particular) is added to the dried cake. As a result, the dilution should take less than 1 minute and should be complete. Its inherent attributes namely, the potency of the active constituent and pH value, should be comprised in the same authorized range of values of the original formulation. The results of either a failed lyophilization process or malfunction of the freeze-dryer are indicated by excessive long reconstitution times, diminution of potency and, /or formation of turbid solutions.

3.4. Principle of optimization of lyophilization process

3.4.1. Optimization problem

Based on the flow of activities constituting a product development process, for example, a drug or sucrose (W.J. Sichina, Perkin Elmer Instruments), which will rapidly be ingested or dissolved in water (aqueous formulation), optimization is needed. Defining the steps of a lyophilization process problem, consists of cooling the aqueous formulation below ambient temperatures and applying a vacuum to remove the free water. Because of energy consumption concerns, finding out the maximum acceptable temperature to which the solution can be cooled before a vacuum is applied is critical. The maximum temperature must be inferior to the glass transition temperature of the product to prevent the crumbling of the freeze-dried cake. This

maximum temperature for the lyophilization of the product is also known as glass transition temperature (**Tg**), it is one critical parameter that has been identified to deepen the understanding of the lyophilization process for a given formulation, and set during the primary drying. Also, the extent to which heat capacity (ΔCp) is varying at Tg, accompanied by recrystallization event requires sufficient information to bypass glass temperature, and this would determine the success or failure of the drying process. Therefore, accurate glass temperature data collection is needed for an optimal primary drying process.

3.4.2. Optimization solution by DSC (differential Scanning Calorimetry)

Trial-and-error-method for generating accurate maximum temperature allowed for each product would be time-consuming. Instead, the differential scanning calorimetry offers the answer to the question of how?

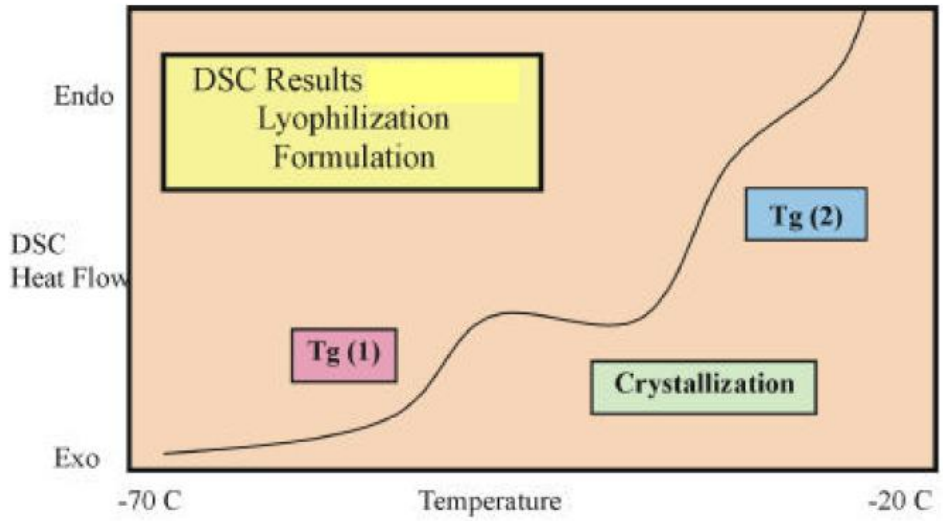

Figure 11. Plot of Differential Scanning Calorimetry (DSC) results for lyophilization Optimization

To address the main issues surrounding the production of a successful lyophilized material, aqueous lyophilization *formulations*, in particular, W.J. Sichina (Perkin Elmer Instruments) describes the concept development for sucrose by measuring the following parameters: temperature of Tg(s), the magnitude of Tg(s) or ΔCp, and occurrence of recrystallization

(1) The analysis is conducted in an open aluminum pan since the properties of interest are below 0 C. Between 10 to 20 mg of the solution is injected into an open pan and then analyzed with the DSC.
(2) The sample is quickly cooled to a temperature of -75 C, held for 5 minutes, and then heated at a rate of 5 or 10 C/min back to room temperature.

Displayed in the figure above are the DSC results representing those obtained from a solution containing 5% sucrose. The results are presented in high sensitivity scaling emphasizing the small transitions below the main melting transition of the ice phase. The Tg of this solution is observed at -45 C. Upon further heating, the solution may undergo recrystallization at -39 C. There is evidence that formulations show recrystallization event during heating will lyophilize successfully regardless of the product temperature and the magnitude and temperature of Tg. At approximately –27 C, a second, higher temperature Tg is believed to occur. The exact nature and interpretation of the DSC results obtained in the sub-ambient regions on sucrose solutions or formulations is a matter that is still being researched and discussed. However, the proper understanding of this transition is certainly critical for obtaining a better handle on the overall freeze-drying process.

3.5. Principles - Spray-Lyophilization for the synthesis of nanoparticles

The starting idea of the Spray-Lyophilization technique is a liquid phase synthesis method that precipitates nanoparticles from an aqueous solution of the Titanium precursor compound. However, the overall process carries out principles that are based on four main concepts namely:

1. The chemical products by design using lyophilization, a physicochemical method that manufactures nanostructured materials from precursor solutions, should be chemically **stable** and **homogeneous** (composition) with a long shelf-life.
2. The control of the characteristics (properties) of the lyophilized product is achieved in consideration of the application of principles of Chemistry, in direct dependence relation to precursor solution variables during its preparation and processing (Freezing-Drying). As a result, the lyophilized materials are 1). **Physically homogeneous** (monodispersed), 2) **nano-size**: **1-100nm;** with **narrow -size distribution**, and); 3. **Mono-phased polymorphs** (nanostructured), obtained as a

result of the **optimized process**; 4. Various **optimized morphologies** (well-shaped defined) are obtained,

3. The Nano-technological strategy is a **green method** implemented in four-step materials processing namely: 1). Precursor solution selection; 2). Atomization though Spraying; 3). Freezing in a liquid medium (e.g. He, N2); 4). Drying by sublimation of the solvent in a conditioned environment (chamber), 5). Decomposition / Annealing (Calcination) in a controlled atmosphere.

4. The first and second laws of thermodynamics are applied as theoretical background explaining and estimating **optimal parameters in transport** phenomenon and in consideration of necessary **phase changes** (transformations) required to make quality Nanoparticles

3.5.1. Dissolution and homogenization of the precursor solution

To make nanostructured materials from precursor solutions, the solutions must be **chemically stable** and **homogeneous (composition)**, a **single phase**. Solutions are described as homogeneous mixtures of two or more compounds, which can be gaseous or liquid, or solid. In context, considering only liquid solutions and solid solutions, and the two terms frequently discussed when dealing with solutions, solute, and solvent. Liquid solutions are formed by dissolving a gas, liquid, or solid in a liquid. The terms solute and solvent go hand in hand with the concept of solution. The solvent is the substance in a large amount, while the solute is the substance in a smaller amount. Also, the term solvated is used to describe species that result from the interaction of one or more molecules of solvent and solute. In the case of an aqueous solution, instead of solvated, the term used is hydrated. If the latter is water, the solution is termed an aqueous solution. Whereas, the solid solutions are those in which one component is dispersed on an atomic scale in another component.

3.5.2. Primary Nucleation, phase homogeneity (percent phase composition) by a solvent molar factor, and particles' size distribution effect

Consider the kinetic representation of an aqueous precursor salt in solution, the precursor molecules are distributed randomly across the bulk solution. If the system is a pure crystal, the packing is in a certain order, however, the lattice points are occupied randomly by one or another kind of atom

A lot of chemical syntheses of nanoparticles are described by the primary nucleation model per definition by Mullin, J. W. (1977). This is understood as the process whereby nuclei or seeds are considered templates for crystal growth. Also, primary nucleation takes place without the presence of other crystalline matter. However, according to Nguyen T.K et al. (chemical review, pubs.ac.org/doi/pdf/10.1021/cr400544s)," the formation of porous solids does not always follow the classical pathways of crystallization in solution".

Homogeneous nucleation occurs when nuclei form uniformly throughout the parent phase, whereas, heterogeneous nucleation is formed due to structural inhomogeneity (surfaces, impurities, grain boundaries, dislocations). In the liquid phase, heterogeneous occurs much easier, since a stable nucleating surface is already present. The process of homogeneous nuclei formation can be considered thermodynamically 25,30 by looking at the total free energy of a nanoparticle defined as the sum of the surface free energy and the bulk free energy. For a spherical particle of radius r, the surface energy γ and the free energy of the bulk crystal (ΔGv), giving a free energy ΔG. The crystal-free energy itself is dependent upon the temperature T, Boltzmann's constant k_B, the super-saturation of the solution S, and its molar volume, v. ΔGv

3.5.3. Particle size growth by Solvent type and concentration factors

Generally, the difference in the particle interaction potential of individual solvent, following nucleation, causes the particles to grow in size by molecular addition or aggregation. This particle growth is affected by the kinds of solvents used (Nyamukamba P. et al. According to Moon Y.T. et al. (1995), "the increase in the amount and molecular weight of the "water/no-alcohol" mixture ratio was found to increase the size of the particles and, the smallest size was obtained in the experiment without. This is because an increase in both concentration and molecular weight leads to a decrease in the dielectric constant of the solvent resulting in decreased stability and enhanced rate of re-aggregation and larger particle size. Furthermore, Park J. et al. (2007) elaborates: " re-dispersing the product powders obtained in such a case, a set of three different solvents (ethanol, propanol,

methanol), results in the increase of the degree of aggregation following a typical pattern, namely: methanol > ethanol > propanol. In other words, the solvent having the least molecular weight in the group should show the highest degree of aggregation. It follows to say that the colloidal perturbation is the primary mechanism by which these solvents affect particle size".

3.5.4. Control of features of nanostructured materials via synthesis conditions

Extensive research in materials science and nanotechnology has been devoted to discussing the formation and manipulation of size, structure (phase) and, morphology (shape) of nanostructures. The principles underlying this activity have been investigated by analyzing specific synthesis methods, in terms of their content and the conditions essential for generating the requirements they impose on these features. This issue has been considerably addressed in several studies about identify and describe the qualities of nanostructured end product materials required by technological applications for successful performance.

The characteristics of the structure, size, and shape properties and the mechanisms by which they are created have been studied in connection with the analysis of materials selection in the nano-technological designing activity. This problem has been investigated most intensively as part of an analysis of the appealing conditions that create effective synthesis methods. It would be unthinkable to list all the works in this field. The underlying principles of controlling nanostructured features have been identified in terms of filling the gaps that only freezing-drying (Lyophilization) can address.

Freezing and freezing-drying of porous and nanostructured materials are processes that control parameters such as pore size, pore-volume, and shape. The latter is a function of aqueous solutions, organic solutions, colloidal suspensions, and supercritical CO_2 solutions. He implies that one effect of freezing aqueous solutions is the formation of a gradient concentration of the solute and the increase of the ice front. The ice grows as the result of the reduction of the melting point of the solution which formed a "constitutional super-cooling" zone that breaks down the "planar interface".

The formation of nanostructured particles and their characteristic features including size, crystallographic structures (phase) and, photocatalytic activity property are

controllable (Masoudeh Ahmadi et al., 2011). The controlling factors are the pH of the solution, the ratio of the initial concentration of the reactants of the aqueous solutions, colloidal suspensions and emulsions, calcination temperature, and aging time.

3.5.5. Residual water

The amount of time needed to eliminate the necessary quantity of residual water in the dried product, at the same time, keeping up the product quality intact is controllable by the product temperature below the maximum allowed value (glass temperature, $\mathbf{T_g}$), the optimal pressure applied, the residual ice content, and the mass-transfer operating conditions.

CHAPTER 4: EXPERIMENTS, RESULTS, AND DISCUSSION

4.1. Experiment I: Ti (III) chloride Precursor-based TiO_2 NPS

4.1.1. Objectives

(1)To investigate the size dependence of the anatase-rutile structural phase transition in lyophilized **TiO_2** nanoparticles.

(2) To investigate the effect of optimal solubility and low decomposition temperature (100-400°C) for the synthesis of **TiO_2** NPS, and

(3) To characterize the size and structure by XRD, the composition by EDS, and morphology by TEM, vibrational modes and, a high-pressure investigation by Raman spectroscopy.

4.1.2. The formulation prepared on basis of Ti (III) chloride precursor solution:

The solution preparation process was carried out as follows: In the first case, a certain number of moles concentration of $TiCl_3$ and a certain number of mole NH_4OH were dissolved in 250 ml distilled water (DW). The decomposition of hexahydrate titanium (III) chloride produced the $TiCl_3$ that was used such as $TiCl_3 \bullet 6H_2O \rightarrow TiCl_3 + 6H_2O$ (2) pH observation: After mixing of titanium chloride, ammonia, the color of the solution was observed in the beaker. The pH value of this solution was measured by pH test strips (Sigma Aldrich: P3536 range: 6.0 – 7.7, resolution 0.3 – 0.4 pH unit (3) Desired pH calibration: In the third step, the pH value of the solution was adjusted to the desired value (Ph~7.0) by using 1 mole NaOH and 1-mole HNO_3 solution (each in 100 ml deionized distilled water) and was added drop by drop.

4.1.3. Results

The TiO_2 quantum dots were synthesized by the lyophilization process using a Christ 2000 lyophilizer at thedvanced Nano-Materials & Nano-Scale Physics of the University of the Witwatersrand: Using the Titanium Chloride (III) $TiCl_3$ salt. The latter has been chosen as a precursor due to its significant water solubility and its relatively low decomposition temperature (440°C). After an optimization phase, the optimized solution of $TiCl_3$ was sprayed under the form of droplets (80µm in average/laminar flow) in liquid nitrogen. The frozen network has been transferred to the lyophilization vacuum chamber. The frozen slat network was submitted to a sublimation process. By controlling both the heating temperature and in-situ vapor

pressure, the water component was fully removed from the salt precursor. The obtained white precursor was eminently porous possessing a dendrimeric configuration

4.1.3.1. Thermogravimetric Measurements (TGA)

In order to determine the decomposition temperature, sample of the white porous precursor of $TiCl_3$,-based was analyzed by the thermo-gravimetric experiments. . The expectation was that the results could be different from the corresponding bulk liquid $TiCl_3$ on basis of free energy considerations. The figure 12 shows the corresponding thermogravimetric profile in a flow of oxygen-argon. A sharp drop in the profile is observed at about 200°C. As confirmed by X-rays investigations, this conforms to the total decomposition of the precursor resulting in a pure TiO_2 compound. This temperature of decomposition of 200°C is inclusively different from that of the bulk liquid $TiCl_3$ which is 440°C. The difference in the TGA results could be related to the high degree of porosity of the precursor which could minimize the free energy during the chemical decomposition. Knowing the decomposition temperature of the ultra-porous precursor, this later has been decomposed in the normal atmosphere for 10 minutes. Such duration has been fixed to obtain quantum-dots / nano-particles of TiO_2 with an average size of about 5 nm. As expected, it has been found that the decomposition time controls the growth-coalescence process of the nano-particles.

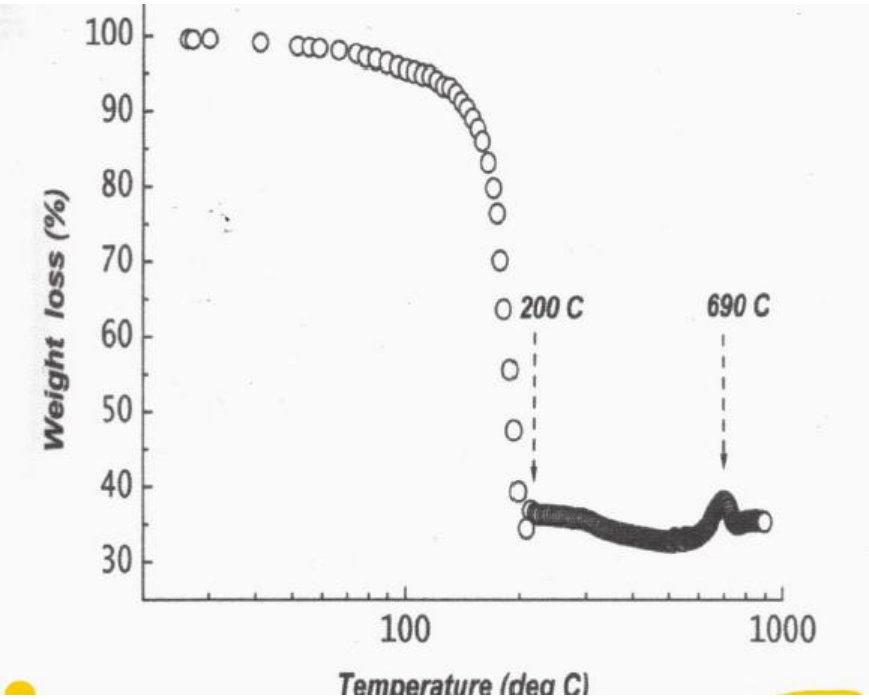

Figure 12. The thermogravimetric profile of the $TiCl_3$-based lyophilized TiO_2 NPS

4.1.3.2. Elemental composition characterization

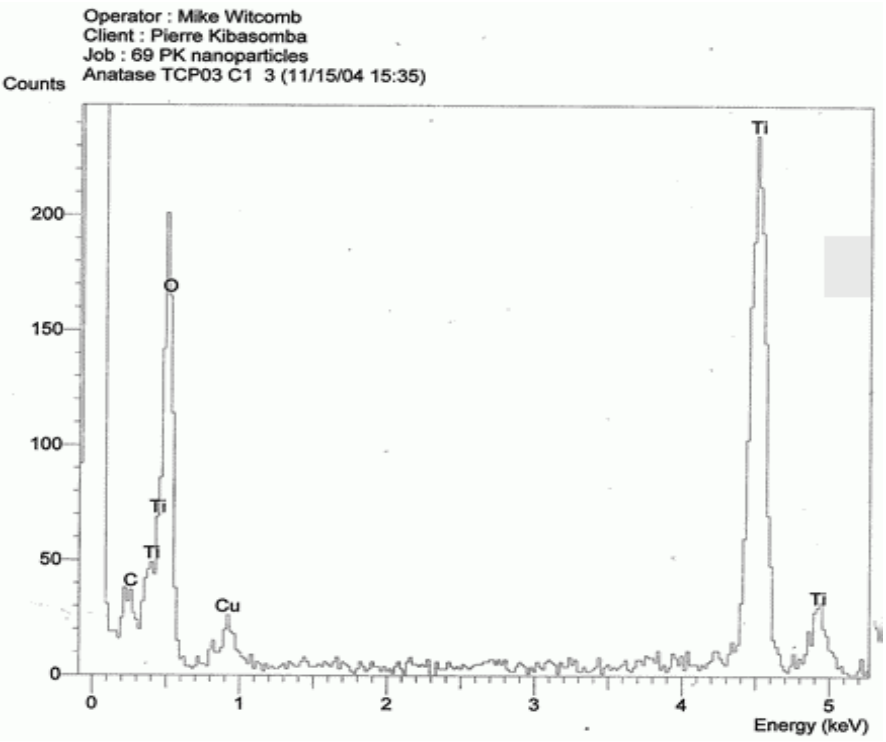

Figure 13: EDS chemical elementary composition of lyophilized sample TCP03-C

Table 1: EDS chemical elementary composition of lyophilized sample TCP03-C1

Nanoparticles	Elements content (wt %)			
	Ti	O	C	Cu
TiO_2 (Sample: TCP03-C_1)	62.0	30.2	5.7	3.7

The EDS measurements show the composition of lyophilized TiO_2 nanoparticles, samples (TCP03-C1). As indicated in the figure 13, there are four peaks of the Ti element amounting to 62.0 of wt% (one 0.46KeV, one at 0.47KeV, one peak at 4.5KeV, and one at 4.9KeV). It also shows one strong peak of Oxygen (30.2wt %) at 0.49KeV, and carbon (5.7wt %) element at 0.33keV and Cu (3.7wt %) at 0.9KeV. The presence of elemental carbon and element of copper at a weak percentage, far from being impurities due to the synthesis process, is most likely due to contamination from the copper sample stage and electrically conductive carbon tape used to fasten the sample on the sample stage. With this assumption, the purity of the lyophilized TiO_2 (92.2 wt %) can be said to have been conserved through the synthesis process.

4.1.3.3. Morphological investigation (HRTEM)

The lyophilized TiO_2 samples, obtained from precursor titanium $TiCl_3$ precursor were characterized for size and morphology, and compared to Degussa P-25 nanoparticles samples that were also characterized for the same purpose by the high resolution transmission microcopy (HRTEM) at CSIR. In 2018. The results show well-shaped nanoparticles with very degree of polydispersity and the particle size range: size=10 – 50nm. The Figure 13 (a) and (c) depicts the HRESM micrograph of the TiO_2 Degussa-P25, whereas the lyophilized Titania, anatase nanoparticles are shown in figure 14: (b) & (c) (10 -12nm).

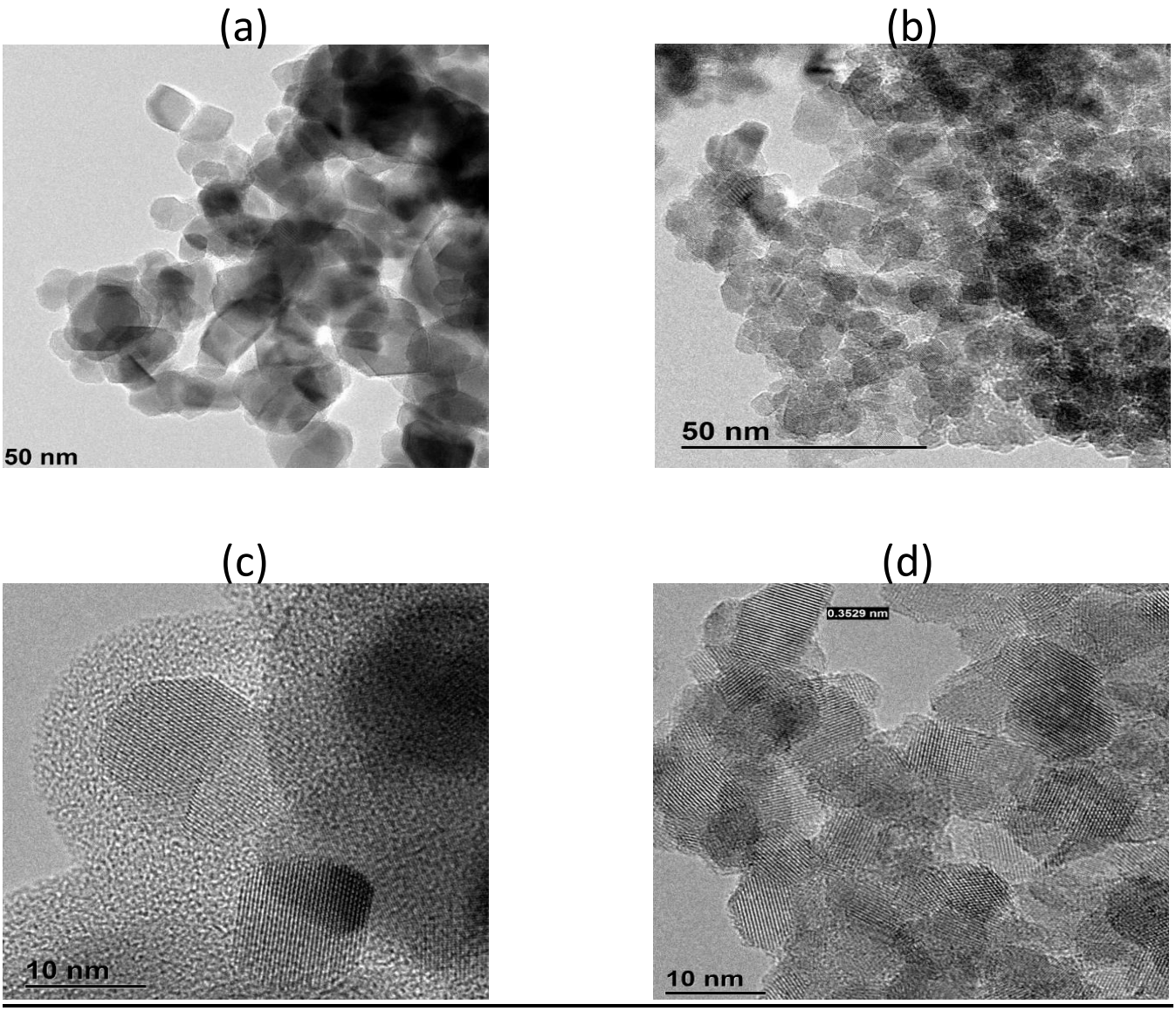

Figure 14: The TiO_2 NPS, HRTM micrographs: a & c Degussa P25 (Ø~10-50nm), b & d lyophilized from TiC_{l3} precursor (Ø~10 – 12nm), CSIR in 2018

The morphological investigation by Transmission Electron Microscopy is also fairly good evidence of lyophilized $TiCl_3$-based TiO_2 Nanoparticles products. The figure below is illustrative of this fact:

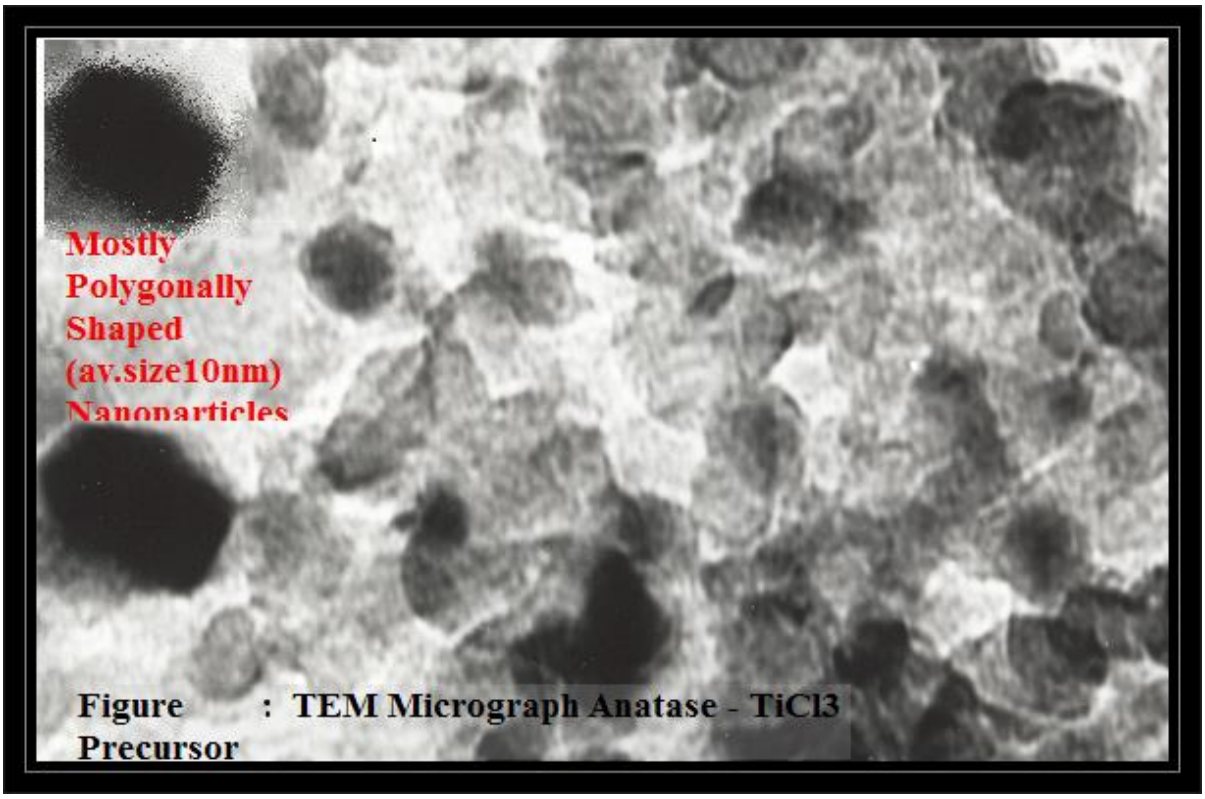

Figure 15: TEM Micrograph of TiCl3-based lyophilized Anatase phase

4.1.3.4. Crystallographic investigation

To analyze the crystallograph*ic* structure of the synthesized TiO_2 quantum dots / nano-particles**,** X-ray diffraction measurements have been performed at room temperature on TiO_2 nano-powder at the XRD unit of the Physics Department of the University of the Witwatersrand. As shown in Figure 6, the Bragg diffraction peaks are significantly broad, a signature of the nano-size of the TiO_2 quantum dots / nano-particles. Using the Debye-Scherrer approximation, the size was found to be <70 nm> which fits well with the value deduced from transmission electron microscopy measurements.

Using the ASTM database, the TiO_2 quantum dots/nano-particles decomposed at the chosen temperature of 300°C are pure anatase. A finer investigation of the reticular plans distances of the nano-anatase and the standard bulk anatase, shows clearly that the TiO_2 quantum dots / nano-particles are under stress due to the crystalline mismatching of 4.5% which is, undoubtedly, due to the surface/volume effect.

As mentioned previously, the temperature of decomposition seems to play a major role in the growth-coalescence process of the obtained TiO_2, quantum dots/nano-particles. Therefore a consecutive study on the crystallography of the TiO_2 quantum dots / nano-particles versus the decomposition temperature has been conducted. Figure 7 shows the corresponding experimental phase diagram. For the considered initial concentration, the results are 195-247°C Brookite crystallographic form, 250°C Anatase crystallographic form, 610-750°C both Anatase-f-Rutile crystallographic forms and over 750 pure rutile crystallographic form. Such phase transitions will be investigated deeply and scrupulously in light of future experiments.

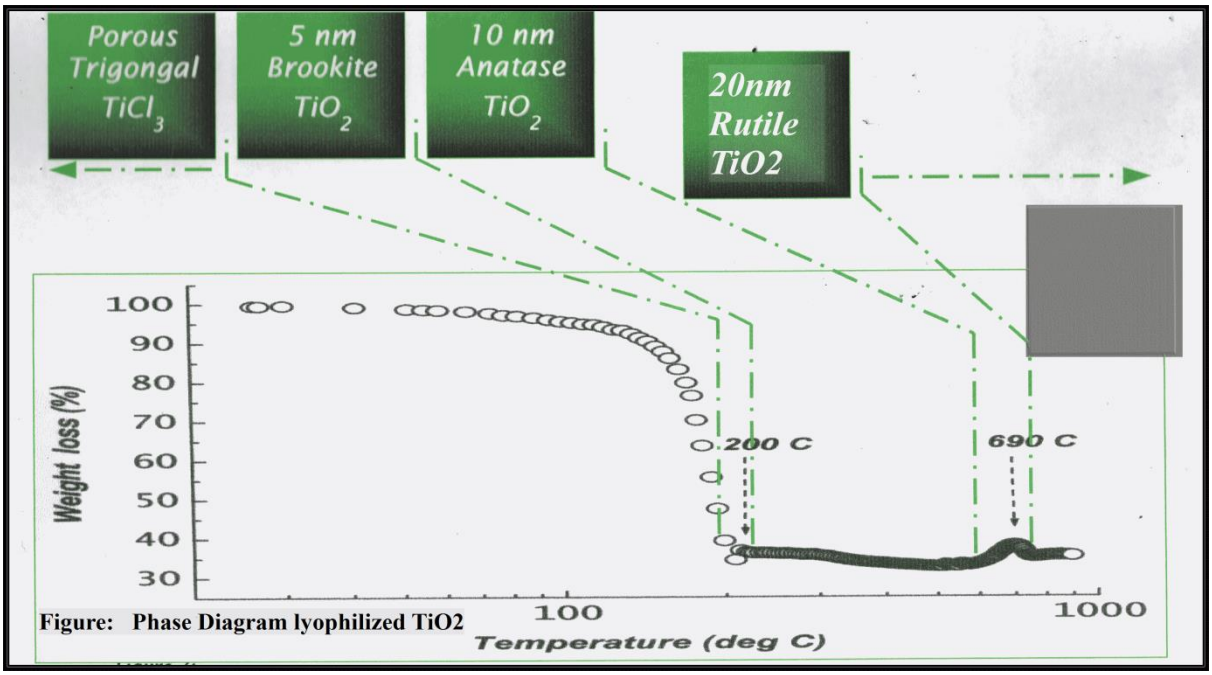

Figure 16: Phase Diagram of TiC_{l3}-based lyophilized TiO_2 NPS

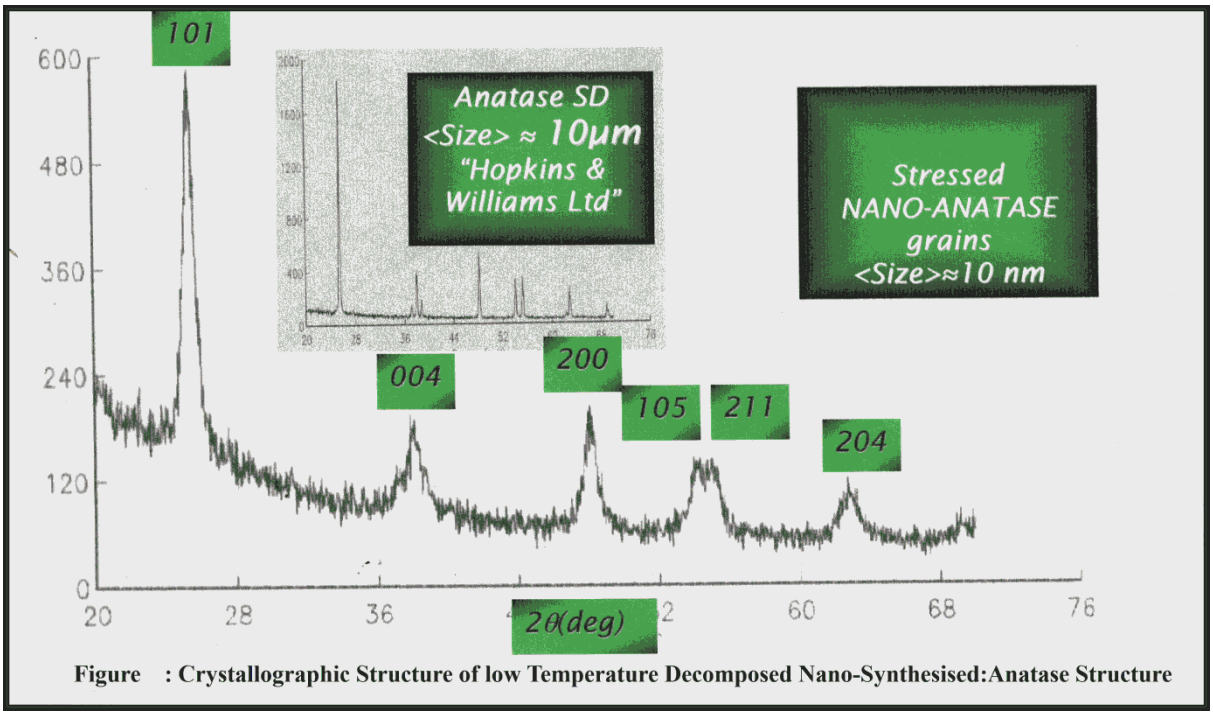

Figure 17: The XRD pattern of $TiCl_3$ based lyophilized, low-temperature decomposed –Anatase phase.

4.1.3.5. Vibrational properties

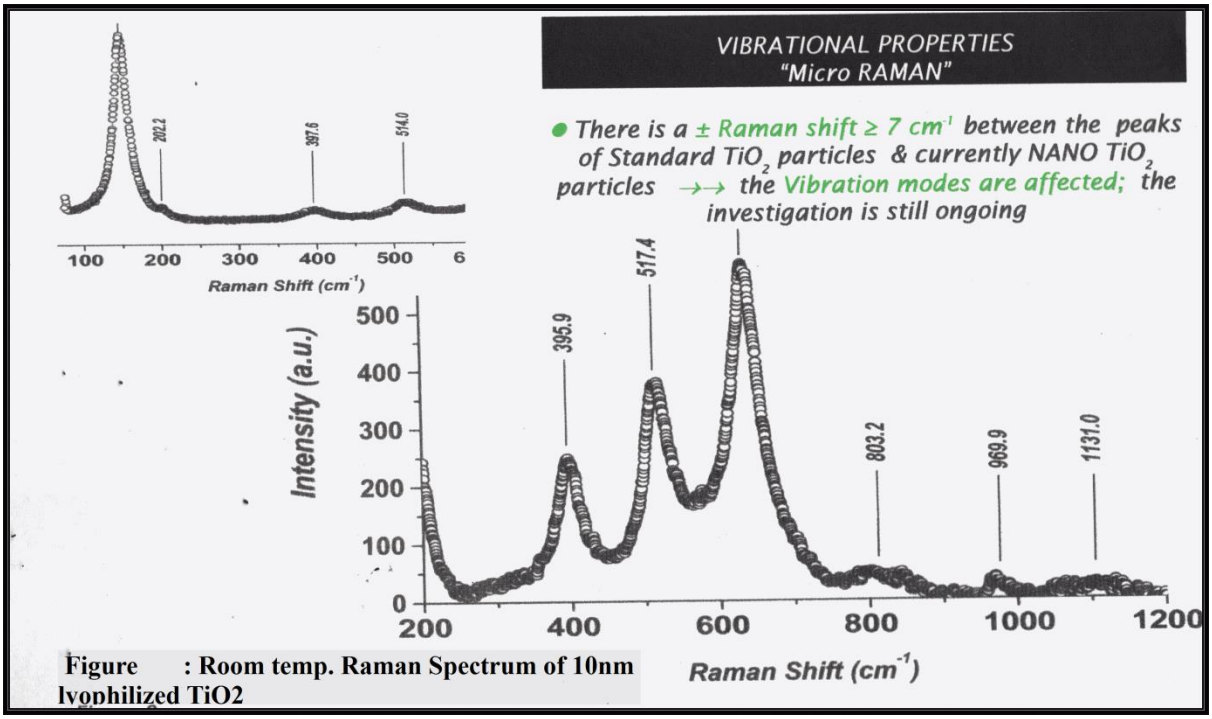

Figure 18: The room temperature Raman Spectrum of 10nm lyophilized TiO_2

4.1.3.6. The ultra-high pressure properties & phase transition phenomena

As the TiO_2 quantum dots / nano-particles were found to be under stress conditions, in particular, the anatase form, crystallographic phase-transition study under ultra-high pressure has been conducted with the high-pressure group in the Physics Department. The investigations were carried out using Raman spectrometry which is very sensitive to atomic vibrational properties, see Figure 18 above... The nano-powder was stored in a diamond cell anvil and Raman spectra were collected for different applied pressures. For comparison purposes, the same study has been conducted on bulk anatase, titanium oxide powder.

The figure 19, given below shows the corresponding experimental results. As one can observe, both the bulk and TiO_2 quantum dots/nano-particles undergo the expected anatase-rutile phase transition under pressure. The phase transition for TiO_2 quantum dots / nano-particles occurs at a significantly higher pressure, 34 GPa instead of 15 GPa. Moreover, during the phase transition with the TiO_2 quantum dots / nano-particles, there is an unidentified phase that appears around 14.9 GPa. These exciting new results indicate that the TiO_2 quantum dots / nano-particles are harder than the bulk TiO_2.

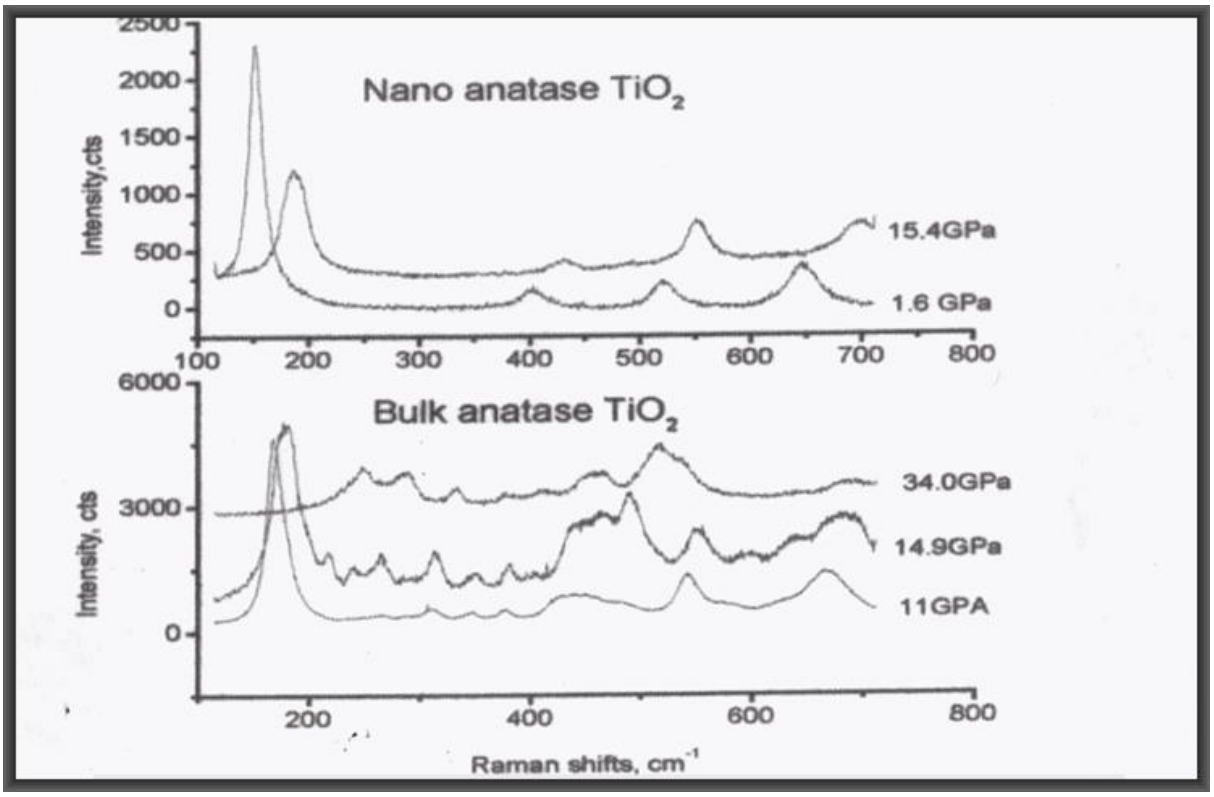

Figure 19: The pressure phase transition in $TiCl_3$-based lyophilized nanosized-Anatase and Bulk Anatase – Investigation by Raman Spectroscopy

The more elaborated report on size-effect influence on structural phase transitions in nano-anatase TiO_2 NPS was submitted elsewhere. This consisted of an entire paper submitted as the second report to GOOT PROGRAMME / University of Witwatersrand (2001) and which contributed to the publication in Physics Rev B. 70, 134102 (2004), entitled " Effect of grain size on structural transition in anatase TiO_2: A Raman spectroscopy study at high-pressure". We include the paper as a sub-section in the study of $TiCl_3$-based lyophilized **TiO_2** NPS and the publication is attached in the list of appendices.

4.1.3.7. The size-effect influence on structural phase transitions in nano-anatase

Micro-vibrational "Raman" spectroscopy has been used to investigate the crystallographic structural stability of nano anatase (TiO_2), of -10 nm average grain size, up to pressures of -40 GPa in a diamond-anvil cell. This has been compared versus the behavior of bulk TiO_2 anatase which undergoes a

structural transition from the tetragonal unit-cell to the orthorhombic a-PbO_2-type intermediate near ~5GPa before transforming to monoclinic baddeleyite structure as pressure rises above ~10 GPa.

Within the frame of this study, by contrast, the nanophase anatase TiO2 compound maintains the structural integrity of the original anatase structure up to ~17GPa before transforming directly to the baddeleyite structure. The pressure dependence of the vibrational Raman modes is similar. for both the nanophase and bulk anatase compounds which suggests that they have similar compressibilities The linewidth of the Eg Raman mode, in nano anatase decreases monotonically to a minimum at ~5 GPa, in contrast to the behavior of the bulk phase, and then increases monotonically as pressure rises further.

It is suggested that this is the result of pressure-induced grain growth of the nanophase anatase in which interfaces and grain boundaries are destroyed. The direct transformation to the baddeleyite structure from nanostructured represents a minimum energy pathway because the reduction in free energy from the loss of interface contributions likely supersedes the reduction in energy free contribution that would occur upon nucleation and growth of the α-PbO2-type intermediate.

In recent years, there has been increasing interest in the application of nano-sized Titania (TiO_2) for catalysts and supports, ceramics, inorganic membranes, gas sensing, and water purification. Due to its high dielectric constant, TiO_2 is a technologically promising candidate as the dielectric layer coating of ultra-thin capacitors. In connection to its bandgap and chemical inertness, TiO_2 is being investigated extensively for solar energy conversion purposes. Nanosize Titania is attractive for these applications because of its large effective surface area which enhances the surface reactions. Titania TiO_2 exists in three main crystallographic forms that exist at standard pressure; anatase, rutile, and brookite. Each structure exhibits different physical properties, such as refractive index, chemical reactivity, and photochemical reactivity. Each application that is based on TiO_2 requires a specific crystal structure and, usually, also a specific size. Thus, it is important to investigate the phase transition phenomena and their nature in nano-sized TiO_2 systems. Under the high surface/volume ratio in this nano-

sized TiO_2, the mentioned phase transitions which can be induced by numerous external perturbations such as pressure and temperature should be governed and driven by side effects and not by macroscopic thermodynamic parameters. Indeed concerning the bulk, there is a possibility of phonon confinement effects in the Raman spectrum of such nanosized crystals of Titania as Deported by several authors [12-18].

Coherently to the projected timing methodology program, fundamental investigations were carried out on the effect of high pressure on the phase transitions phenomena in Nano-sized Anatase TiO_2 using mainly vibrational micro-Raman spectroscopy. The three natural phases for Titania TiO_2 i.e. anatase, rutile, and brookite have a different degree of symmetry. Anatase is tetragonal (D^{19}_{4h}) with two formula units per unit cell and six Raman active modes (A_{1g} + $2B_{1g}$ + 3 E_g), whereas rutile (Tetragonal D^{14}_{4h}) has two units and four Raman active modes:

(A_{1g} + B_{1g} +B_{1g} + E_g). Brookite is orthorhombic (D^{15}_{2h}) has eight formula units per unit cell and shows 36 Raman active modes ($9A_{1g}$ +$9B_{1g}$ +$9B_{1g}$+9Eg).

Bulk Anatase has the following passage: anatase phase (14 / amd) —-> a-PbO_2-type phase (Pbcn)—> baddeleyite phase (P2 /c). The orthorhombic a-PbO_7 type phase may be quenched to ambient conditions upon decompression. The main experimental results of high-pressure studies of anatase TiO_2 suggest that there are slight changes in the transition pressures at which the structural transitions occur and this is considered to be related to the microstructure of the samples, i. e., whether the sample is polycrystalline or a single crystal. Further suggestion [29] has shown that there may be a transition directly from the anatase to the baddeleyite structure at ~13GPa. They ascribed this to lattice defects and grain boundaries that suppress the transition of anatase to the α-PbO_2 -type intermediate; however, no further details have been provided.

To the best of our knowledge, there is no published work on what effect nanometer-size dimensions have on possible pressure-induced structural transition in nanophase TiO_2, in comparison to an abundance of research already done on the temperature-induced structural changes that occur in nano-anatase [22]. Raman scattering is a convenient and sensitive probe widely used to characterize local structure changes and monitor structural transitions in compounds. Therefore this report presents the micro-Raman investigation up to -40 GPa of nano-anatase TiO_2 of -10 nm size average dimensions, pressurized in a diamond-anvil cell.

4.1.4. EXPERIMENTS

The anatase nanocrystals were synthesized by lyophilization process at the advanced nano-materials & nano-scale physics of the University of the Witwatersrand: a Christ 2000 freeze-dries model was used. Titanium chloride (III) $TiCl_3$ salt has been chosen as a precursor due to its significant water solubility and its relatively low decomposition temperature (440°C). After an optimization phase, the optimized solution of TiCI was sprayed under the form of droplets (~8mm in average/laminar regime flow) in liquid nitrogen. The frozen network has been transferred to the lyophilization vacuum chamber. The frozen salt network was submitted to a sublimation process during -20 hours. By controlling both the heating temperature

and in-situ vapor pressure, the water component was fully removed from the salt precursor after such a lyophilization period. The obtained white precursor was eminently porous possessing a dendrimeric configuration. This later has been decomposed in the normal atmosphere. Taking into account the Transmission electron microscopy investigations, the obtained nano-particles of TiO_2 with an average size of about 5 nm are polycrystalline and significantly faceted (Figure 3). In comparison with spherical nano-crystals of hematite, this later morphological edge geometry has been explained based on the low degree of crystallographic symmetry in the anatase structure. A more accurate and detailed analysis shows that the anatase nano-crystals exhibit a specific anisotropy in shape; they are nano-platelets as in the case of nano-crystals of lithium niobate synthesized by the identical process [30]. Their size can be approximated to ~10nm x10 nm x 3nm.

To analyze the crystallographic structure of the synthesized nano-particles, X-ray diffraction measurements have been performed at room temperature on TiO_2 pressed nano-powder at the XRD unit of the Physics Department of the University of the Witwatersrand. It has been shown that the Bragg diffraction peaks are significantly broad except most intense Bragg peak. All the Bragg peaks are labeled as anatase form but slightly under compression if one takes into consideration the reticular distances. The corresponding Bragg peaks (103), (004), (112) as well as (105), (211) cannot be resolved. This is a signature of the nano-size of the TiO_2 powder. Based on the Debye-Scherrer approximation, the size was found to be <10 nm>. Also, one can distinguish that the most intense (101) Bragg peak is sharper in width than the other labeled peaks. This is an endorsement of a shape anisotropy of the TiO_2 nanocrystals, fitting therefore with earlier electron microscopy inferences. Accordingly and based on the Debye-Scherrer approximate formula, the nano-crystals of TiO_2 can be characterized by a shape form factor of a/b -3.6 nm / 11 nm which is in a thoroughly satisfactory agreement with the transmission electron microscopy results.

For high-pressure investigations, a piston-cylinder-type diamond anvil cell (DAC) with anvil culets of dimensions 540 um was used to generate high pressure up to

near 38 GPa. The sample was loaded into a cavity spark-eroded in the T301 steel foil gasket pre-indented to -40 um from a starting thickness of ~250nm. In one series of measurements, our new multi-aperture gasket technique was used to obtain Raman spectra in a single sequence of compressions of both nano-phase and bulk crystalline anatase loaded into two separate cavities (0-100 nm each) of the same pre-indented gasket. The second series of pressure measurements were performed on the nano-phase sample alone. Liquid nitrogen was loaded into each sample cavity to serve as a pressure-transmitting medium by immersing the miniature DAC into a bath of the cryogen and momentarily releasing the thrust-force screws. Raman spectra in back-scattering mode at room temperature and variable high pressures 9 were obtained with a Jobin-Yvon T64000 spectrometer equipped with micro-imaging accessories, a holography grating (1800 grooves mm'^{1}) and, liquid nitrogen cooled CCD detector. The 514.5nm line of an Argon laser was used to cite the Raman scattering with the spectrometer operated in the double-tractive mode. Power of 55mW at the output port of the laser was onto the samples using an Olympus x20 ultra-long working distance objective which results in a laser spot size of –10 μm diameter. The entrance slit width of the monochromator was set at 200 pm. Under these conditions data, acquisition times ranged from the 30s up to 600s depending on the quality of the spectra. Pressure calibration in the cavity of the gasket was made in terms of the ruby R-luminescence line shift, measured at the same position where the Raman spectrum was obtained. The argon-ion laser-plasma lines 516.3 nm, 516.6nm, 517.6nm, etc. were subsequently used for Raman shift calibration these lines were removed from the Raman spectra presented in the figures of this paper.

4.1.5. RESULTS & DISCUSSION

The pressure evolution of the Raman spectra of nano-anatase is compared to Raman spectra at selected of the bulk commercial sample. Under ambient conditions. The main Raman bands in nano-anatase peaks are at 146.4 cm'' , 202.2 cm'^{1}, 397.6cm'^{1}, 514.0 cm''', 641.3m' , whereas for bulk anatase the corresponding bands are at 141.3cm'^{1}, 394.4 cm'^{1}, 516.1cm'^{1}, 636.7cm'^{1}. These bands are

assigned to six Raman active modes [19] i.e. Ag + 2B1g + 3Eg as labeled in the figure. The E Raman mode near 146.4cm^{-1} is too weak to be recognized on the scale used in Figure 6. The pressure evolution of the Raman spectra of bulk anatase exhibits similar behavior to that reported in previous high-pressure studies [20]. As the pressure increase to ~5.6CPa, several weak peaks appear at 331.0, 344.5 & 372.8 cm'^{1}, characteristic of the a-PbO_2 -type phase. As pressure increases further, the intensities of these new peaks increase and are discerned at pressures over &7.5GPa and beyond. The structural transition of bulk poly-crystalline anatase to c-phase was slight, as found previously [20], coexisting with the original anatase structure up to ~15GPa. Beyond this pressure, entirely new Raman bands become apparent. These are supposed to be characteristic of the high-pressure baddeleyite phase. The behavior of the Raman spectrum of the current nano-anatase compound is quite different. Similar to ambient pressure, no new peaks appear up to -16 GPa, indicating that the anatase phase in the nanostructured compound is stable to well beyond the transition pressure of ~5 GPa, characteristics of the bulk anatase. When the pressure is increased to 17.7CPa, (See figure 6-7), several new bands are discerned, which appear to correspond with those found for the high-pressure baddeleyite, phase and remained at a maximum pressure of -39 GPA. These results demonstrate that the nanophase sample directly transforms from the anatase to baddeleyite structure at 17.7 GPa**,** without transiting via the a-PbO_2-intermediate phase. However, the sample is decompressed from the maximum pressure, the nanophase sample is quenched from the baddeleyite phase to the α-PbO2 -type phase, similar to the behavior of the bulk compound. Raman mode shifts of the nano-phase sample as a function of pressure was observed. The pressure dependence of the Raman shifts, slopes dV/dP have been obtained by linear fits (solid curves) over the pressure range before and after the structural transition that occurs at 18 GPa. The hollow and filled symbols simply delineate measurements from the two different series of measurements. The slope dvldP averaged over the most intense bands of nanophase anatase is 2.58±0.22cm^{-1} GPa^{-1} compared with bulk anatase where slope DV/DP average is 2.70±0.13 cm^{-1} GPa^{-1}, indicating that the anatase phase in both compounds has very similar compressibility.

After the transition of nano-phase anatase to the baddeleyite structure, the average DV/DP of the high-pressure phase is 1.65±0.21 cm'^{1} GPa', which suggests that the baddeleyite phase is less compressible than the low-pressure anatase phase. This is consistent with the compressibilities derived from the recent X-ray diffraction measurements. The pressure-induced changes of the line-width of the Eg band of the bulk anatase compound: the line-width changes from 7cm'^{1} at ambient pressure to 25cm^{-1} at ~15 GPa. There is an inflection at pressure ~5 GPa near to the structural transition pressure attributable perhaps to the volume reduction that occurs when anatase transforms into the a-PbO_2 type phase.

The linewidth of the Eg mode of nanophase anatase by contrast, it displays an entirely different pressure behavior shown in Figure. The linewidth first decreases monotonically, reaching a minimum at ~5 GPa, followed by an upturn and monotonic increase as the pressure rises beyond 5 GPa. The pressure at which the minimum occurs is close to the transition pressure 5-6 GPa where bulk anatase transforms into the a-PbO_2-type structure. The results suggest that at least two effects with opposite pressure dependencies' are operative, one causing the linewidth to decrease and the other causing an increase.

In general, the linewidth or line-shape of the intense E_g band (located at 144cm^{-1} at ambient pressure) of anatase, which arises from external vibrations of the anatase structure, is affected by various mechanisms, including, non-stoichiometry due to oxygen deficiencies, disorder induced by minor phases, a pressure effect induced by the surrounding particles and phonon confinement effects in nano-dimensional particles. Several authors have discussed the relation between linewidth of E_g of nanophase anatase and particle size using the concept of phonon confinement. Their results show that the linewidth increases as the particle size decreases. The correlation of the linewidth of the Raman Eg band with that of the particle size has been corroborated by measurements of particle size deduced from x-ray diffraction and TEM. To explain the behavior at low pressures shown in Figure 9(b), we suppose that phonon confinement effects proffer a reasonable explanation for the pressure-induced changes of linewidth, likely due to pressure-induced grain growth or

inter-grain interactions. At sufficiently high pressures the effect of reduced unit-cell volume becomes dominant, i.e., intra-grain modifications occur and the linewidth then has a similar pressure behavior to that of bulk anatase.

According to a thermodynamic picture of nucleation and growth of crystalline material, the free energy of nanostructured anatase can be reduced by grain growth into larger ones. On the other hand for compacted nano-particles of anatase, more grain boundaries may be produced compared with how compaction may occur in bulk powders where it is more advantageous for the nucleation of a new α-PbO_2 -type phase to occur to minimize interface and stress-free energies. Studies of the temperature-induced structural transition of nanostructured anatase to rutile have suggested a coexistence situation where there is the nucleation of the new rutile phase and concurrent with the growth of nano-phase anatase particles. A similar situation may occur at the pressure-induced structural transition of nanostructured anatase. The pressure-induced structural transition of bulk polycrystalline anatase to the α-PbO -type phase is a sluggish transformation, whereas in a single crystal sample the transformation occurs in a much narrower range of pressure. This suggests that the slow transition may in part be attributable to a wide distribution of grain sizes typical of bulk poly-crystalline anatase. When the average grain size is only of nanometer dimensions, then grain growth, i.e., coarsening, of anatase would be the main consequence of any pressure-induced structural modification, representing a lower free-energy situation than if nucleation of the new a-PbO -type intermediate occurred. This grain growth mechanism rationalizes how the structural transition to the a-PbO_2-type intermediate phase has been inhibited in the nano-structured starting material. There may be a critical grain size below which anatase would exhibit grain growth in preference to nucleation of a-PbO_2-type intermediate. This may be a general feature of nanostructured systems, indicating that the passage to new structural states to minimize free energies when P or T is changed, maybe quite different from the bulk. In short, pressure-induced phase transitions in nano-anatase TiO_2 were investigated. It has been shown that the phase transition processes in nano-anatase titania are fully different from that of bulk anatase in the range of 0 ~40 GPa. The nanophase anatase TiO_2 maintains its crystallographic

structure of the original anatase form up to ~17 GPa before transforming directly to the baddeleyite structure. The projected subsequent complementary step is to investigate the pressure-induced phase transitions versus the size of the anatase nano-crystals. Through the variation of the surface/volume ratio, this second investigation component should elucidate, if any, the role of the surface in driving the phase transition process and its threshold. In connection to the size effect, phonon confinement effects in both anatase and rutile nanocrystals will be investigated. Such quantum vibrational confinement will be deduced from the dependence of the shape of the Raman peaks, their broadening as well as their frequency shift. An attempt to explain the line broadening with the breakdown of the phonon momentum selection rule Q~ 0, specific to the Raman scattering or in ordered systems. In the case of nanocrystals, this rule is no longer valid as the phonons are confined in space and all the phonons over the Brillouin zone will contribute to the first-order spectra. The weight of the off-center phonons increases as the crystal size decreases and the nondispersive causes an asymmetrical broadening and the shift of the Raman peaks. A simple, confinement model may then be used to calculate the shape of the 144cm^{-1} mode of the anatase at various nano-crystals sizes. The same approach will have ensued for rutile nano-crystals Titania. For this prospective fundamental investigation, the size and shape of both anatase and rutile nanocrystals will be controlled through the initial pH and the concentration of the precursor salt solutions.

4.2. Experiment II: The Step by-step lyophilization experimentation for the Ti (IV) Oxychloride ($TiOCl_2$) Precursor-based TiO_2 NPS

4.2.1. The objective of the experiment

Having selected the Ti (IV) Oxychloride precursor, to illustrate the experimental procedure of lyophilization principle as it applies to the synthesis of ceramic nanostructured material with specific properties (high chemical homogeneity, monodisperse and, high purity, etc.) first, in the scenario pH~1(very acidic formulation), and secondly, in the scenario of and very alkaline (basic) pH=13 formulation. The results are shown in figure 20 and table 2 that follow:

4.2.2. The formulation of Ti (IV) Oxychloride ($TiOCl_2$)

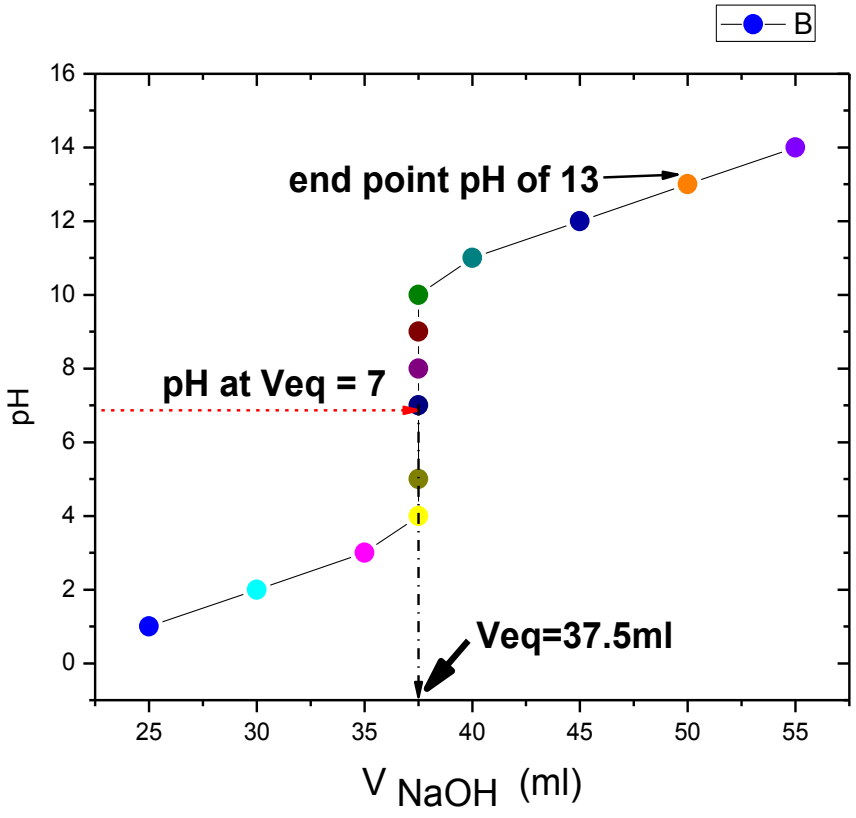

Figure 20:$TiOCl_2$-formulation and lyophilization Optimization

Table 2. $TiOCl_2$ – based FORMULATIONS

pH	Volume (ml) TiOCl2	Volume (ml) H2O Deionized water	Volume and nature of Titrant	Td (°C)	Td (min)	Particle Size	Structure
7	60	200	none	300	60	< 3nm	Anatase
1	90	200	NaOH (25ml)	300	60	16.41± 9.61 nm	Anatase
13	25	200	NaOH (50ml)	300	60	10.32 ± 5.96nm	Anatase
Degussa-P25						8.26±7.29nm	75.30% Anatase; 24.30% rutile

4.2.3. The step-by-step lyophilization Experiment:

TiO_2 anatase nanoparticles were obtained from Ti (IV) Oxychloride ($TiOCl_2$) precursor. A solution (pH~1) was prepared using the procedure such that a volume of 25ml of $TiOCl_2$ mixed with 200ml of deionized water, and 50ml of NH_4OH was added. A homogeneous formulation was obtained by the action of magnetic stirrer for 5min, it was after atomized by spraying under N_2 gas of pressure 50Kpa and for injection duration of 5m, producing frozen snowlike-iced powder instantly when it was dropped-by-drop injected into liquid Nitrogen (-196C). The latter was thereafter quickly transferred into lyophilization (CHRIST Freeze Dryers 2000). The formulation was processed according to the principles of lyophilization (see figure below) such as the operating parameters namely: the vacuum pressure, the shelf temperature, precursor temperature, and the timing are tabulated as shown in the table. Optimizing the lyophilization process for $TiOCl_2$ formulation, the starting point ("A"), indicated in the figure, was found by Differential scanning Calorimetry (DSC) to be -30°C. The details are given in the lyophilization set-up sheet, included in the appendix for records purposes.

By controlling both the heating temperature and in-situ vapor pressure, the water component was fully removed from the salt precursor. The obtained white precursor was eminently porous possessing a dendrimeric configuration.

As an illustration of successful lyophilization procedure, we implemented, from data collected based on the diagram in the figure for the $TiOCl_2$ formulation, and the completion of the cycle:

1: Initial solution; 1 ⟶ 2 freezing; 2 ⟶ 3: Sublimation

The graph in the figure corresponds to the completed lyophilization cycle including the freezing (at point 2) and the sublimation of all iced solvents. We, therefore, executed two successive steps:

First, **the primary drying (sublimation)**, we eliminated all frozen interstitial water (solvent) by maintaining the shelf temperature at (-30°C) as the vacuum pressure was maintained at as low as 0.18 mbar for 45minutes. At this stage, most energy (heat) is

consumed by sublimation. This is shown by the ramp on the curve because the energy from the heating is transferred to the ice and to reach equilibrium. We ensured that the setting of the heating corresponded to obtaining speedy kinetics of sublimation at the same time avoiding the effect of surface burning of the product by excessive heating.

Secondly, **secondary drying** was completed by sublimating all from the formulation. It occurred in the freezer-dryer chamber, when the environmental pressure was increased, the heating of the shelves was maintained and the product started to heat up because the extraction of calories is not compensated by sublimation. The point of inflection (**PI**: **0.18; 0, -4; 90**) on the curve signaled the start of the secondary drying; at this stage-bound water started to desorb progressively. The product temperature started to increase to the point it reached equilibrium. Absence of ice, the heating accelerated because there was no risk of the product could melt. It took a total timing of 18.6hrs to complete the full lyophilization cycle. The figure 21 shows the theortical phase diagram of water-salt system.. The tables 3 and 4 tabulate the values of in si-tu conditions including the vacuum pressure, shelf-temperature, precursor material ure and the lyophilzation duration, respectively for formulations I and II.

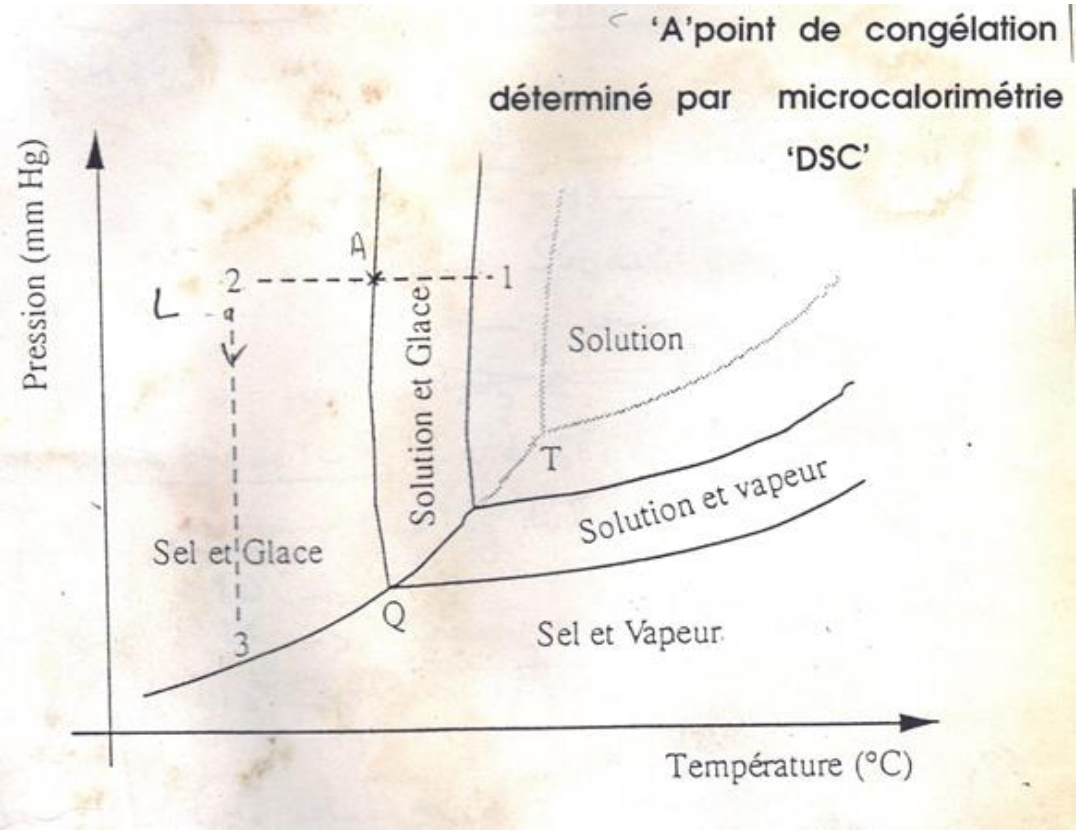

Figure 21: The phase diagram of the water-salt system 1: initial solution, 2: Freezing, 3: sublimation

Table 3: Formulation# 1, pH=neutral (~ 7): 60ml $TiOCl_2$ + 200ml of H_2O (deionized water)

vac. pressure (mbar)	Shelf temp (°C)	Precursor Temp(°C)	Duration (min)
0.18	-30	-50	0
0.18	-30	-36	45
0.18	-10	-7	73
(Pl) 0.18	**0**	**-4**	**90**
0.18	10	0	230
0.2	29	7	425
0.2	50	15	655
0.2	55	17	818

0.2	54	17	993
0.2	55	18	1016
0.2	56	18	1126

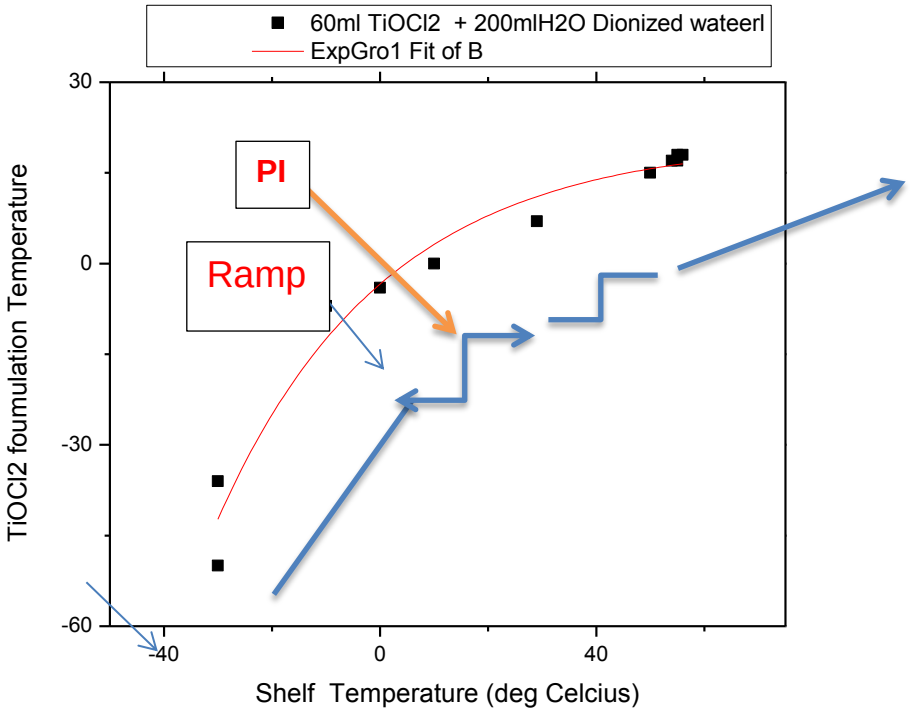

Figure 22: Thermal decomposition of sample Ti-oxy-prec 2; pH: 13

4.2.4. The characterization of the samples

The figures 22, and the figures 23 and 27 refer respectively to the thermal decomposition and the crystallographic characterization of the sample Ti-Oxy prec# 2, pH: 13. Whereas, the figures 28 refers to the XRD characteristic of the Ti-Oxy-Prec# 1, pH:1. The figure 29 and the table 8 refer to data collected with the purpose to compare the lyophilized and the TiO_2 Degussa P25 samples. On the other hand, the figure 30 refers to the scanning electron microsopy of the $TiOCl_2$-based (pH: 13) pertaining to the morphological and monodispersity investigation of the lyophilized TiO_2 NPS.

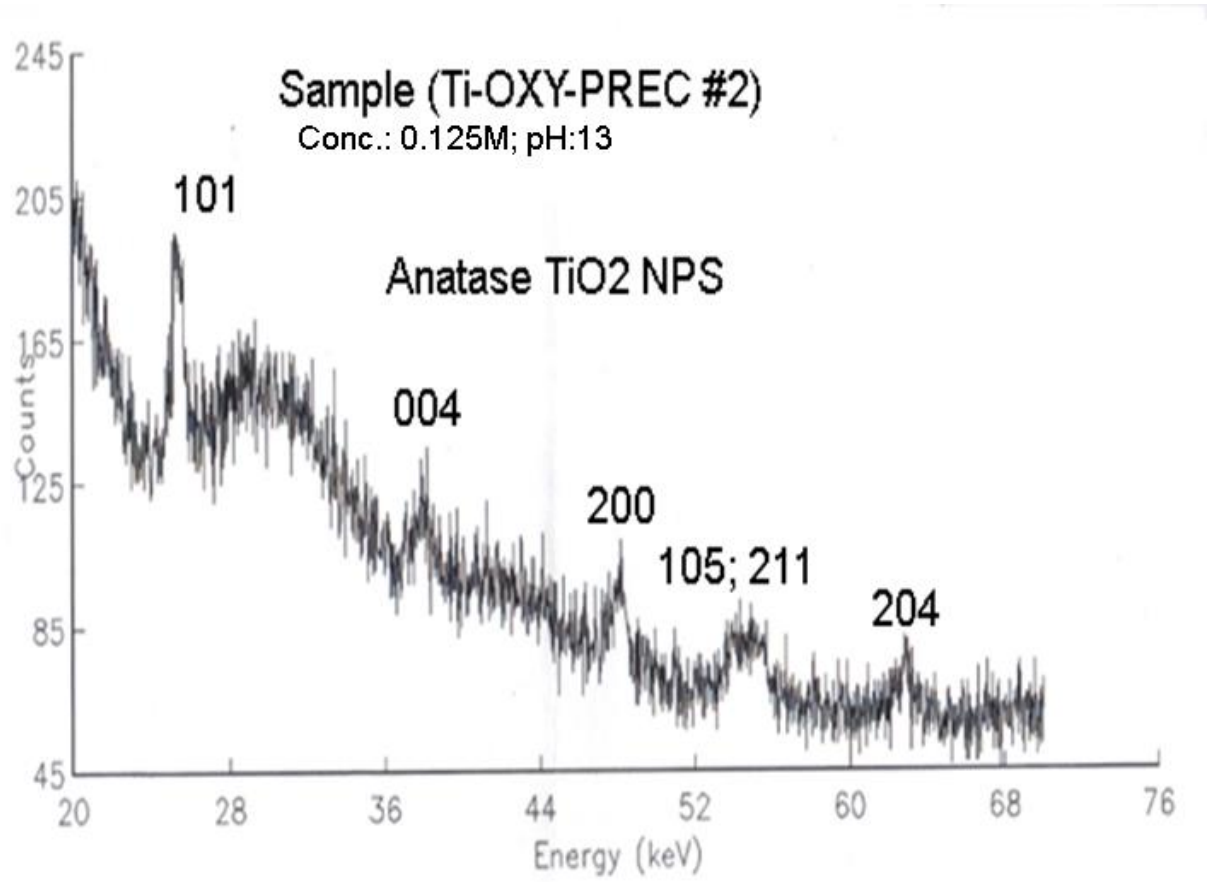

Figure 23: XRD spectrum of sample Ti-Oxy-Prec. 2

Table 4: Formulation II: 25ml of $TiOCl_2$ + 200ml H_2O (deionized water) + 50ml of NH_4OH, pH: 13

Vacuum Pressure (mbar)	Shelf temp	Precursor Temp	Timing
0.07	-30	-29	10hra
PI 0.07	-5	-27	60min

0.07	10	-25	60min
0.08	20	-23	60min
0.08	30	-21	60min
0.08	40	-20	60min
0.08	50	-18	60min

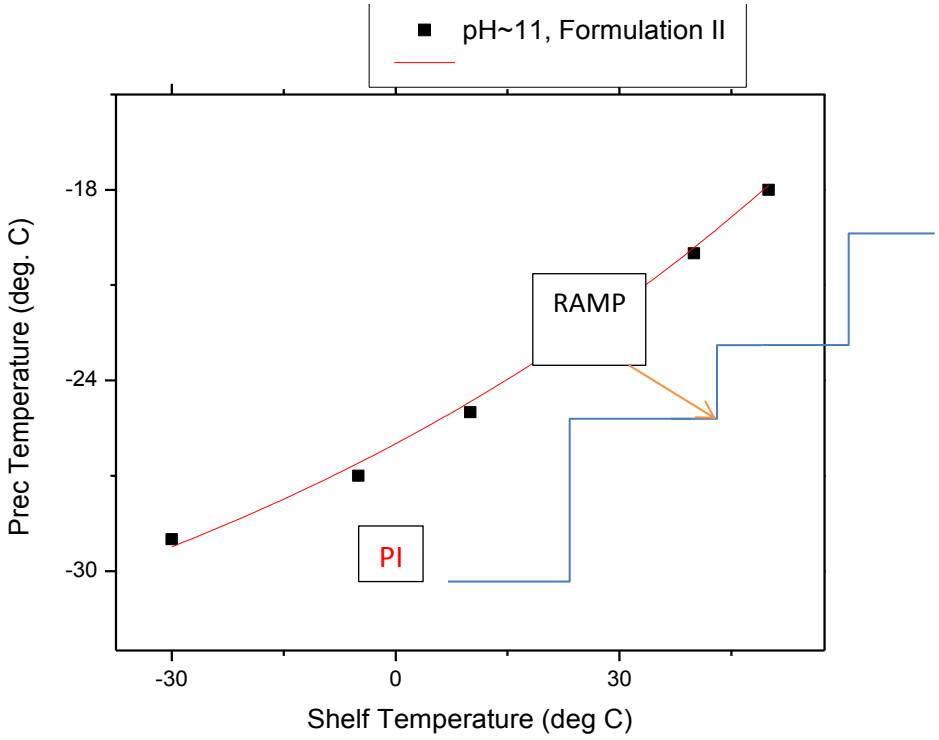

Figure 24. A plot of shelf temperature versus $TiOCl_2$ formulation (pH~ 11) temperature

4.2.5. The thermal gravimetric analysis (TGA) and the differential scanning calorimetric (dsc) characterization of sample Ti-oxy-prec 2; pH: 13

4.2.5.1. The TGA and the DSC characteristics:

The as-obtained lyophilized **TiO_2** powders were characterized using TGA and DSC for the thermal properties. The data collected served for optimizing the decomposition temperature (300°C) of the product. The TGA charactristic is shown in figure 25, and

the DSC characteristic is shown in figure 26. The surface properties (B.E.T), crystallographic properties by XRD for $TiOCl_2$-precursor, pH: 13.

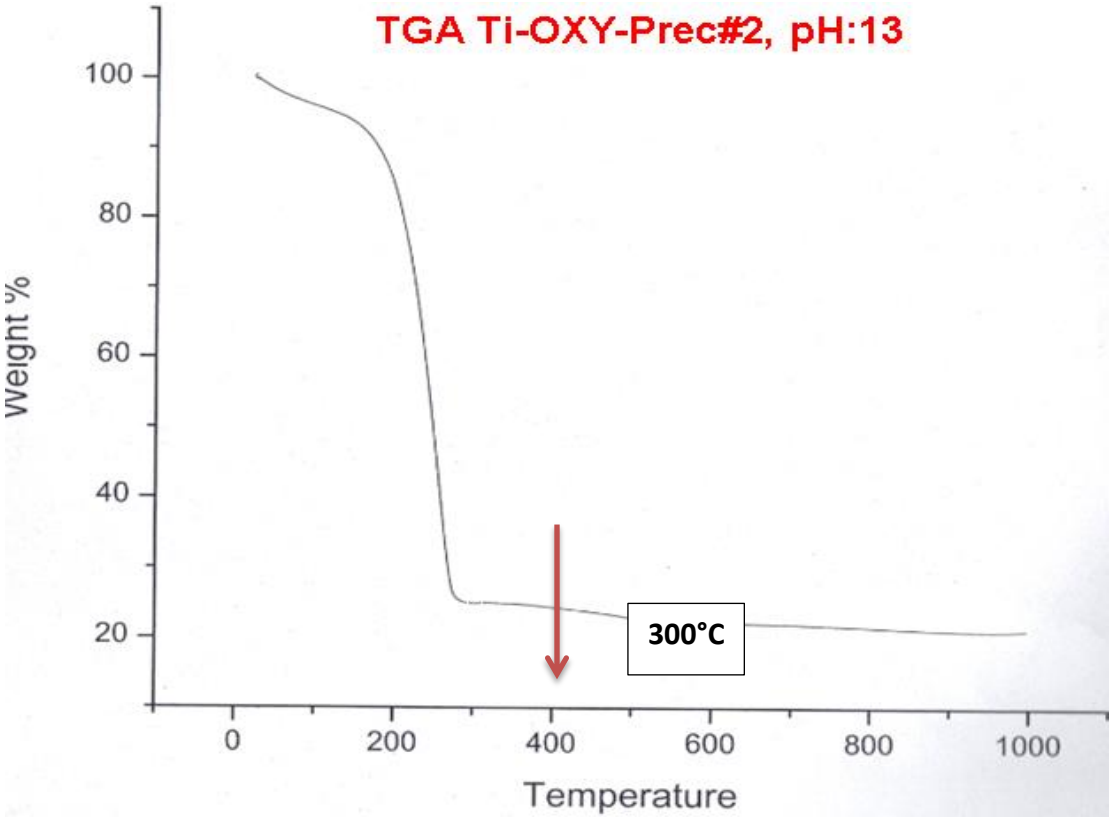

Figure 25: TGA spectrum of $TiOCl_2$ formulation, pH ~ 13

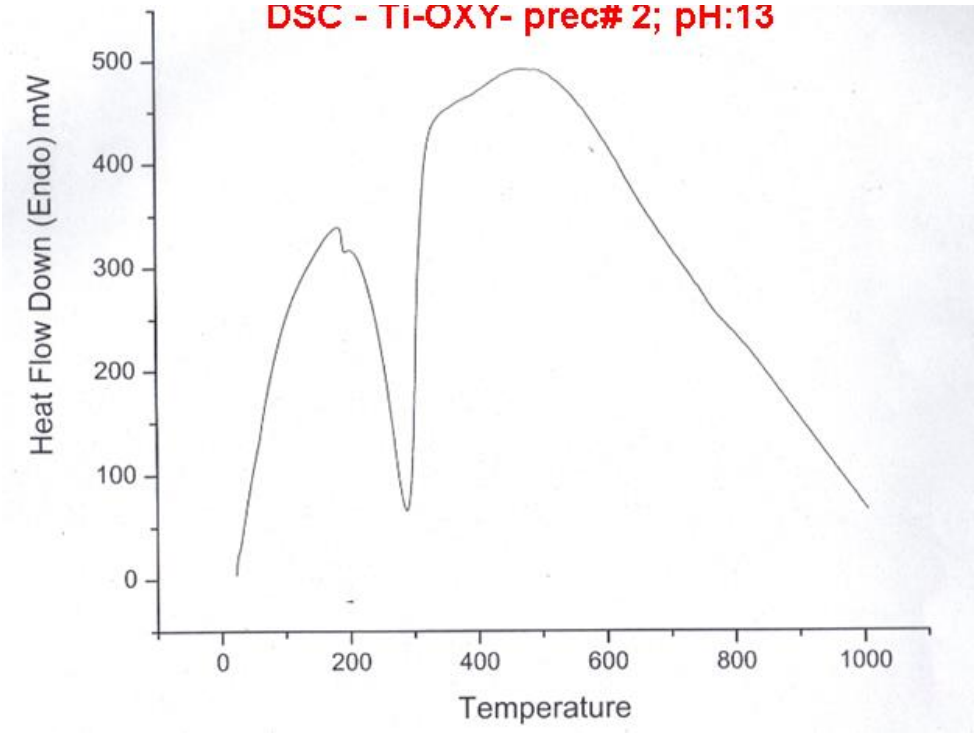

Figure 26: Plot of DSC measurements of $TiOCl_2$-formulation, pH: 13

The table 5 that follows compares the mass balances in respect of the annealing in air of the Ti-OXY, Prec #1(pH: 1 to the annealing of in air of the OXY-Prec # 2, pH: 13.

Table 5: Annealing/thermal decomposition results

	Ti-OXY-PREC #1 pH:1	**TI-OXY-PRE # 2, pH:13**	**Td in air as per DSC**	**Td**
WEIGHT (BEFORE)	0.2848 g	1.3316 g	300°C	1h
WEIGHT (AFTER)	0.0547 g	0.4572 g	300°C	1h
Mass Balance (ΔM)	19.2%	34.0%		
STRUCTURE	Anatase NPS	Anatase NPS		

4.2.5.2. Crystallographic properties (XRD)

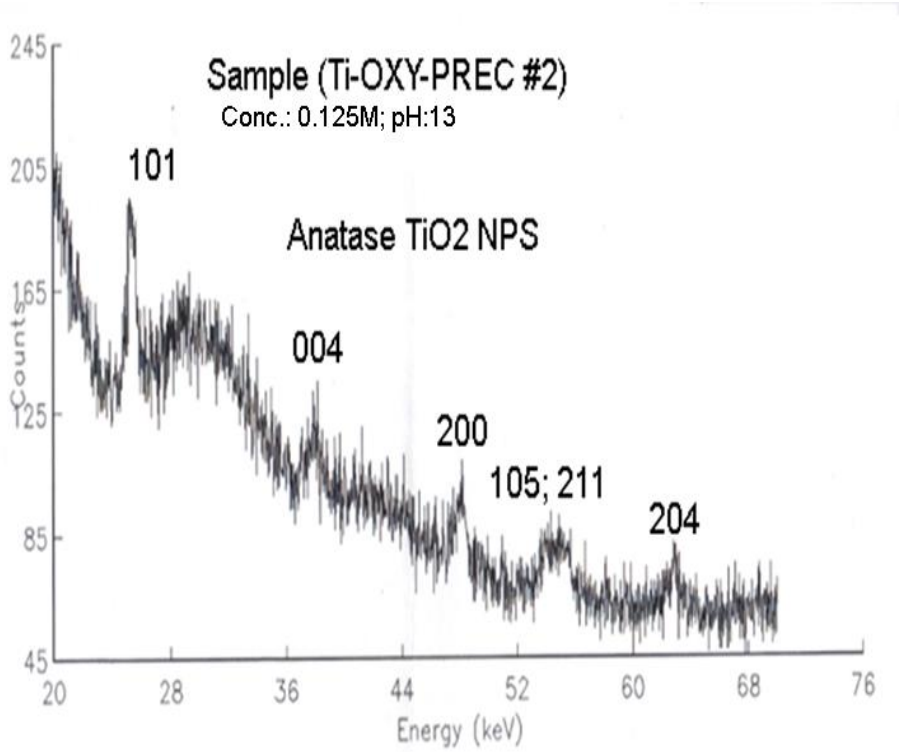

Figure 27: The XRD pattern of sample $TiOCl_2$-based formulation, pH: 13

Table 6: XRD parameters, pH: 13-$TiOCl_2$-based samples, size calculations

2θ	Θ	Cosθ	FWHM	Size (nm)
24.74	12.37	0.980781	0.1998	6.80361712
24.9222	12.4611	0.994464	0.0666	20.6956056
25.0603	12.53015	0.999344	0.0666	20.7971611
25.3163	12.65815	0.995791	0.1332	10.3616114
26.1295	13.06475	0.878358	0.1332	9.13967496
47.9045	23.95225	0.380471	0.2664	1.97947534
48.2471	24.12355	0.532545	0.2992	2.46693844
			Av Size	10.3205834

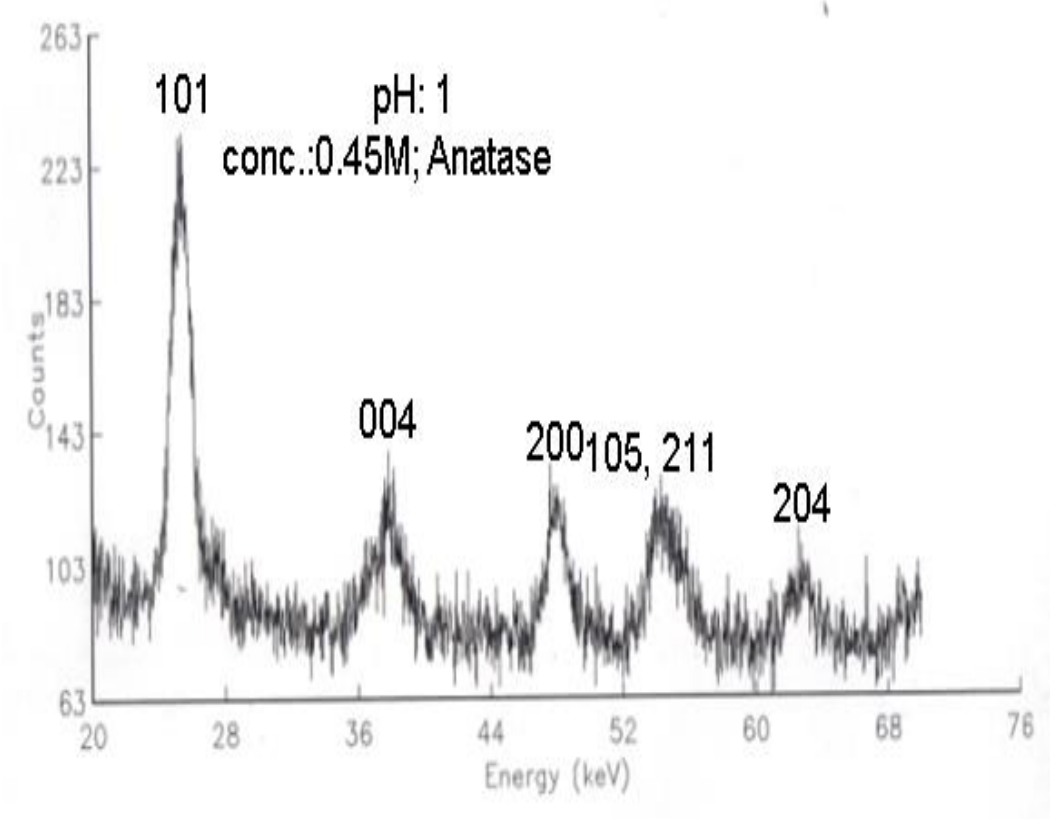

Figure 28: The XRD patterns reveal the crystallographic signature of the pure anatase phase as per peaks namely: (101), 004, 200, 105, 211, and 204 according to miller indices the size of the nanoparticles is 6m as calculated

Table 7: XRD data $TiOCl_2$, pH=1

pH: 1	**CuK_α- λ= 1.541nm; K:0.9,**			
	$\boldsymbol{size\ of\ particle}$: $\emptyset = \frac{K\lambda}{\beta Cos\theta}$ $Scherrer's\ eq.$			
2θ	FWHM	Θ	Cosθ	Size (nm)
25.3737	0.0999	12.68685	0.99275113	13.7733
25.5305	0.0666	12.76525	0.98028859	20.4006
26.04497	0	13.02249	0.89777074	-
37.9554	0.0333	18.9777	0.99180078	41.28036
38.0915	0	19.04575	0.9808156	-
47.8655	0.0666	23.93275	0.36236593	7.541129
55.0475	0.1332	27.52375	-0.7312907	7.609377
55.1266	0.1332	27.5633	-0.7576876	7.884046
			Av size(nm)	16.4148
		.:	Strd Dev **σ**	± 9.6171119

<u>Table 8</u>: The XRD data for DEGUSSA-P25

2θ	**θ**	**Cosθ**	**B_{khl}**	**Particle Size (nm)**	**λ= 1.541À; K_α = 0.9**
25.373	12.686	0.99278	0.2997	4.59422	
27.505	13.752	0.37515	0.5328	0.97655	
37.929	16.964	0.99336	0.0666	20.6891	
54.184.	27.092	-0.37877	0.0333	15.7750	
55.160	27.580	-0.76864	0.2331	4.57326	
62.390	31.395	0.99979	0.4662	2.97428	
			Av. size	8.26326	±7.29052

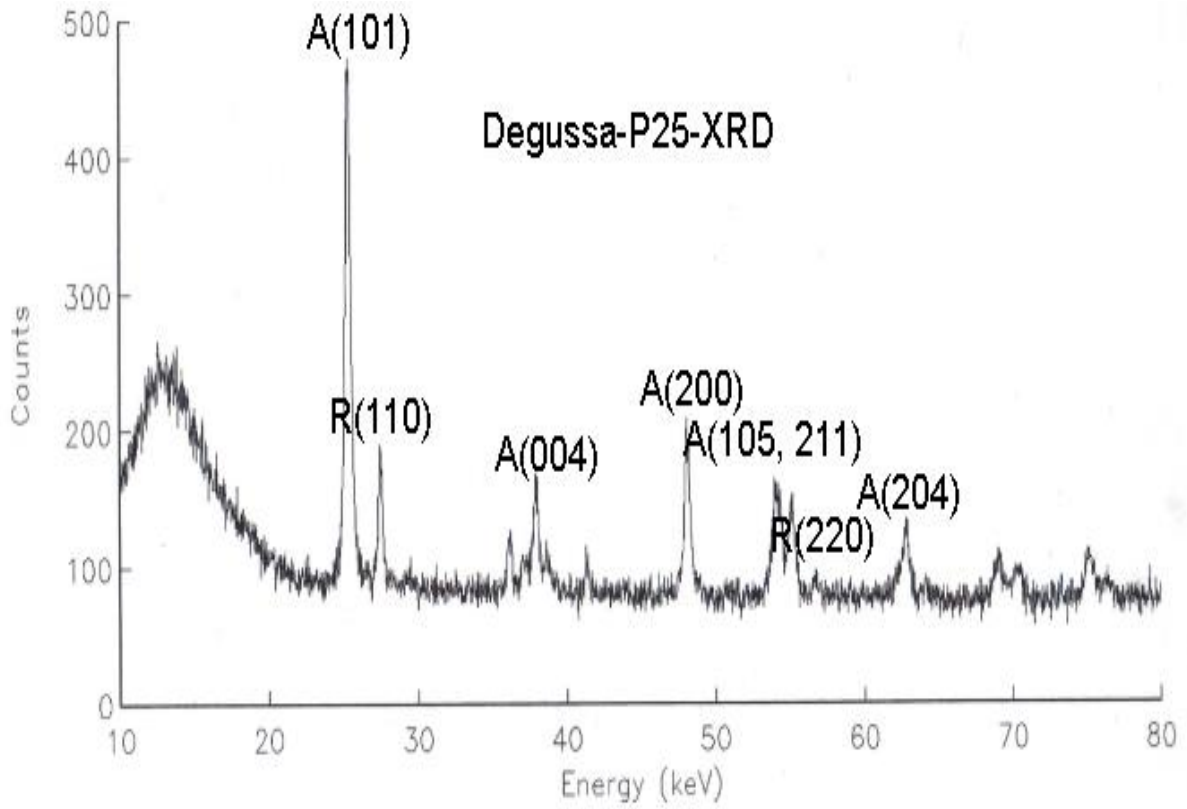

Figure 29: XRD profile of the Degussa P-25

4.2.6. The surface area (BET) results

The BET surface area done on the sample of anatase pH~13 shows BET surface area: 117.8+-0.3478 m^2/g, and molecular cross-section 0.1629nm^2

The B.E.T surface area 117.8m2/g > 45 m2/g (Degussa P-25)

Table 9: BET SURFACE AREA data obtained from sample Ti-OXY-PREC#1/pH:1/Conc.:0.45M and Ti-OXY-PREC#2/pH:13/Conc.:0.125M respectively

Surface Property /sample	**Ti-OXY-PREC#1/pH:1/Conc.:0.45M**	**Ti-OXY-PREC#2/pH:13/Conc.:0.125M**
B,E.T SURFACE AREA	109.7±0.464m^{-2}/g	117.8±0.3478m^2/g
Slope	0.033924±0.000166	0.36598±0.000108
Y-intercept	0.000437±0.000025	0.000368±0.000016
C:	90.720851	100.550798
VM	25.201486cm3/g STP	27.052028cm2/g STP
Correlation coefficient	9.999732e-01	9.999869 e^{-01}
Molecular cross-section	0.1620nm^2	0.1620nm^2

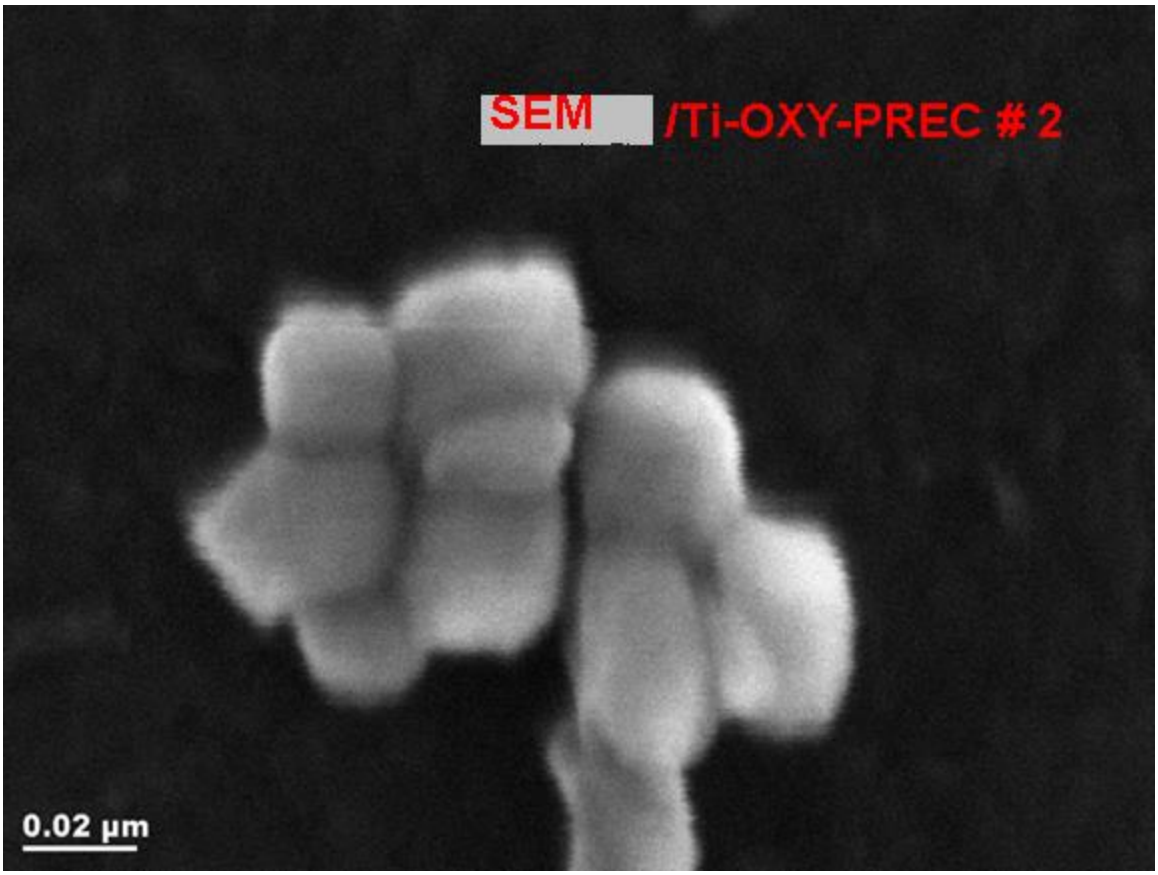

Figure 30: The SEM micrograph of $TiOCl_2$ based sample, pH 13

As can be seen in tables, the surface area of the lyophilized TiO_2 Nanoparticles, decomposed at 200°C, pH 11 is 2.4 times bigger than that of the commercial Degussa P25, and 8 times bigger than lyophilized TiO300 samples. The difference is also remarkably inverse when we compare the pore sizes in the three samples, the sample $TiO_2$00pH11's pore size is respectively smaller than commercial Degussa P25 and the other lyophilized sample TiO300, by 37% and 34%. This observation seems to indicate a particular behavior of the lyophilized TiO_2 nanoparticles that tentatively we can explain by interpreting the hysteresis patterns in isotherm adsorption-desorption curves that are pictured in the figure above.

One observes the presence of three hysteresis loops, which are gaps between adsorption and desorption curves. The hysteresis loop is a characteristic of the mesoporous nature of materials such are the depicted of the three TiO_2 samples in the figure. The mesoporosity suggests the tensile strength effect (TSE) and the capillary condensation being its cause [Ali Qajar, Research Gate). Capillary condensation is a process such that the force exerted on the molecules through the pore walls causes the molecule to adsorb layer by layer. A resulting narrow gap is created by accumulated and collapsed molecules to a lower thermo-dynamical energy state.

Another confirmation of the mesoporous characteristic of the samples is because of the measured pore sizes, all falling within <2 -50 nm) range (Pengfei Zhang, 2016 of Ke Group): the values 15.907nm, 9.31nm, 18,83nm being respectively the diameters of pore for Degussa P25, Ti200pH11, and TiO300.

Further characterization is based on the classification of types of hysteresis (H1, H2, H3, and H4) which provides information on the state of agglomeration, shape of particles present, width of pores, size distribution of the particles. The classification of the adsorption process uses the graph of the amount of adsorbate (Nitrogen gas) adsorbed on the surface of adsorbents, TiO_2 Degussa P25, lyophilized $TiO_2$00pH11, and TiO300 at STP (standard pressure and temperature). Baboo (2015) suggests that by using the four types of the BET adsorption isotherm, the classification and extent of adsorption on these three adsorbents, depending on either one or many factors including Nature of adsorbate and adsorbent, the surface area of adsorbentctivation of adsorbent, experimental conditions (temperature, pressure) would be characteristic of

the adsorbent particles under study. Therefore, the characterization of the particles of adsorbents based on the hysteresis loop is as follows:

Firstly, the Degussa P25 sample is characterized by the most predominant hysteresis in figure (a) being of type H1 loop, suggesting the presence of agglomerates, spherical particles, and uniformly ordered - connected pores.

Secondly, the Ti200pH11 sample is characterized by a predominantly narrow-Hysteresis loop in figure (c) being a mixture of types H1 and H2, indicating additional information on the presence of pores with narrow mouths (ink-bottle), elongated-shaped and networked pores. Thirdly, the Ti300 sample is characterized predominantly by a double-hysteresis loop of type H4 figure (c), suggesting the presence of slit-like pores, irregularly shaped-particles presenting voids of large size distribution, hollowed-walled-ordered spherical mesoporous particles.

4.3. EXPERIMENT (III): Optimization of TiO_2 NPS by lyophilization process: the control of the synthesis conditions (pH, solution concentration and type of precursor factors)

4.3.1. Objective

To experiment on effects of lyophilization synthesis conditions on degree of dispersion (size and size distribution), stability, phase composition, and morphology of TiO_2 NPS.

4.3.2. Introduction

It has been reported that the performance of material for various applications depends much on the corresponding properties, of which synthesis conditions played a deterministic role. Finding the correct values for the synthesis parameters, account much for the success of the Spray-Lyophilization process under current investigation.

Having considered four optimization parameters namely: (i) pH of the solution, (ii) calcination temperature, (iii) nature of Titanium precursor and, (iv) Ratio of the initial concentration of reactants. It follows that the results /effects of those parameters on particle dispersion (size and size distribution), the structure (phase) and, the

morphology are found by at least two out of five characterization techniques, namely: X-Rays Diffraction of the powders, Raman Spectroscopy, SEM / TEM / HR-TEM, UV-Vis spectroscopy, and Photoluminescence (PL) or cathode Luminescence (CL). Mainly, the purpose is to optimize using DTA / DSC thermal analytical techniques to guide the lyophilization synthesis of the TiO_2 NPS to pinpoint the right decomposition temperature of the salt product of the lyophilization process. Furthermore, we test the photo-responses and properties of the lyophilized TiO_2 NPS in water purification scenarios.

4.3.3. Materials and method

Water-solubility of the Ti-precursor had been the main criterion of selection of the four **TiO_2** NPS starting materials, and dividing the study into case studies, based on experimental objectives, we consider the following::

4.3.3.1. Case study III: Ti(IV) isopropoxide

(1) Samples **Ti-iso-2** and samples **Ti-iso-6** are lyophilized-amorphous powders obtained by dissolution in distilled water of Ti(IV) isopropoxide, and addition of NH4OH / HCl, and pH:1 and pH: 9 respectively. These were investigated by DSC / DTA for the optimal temperature of thermal decomposition and X-rays Diffraction for combined effects of pH and annealing temperature (300°C - 900°C) on size, structure and, morphology. Observation is made for any difference by comparing Ti (IV) isopropoxide-based **TiO_2** NPS from acidic and alkaline solutions respectively.

(2) Samples **Ti-iso-pH**: All Ti (IV) isopropoxide-based powders samples from formulations of pH: 1.5; 3.5; 9; 11 were annealed at 650°C and investigated for structural, size and, morphology differences by X-rays Difference.

4.3.3.2. Case study IV: Ti(III) chloride precursor

Samples Ti-Chloro (pH=9 -11) and Ti- Chloro (pH=0.8 - 1.63) are lyophilized powders from formulations of pH: 9-11(alkaline) and acidic (pH: 0.8 – 1.63) respectively made based on dissolution of Ti (III) chloride in distilled water and by adjustments the pH of a solution using HNO_3 / NH_4OH. The samples were annealed at temperatures 300^0C – 900^0C and analyzed by X-Rays Diffraction for the effect of pH on size and structure and

morphology. They were also compared to samples of Ti-Iso samples (pH~1 & pH: 9).for any differences in **TiO_2** NPS formation and features.

4.3.3.3. CASE STUDY V: Ti (IV) Oxychloride: Sample 1 (pH: 7); Sample 2(pH: 1), Sample 3 (pH: 11).

These are amorphous TiO_2 NPS powders samples obtained from the lyophilization process of Ti(IV) Oxychloride-based formulations of neutral solution (pH~7, pH:1(acidic) and pH:11 respectively. They were analyzed by X-Rays Diffraction and compared for any difference in size and structure of TiO_2 NPS with dependence in the ratio of initial reactants (concentration), i.e. volume of Ti (IV) oxychloride over the volume of Deionized water, and effect of pH of the initial solutions.

4.3.3.4. CASE STUDY VI: Ti (IV) Acetylacetonate (samples concentrations: C_1, C_2, C_3, and C_4):

These are the four amorphous powders samples, of different concentration i.e. volume ratio of Ti (IV) acetylacetonate over the volume of distilled water (solvent), but same pH (neutral). The derivation of the model of TiO_2 nanoparticles' size with dependence on concentration from first principles was done to predict optimal concentration based on Ti-acetylacetonate. They also served to characterize by XRD, and TEM the effect of concentration on size, morphology, and size of the TiO_2 NPS.

4.3.3.5. CASE STUDY VII: EFFECT OF THE NATURE OF Titanium precursors

The differences in the results of XRD, TEM, and RAMAN characterization on the above-described samples are indicators of the effect of the nature of Ti-precursors for the production of TiO_2 nanoparticles. Therefore, samples decomposed in the same conditions, namely Ti-so samples, Ti-Chloro, Ti (IV) Oxychloride-based TiO_2 NPs and, Ti (IV) acetylacetonate are compared.

4.3.4. Sample preparation methodology

(i) Samples (Ti-ISO) Prepared by varying pH of Ti (IV) – isopropoxide

The size, phase, and morphology of particles can be controlled by well-selected preparation conditions of the initial solution, particularly the hydrogen potential (pH) change. It is well known that pH is of great importance for the crystallization process, including nucleation, crystal growth, and crystal aggregation. As an example, its importance was shown to be paramount in the crystallization conditions for the transformation of Kanenite into silicate. Assuming many properties of metal oxides nanoparticles follow that of the reference semiconductor material, Silicate (SiO_2), the formation of TiO_2 would be favored by using highly basic conditions during stirring of the suspension at fixed temperature °C and the adjustment of the pH after stirring [Martine Salou et al.]. Similarly, nucleation, crystal growth and, phase transformation of TiO_2 must be dependent on starting solution pH. These processes, particularly when the particle is in the metastable phase, are important stages whereby size, phase, and morphology are well defined. Not only that we assume the size, phase, and morphology of TiO_2 would be dependent on the parameter pH of the initial solution precursor solution, we also assume the lyophilization process will conserve the pH effect through its different stages.

The method followed the steps that consisted of varying the pH of the solution while keeping other synthesis parameters constant, including concentration, processing time, pressure and the temperature of annealing decomposition. It is an important technique in tracing the effect that the pH changes play on nanostructures' and thermodynamic character of the **TiO_2** material. In the present study, firstly we carried out the calibration of pH values using titanium trichloride, $TiCl_3$, distilled water, HNO_3 (nitric acid) and, sodium hydroxide (NH_4OH) as precursors for samples **S1**. Secondly, using the precursor's titanium isopropoxide Ti $\{OCH\ (CH_3)_2\}_4$, distilled water, and the titrants: NH_4OH and/ or HNO_3 we prepared samples.

(ii) SAMPLES (Ti- Chloro): Prepared by varying pH of Ti (III) Tri-chloride ($TiCl_3$)

The solution preparation process was carried out as follows: In the first case, a certain number of moles concentration of $TiCl_3$ and a certain number of mole NH_4OH were dissolved in 250 ml distilled water (DW). The decomposition of hexahydrate titanium (III) chloride produced the $TiCl_3$ that was used such as $TiCl_3 \bullet 6H_2O \rightarrow TiCl_3 + 6H_2O$ (2)

pH observation: After mixing of titanium chloride, ammonia, the color of the solution was observed in a beaker. The pH value of this solution was measured by pH test strips (Sigma Aldrich: P3536 range: 6.0 – 7.7, resolution 0.3 – 0.4 pH unit (3) Desired pH calibration: In the third step, the pH value of the solution was adjusted to the desired value (from 1.63 to 11) by using 1 mole NaOH and 1-mole HNO_3 solution (each in 100 ml deionized distilled water) and was added drop by drop. Alkaline solutions are obtained by using NH_4OH and the acidic solutions are obtained by adjusting the pH by the addition of HNO_3 according to the following Titanium Oxide Meta-synthesis reaction. For sample S1, the following reaction is considered, whereas reaction 4 has been considered for sample S2: $2\ TiCl_3 + 6\ NH_4OH + 2\ H_2O = 2\ TiO_2 + 6\ NH_4Cl + H_2$. A two steps-reaction (reaction 2 &3) leads to the product ($TiO_2 + NH_4Cl$ +H2) is considered alternatively, when the nitric acid is added to adjust the pH such that:

$3\ NH_4OH + HNO_3 = 2\ NH_4NO_3 + 4\ H_2$ (reaction 2)

$2\ TiCl_3 + 3\ NH_4NO_3 + 5\ H_2O = 2\ TiO_2 + 6\ NH_4Cl + 11\ H_2$ (reaction 3)

$Ti\ \{OCH\ (CH_3)_2\}_4 + 2\ H_2O \rightarrow TiO_2 + 4\ (CH_3)_2CHOH$ (reaction 4)

For this investigation, two sets of samples were prepared based on precursor solutions. Titanium isopropoxide, and titanium trichloride. These were respectively named: P-iso and P-3 - Chloro.

i. Ti-ISO samples

A mass of 1.0g (100mg) of salt of Titanium (IV) isopropoxide was dissolved in 150ml of distilled water. The pH of it was controlled to prepare different samples (solutions) namely, P-ISO-1, P-ISO2, P-ISO-3, P-ISO-4, and P-ISO-5 corresponding, respectively, to pH: 1.5; 3. 5; 5; 9 and 11. The pH in the samples was measured using a pH-meter immediately before and after processing.

ii. Ti-CHLORO Samples:

A solution of Titanium(III) trichloride, dissolved in distilled water was made. The pH in the solutions was adjusted using NH_4OH or/and HNO_3, to a neutral solution, pH=7, alkaline solutions of pH's ranging from 8 – 14 and, acidic solutions of pH's ranging from 0 – 6.5. The synthesis steps are the same as previously described, and again, the pH-meter was used to measure the pH before and after lyophilization processing.

Schematically, the diagram below summarizes the solution samples as prepared by varying the pH of two different types of the precursor.

The figure 31 presents the optimization method of TiO_2 NPS from two different types of Titanium precursor, Ti (IV) isopropoxide and Ti (III) Chloride with variable pH parameter.

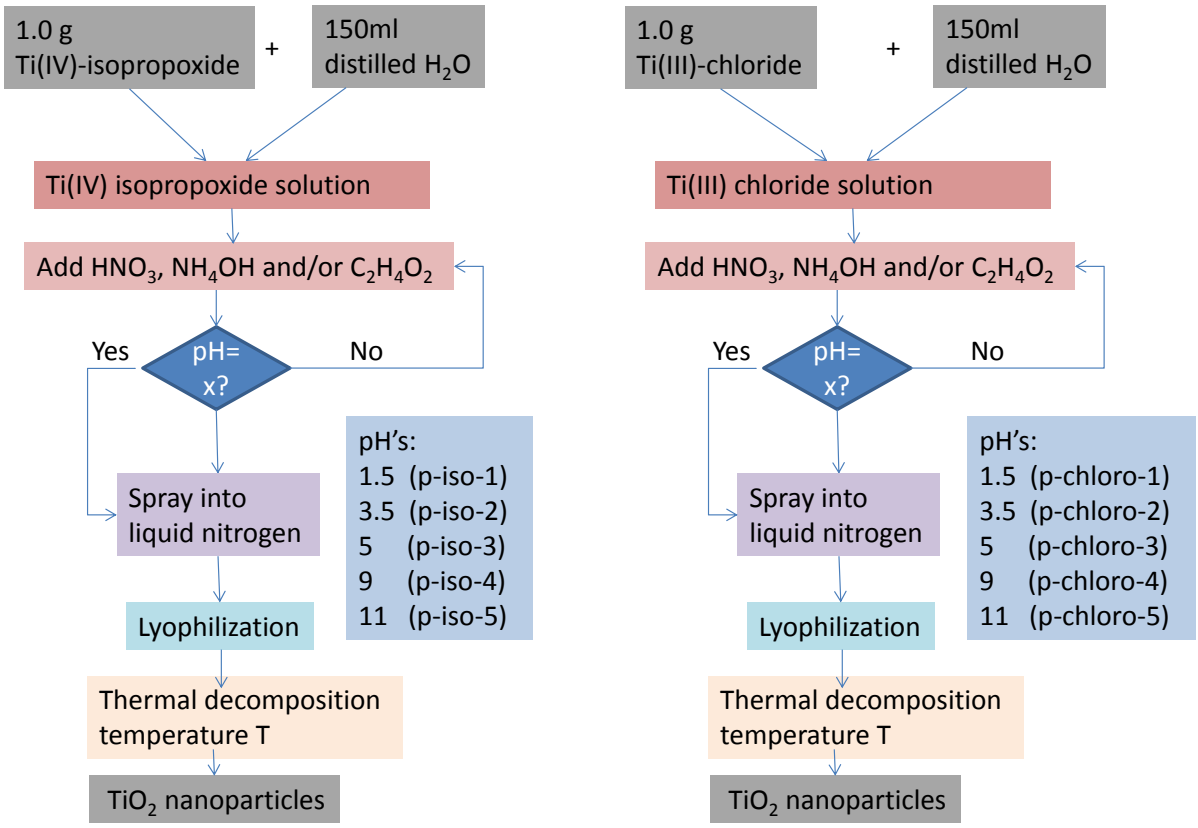

Figure 31: Flowchart summarizing the synthesis method of TiO_2 NPS from two different types of Titanium precursor, Ti (IV) isopropoxide and Ti (III) Chloride with variable pH parameters

(iii) SAMPLES (Ti-acetyl): Samples from Titanium (IV) oxide acetylacetonate ($C_{10}H_{14}O_5Ti$)

The **TiO_2** nanoparticles were synthesized by a multi-step, adapted version of the lyophilization technique. 1.0 g of titanium acetyl-acetonate was dissolved in 150ml of distilled water and brought to a pH of 7. The solution was sprayed "laminar regime" into liquid nitrogen to generate droplets rich in water (-90%). These droplets were then sublimated in a lyophilization chamber to yield a very porous precursor.

4.3.5. Results and discussion

4.3.5.1. Optimization method by DSC / DTA and X-RAYS diffraction investigations

The Aim is to run thermal analysis experiments -DSC / DTA to optimize the results (changes in size, structure, shape) at annealing temperatures of as-synthesized products corresponding to the predicted DTA / DSC results**.**

4.3.5.2. Experimental Procedure (DSC/ DTA)

The principle of the Differential thermal analysis is based on comparing the temperature of the sample being examined with the temperature of a thermally inert substance. By plotting differential temperature (ΔT) against time, or temperature, the enthalpy change can be measured by considering the area under a DTA peak, without affecting the heat capacity of the sample. The change of properties with temperature could be either physical or chemical. The physical change includes phase change (melting, vaporization, crystallization, structural transitions, changes in microstructures, volume changes such as expansion or contraction, it could also be changed in mechanical properties. Whereas chemical changes include: reactions forming new products, oxidation, corrosion, the materials could decompose, dehydrate, chemisorption, etc.

The similarity between Differential Scanning (DSC) and DTA is considered in many aspects. It is mainly a differential technique, with a sample and a reference, and the setup is heated or cooled at a constant rate. However, the difference between the two is that in DTA the temperature difference between the sample and the reference is monitored, and in DSC, the difference in power to the sample and the reference to keeping to maintain the heating or cooling the two at the same rate is measured.

DSC analysis was performed by heating a constant rate of 10◦ C/min in nitrogen, the purge gas system to provide inert or reactive atmosphere, over a temperature range of 1000°C, with sample weights of about 5 mg. The thermal stability analysis was done using a thermogravimetric analysis instrument. The TGA was equipped with a microbalance, measuring continuously sample weight, and the furnace around the

sample holder, together with the purge gas ensures an inert or reactive atmosphere. The computer controls the furnace and collects data (weight against sample temperature).

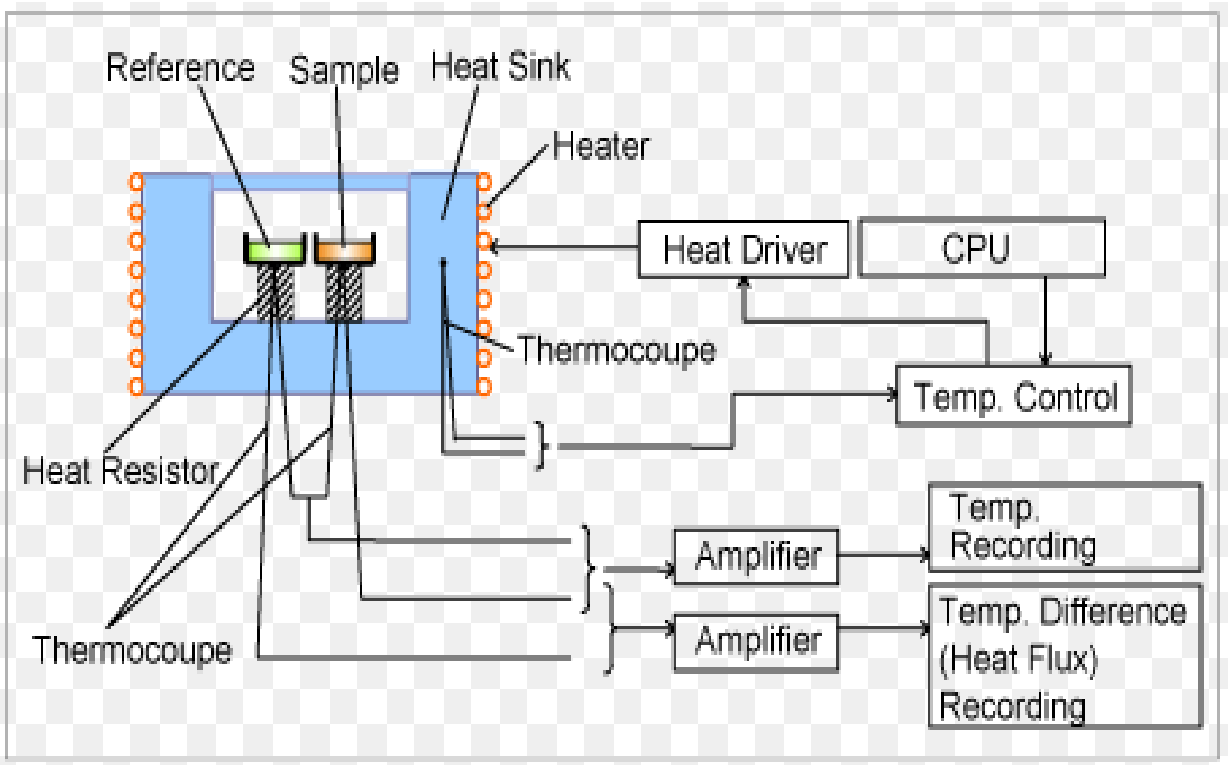

Figure 32: Principle of thermal Analysis (DSC, TG / DTA. TMA & DMA).

4.3.5.3. Thermal decomposition and DSC/DTA results

The results obtained from DSC / DTA thermograms of samples Ti-iso-2 (pH: 0.8 – 1) and Ti-iso-6 (9 -11) are depicted in figures (a) and (b), shown respectively as representative of acid and alkaline-based samples, they are also given for analysis purpose to discussion changes (size, phase or structure and morphology) **i.e.** post lyophilization transformations by decomposition / thermal annealing of the samples.

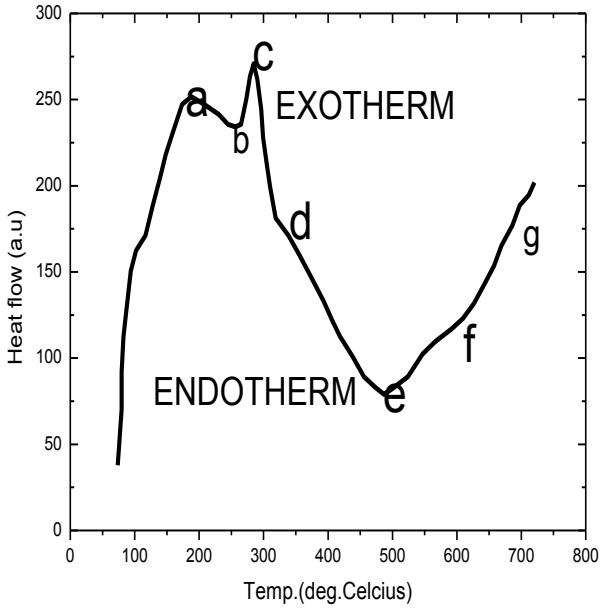

DSC / DTA curve, Ti_iso_2, pH ~ 1

DTA Peak	Decomp T (°C)
A	185
B	250
C	278

Figure 33: DTA Thermogram for TI-iso-2, pH: 2 and its associated table

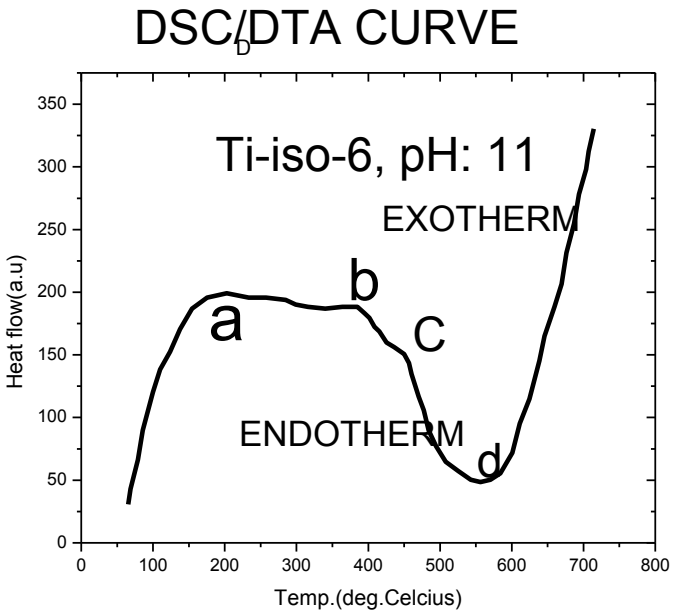

DTA peak	Decomp. Temp. (°C)
a	196.36
b	385.94
c	461.71
d	560.96

Figure 34: (b): DTA curve for sample Ti-iso-6, pH~11; Plot of differential temperature versus temperature

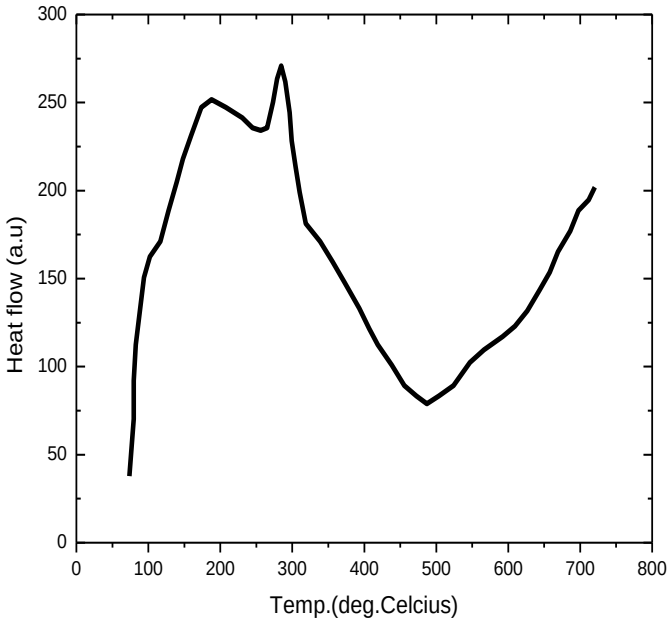

Figure 35: (a) DTA-Thermogram of sample Ti-iso-2, pH=1

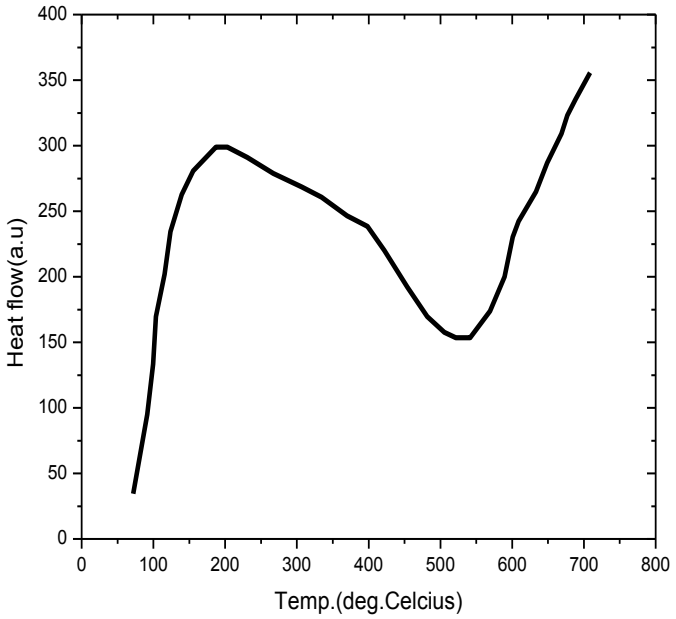

Figure 36: DTA Thermogram of sample Ti-iso-3, pH: 3

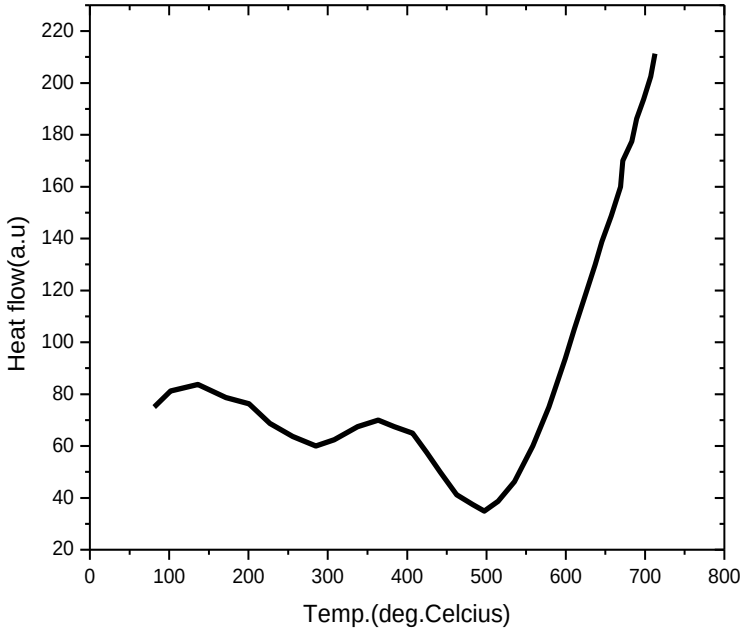

Figure 37: DTA-Thermogram of sample Ti-iso-4, pH=5

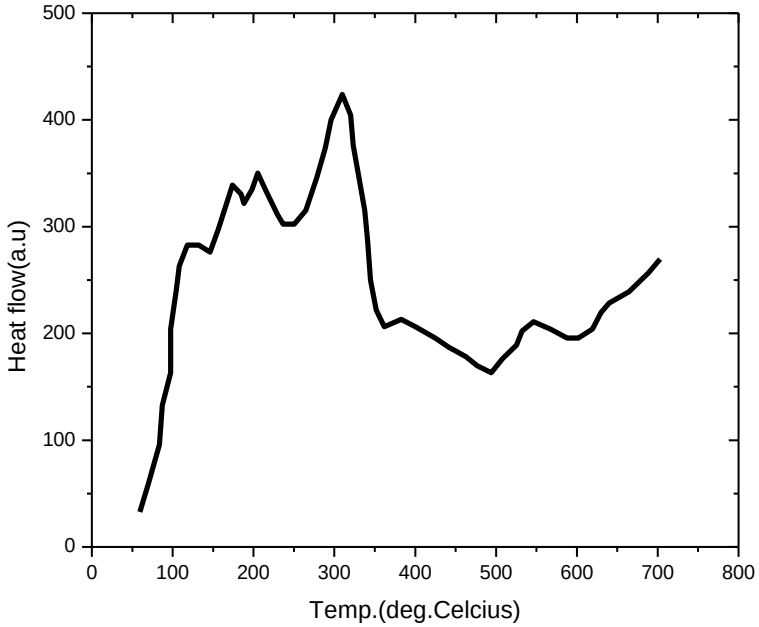

Figure 38: DTA-Thermogram of sample Ti-iso-5, pH=9

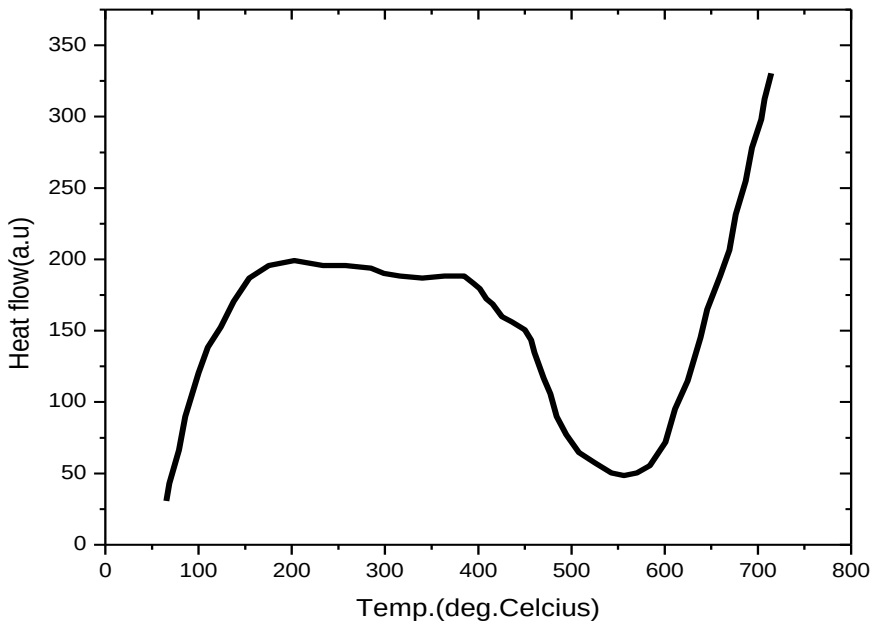

Figure 39: DTA-Thermogram of sample Ti-iso-6, pH:11

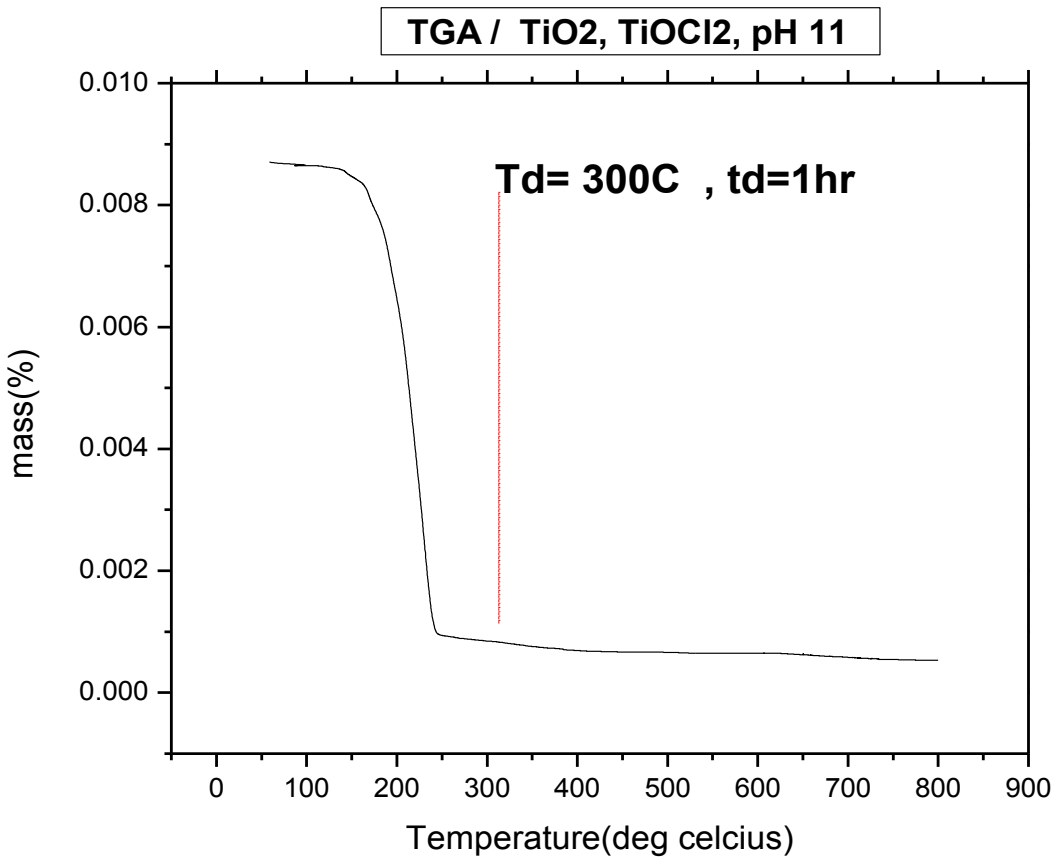

Figure 40: TGA plot $TiOCl_2$ sample pH: 11

The mass ratio (%) = 1/8 (12.5%); Compared to Thermal annealing ~ 1/5 (19.2%) or 0.0547g/0.2848g)

Theory of thermal decomposition of the samples:

(i) Ti -iso-2, pH: 1 & Ti-iso-6, pH: 11

Amorphous **TiO_2** powders were obtained from the titanium isopropoxide precursor precipitated under different pH values by adding aqueous ammonia. Under these conditions, considering the nature of Ti(IV) isopropoxide, the role of NH_4OH, the formation of **TiO_2** NPS, the structural and morphological evolution could be explained based on the following reaction and assumptions:

: $$Ti(OP_r)_4 \rightarrow TiO_2 + 4C_3H_6 + 2H_2O$$

- Assuming an activation barrier of ~57Kcal/mol (K. Ershov et al., Jan2018), the thermal decomposition of Ti $(OP_r)_4$, several propylene molecules have been released.
- The **TiO_2** powders are the products of decomposition of titanium hydroxyl compound $Ti(OH)_4$, intermediate products after the following mode:

$$Ti(OP_r)_4 \rightarrow (PrO)_3 TiOH + C_3H_6$$

- The effective first-order rate constant of TTIP thermal decomposition (propylene formation) is estimated to be: $k = 3.96 * 105 * e^{(-\frac{8479.7}{T})S^{-1}}$
- The gas-phase products of titanium isopropoxide's decomposition consist of acetone, propylene, methanol, and ethanol
- Surface reactions are the most predominant interactions

(ii) Ti -3-Chloro, pH: 11

Samples of amorphous Titanium dioxide (Titania) powder have been obtained from precipitation of $TiCl_3$ and NH_4OH initial material in solutions of varied pH between 1 and 11, were investigated with different calcination temperatures. The result of TG and XRD showed that the NH_4Cl decomposed between 235-372^oC. The XRD result showed that the anatase **TiO_2** only contained a single phase with the calcination temperature of the precursor at 400^oC for pH =1 - 7 and rutile for pH = 8 -11 at 400°C.

4.3.5.4. Experimental procedure (XRD)

(i) The principle of XRD analysis

The principle of the X-ray analysis is based on constructive interference between monochromatic X-rays and the sample, usually crystalline structure. The former is generated by a cathode tube, which when they are filtered, produces monochromatic electromagnetic waves. By collimation, they are concentrated on the sample, interact with the sample to generate, not only constructive interference but also diffracted rays following Bragg's law such that: $\boldsymbol{n\lambda = 2d\,sin\phi}$.

The X-ray diffraction patterns are characteristic of each crystalline sample, which could be used for the identification of the unknown material by cross-examination concerning **ASTM** International, formerly known as the American Society for Testing and Materials.

The experimental procedure is based on the setup given next:

1) The X-ray beam is irradiated on the sample; 2) The sample emits characteristic X-ray patterns; 3) To analyze crystal, rotate the detector by angle 2Ø accurately to expose each wavelength in such a manner Bragg's law is satisfied, meaning: $\boldsymbol{n\lambda = 2d\,sin\phi}$; 4) The position and the intensities of peaks are measured by the detector as X-rays are diffracted by the sample at different angles Ø; separating wavelength (λ), it identifies elemental components of the sample as per ASTM signature peak positions.

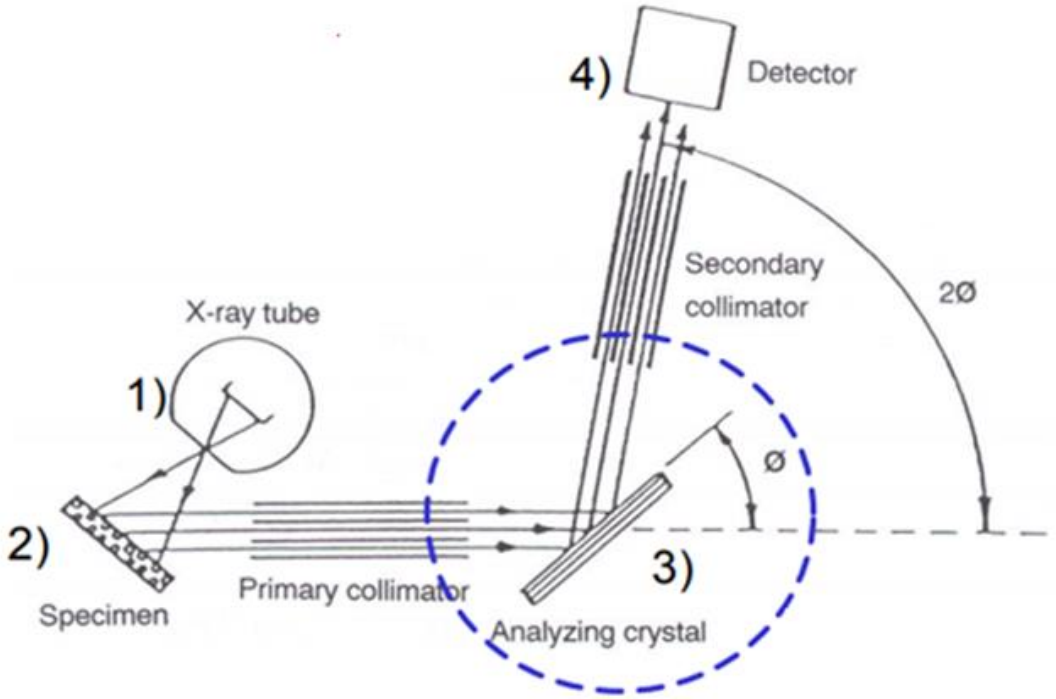

Figure 41: Setup for the experimental procedure of X-ray diffraction analysis.

(ii) XRD results for samples Ti-iso-2 and Ti-iso-6 are presented in the figure that follows.

(a)

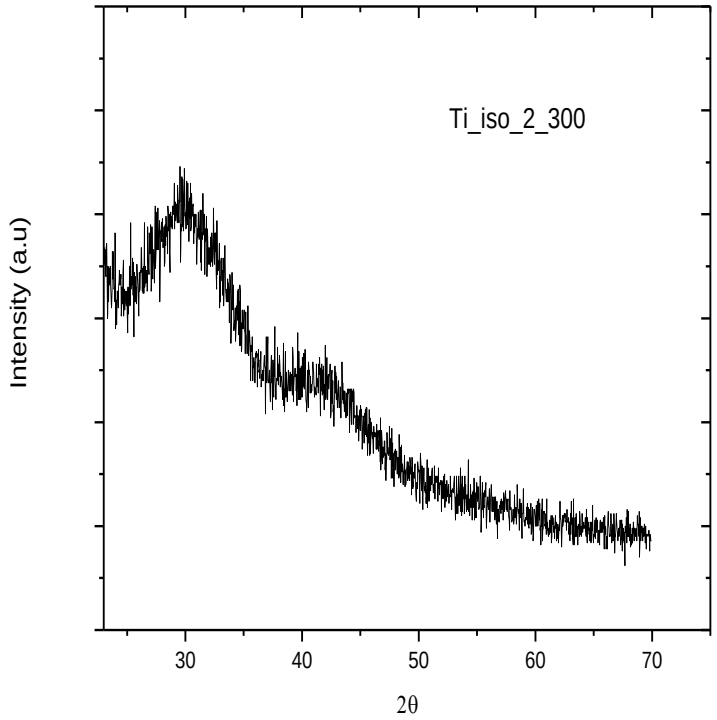

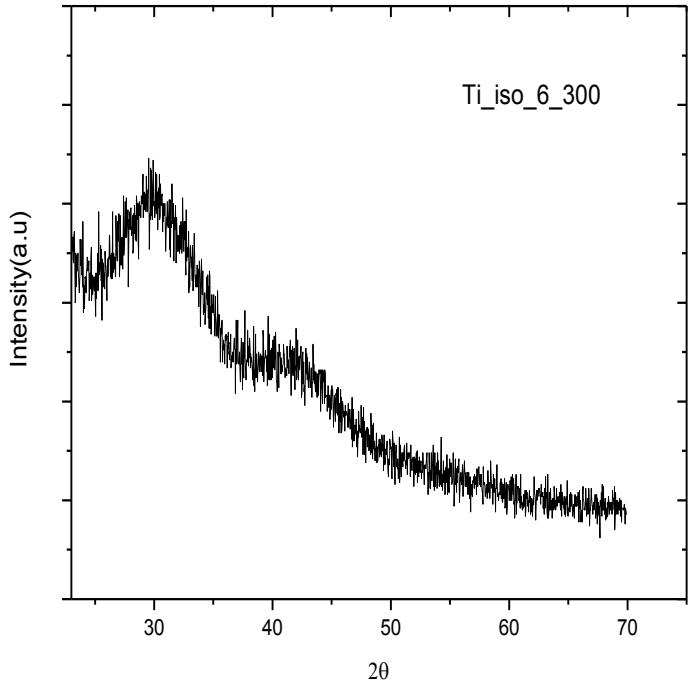

(b)

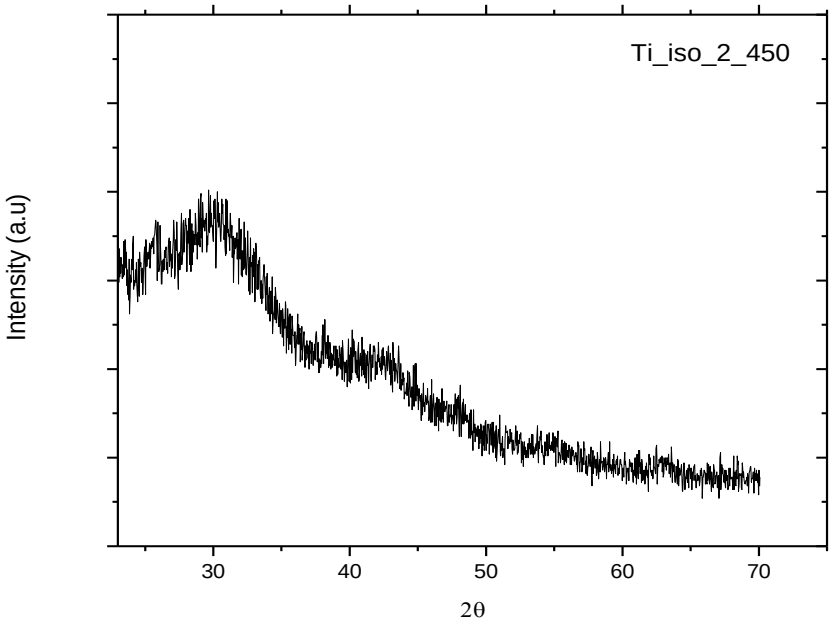
Ti_iso_2_450
Intensity (a.u)
30
40
50
60
70
2θ

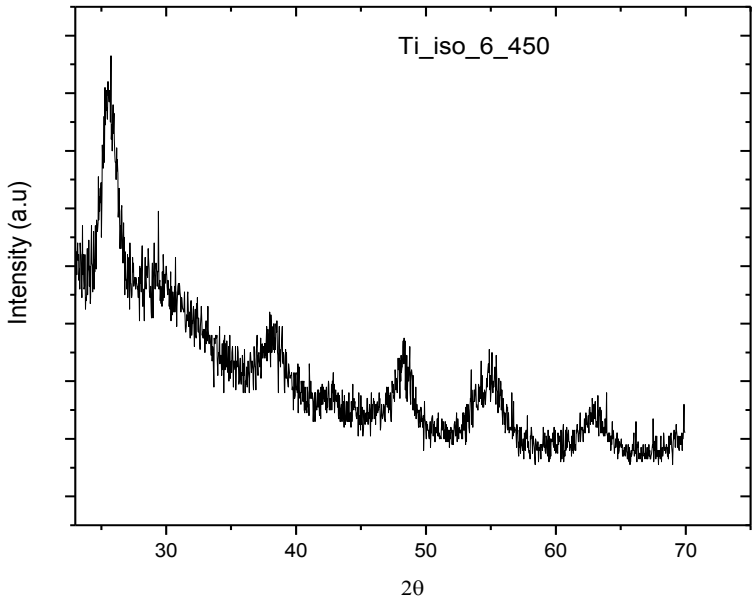
Ti_iso_6_450
Intensity (a.u)
30
40
50
60
70
2θ

(c)

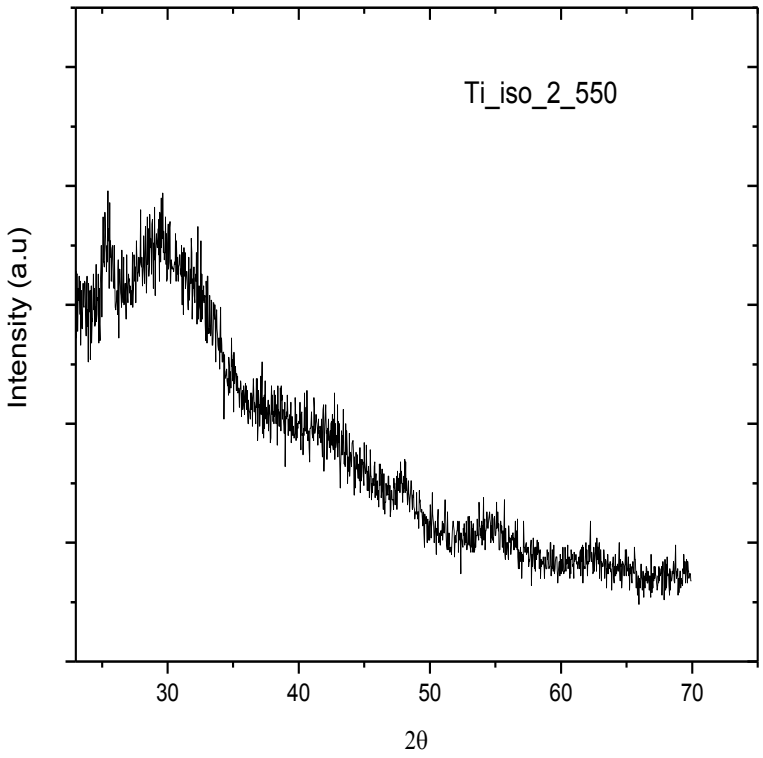
Ti_iso_2_550
Intensity (a.u)
30
40
50
60
70
2θ

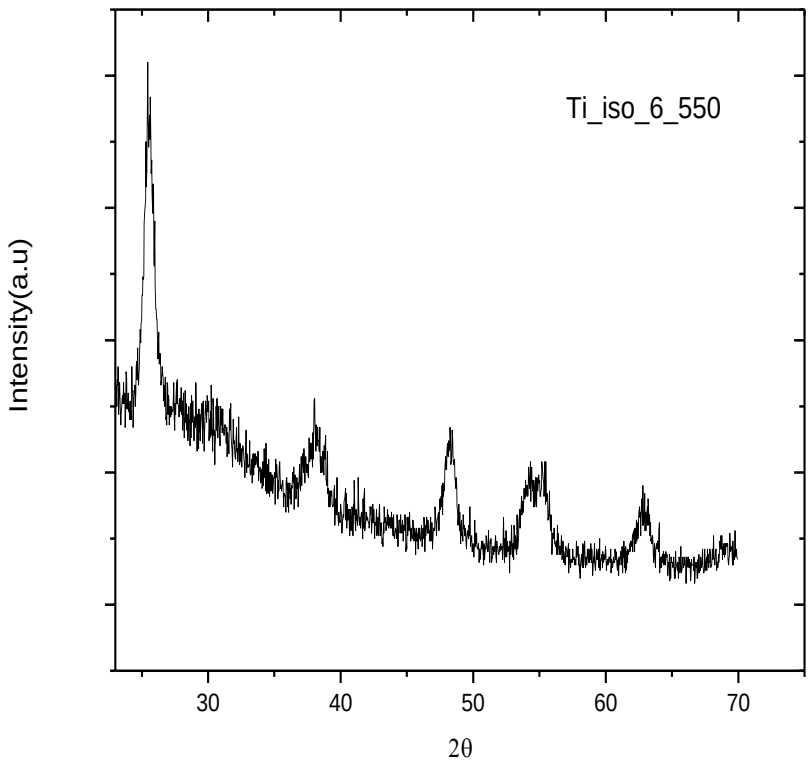
Ti_iso_6_550
Intensity(a.u)
30
40
50
60
70
2θ

(d)

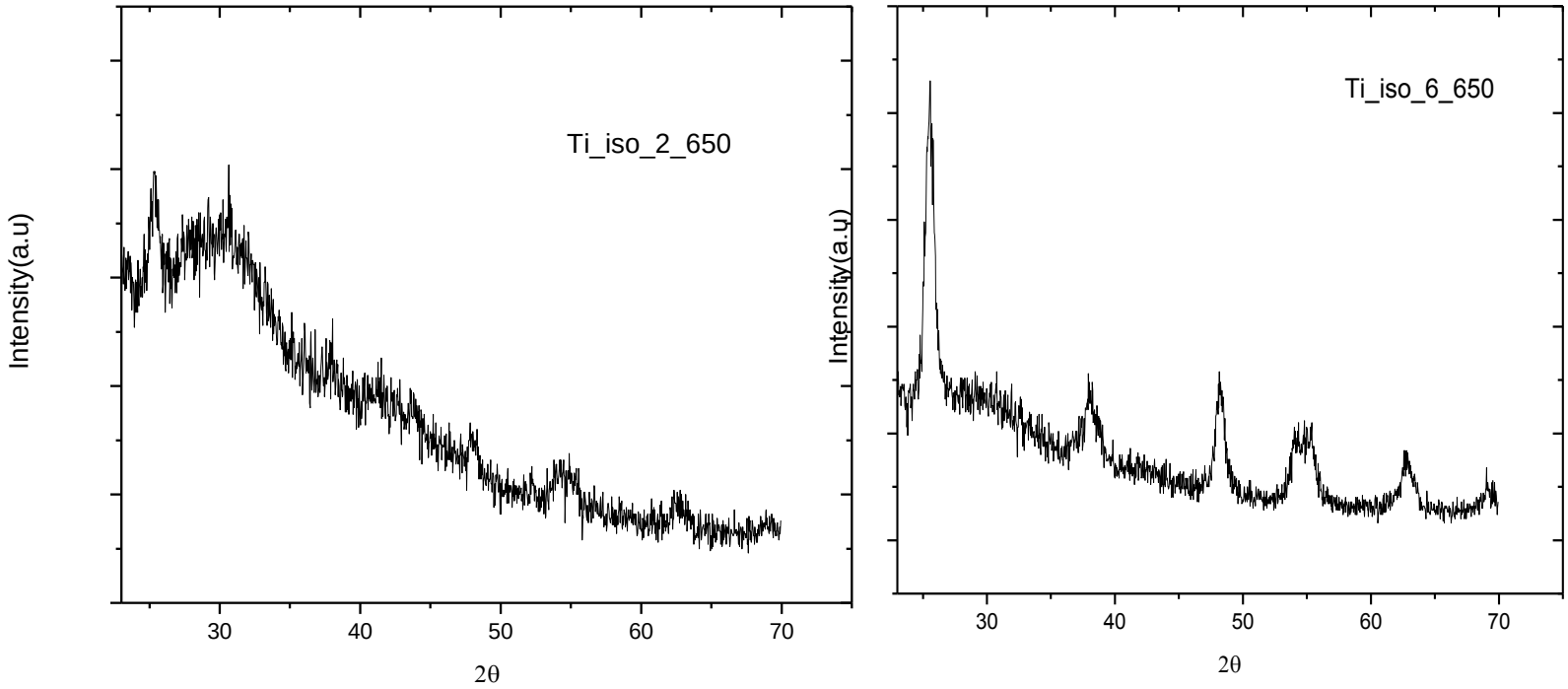
Ti_iso_2_650
Intensity(a.u)
30
40
50
60
70
2θ
Ti_iso_6_650
Intensity(a.u)
30
40
50
60
70
2θ

(e)

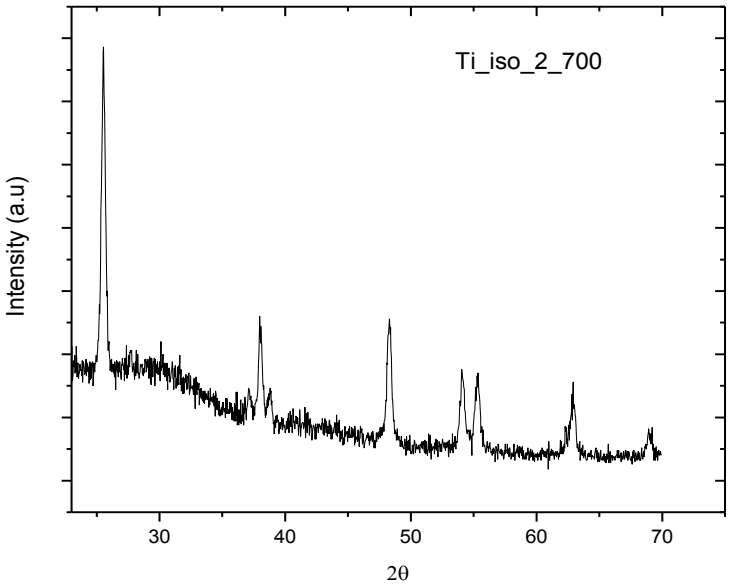
Ti_iso_2_700
Intensity (a.u)
30
40
50
60
70
2θ

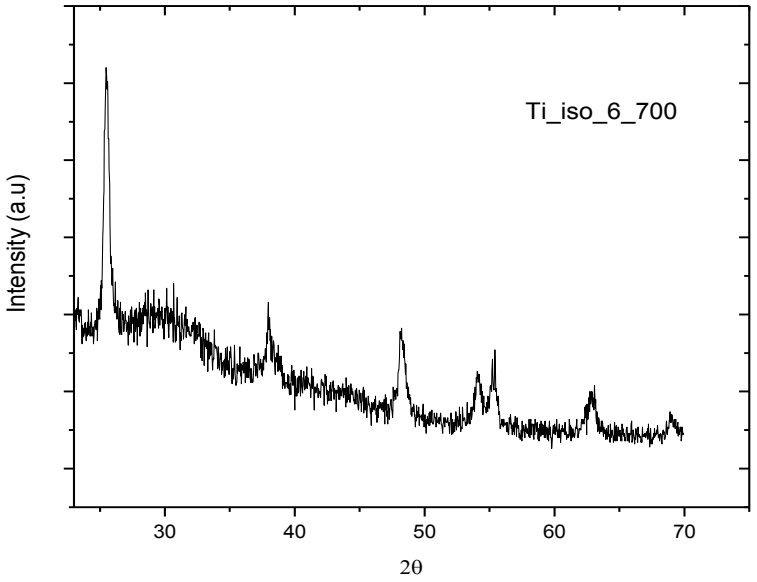
Ti_iso_6_700
Intensity (a.u)
30
40
50
60
70
2θ

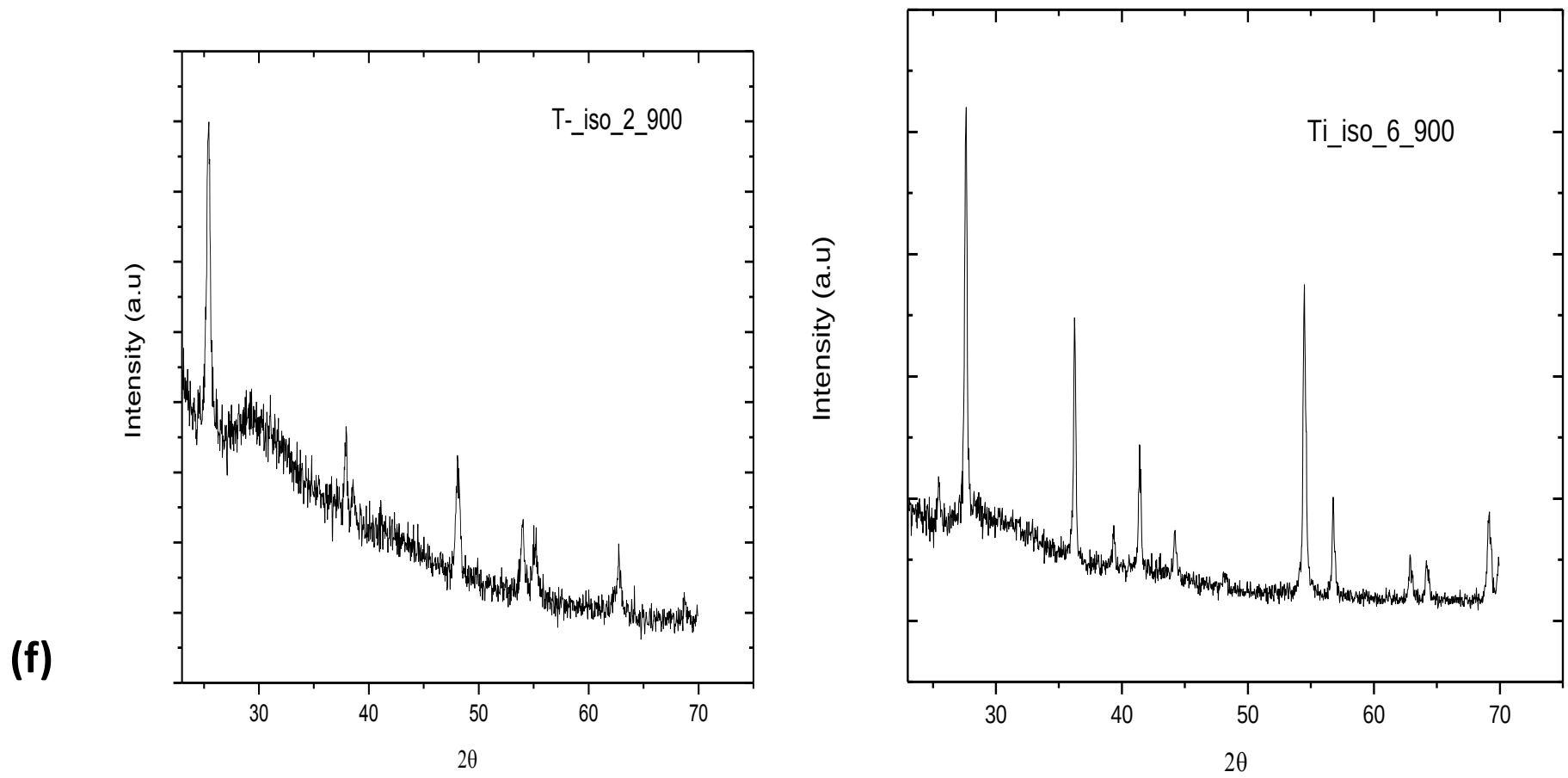

Figure 42: (a) Ti-iso-2 (300C)/Ti-iso-6 (300C); (b) Ti-iso-2(450C)/Ti-iso-6(450C); (C) Ti-iso-2(450C)/Ti-iso-6(450C);Ti-so-2(550C) -Ti-iso-6 (550C); (d) Ti-iso-2 (650) - Ti-iso-6 (650); (e) Ti-iso-2(700C)/Ti-iso-6 (700C), (f) Ti-iso-2(900C)/Ti-iso-6-900C

Figure 43: Ti-iso-2-450-matched characteristic (2θ) angles, Intensities and reticular distances

Phase	(2θ)	Int-f	h k l
B	25.724	19.1	110
B	30.055	22.4	111
B	42.826	12.6	130
A	47.722	7.7	200
B	54.722	5.9	134

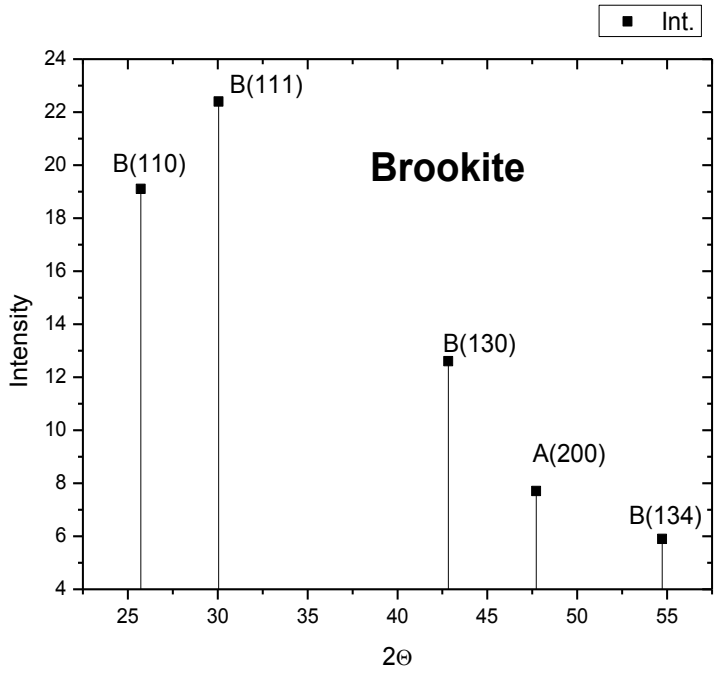

Figure 44: Ti-iso-2-550: matched characteristic (2θ angles), Intensities and, reticular distances

Phase	(2θ)	Int-f	h k l
A	25.456	24.9	101
B	29.596	24.2	111
A	48.110	11.6	200
A	54.489	10.4	211
A	63.185	10.4	204

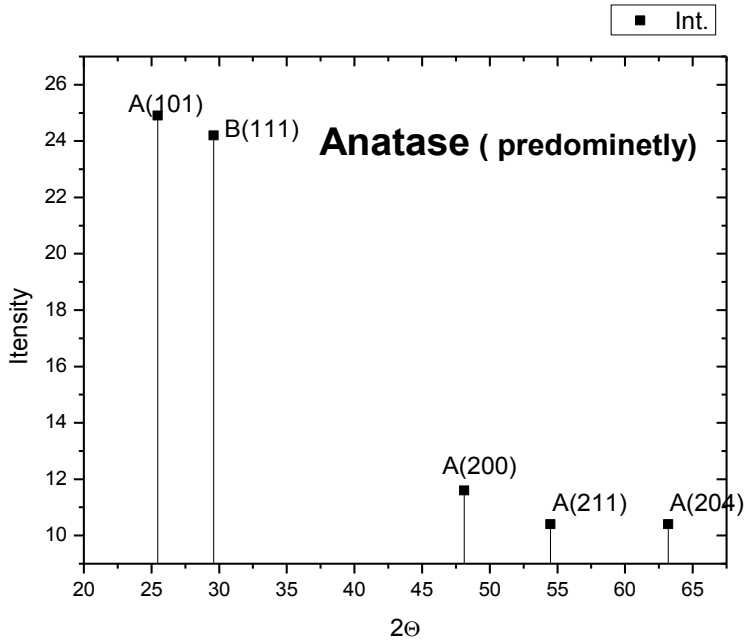

Figure 45: Ti-iso-2-650. Matched characteristic (2θ) angles, Intensities and reticular distances.

Phase	(2θ)	Int-f	h k l
A	25.349	44.4	101
R	27.858	15.3	110
B	30.671	30.3	111
A	37.949	14.0	004
R	41.283	11.5	111
A	47.638	14.8	200
R	54.166	15.5	211
A	62.405	11.8	204

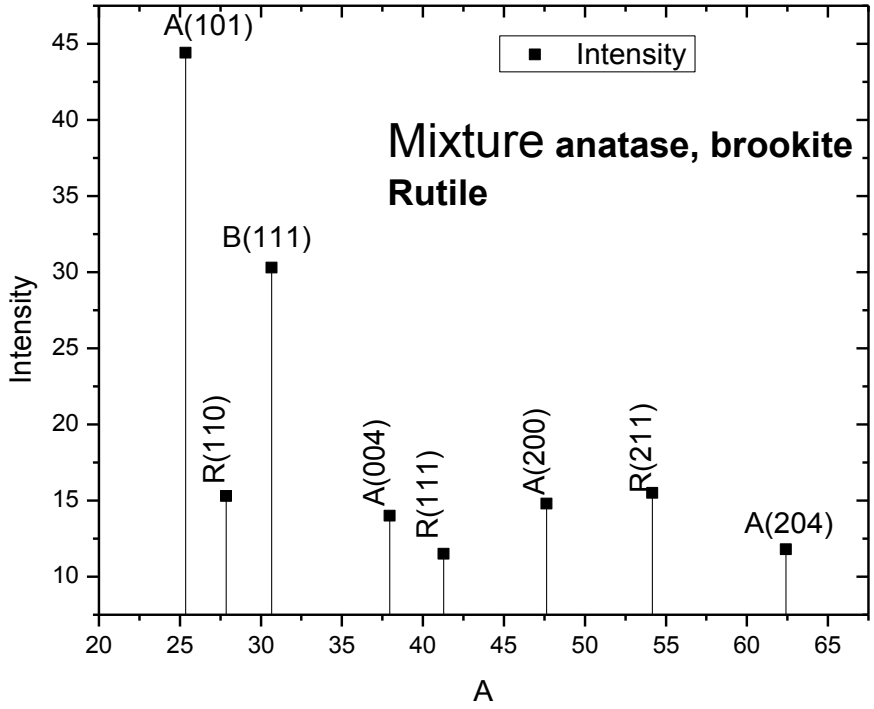

Ti-iso-2-700. Matched characteristic (2θ) angles, Intensities and reticular distances.

Phase	(2θ)	Int-f	h k l
A	25.540	198.7	101
A	38.026	59.4	004
A	48.289	83.7	200
A	54.106	50.1	105
A	55.305	48.9	211
A	62.908	40.0	204

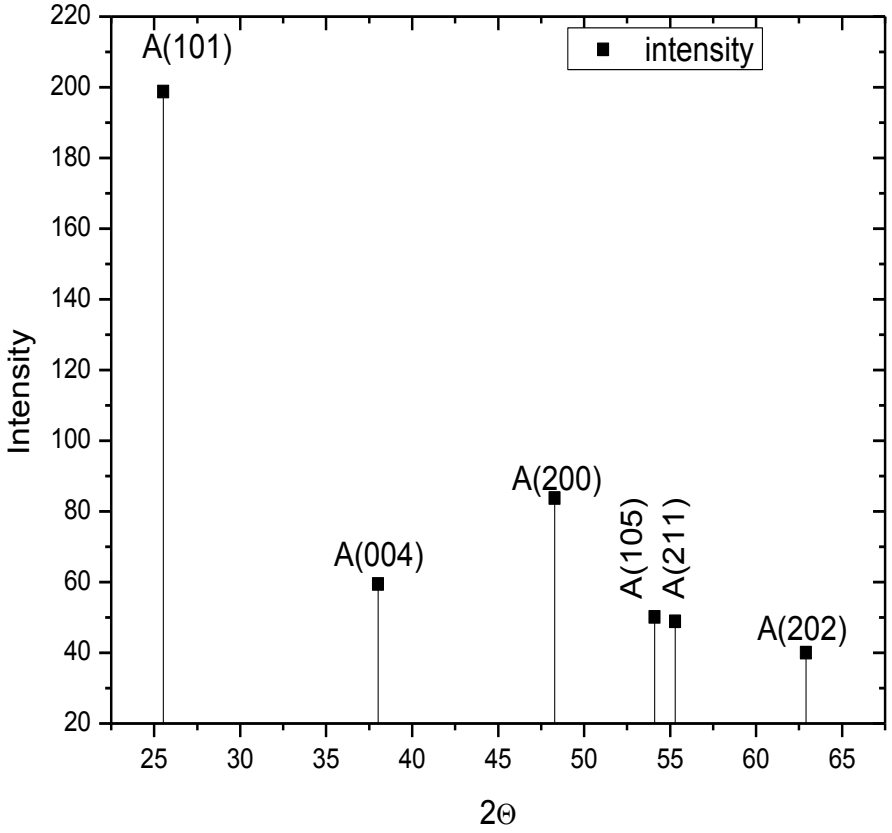

<u>Figure 46</u>: Ti-iso-2-900 Matched characteristic (2θ) angles, intensities and reticular distances

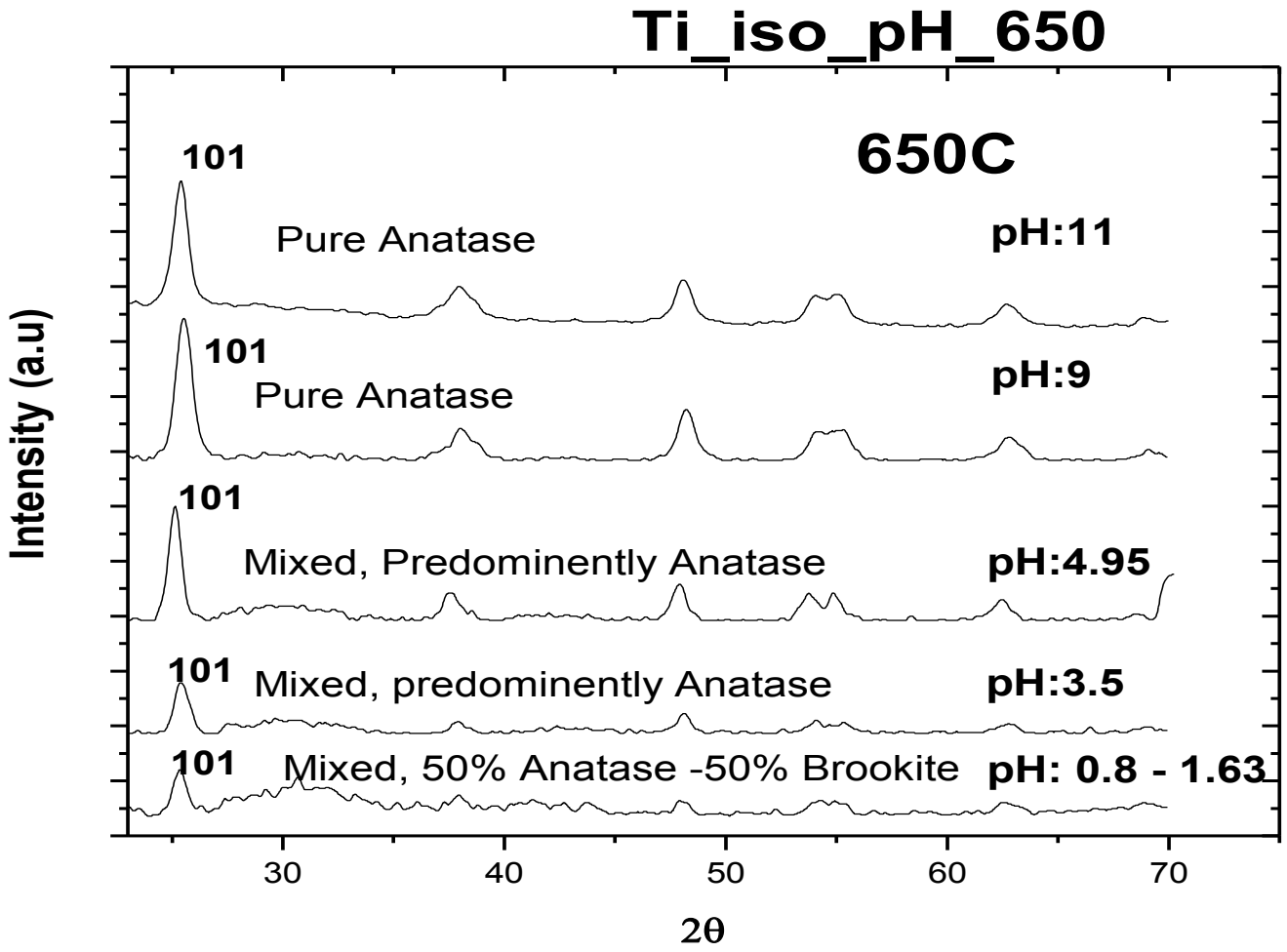

Figure 47: pH - programmed XRD patterns of samples decomposed at 650C

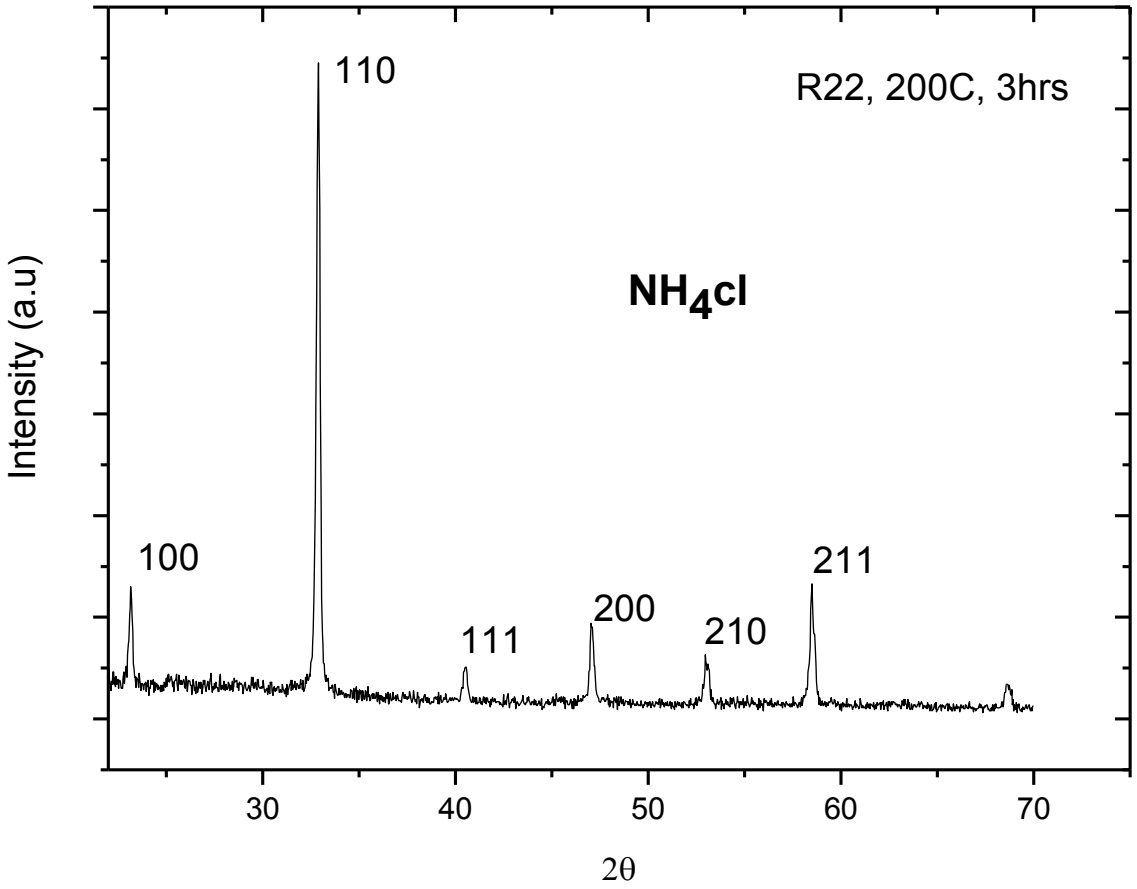
R22, 200C, 3hrs
NH4cl
Intensity (a.u)
110
100
111
200
210
211
30
40
50
60
70
2θ

(a)

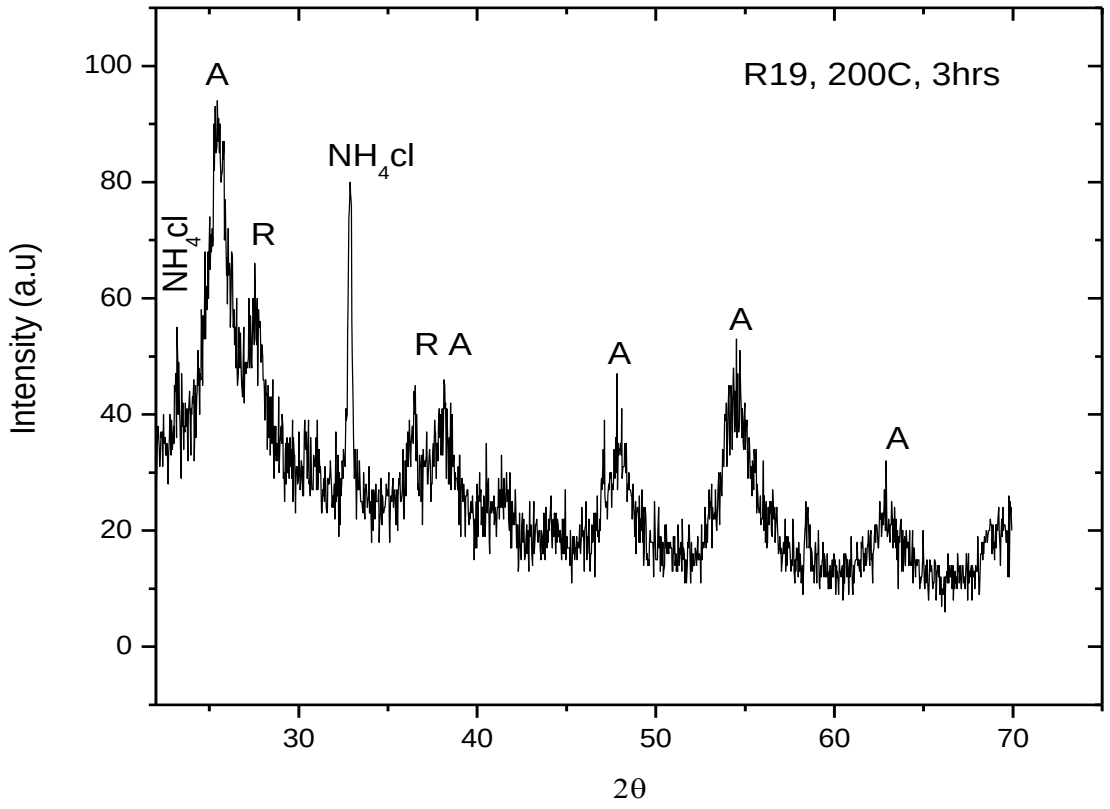
R19, 200C, 3hrs
Intensity (a.u)
2θ
100
80
60
40
20
0
30
40
50
60
70
A
NH4cl
R
NH4cl
R A
A
A
A

(b)

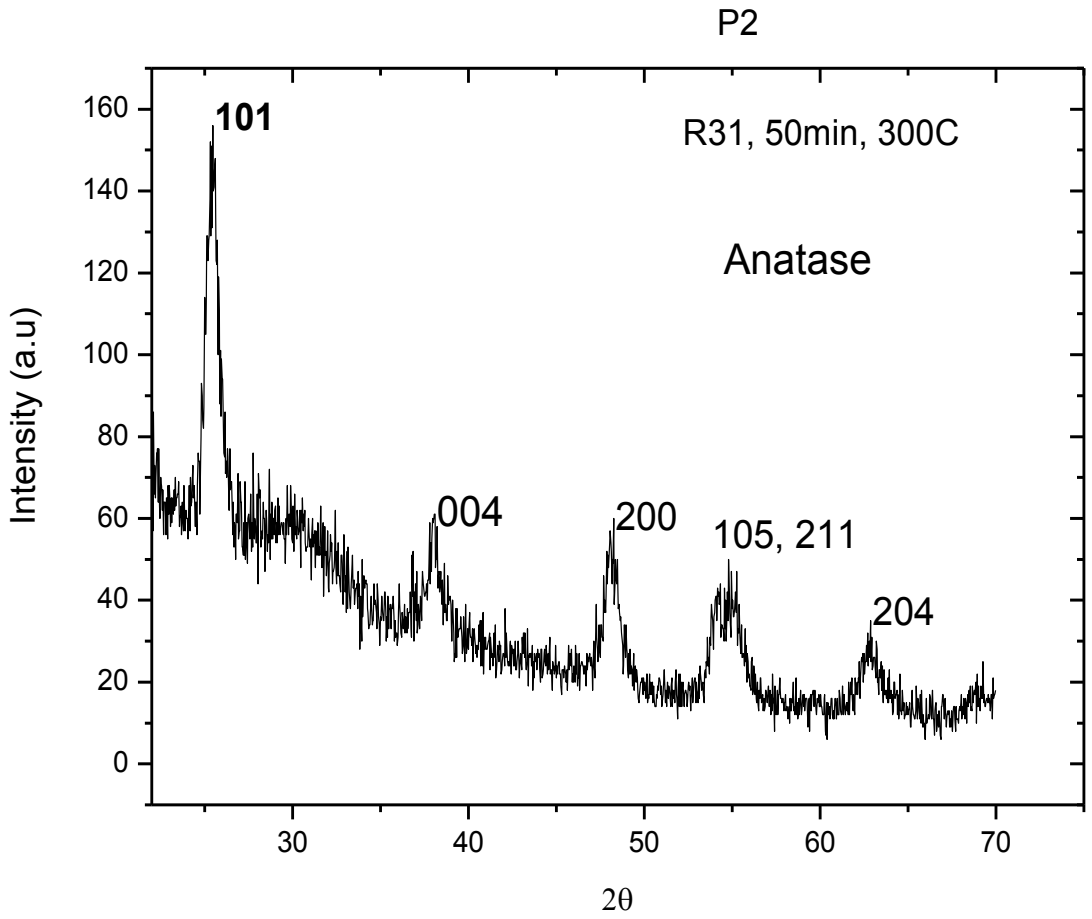
P2
101
R31, 50min, 300C
Anatase
004
200
105, 211
204
Intensity (a.u)
2θ
0
20
40
60
80
100
120
140
160
30
40
50
60
70

(c)

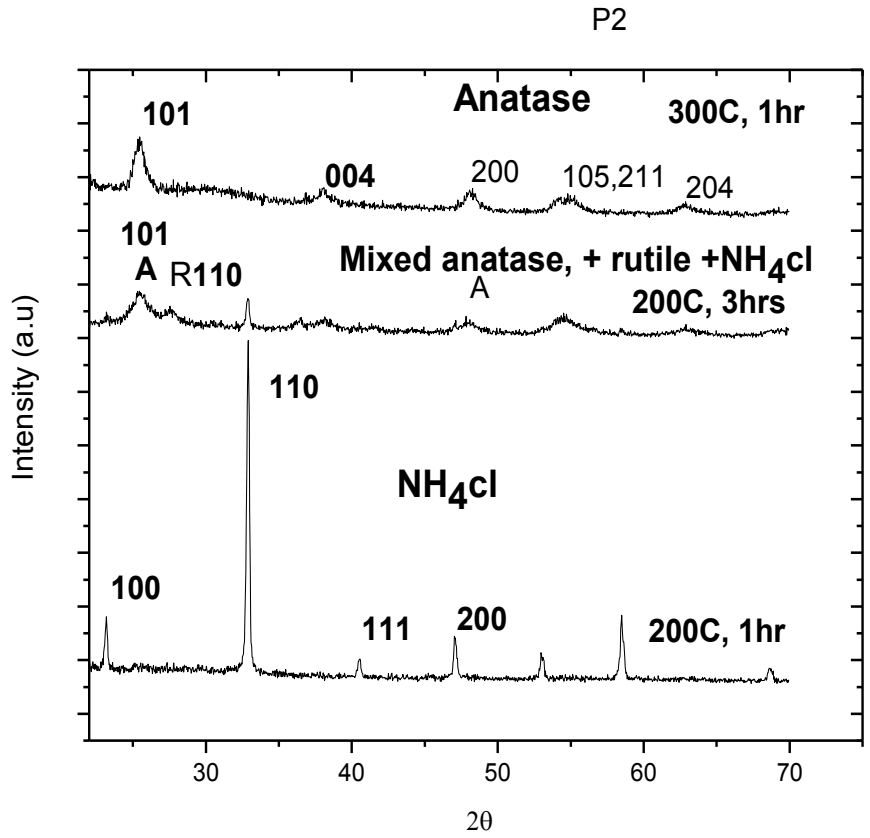

(d)

Figure 48: XRD patterns of P- Chloro samples, alkaline pH: 9, showing nucleation process from decomposition temperature of 200^{0}C to 300^{0}C, at different time duration: (a) Td =200C, 1hour heating time, (b) Td = 200C, 3hours heating time and (c) Td=300, 1 hour

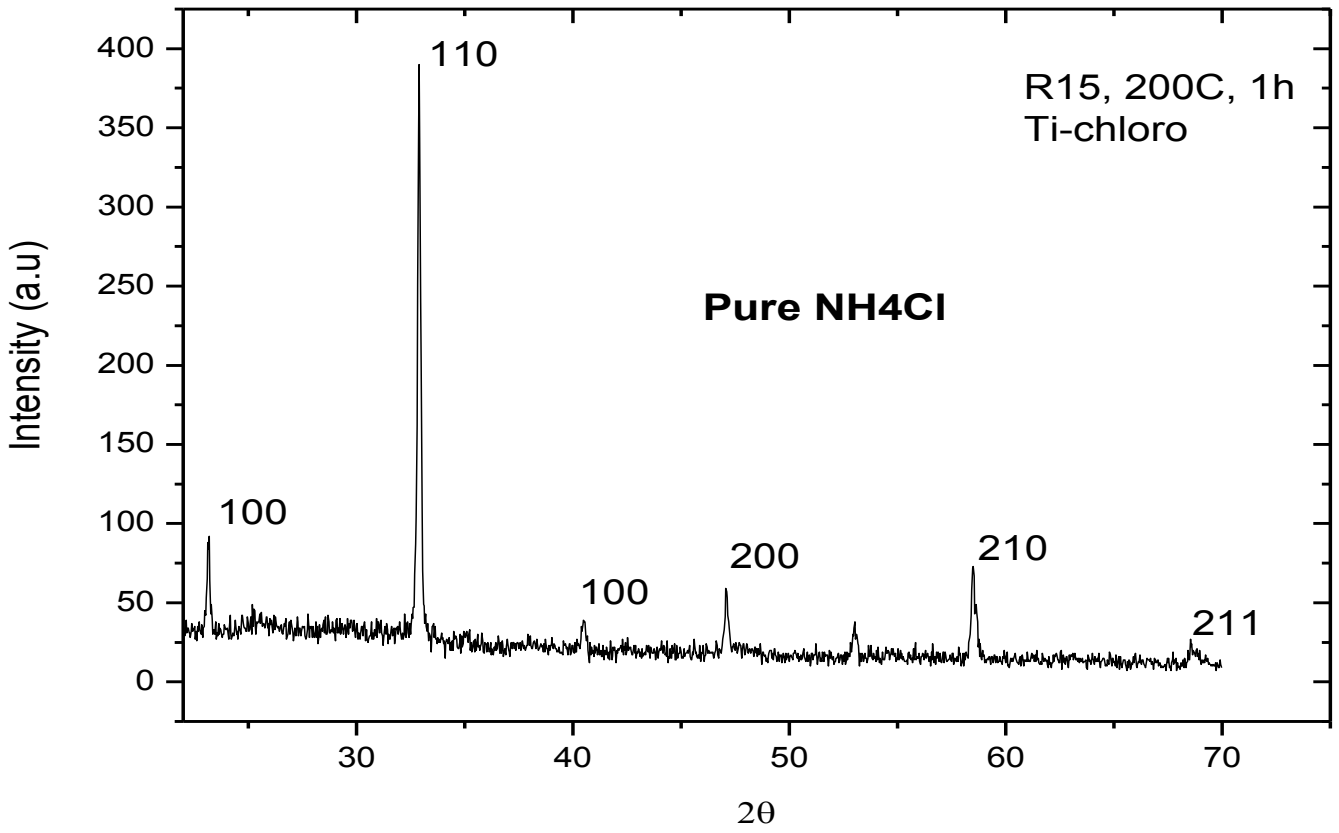
Intensity (a.u)
400
350
300
250
200
150
100
50
0
30
40
50
60
70
2θ
110
100
100
200
210
211
R15, 200C, 1h
Ti-chloro
Pure NH4Cl

(a)

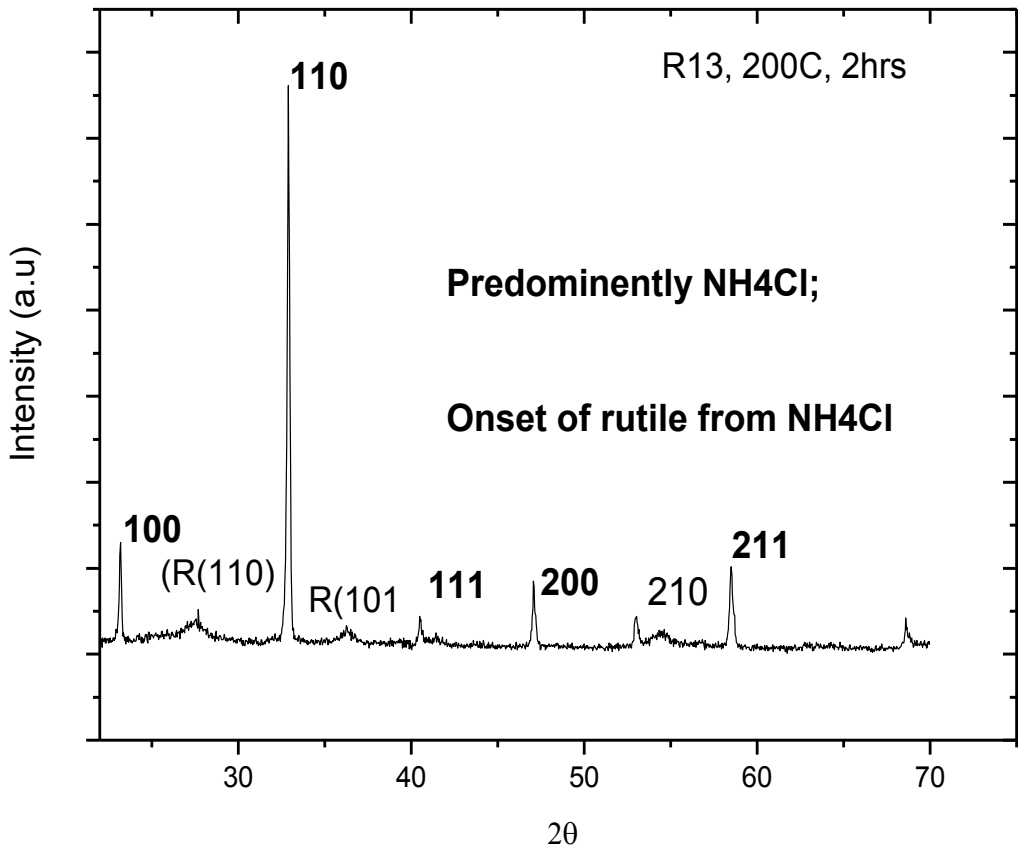
R13, 200C, 2hrs
110
Predominently NH4Cl;
Onset of rutile from NH4Cl
100
(R(110)
R(101
111
200
210
211
Intensity (a.u)
30
40
50
60
70
2θ

(b)

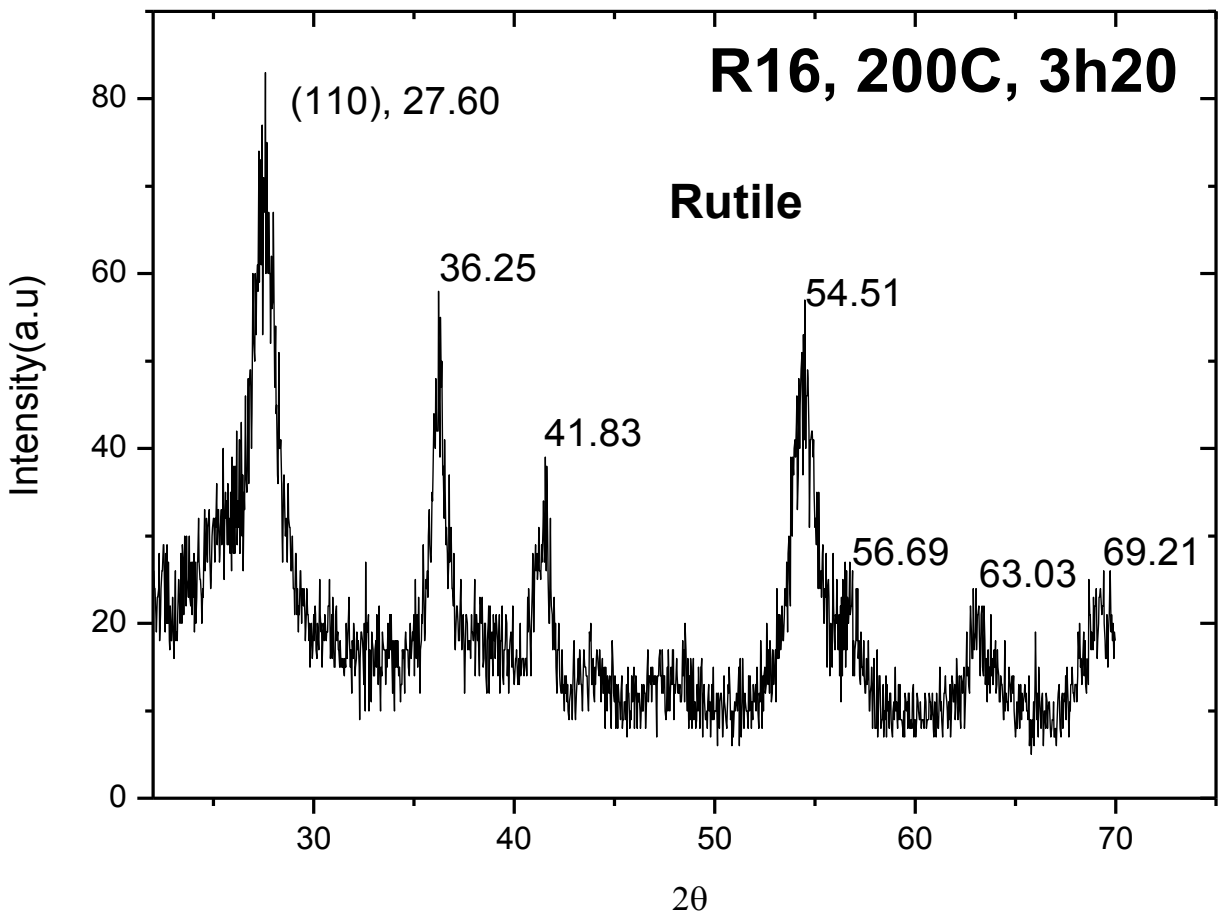
R16, 200C, 3h20
(110), 27.60
Rutile
36.25
54.51
41.83
56.69
63.03
69.21
Intensity(a.u)
2θ
0
20
40
60
80
30
40
50
60
70

(c)

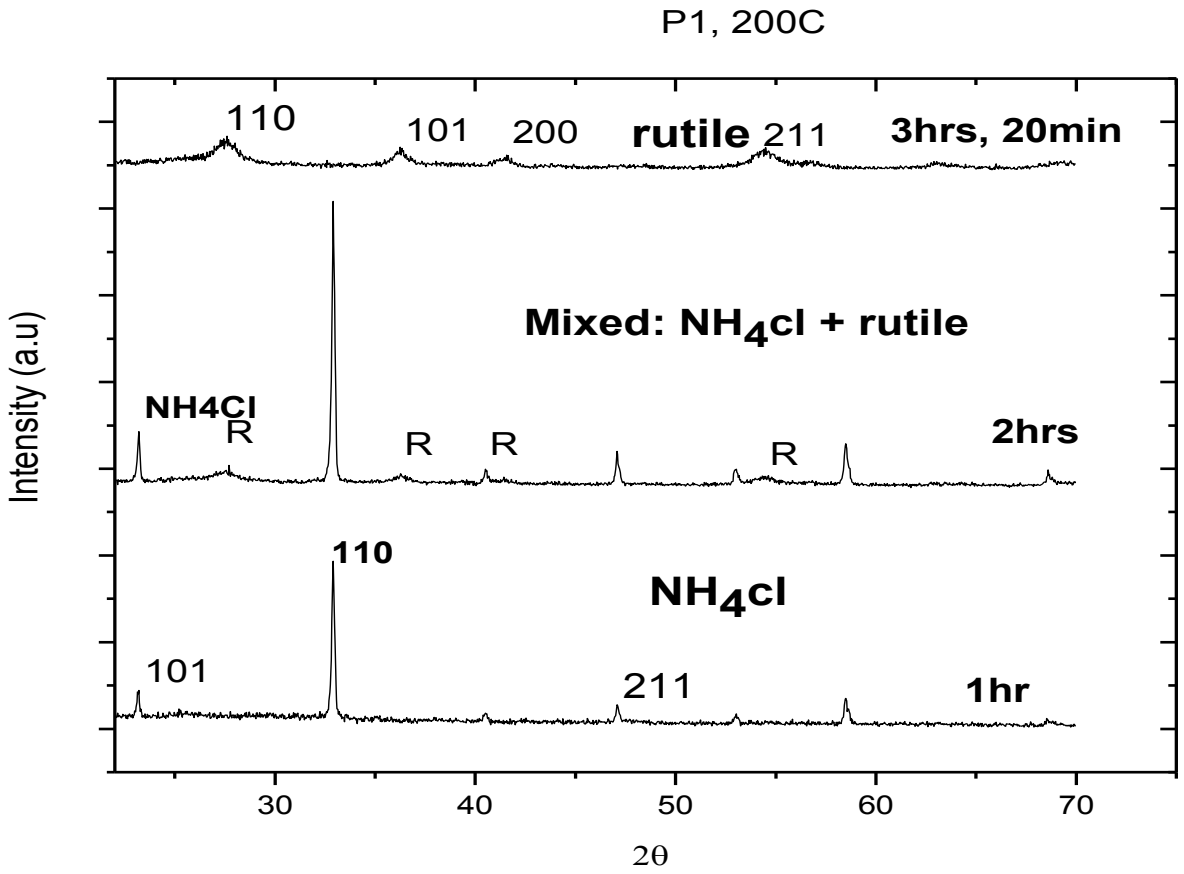

(d)

XRD patterns of P- Chloro samples, acid pH: 2 showing nucleation process, at decomposition temperature Td:

200C, at different annealing times, (a) at 1 hour, (b) at 2hours, (c) at 3hours and 20 minutes, (d) stack graph.

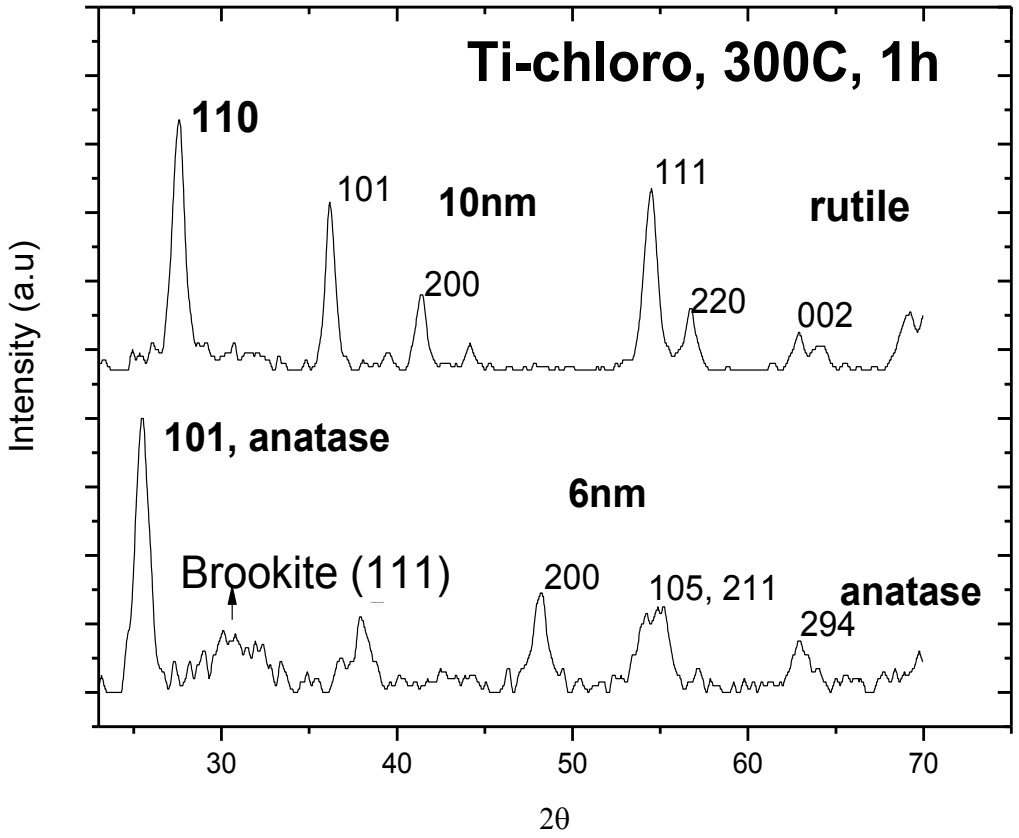

(a)

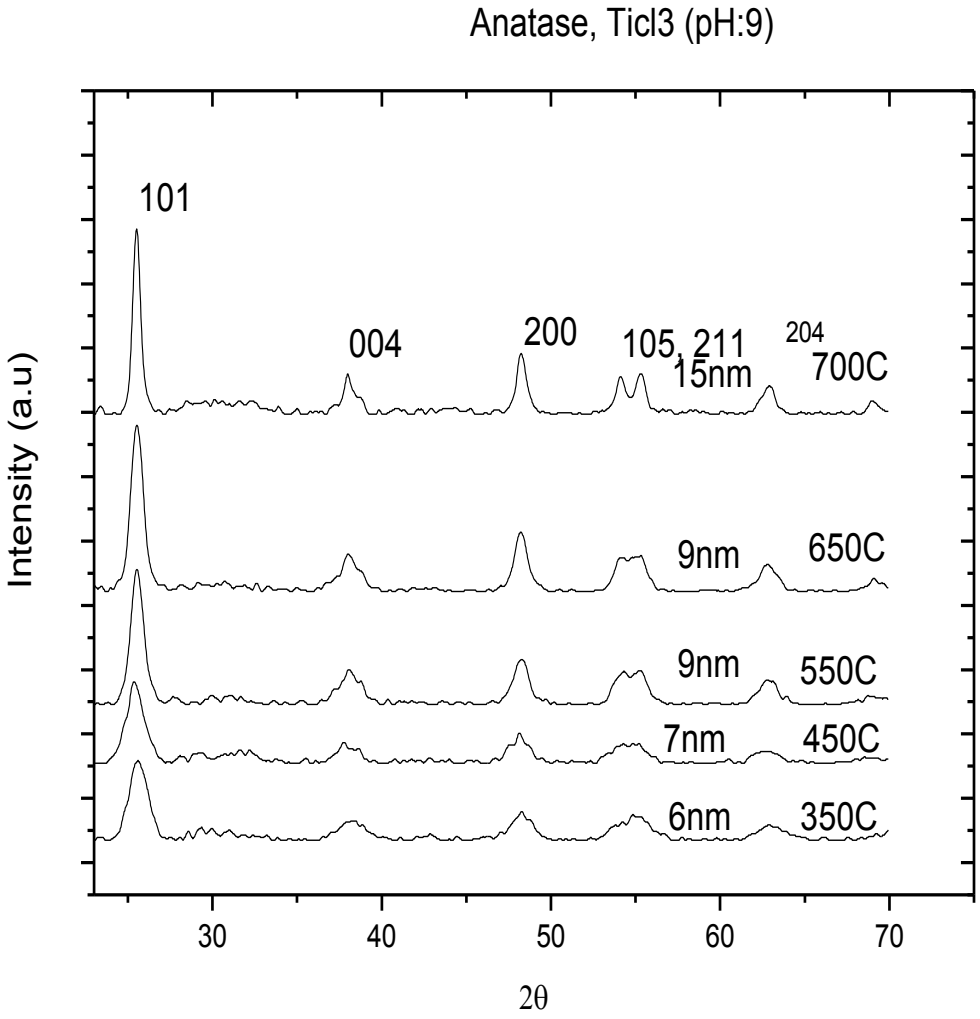
Anatase, Ticl3 (pH:9)
Intensity (a.u)
101
004
200
105, 211
204
15nm
700C
9nm
650C
9nm
550C
7nm
450C
6nm
350C
30
40
50
60
70
2θ

(b)

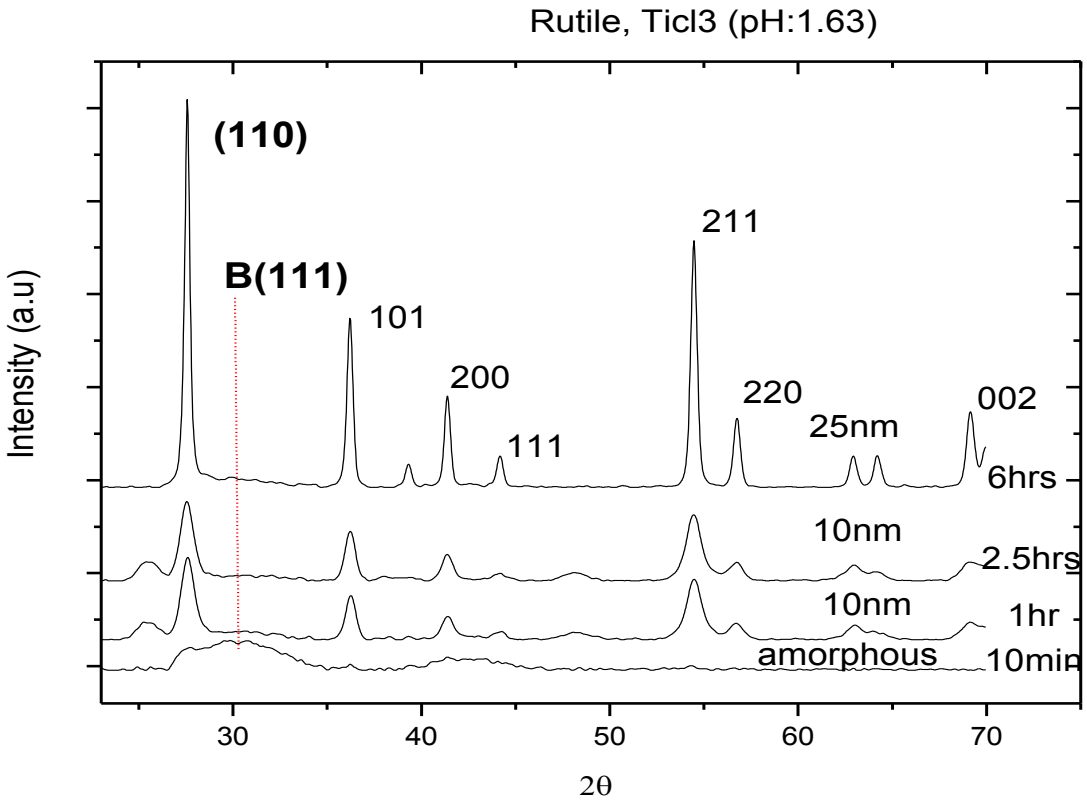

(c)

Figure 49: XRD patterns, (a) comparison between alkaline pH derived-anatase and acidic pH derived rutile phase,

at 300C annealing temperature, (b) shows growth process of anatase grains by annealing at temperatures 350C –

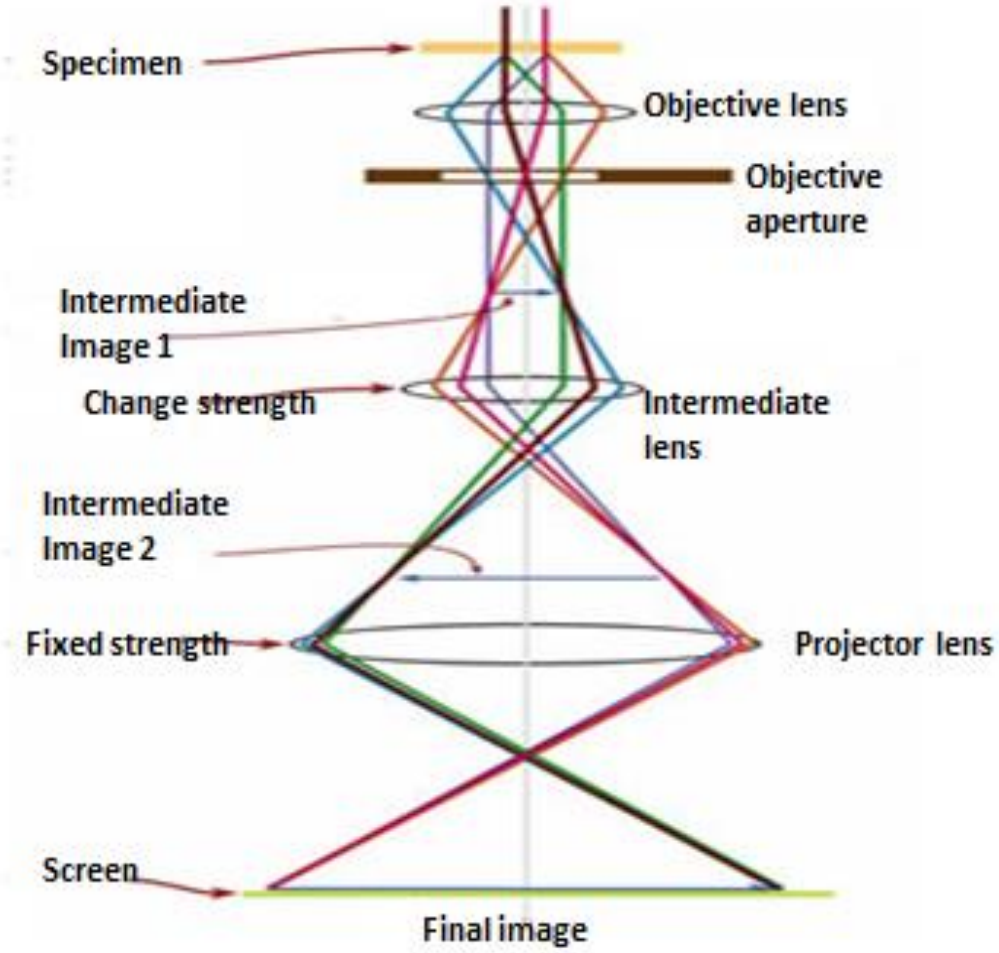

700C, and (c)

Figure 50: Transmission Electron Microscopy (TEM / HR-TEM) Principle I

TEM micrographs: Lyophilised TiO_2 nano-particles

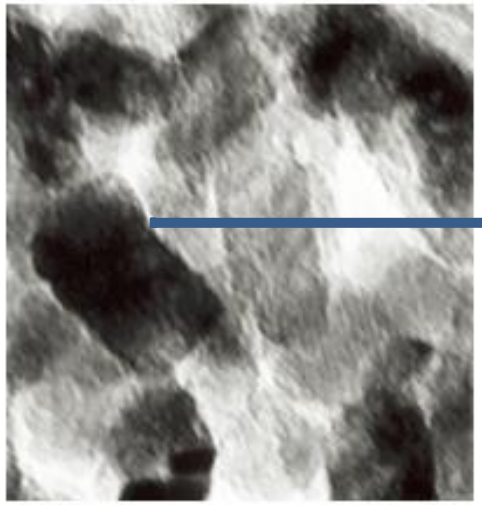

Fig.1 Rutile Nano (elongated)

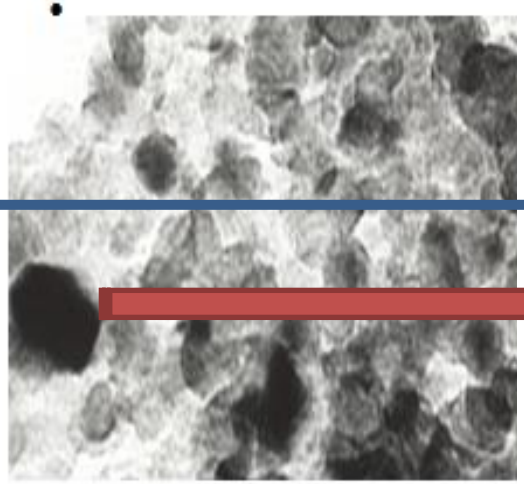

Fig.2 Anatase Nano (rounded & cubic)

Morphology (shape) difference between lyophilized TiO_2, TiCl3-based rutile vs anatase NPS

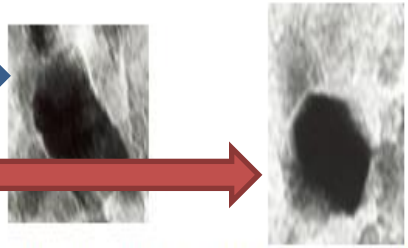

(a) Rutile Nano NPS (b) Anatase nano-NPS

TEM Micrographs

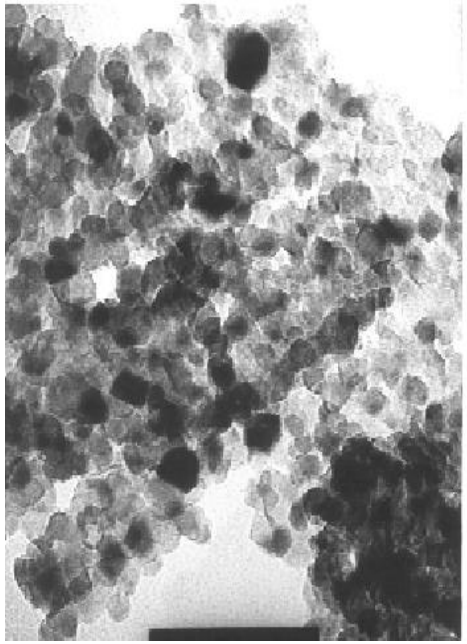

Anatase, Ti - Chloro, 5-10nm

(a)

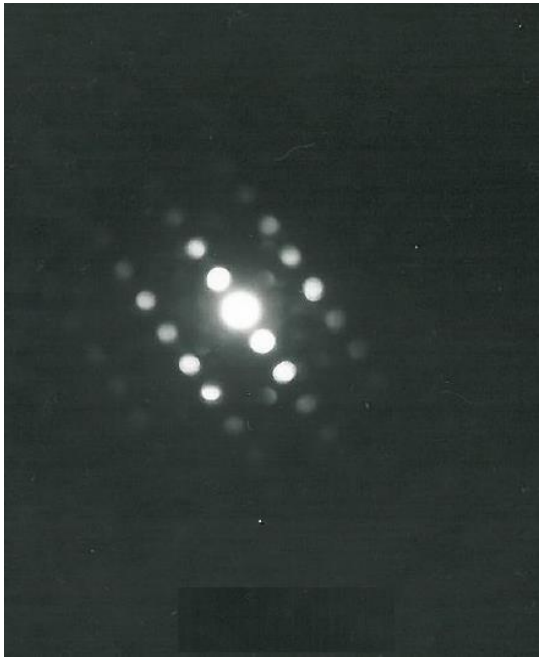

Diffraction pattern, Ti-chloro

Rutile

(c)

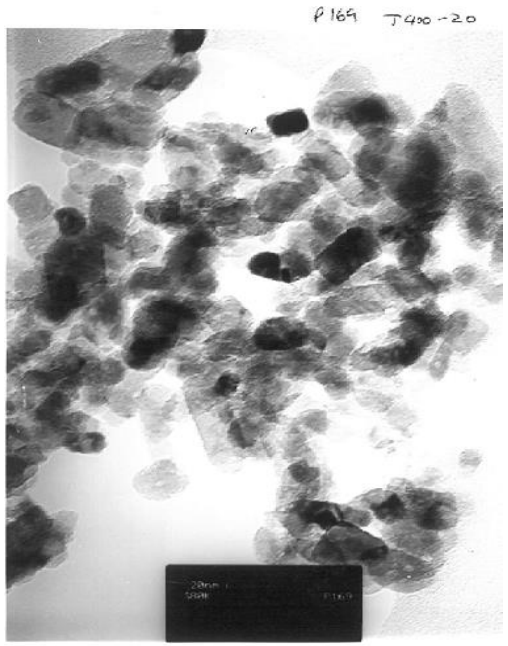

Ti- chloro, rutile, 10-20nm

(b)

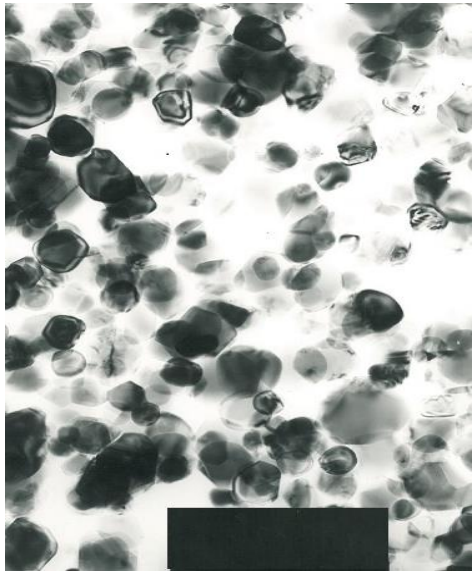

TiO_2 Bulk, 60 -150nm

(d)

(f)

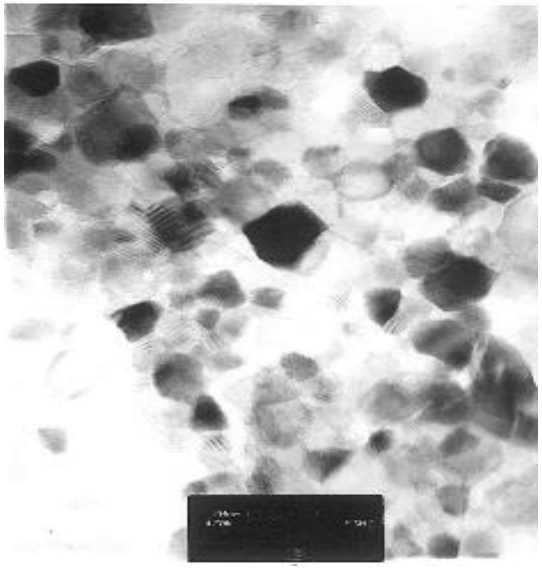

Anatase, Ti-iso-LT-pH11, 5-10nm

(e)

Figure 51: Morphological and size effects studies by TEM

TEM images of the nanoparticles prepared by the lyophilization process are shown in figures 51(a), (b) and, (e) whereas the figure (d) shows the TEM image of the **TiO_2** bulk anatase as purchased. Qualitatively, nanostructures can be observed having a grain size of 5-10nm for the lyophilized samples. The crystallite size as observed from TEM, in this case, is ~ 5 nm. The TEM image of the nanoparticles of the bulk prepared by the hydrothermal method is shown in Figure 51 (d). Grain size, in this case, is ~ 100 nm. Comparing figures 51 (a) and figure (e), the difference in morphology is such that, though Ti-chloro3 and Ti-iso-LT-pH11 samples are of the same anatase phase, the difference is depicted in more or less spherical nanoparticles in the Ti-chloro3, whereas more multi-faceted nanoparticles are observed in the case of Ti-iso-LT-pH11. Figure 51 (b) being micrograph of phase rutile, morphologically, the nanoparticles are more or less elongated compared to either anatase phase Ti-iso-LT-pH11 or Ti-cholro3 samples.

4.3.5.5. RAMAN Spectroscopy

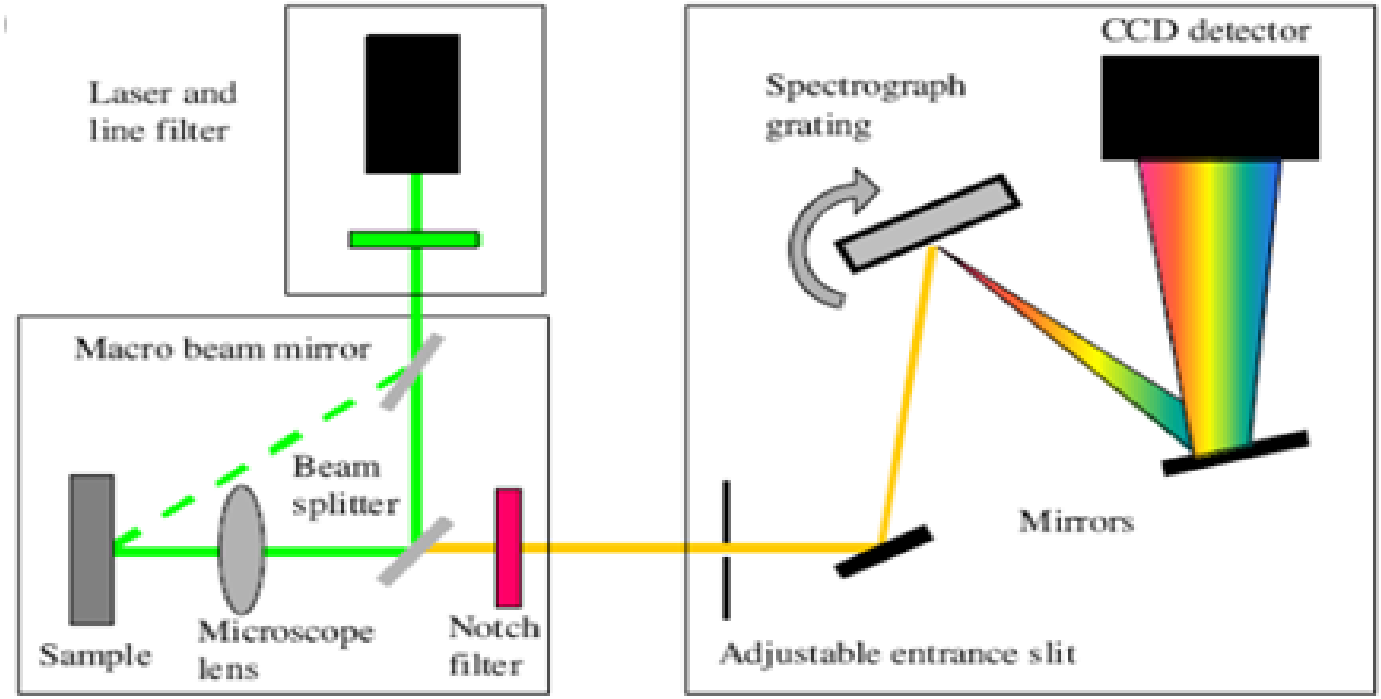

Figure: Schematic setup for the RAMAN SPECTROSCOPY
Ref: https://www.sas.upenn.edu

Figure 52: Illustration of Principle of Raman Spectroscopy

Focusing a monochromatic laser beam on a sample interacts with that sample, it can be reflected, absorbed or, largely scattered elastically (Rayleigh scatter). A little amount of radiation is scattered inelastically, and Raman scattering is said to be composed of stokes and anti-stokes. The importance of the Raman scattered is that it carries information about the molecular structure of the sample. Measuring the spectrum with laser line as a reference serves to determine the shift from it as the measure of the positions of the peaks. The latter is determined by the vibrational energies associated with the bonds in the molecules the samples are made of.

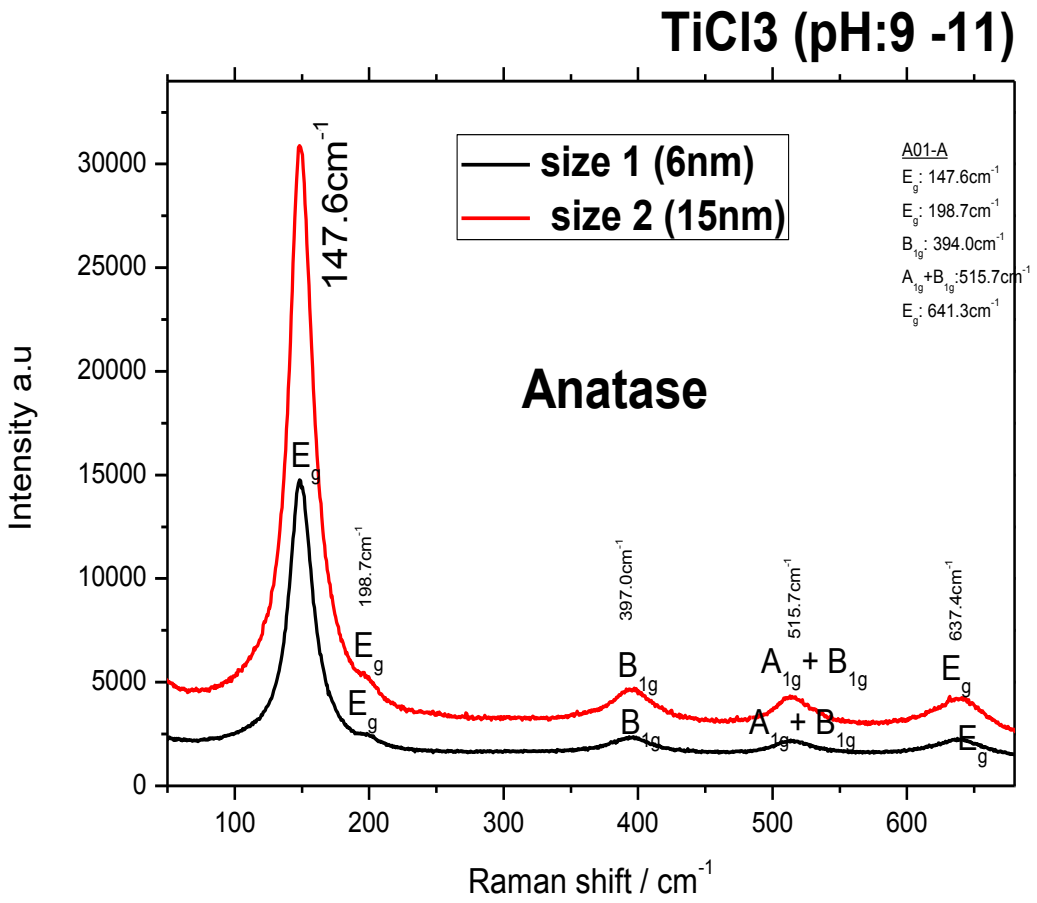

Figure 53: Raman spectroscopy the study of size effect on $TiCl_3$-based anatase sample, pH= 9 - 11

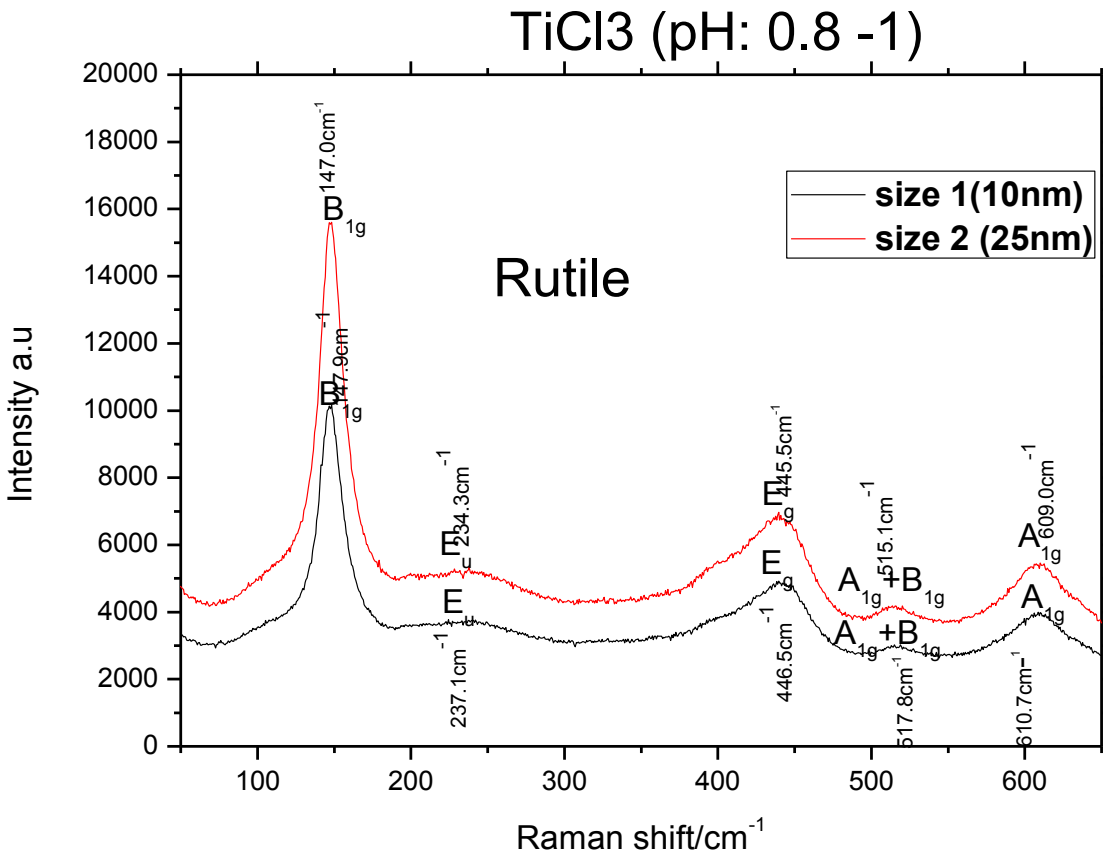

Figure 54: Raman spectra: the study of size effect, rutile pH_ 0.8

Table 10: Raman modes for anatase and rutile

	E_g (cm^{-1})	E_g(cm^{-1})	B_{1g}(cm^{-1})	$A_{1g}+B_{1g}$(cm^{-1})	E_g(cm^{-1})
Ref. **TiO_2** (anatase)	143.0	196	396.0	514.0	637.0
Sample A01	147.6	198.7	394.0	514.7	641.3
Sample A02	147.6	196.7	397.0	515.7	637.4

	B_{1g}(cm^{-1})	Eu(cm^{-1})	E_g(cm^{-1})	$A_{1g}+B_{1g}$(cm^{-1})	A_{1g}(cm^{-1})
Ref. **TiO_2** (rutile)	143.0	-	447.0	-	612.0
Sample R01	147.9	237.1	446.5	517.8	610.7
Sample R02	147.0	234.3	445.5	515.1	609.0

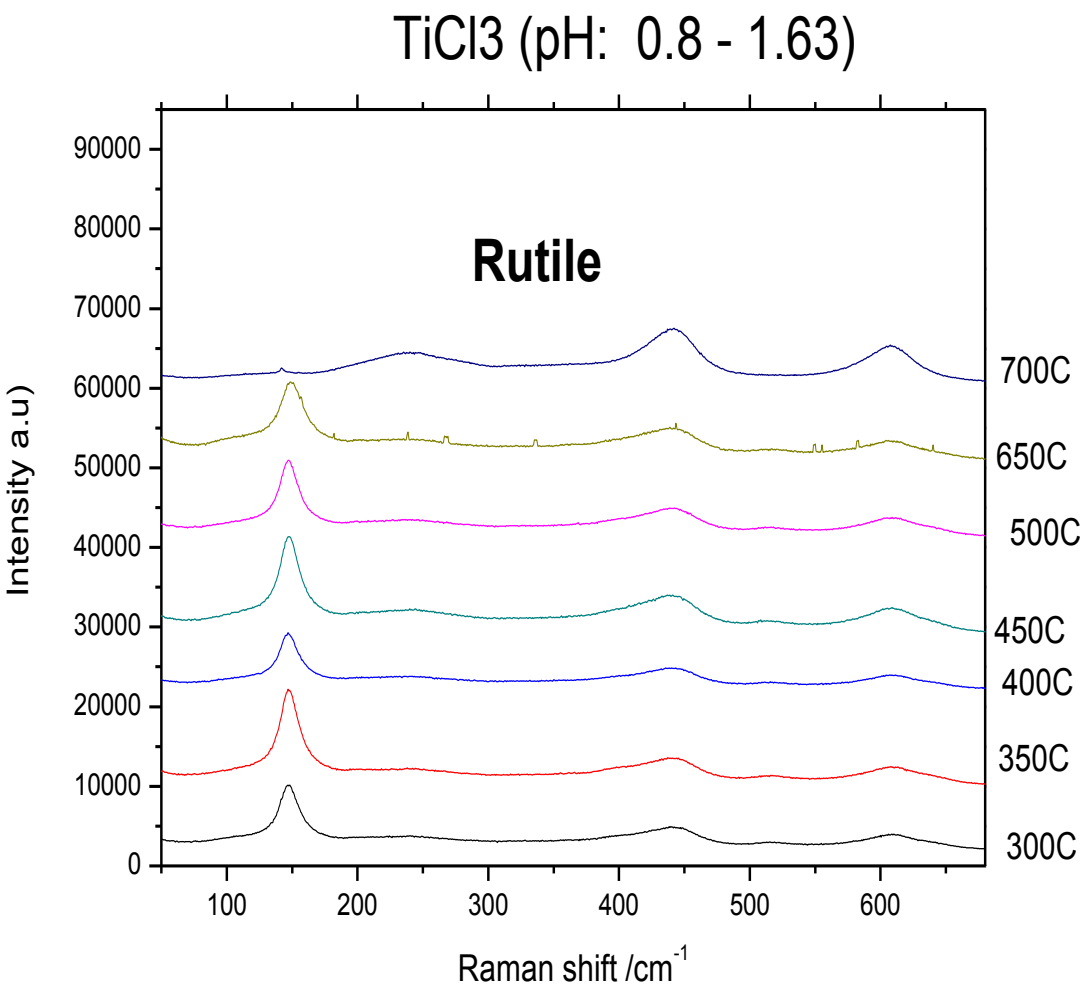

Figure 55: The Raman study of phase and size evolution of the lyophilized rutile TiO2

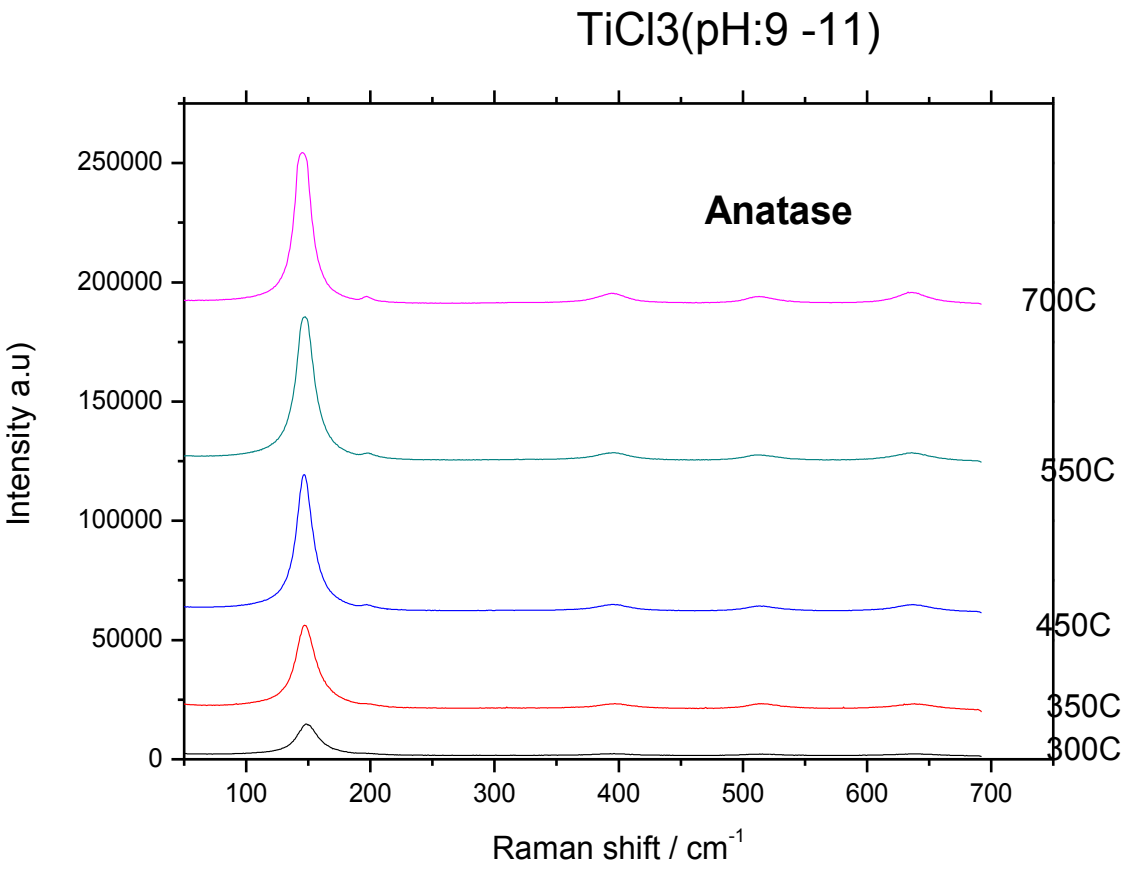

Figure 56: The Raman study of phase and size evolution of the lyophilized anatase TiO2

4.3.5.6. UV-Vis Spectroscopy

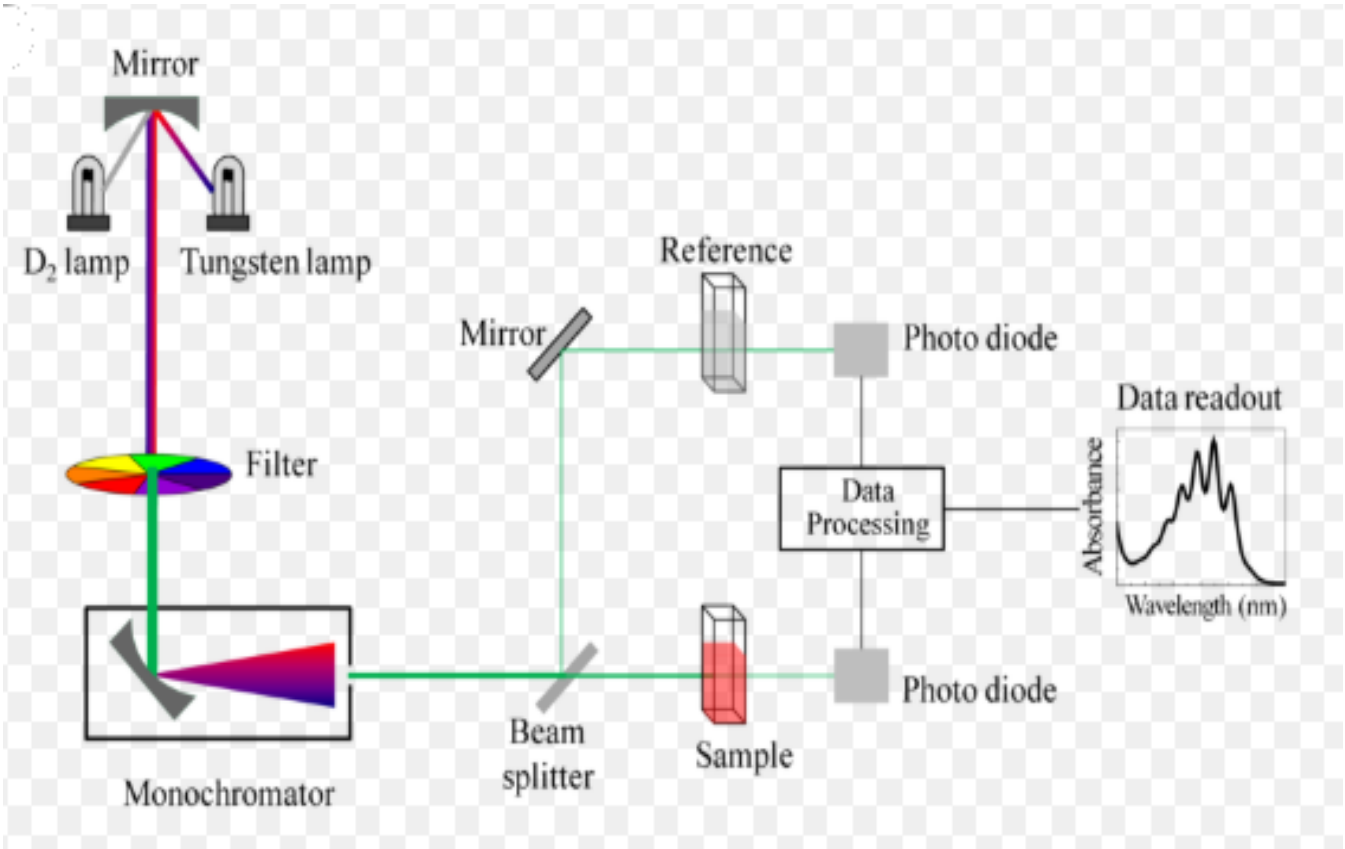

Figure 57: Principle of UV-visible spectrometry

The quasi totality of molecules absorbs light in the 100-400nm region of the spectrum, but also the visible region i.e. from 400-700nm. While the technique is operated mainly with a deuterium lamp as the source of light for the region 170-375nm, the tungsten filament light is used as the source of light covering the much wider region 350-2500nm, including the visible.

By focusing light on a transparent sample, it is transmitted and sensed by the detector. The signal from the latter is recorded on the computer for processing and displaying data of the measurements. Figure (a) below displays the results of the UV-vis spectrum recorded on the experiment on the lyophilized TiO_2 sample ($TiO_2$00pH11). Whereas, Figure (b) is a Tauc plot from the UV-vis spectrum in figure (a) that serves for measuring the bandgap of the TiO_2 NPS under investigation.

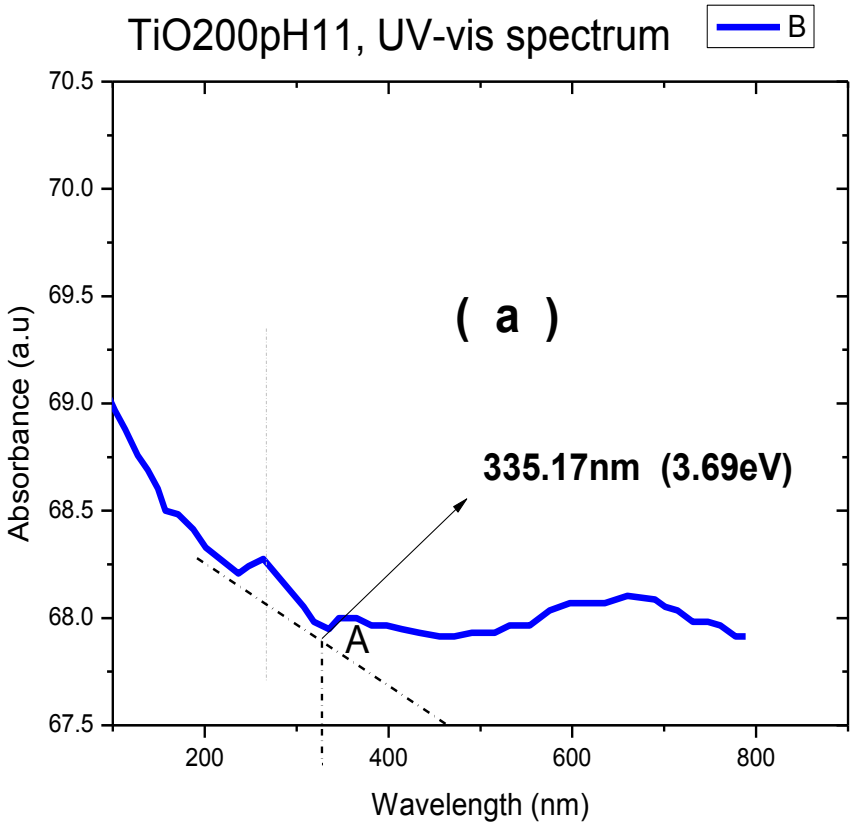

Figure 58: UV- Vis spectrum, the determination of Bandgap Energy (Eg) from the UV-vis spectrum:

The bandgap energy is calculated using the Tauc plot generated from the UV-vis spectrum.

4.3.5.1. Method

Getting the value of the optical band gap energy (E_g) using the absorption coefficient ***α,*** it makes use of the Tauc equation that follows:

$$\alpha h\nu = B\,(h\nu - E_g)^n \qquad (eq.1)$$

Where α= coefficient of absorption, h= Planck constant (6.62620 *10^{-34} J.S), B=constant of proportionality, n= electronic transition type, V=frequency, E_g = optical band gap energy.

It is sufficient to only have the value of the transmission to be able to calculate the absorption coefficient from the relation that follows:

$$\alpha = \frac{1}{t}\ln\left(\frac{1}{T}\right) \qquad (eq.2)$$

Considering: *t* is the sample thickness, *T* is the transmission, and *(hv)* is the photon energy.

Whenever **$(\alpha h\nu)^{1/n}$** is plotted against **(hv)**, it generates a straight line. This line intersects the X-axis at **$(\alpha h\nu)^{1/n} = 0$**, therefore the values of E_g could be estimated from the value of intercept.

Depending on the electronic transition type, **n** could be equated to "**1/2"** for direct allowed transition, **to "2"** for indirect allowed transition, to "**3"** for direct forbidden transition and, "**3/2"** for the indirect forbidden transition. Therefore, the selection of the suitable value of n is paramount for samples and their preparations.

On the other hand, the value of the absorption coefficient could be obtained from the following relationship with the absorbance (Hadi M. et al. (2018)):

$$\alpha = 2.203 * \frac{\mathrm{A}}{\mathrm{t}} \qquad eq.3$$

Considering **α** being absorption coefficient, A is the absorbance and **t** is the thickness of the sample. According to Hadi M.et al. (2018), the coefficient of absorption for Titania, α is approximatively equal to 0.9 * $10^{-2}nm^{-1}$ for TiO_2 sample of thickness t=110nm, exposed to incident light at wavelength λ=335.17nm. Henceforth, we convert the UV-vis spectrum in the figure above to the Tauc plot for our lyophilized sample (TiO_2, pH11) and obtain the value of the optical band gap (E_g) equal to.2.93 ± 0.07eV.

The figure that follows is the Tauc plot generated from the UV-vis spectrum of the lyophilized sample $TiO_2$00pH11. Based on the Tauc plot, and considering only the direct allowed transition, we consider n=1/2, and calculate the value of the optical bandgap energy, as follows:

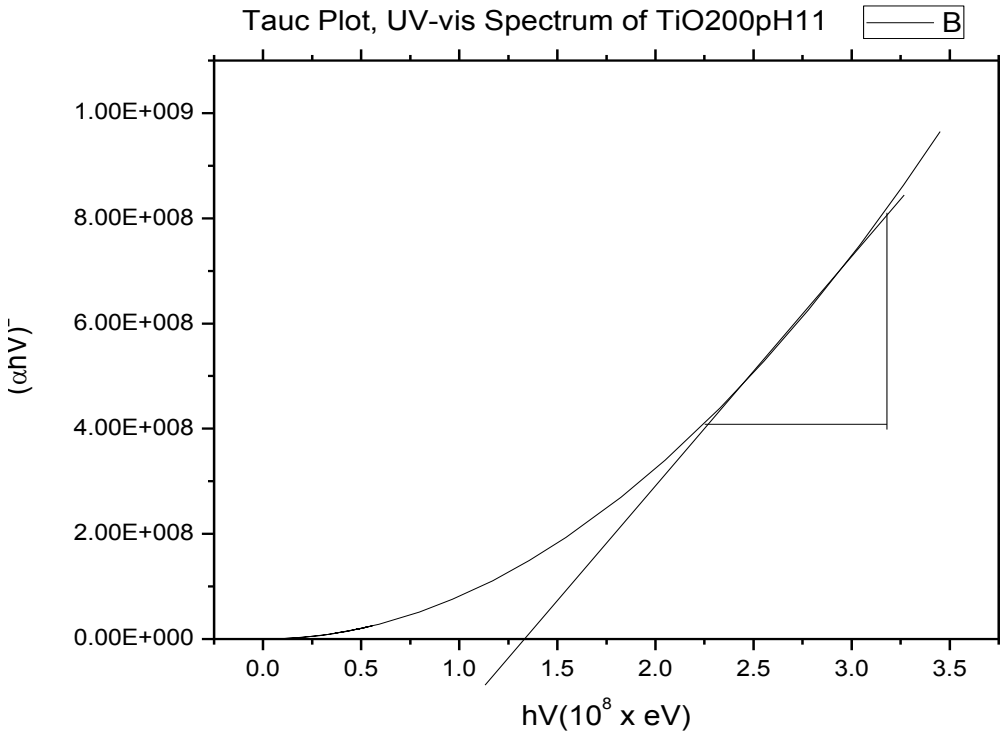

Figure 59: Tauc plot, UV-vis spectrum of TiO2

The slope m and the X-intercept is found from the graph above as follows:

$m = \frac{\Delta(\alpha hV)^2}{\Delta(hV)} = 45364038 = B^2$

and the X-intercept is $C = -B^2 * E_g = 1.36*10^8$

Thus, $\boldsymbol{E_g = \frac{1.36*10^8}{45364038} = 2.93eV}$

4.3.6. Effects of initial concentration of precursor solution

Samples from Titanium (IV) oxide acetylacetonate ($C_{10}H_{14}O_5Ti$)

4.3.6.1. Effect of concentration on the size, size distribution, and structure of the lyophilized TiO_2 NPS

ABSTRACT

The controlled synthesis of TiO_2 nanoparticles (NPs) in the size range of 1 to 10 nm is the focus of this study. The TiO_2 NPs were prepared by the dissolution of 1.0g of Titanium acetylacetonate in volume of deionized water expressed as $V_n(ml)= 50 \times 2^n$ with n=0, 1, 2, 3; and corresponding to four concentrations [$C_n=1.0g/V_n$], namely $C_1(g.ml^{-1})$ = 0.0200; $C_2(g.ml^{-1})$ = 0.0100; $C_3(g.ml^{-1})$=0.0050; $C_4(g.ml^{-1})$ = 0.0025 to control the size of the obtained TiO_2 NPs. The pH of each solution was controlled ~ 7 (neutral solutions)

The solution was sprayed "laminar regime" into liquid nitrogen to generate droplets rich in water (-90%). These droplets were then sublimated in a lyophilizer chamber to yield a very porous precursor. The precursor was then thermally decomposed at 400°C in the air for about 20 minutes. Using XRD and TEM techniques the structure, size and, morphology of obtained TiO_2 NPS were determined. The structure (phase) was found to be anatase, and it was also found that by decreasing concentration from 0.0200 to 0.0025 $g.ml^{-1}$, a decrease in crystallinity and therefore a decrease in size (reduced average particle size from 10nm to ~3.7nm, amorphous) along with a significant increase in their size distribution, broader bell- shape.

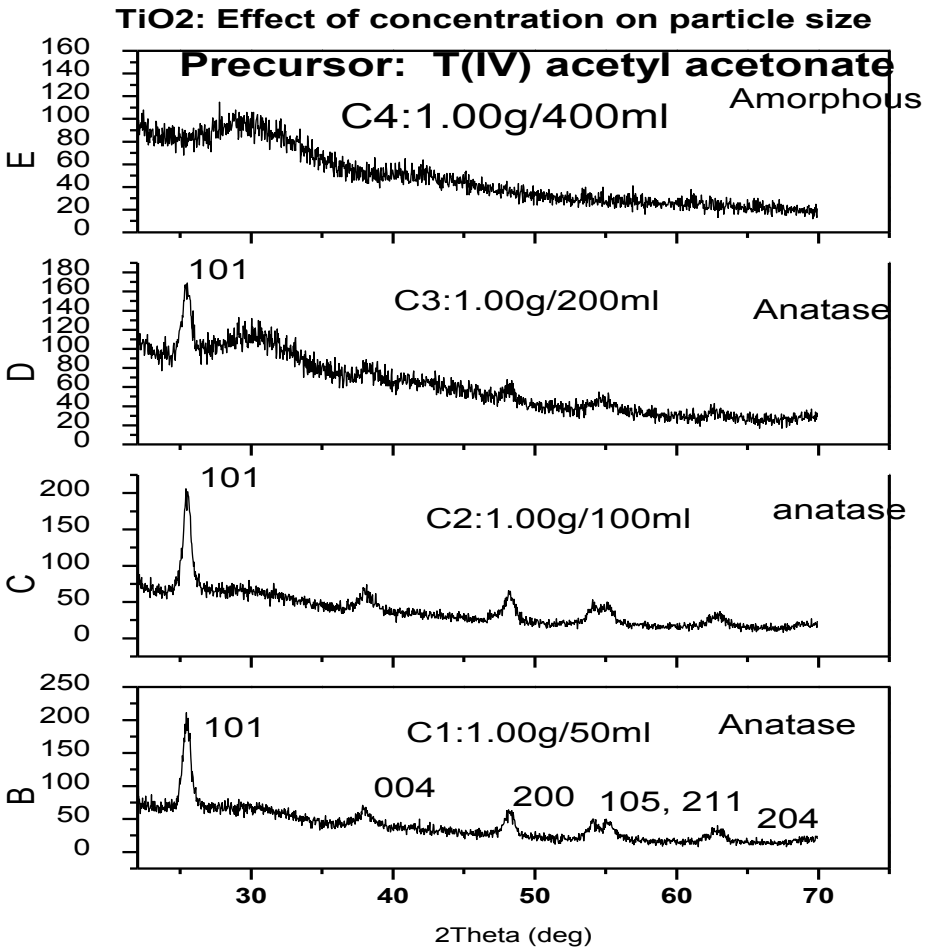

Figure 60: TiO2 NPS anatase form precursor Ti (IV) acetylacetonate (decomposed at 400°C for 1hr)

Decreasing the volume of solvent (distilled water) from 400ml to 200ml, 100ml, and 50ml, the concentration increased from 0,0025M to 0,005M, 0.01M and 0.02M. In the same ratio, the particle size increased exponentially.

The X-ray Diffraction (XRD) patterns of the samples correspond to that of a well-known anatase structure (phase). By the width of the diffraction lines, we obtained the following mean sizes of the crystals: 9.06nm (for the sample C1), 9 nm, (for the sample C3), 5 nm (for sample C3), and amorphous form (for sample C4). Graph 1 shows the variation of the particle as a function of concentration whereas Graph 2 shows the X-ray diffraction for all four samples.

X-ray diffraction (XRD) measurements show a decrease in particle size as the concentration increases. The calculation of C1 indicates the presence of 754 molecules of water per molecule of Titanium (IV) oxide acetylacetonate. The reasons why there is a decrease in the size of the particle can be well explained by considering a further calculation of several molecules per drop based on the following assumptions:

1) The drop of a homogeneous solution of Titanium (IV) oxide acetylacetonate is spherical and of approximately 50nm diameter. The volume of the drop is given by:

$$V_{drop} = \frac{4}{3}\pi \cdot r^3 = \frac{4}{3}\pi \cdot (2.5 \times 10^{-6})^3 = 6.54 \times 10^{-17} cm^3$$

2) The number of molecules of water per molecule of $C_{10}H_{14}O_5Ti$ per drop can be calculated from the following relationship:

$$N_{ac} = \frac{\rho \cdot V_{drop} Na}{M_w \cdot C}$$

For concentration C_1, $N_{ac} = \frac{1.00 \times 6.53 \times 10^{-17} \times 6.02 \times 10^{23}}{18.0148 \times 754} = 28 \cdot 807 \approx 2.9 \times 10^4$

C2, $N_{ac} = \frac{1.00 \times 6.5 \times 10^{-17} \times 6.02 \times 10^{23}}{18.0148 \times 1508} = 14 \cdot 470 \approx 1.5 \times 10^4$

C3, $N_{ac} = \frac{1.00 \times 6.5 \times 10^{-17} \times 6.02 \times 10^{23}}{18.0148 \times 3016} = 7 \cdot 240 \approx 0.72 \times 10^4$

C4, $N_{ac} = \frac{1.00 \times 6.5 \times 10^{-17} \times 6.02 \times 10^{23}}{18.0148 \times 6032} = 3615 \approx 0.36 \times 10^4$

These results can be summarized in the Table given below:

Table 11: Correlation particle size - concentration

Concentration		Nac	Particle size (nm)
C_1	754	2.807 x 10^4	9
C_2	1508	1.4470 x 10^4	9
C_3	3016	0.7240 x 10^4	5
C_4	6032	0.3620 x 10^4	amorphous

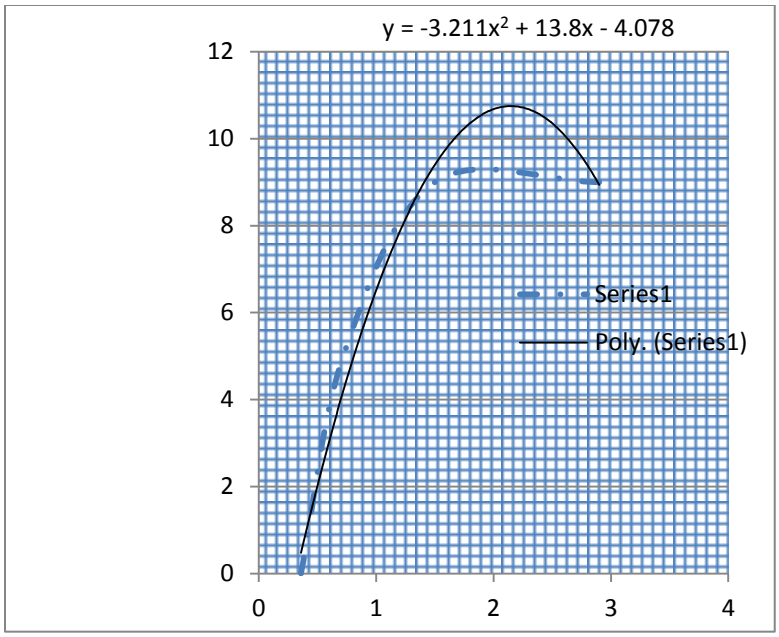

Figure 61: Modelling: Plot of concentration versus particle size

These results demonstrate that: as the concentration (molecules of water per molecule of $C_{10}H_{14}O_5Ti$) increases, the number of molecules of Titanium (IV) oxide acetylacetonate per drop of the solution decreases and the particle size decreases.

Further analysis of these results indicates an anisotropic property of the sample C1, **TiO_2** material such that the crystallization is different in different directions. The crystallization is determined by the first peak position, diffraction angle=25.4947 degrees, and plane 101. The size distribution is different in the different planes 101, 004, 200, 105, 211, and 204 corresponding respectively to peak positions 25.4947^0, 37.9694^0, 48.1759^0, 54.1471^0, 55.1886^0.

The X-ray Diffraction (XRD) patterns of the samples correspond to that of a well-known anatase structure (phase). By the width of the diffraction lines, we obtained the following mean sizes of the crystals: 9.06nm (for the sample C1), 9 nm, (for the sample C3), 5 nm (for sample C3), and amorphous form (for sample C4). The graph shows the variation of the particle as a function of concentration whereas Graph 2 shows the X-ray diffraction for all four samples.

4.3.6.2. Surface properties characterization

The aim here is to evaluate the surface characteristics of as-synthesized nanoparticles. A typical study looks at results by measuring surface area, the roughness of the surface, pore size and, reflectivity of the surface of the Nanoparticles. The importance of characterizing the surface of the nanoparticles is found in the monitoring of the activity, sensitivity, and stability of the photo-catalyst.

Two techniques, one based on Langmuir's model and the other based on B.E.T (after Brunauer, Emmet and, Teller) Equation, was used to measure the surface area, the pore size and, the pore volume of the lyophilized nanoparticles. The measurements were performed on 25/02/2016 at CSIR using TriStar Unit 1, Port1-equipment on lyophilized samples **TiO_2**00-pH11 (precursor Titanium-isopropoxide, decomposed at 200°C and prepared at pH11), TiO300-pH11 (precursor Titanium, decomposed at 300°C and prepared at pH11) and, the commercial sample Degussa P25.

4.3.6.3. Surface chemical properties measurement

Measuring the surface properties is underlined by the following two-fold principle:

First, to calculate the surface area of the adsorbent (m^2/g), using Langmuir's model [ ], $\mathbf{X_m}$ (the maximum quantity of adsorbate adsorbed, expressed in mg per gram, that is required to form a monolayer) is specified. Also, knowing **M** (molecular weight of the adsorbate expressed in mg/molecule), **N** (Avogadro number) and, **S** (approximated contact area of the adsorbent molecule), expressed in m^2/molecule, the surface area of the adsorbent (SA_{ads}) can be computed as per equation (3, 13.3,).

$$SA_{ads}\left(\frac{m^2}{g}\right) = \frac{X_m\left(\frac{mg}{g}\right) * N * S\left(\frac{m^2}{molecule}\right)}{M} \qquad \textit{eq. (3.3.3.1)}$$

Secondly, from adsorption data, the specific surface area is obtainable using the BET equation (3.3.3.2). The volume of gas required to form a monolayer, V_{mono}, on the surface of the sample is also obtainable from surface area by computation.

$$\frac{Z}{(1-Z)} * \frac{1}{V} = \frac{(c-1) * Z}{c * V} + \frac{1}{c * V_{mono}} \qquad eq.(3.3.3.2)$$

With **Z** defined as the ratio of the pressure of the gas (P) and pressure at saturation (P*), the symbols are **V** (volume of gas absorbed at pressure P, and **c** is a constant.

Furthermore, the sensitivity of the measurement depends largely on the amount of surface area such that for high surface area, Nitrogen gas is used and for low surface area, either argon or krypton gas is used instead as their saturation vapor pressures at liquid nitrogen temperature are low.

A note taken from Research gate by Mithil Fal Desai, a researcher at Goa University, Dept. of Chemistry, suggests that B.ET. The surface area could be measured accurately from the N_2 Adsorption isotherm being a straight line below 0.3 (partial pressure). In such a case, the B.E.T surface area is obtainable by measuring 'C' and the slope of the straight line. Otherwise, whenever the partial pressure is beyond 0.3, in the case of the multilayer process, the adsorption isotherm is nonlinear. The adsorption isotherm is important in finding what type of isotherm the material belongs to. It also characterizes the behavior of the gas as it interacts with the surface of the material at a given temperature. In the process, the increase of partial pressure in the sample cell causes the gas to adsorb and condense over the surface.

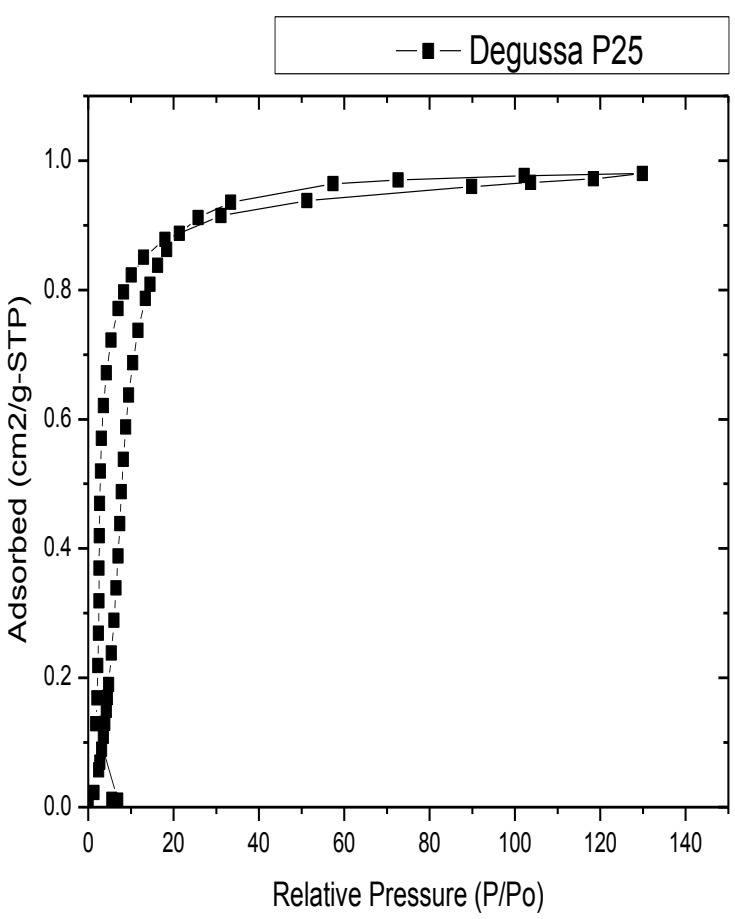
Degussa P25
Adsorbed (cm2/g-STP)
Relative Pressure (P/Po)
0.0
0.2
0.4
0.6
0.8
1.0
0
20
40
60
80
100
120
140

(a)

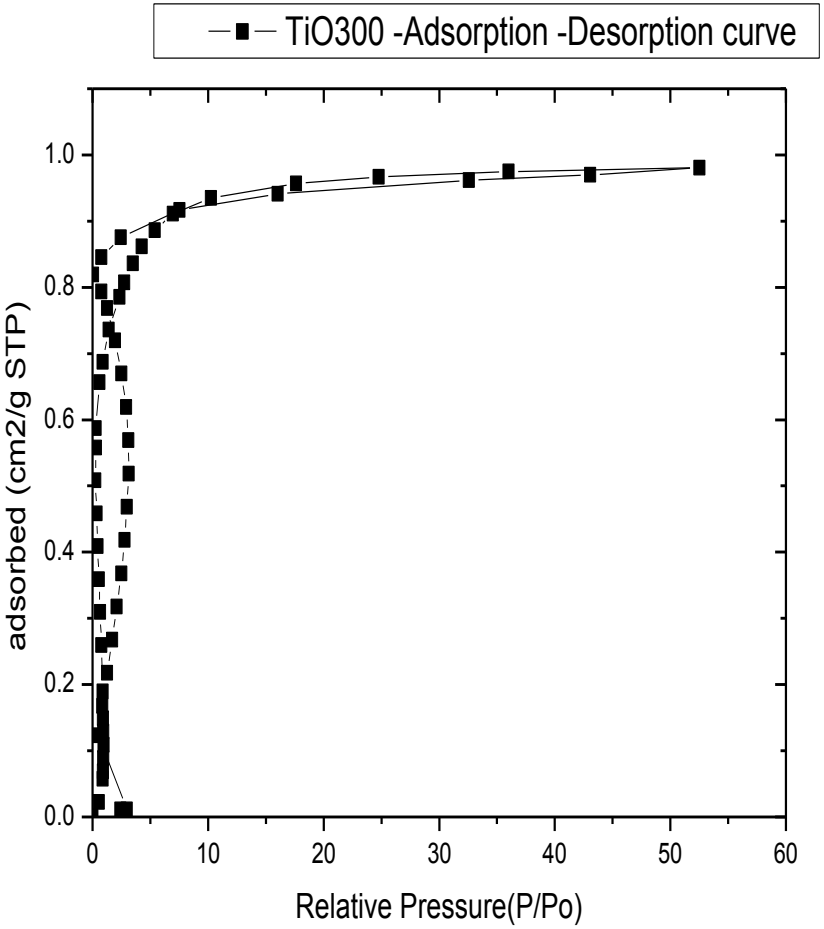
TiO300 -Adsorption -Desorption curve
adsorbed (cm2/g STP)
Relative Pressure(P/Po)
0.0
0.2
0.4
0.6
0.8
1.0
0
10
20
30
40
50
60

(b)

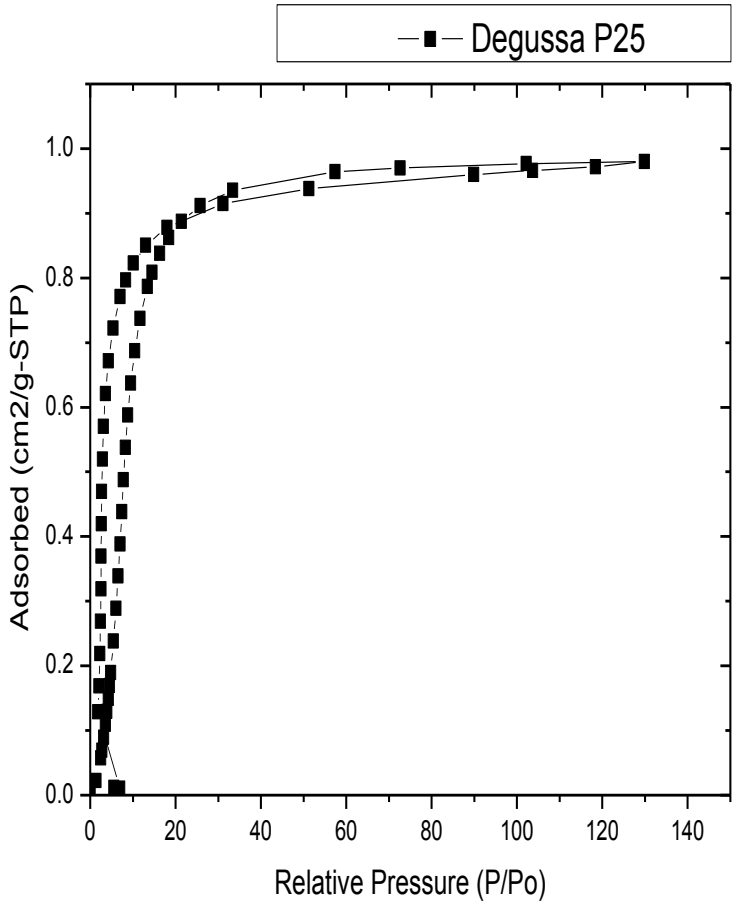

(a)

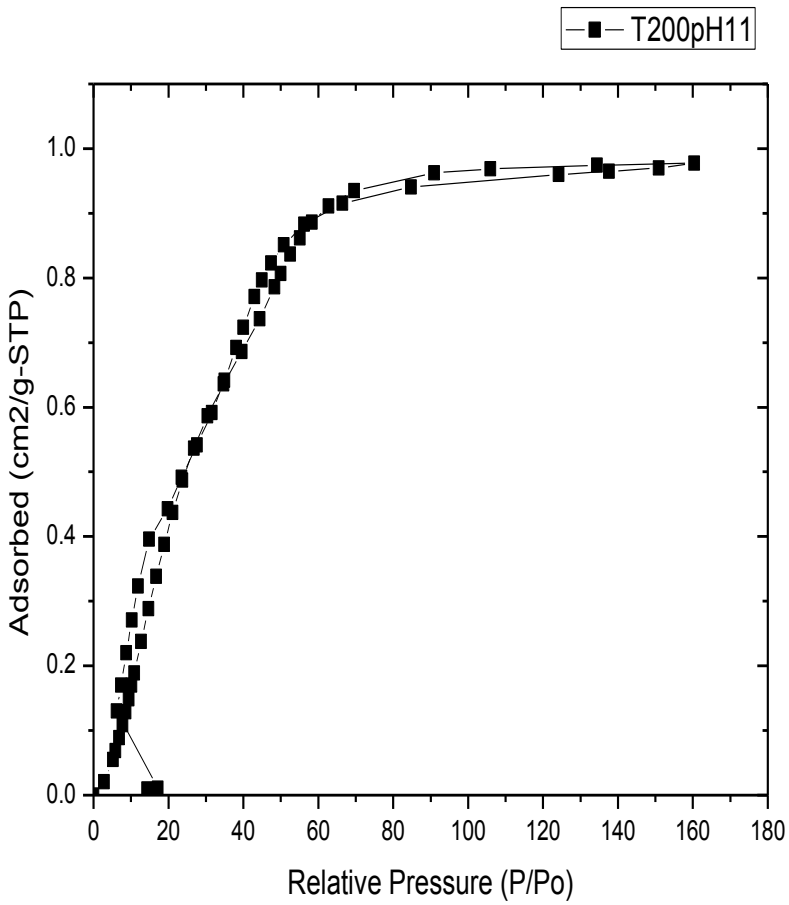

(c)

<u>Figure 62</u>: Isotherm adsorption – Desorption curves: (a) Degussa P25, (b) lyophilized TiO2, decomposed at 300°C (sample TiO300), (C) Lyophilized TiO2, decomposed at 200°C (sample: TiO200pH11)

The results of measurements performed on the lyophilized **TiO_2** nanoparticles are shown in the Table that follows.

Table 12: B.E.T measurements of Lyophilized Nanoparticles and TiO2 Degussa P25

TiO_2 Sample	**Degussa P25**	**T200pH 11**	**TiO300**
Surface Area (m^2/g)			
Single point surface area at P/Po = 0.199761112:	40.9739	97.522	13.4283
BET Surface Area:	42.4333	100.6626	12.8053
BJH Adsorption cumulative surface area of pores			
between 1.7000 nm and 300.0000 nm diameter:	25.557	87.085	7.344
BJH Desorption cumulative surface area of pores			
between 1.7000 nm and 300.0000 nm diameter:	24.5733	87.3637	9.9824
Pore Volume (cm^3/g)			
Single point adsorption total pore volume of pores			
less than 152.4783 nm diameter at P/Po = 0.987593833:	0.16875	0.234422	0.060296
BJH Adsorption cumulative volume of pores			
between 1.7000 nm and 300.0000 nm diameter:	0.208638	0.277608	0.087506
BJH Desorption cumulative volume of pores			
between 1.7000 nm and 300.0000 nm diameter:	0.217723	0.284122	0.093965
Pore Size (nm)			
Adsorption average pore width (4V/A by BET):	15.90729	9.31518	18.83475
BJH Adsorption average pore diameter (4V/A):	32.6541	12.751	47.6592
BJH Desorption average pore diameter (4V/A):	35.4406	13.0087	37.6525

As can be seen in table 3.3.3.1, the surface area of the lyophilized **TiO_2** Nanoparticles, decomposed at 200°C, pH 11 is 2.4 times bigger than that of the commercial Degussa P25, and 8 times bigger than lyophilized TiO300 samples. The difference is also remarkably inverse when we compare the pore sizes in the three samples, the sample **TiO_2**00pH11's pore size is respectively smaller to

commercial Degussa P25 and the other lyophilized sample TiO300, by 37% and 34%. This observation seems to indicate a particular behavior of the lyophilized **TiO_2** nanoparticles that tentatively we can explain by interpreting the hysteresis patterns in isotherm adsorption-desorption curves that are pictured in figure 3.3.2.2 above.

One observes the presence of three hysteresis loops, which are gaps between adsorption and desorption curves. The hysteresis loop is a characteristic of the mesoporous nature of materials such are the depicted of the three **TiO_2** samples in the figure. The mesoporosity suggests the tensile strength effect (TSE) and the capillary condensation being its cause [Ali Qajar, Research Gate). Capillary condensation is a process such that the force exerted on the molecules through the pore walls causes the molecule to adsorb layer by layer. A resulting narrow gap is created by accumulated and collapsed molecules to a lower thermo-dynamical energy state.

Another confirmation of the mesoporous characteristic of the samples is because of the measured pore sizes, all falling within <2 -50 nm) range (Pengfei Zhang, 2016 of Ke Group): the values 15.907nm, 9.31nm, 18,83nm being respectively the diameters of pore for Degussa P25, Ti200pH11, and TiO300.

Further characterization is based on the classification of types of hysteresis (H1, H2, H3, and H4) which provides information on the state of agglomeration, shape of particles present, width of pores, size distribution of the particles. The classification of the adsorption process uses the graph of the amount of adsorbate (Nitrogen gas) adsorbed on the surface of adsorbents, **TiO_2** Degussa P25, lyophilized **TiO_2**00pH11, and TiO300 at STP (standard pressure and temperature). Baboo (2015) suggests that by using the four types of the BET adsorption isotherm, the classification and extent of adsorption on these three adsorbents, depending on either one or many factors including Nature of adsorbate and adsorbent, the surface area of adsorbent, Activation of adsorbent, experimental conditions (temperature, pressure) would be characteristic of the adsorbent particles under study. Therefore, the characterization of the particles of adsorbents based on the hysteresis loop is as follows:

Firstly, the Degussa P25 sample is characterized by the most predominant hysteresis in figure 3.3.2.2 (a) being of type H1 loop, suggesting the presence of agglomerates, spherical particles, and uniformly ordered - connected pores.

Secondly, the Ti200pH11 sample is characterized by a predominantly narrow-Hysteresis loop in figure 3.3.2.2 (c) being a mixture of types H1 and H2, indicating additional information on the presence of pores with narrow mouths (ink-bottle), elongated-shaped and networked pores. Thirdly, the Ti300 sample is characterized predominantly by a double-hysteresis loop of type H4 figure, suggesting the presence of slit-like pores, irregularly shaped-particles presenting voids of large size distribution, hollowed-walled-ordered spherical mesoporous particles

4.4. Discussions

Based on the experimental results obtained from (multi-step) conditioned- preparation and lyophilized **TiO_2** nanostructured material, the analysis demonstrates capabilities to control the key features of nanostructured material, namely: structure, size, size distribution, vibrational modes, surface area, porosity, and shape. The focus has been placed on these characteristic properties as examined by XRD, HRTEM / TEM, RAMAN spectroscopy, and B.E.T measurements. The crystallographic description of **TiO_2** is done according to ASTM-specified angles (°) and peak intensities as per tables 10.1 (a), (b), and (c). The optimization strategies used to control these properties are also discussed. These include the control factors of nanostructured characteristics namely: initial concentration, pH, and nature of precursors.

Table 13: (a): TiO2-anatase characteristic (2θ) angles, Intensities, and (hkl) crystallographic planes

Angle (2θ)	Int-f	h k l
25.322	999	1 0 1
37.863	159	0 0 4
48.064	260	2 0 0
53.975	160	1 0 5
55.094	134	2 1 1
62.756	87	2 0 4
75.141	75	2 1 5

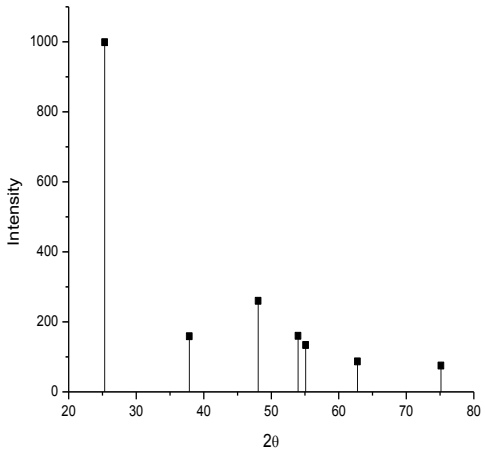

Table 14: TiO2-brookite characteristic (2θ angles), Intensities, and crystallographic planes

Angle (2θ)	Int-f	h k l
25.443	401	1 1 0
31.382	999	1 1 1
42.600	164	1 3 0
53.887	121	1 3 0
55.134	134	2 0 2
55.754	243	2 2 1
66.909	141	1 3 2

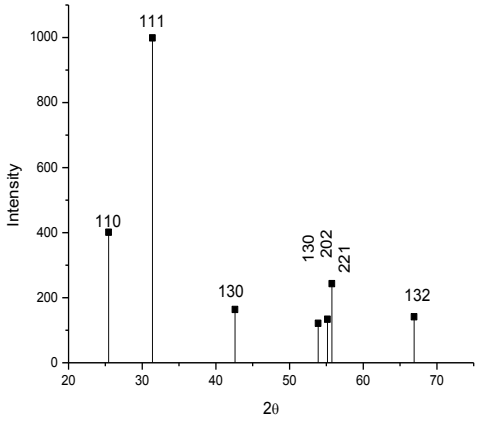

Table 15: TiO2-rutile characteristic (2θ) angles, Intensities, and crystallographic planes.

Angle (2θ)	Int-f	h k l
27.445	999	1 1 0
36.095	431	1 0 1
41.059	172	1 1 1
54.342	479	2 1 1
56.646	138	2 2 0

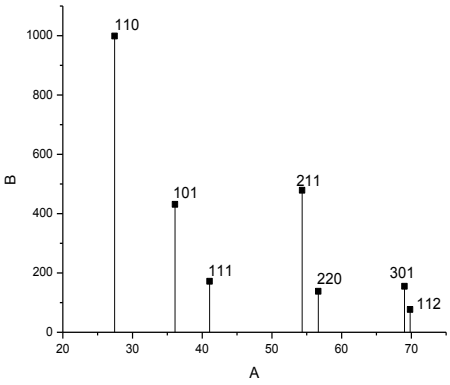

69.032	155	3 0 1
69.835	77	1 1 2

Controlled properties of as-prepared nanostructured TiO_2 material:

Table tabulates different samples prepared from a variety of titanium precursors, pH conditioned aqueous-solutions (acidic and/or alkaline), different degrees of concentration, range of thermal treatment, different characterization techniques used, and the resulting structures obtained.

The following are the phases, phase transformation, and associated phase transition temperatures:

4.4.1. XRD CHARACTERIZATION OF TiO_2 isopropoxide Precursor SAMPLE

(i) The Sample Ti-iso-2, pH: 0.8 ~ 1 (figure 10.1), thermally treated from 300°C - 900°C temperature range; the analyzed Phase transformation suggests there is an evolution from amorphous (300°C) to brookite structure from 450°C, from brookite to anatase up to 650°C, then further phase transformation up to 900°C is described as anatase phase crystallization. Indeed, the two main brookite peaks (31.382°; 999; 111) and (25.443°; 401; 110) described in terms of angle (2θ), Intent-f, and reticular distances have been identified respectively at an angle (2θ): 30.84° and 25.81° (with corresponding intensity levels). This observation is shown in Figures 10.1(a) and (b). Whereas, the onset of anatase crystallization is 700°C and the anatase-to-rutile phase transition occurs at 900°C. Considering the XRD pattern (700C) in figure 10.1, corresponding to the pure anatase phase, the six peaks appearing are typical to anatase crystallographic (angle 2θ; Intent-f; and reticular planes pattern given in table 10. (a).

The significance of this result is wide thermal phase stability (without changing to rutile) of anatase; the rutile structure is inhibited or delayed to very higher temperatures exceeding 1000°C

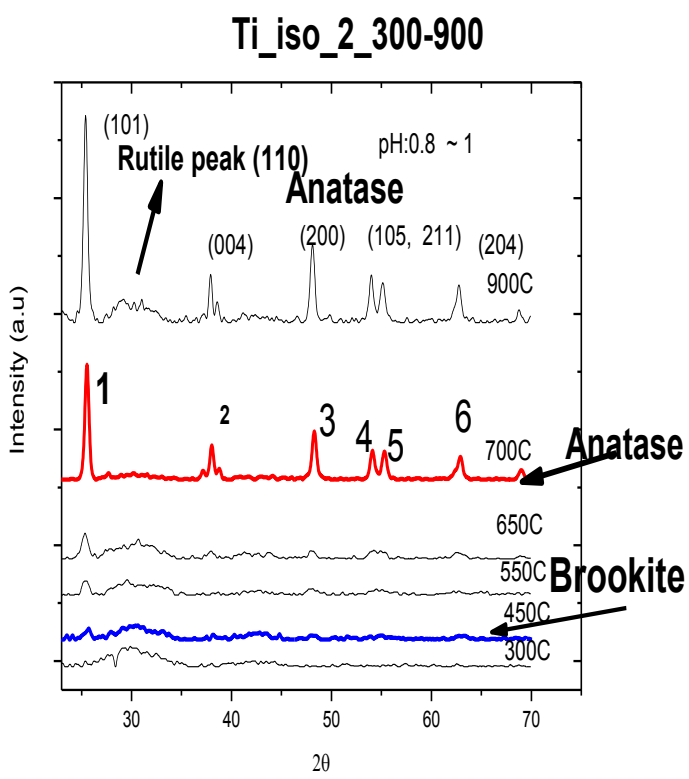

Figure 63: (a) XRD patterns of TiO2 isopropxide Precursor SAMPLE Ti-iso-2, annealed at 300 - 900°

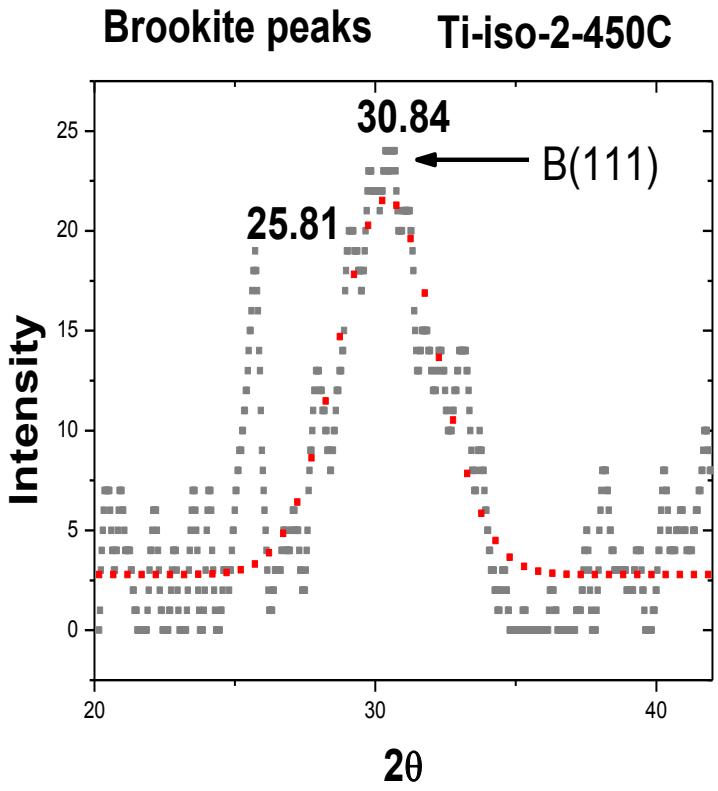

(b) XRD pattern of Ti-iso-2, annealed at 450°C

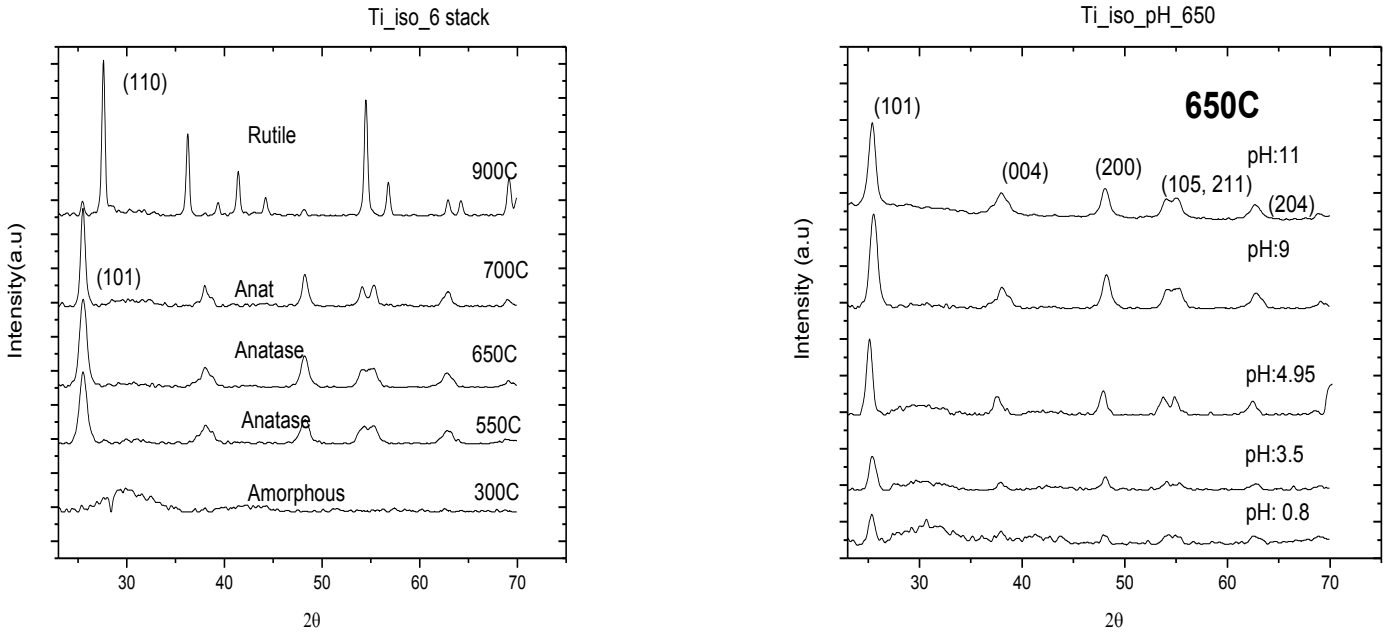

Figure 64: (a): XRD patterns of Ti-iso-pH: 9 – 11, annealed in the range of 300 – 900°C

Sample Ti-iso-6: pH: 9 – 11, heat-treated in the range: 300°C -900°C

The occurrence of the rutile structure is a result of phase evolution from amorphous-to-anatase-to-rutile, and phase transition occurs exactly 900°C.

Major Finding # 1, the effect of alkalinity over-acidity of titanium isopropoxide - prepared precursor-solution lowers of a couple hundred degrees the anatase-to-rutile phase transition. The energetic (thermodynamic) significance of this, is an important energy-saving factor. Also, the brookite polymorph is inhibited in the phase transformation process. Therefore, alkalinity is an inhibiting factor.

Major Finding # 2, the advantage of acidity over alkalinity of titanium - isopropoxide - prepared precursor-solution is an exhibition of the brookite phase in the phase diagram. The phase transformation evolves from amorphous to brookite (450°C-550°C)-to-anatase.

4.4.2. TiO_2 $TiCl_3$ Precursor-based NPS

(i) The sample $TiCl_3$, pH: 9 ~11, was thermally heated within 450°C - 700°C temperature range; the phase change evolves from amorphous to anatase- eventually at higher temperatures above 700°C, to rutile phase.

The growth of particles was noticed to take place concurrently as the phase transformation. In the temperature of interest, the deviation in the main crystallographic peak of the anatase structure (101) was calculated and found to be $\Delta\theta=0.27°$.

(ii) **The sample $TiCl_3$, pH: 0.8 ~ 1.63**, was thermally treated at 400°C for time durations ranging from 10 min, 60min, 120min, and 360min. The phase transformation is such that the rutile phase is the main phase that evolved directly from the amorphous phase. Phase stability is also observed,

, unchanged rutile phase for the duration of 6hrs, and an increase in particle size from 0nm to 25nm, grown at a rate of 0.06nm/min:

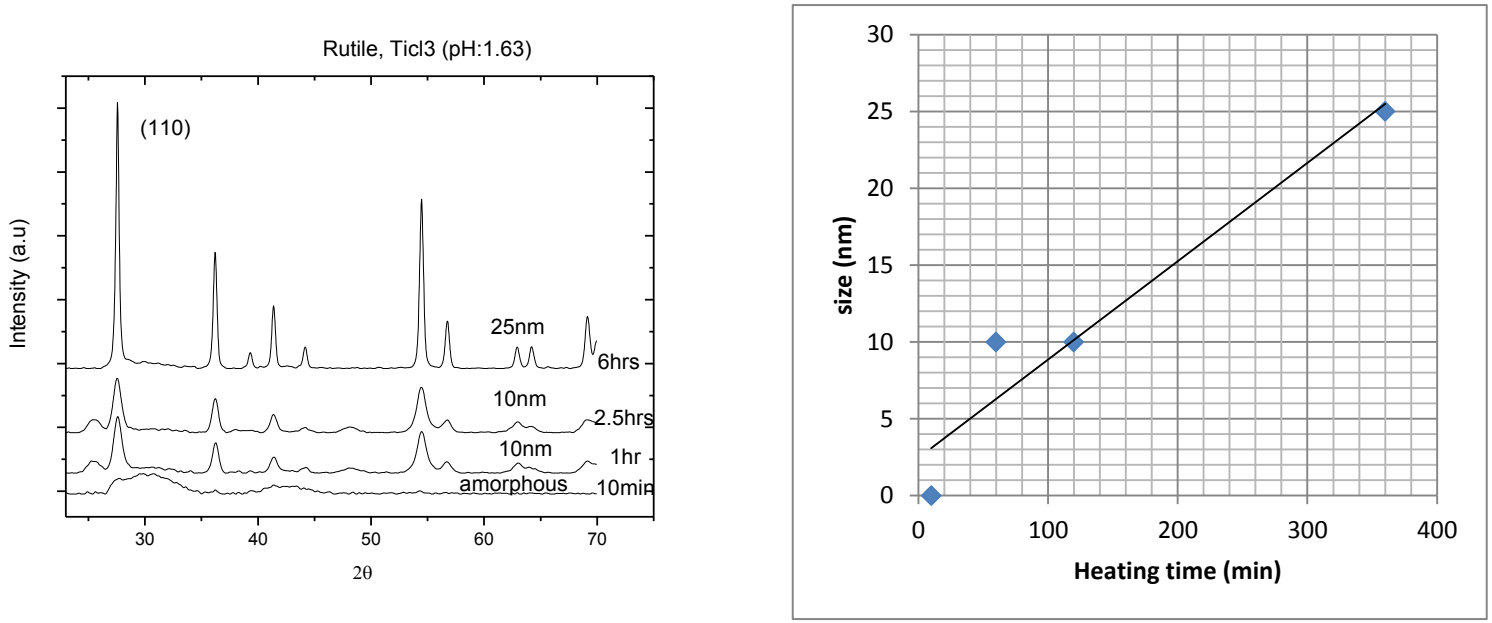

Figure 65: XRD patterns of TiCl3, pH:0.8 -1.63 annealed at 350°C for 10min, 1hr, 2.5hrs, and 6hrs

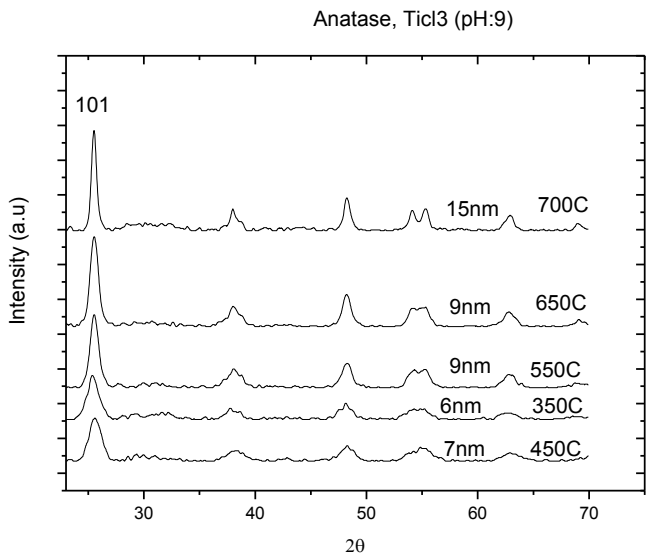

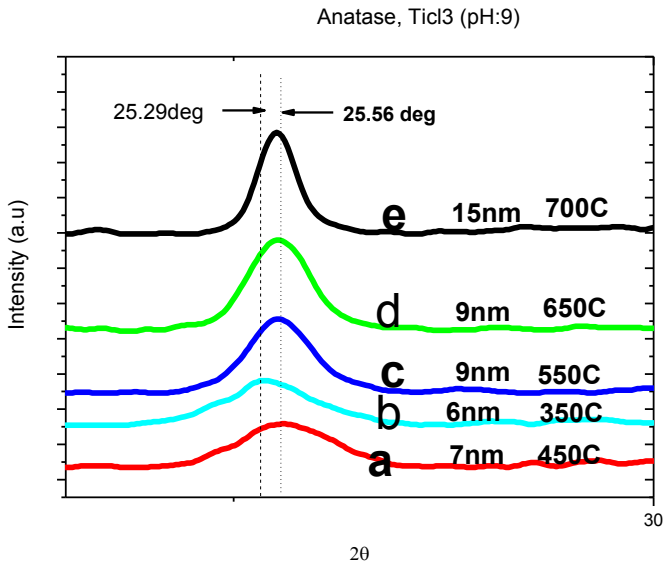

Growth Rate ($\frac{\Delta S}{\Delta T} = 0.02 nm/°C$)

- Change in crystal orientation in **TiO_2** anatase main plane (101), Δθ=0.27°
- The phase transformation from mixed phases(brookite and anatase) at 350°C to pure anatase

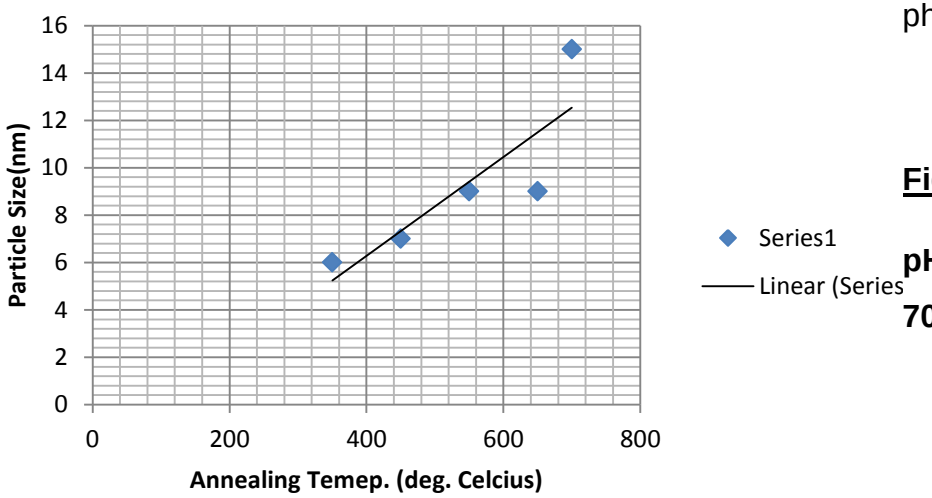

phase from 550°C – 700°C

<u>Figure 66</u>: Heat treatment of sample TiCl3, pH=9 ~11, from 350°C, 450°C, 550°C, 650°C, and 700°C.

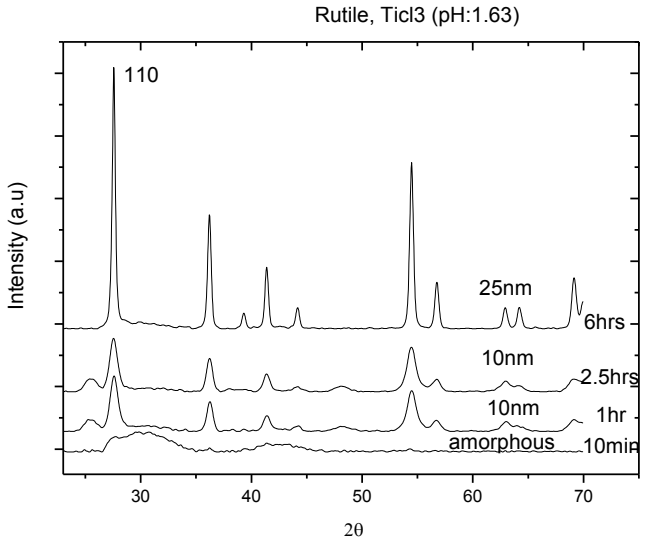

Figure 67: XRD patterns of TiCl3, pH:0.8 -1.63 annealed at 350°C for 10min, 1hr, 2.5hrs, and 6hrs

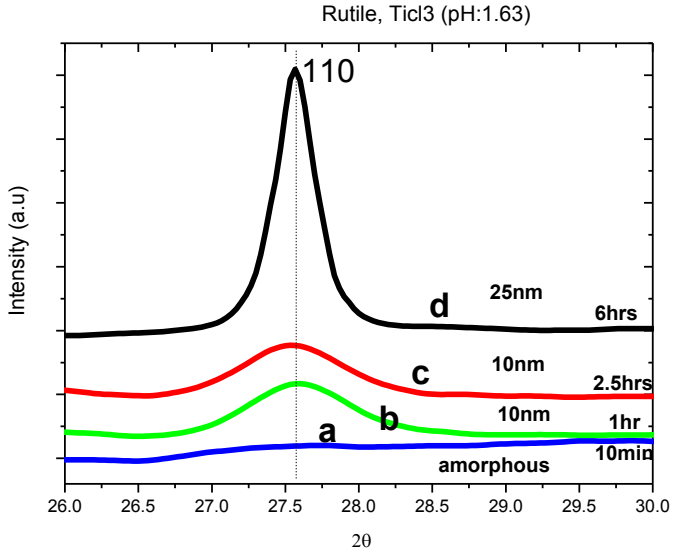

Peak Broadening spectra (a, b, c, and d), TiCl3, 0.8

4.4.3. RAMAN spectroscopy characterization of $TiCl_3$ precursor samples

The underlying theory behind the characterization of a sample by Raman scattering is based on assumptions such that upon laser light is incident on a molecule on the surface of the material under experiment, the molecular vibration that is generated, scatters light of certain energy (enhanced or diminished). The energy of elementary excitation determines the energy difference between incident and scattered light. According to Yang X.X (2012), there exists a relationship between the coupling strength ($\sqrt{W}$), the length of bonding (d), the effective mass ($\sqrt{m}$) of the interacting atoms and the energy change such that:

$$\Delta E \sim \frac{1}{d}\sqrt{\frac{W}{m}}. \qquad \text{eq. 10.1}$$

Molecules and chemical bonds are described in terms of translational, rotational, and vibrational motions. An amorphous material, for example, is described by inhomogeneous and broadened Raman lines created at different positions, because of chemical compositions and molecular chain length. These changes affect different Raman line energies, therefore the integrated spectrum over the entire area, made of molecular variations results in a significant broadening. Raman line's width describing local changes in molecular vibrations henceforth is a key element in the identification of chemical and mechanical property changes of the surface of a material. The purpose of mostly examining Raman spectra remains the identification of Raman signatures of anatase, rutile, and brookite. According to most Research, the peak position (PP) shift in the $144E_g$, of anatase and its FWHM's broadening explains the phenomenal phonon confinement and quantum size effect occurring at the nanoscale.

Table 10.2 gives the frequencies of vibrations for anatase (space group:D_{4h}^{19}, **I4l /amd**) and rutile (space group $D_{4h}^{14}\,P42\,/mnm$) of Titania of which symbols (w: weak), (m: medium), (s: string), and (vs very strong).

Table 16: Vibration frequencies (active modes) of anatase and rutile of Titania

Anatase		Rutile	
E_g	144cm^{-1} (VS)	E_{g1}	143cm^{-1} (w)
E_g	197cm^{-1} (w)	Eg	447cm^{-1} (S)
B_{1g}	399cm^{-1} (m)	A_{1g}	612cm^{-1} (S)
A_{1g}	515cm^{-1} (m)	B_{2g}	826cm^{-1} (S)
B_{1g}	519cm^{-1} (m)	-	-
Eg	639cm^{-1}(m)	-	-

Figures 10.5 (a) and (b) contain respectively Raman spectra of samples TiCl3 (pH: 9 ~ 11) and TiCl3 (pH: 0.8 ~ 1.63), both thermally treated at 350°C, 450°C, 550°C and 700°C. These serve for the identification of the phase of titania-based on the frequencies as per table 10.2, and also for investigating amorphous to crystalline phase transition in **TiO_2**. While figures 10.5 (c) and (d) are Raman spectra for peak position shift to higher energy side and broadening in full width at half maximum (FWHM), a study of quantum size effect using two samples of two different nanosized.

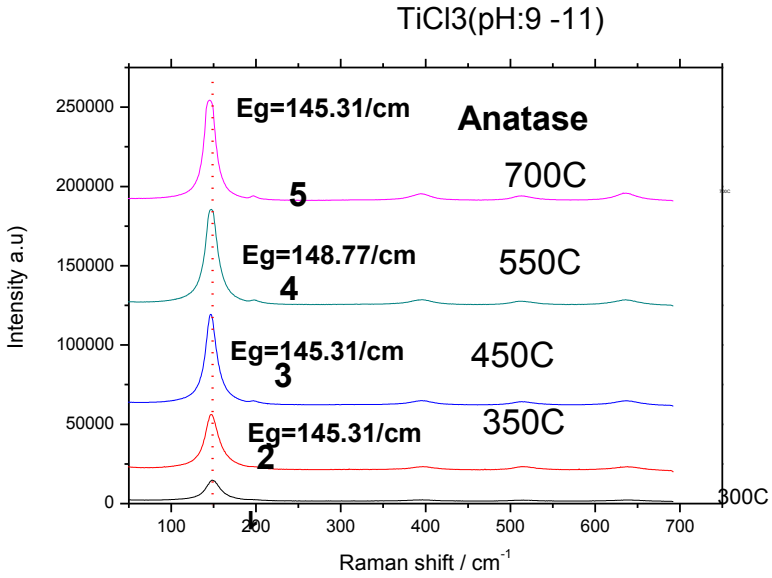

(a) Raman spectra of Sample TiCl3(pH:9~11) thermally treated at 350°C, 450°C, 550°C, and 700°C

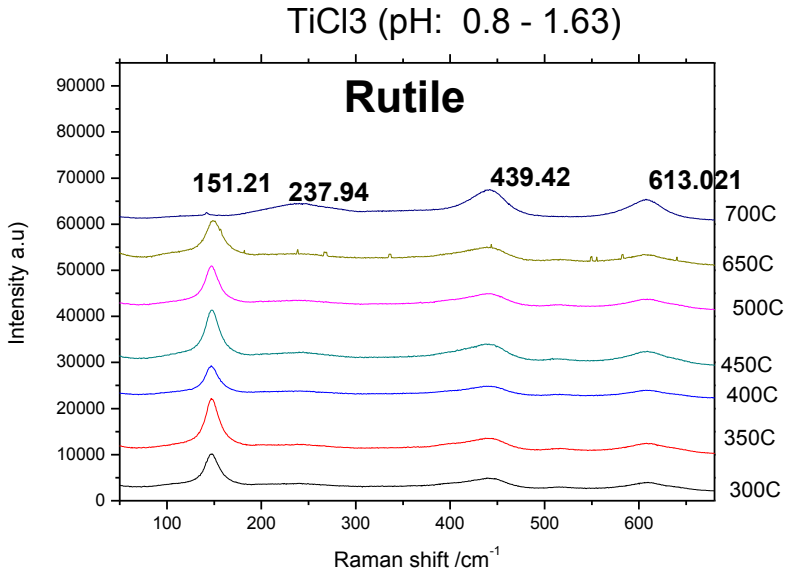

(b) Raman spectra of sample TiCl3 (pH: 0.8 ~1.63) thermally treated at 300°C, 350°C, 450°C, 550°C, and 700°C

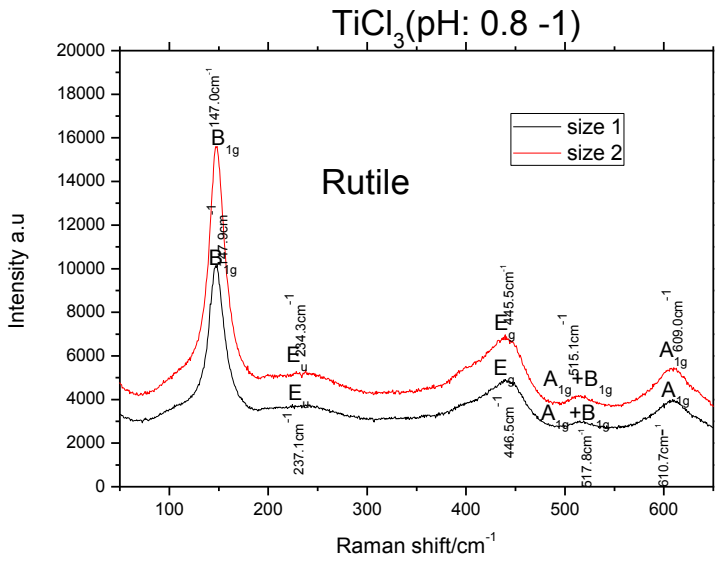

(c) Raman spectra, peak shift difference in samples $TiCl_3$ (pH:0.8~1.63) of different sizes, rutile phase

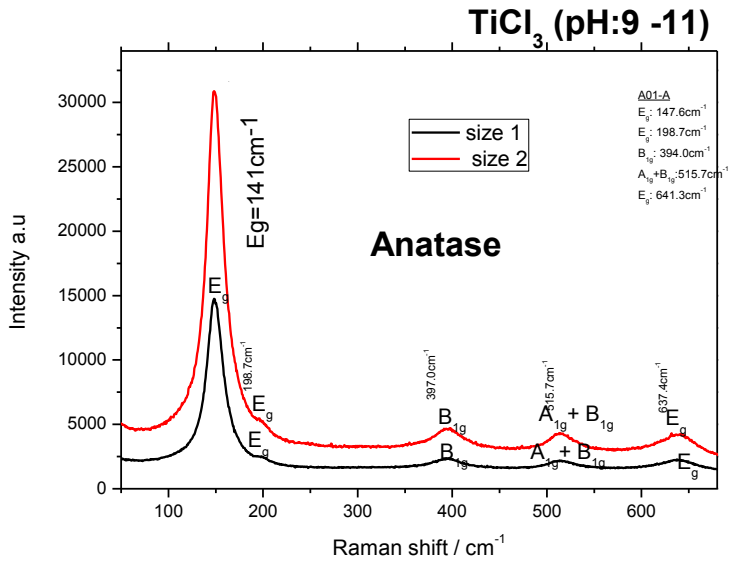

(d) Raman spectra, size effect on peak shift, sample $TiCl_3$ (pH:9~11), anatase

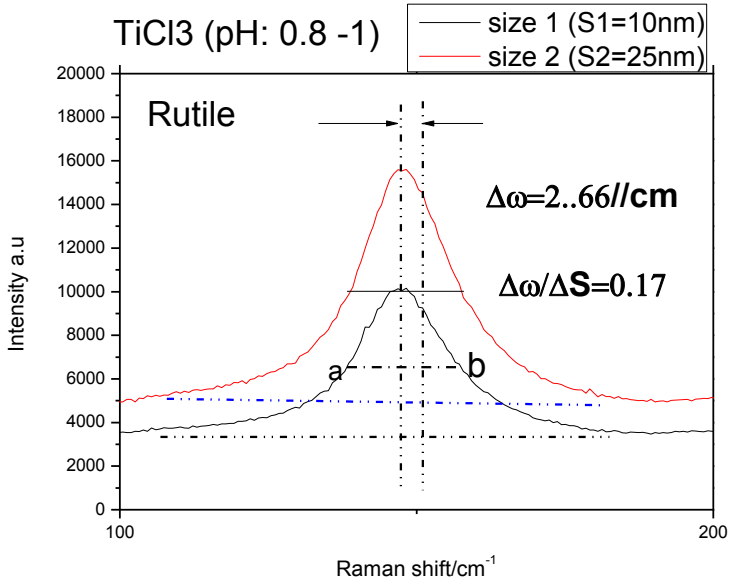

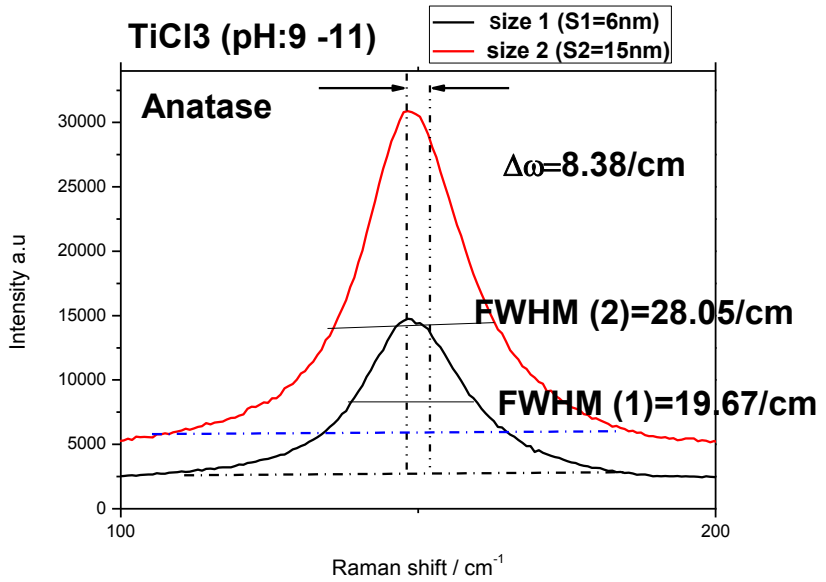

(e) Raman spectra, peak shift difference in samples $TiCl_3$ (pH:0.8~1.63) of different sizes, rutile phase

(f) Raman spectra, size effect on peak shift, sample $TiCl_3$ (pH:9~11), anatase

Figure 68: RAMAN spectra $TiCl_3$-based samples, comparing acidic versus alkaline samples

4.4.4. HRTEM / TEM characterization of as-synthesized TiO_2 NPS

Both tools, the high-Resolution Transmission Electron Microscope, HRTEM, and the Transmission Electron Microscope, TEM, have been used in a case-by-case analysis of as-synthesized materials. These operate definitely at the nanoscale (1 – 100nm), by far much smaller than optical microscopy. Depending on the availability, we utilized them mainly to identify the phases and crystal structures present in the material, but it could also be used to characterize and identify defects in the form of antiphase boundaries, dislocations, or stacking faults in the crystal structure and to determine modes of deformation. Keith L. (1999) lists other uses of TEM namely, to determine "site occupancy preferences" of the atoms within the crystal structures, to determine the growth directions of precipitates and the type of interfaces between different phases, to image atomic planes and defects attached to dislocations or interfaces, and to do a compositional analysis of individual phases. Operating differently from the scanning electron microscope (SEM), in a TEM, the electron beam is passed through the sample, and uses the transmitted electron beam to produce an image containing both diffracted and direct electron beam. The characteristic x-rays that are generated from the sample are collected by Detectors allowing the compositional analysis.

4.4.5. TEM Micrographs

Given the powder nature of the samples, Ti-iso-2, Ti-iso-6, $TiCl_3$ (pH: 0.8 ~ 1.63), $TiCl_3$, and (pH: 9 ~ 11), HRTEM / TEM were suitable tools for characterizing the lyophilized samples, which were mostly amorphous. The selected TEM micrographs are presented in figures: 3.3, 3.4, 3.5, and 10.6, 10.7.

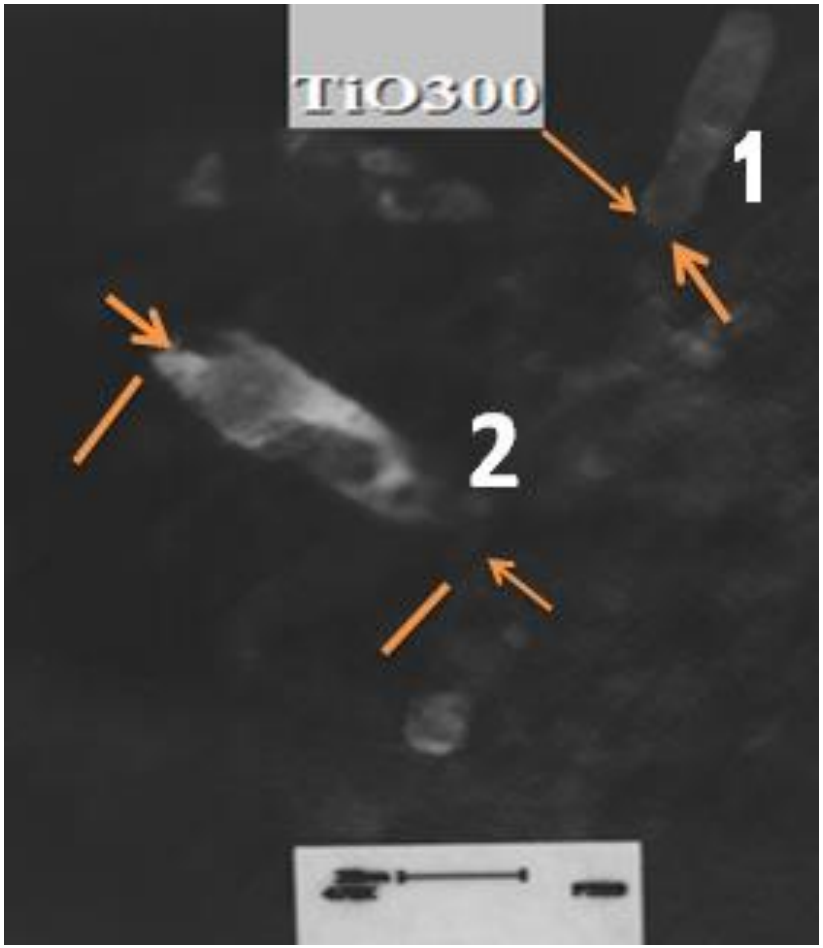

(a) TEM micrograph (negative) for sample Ti-iso-2, annealed at 300°C for 24hrs, showing (1) Nanorod, 400nm long, 85nm wide)

(b) TEM micrograph (negative) for sample Ti-iso-2, annealed at 200°C for 24hrs, showing (1) Nanorod, 400nm long, 85nm wide)

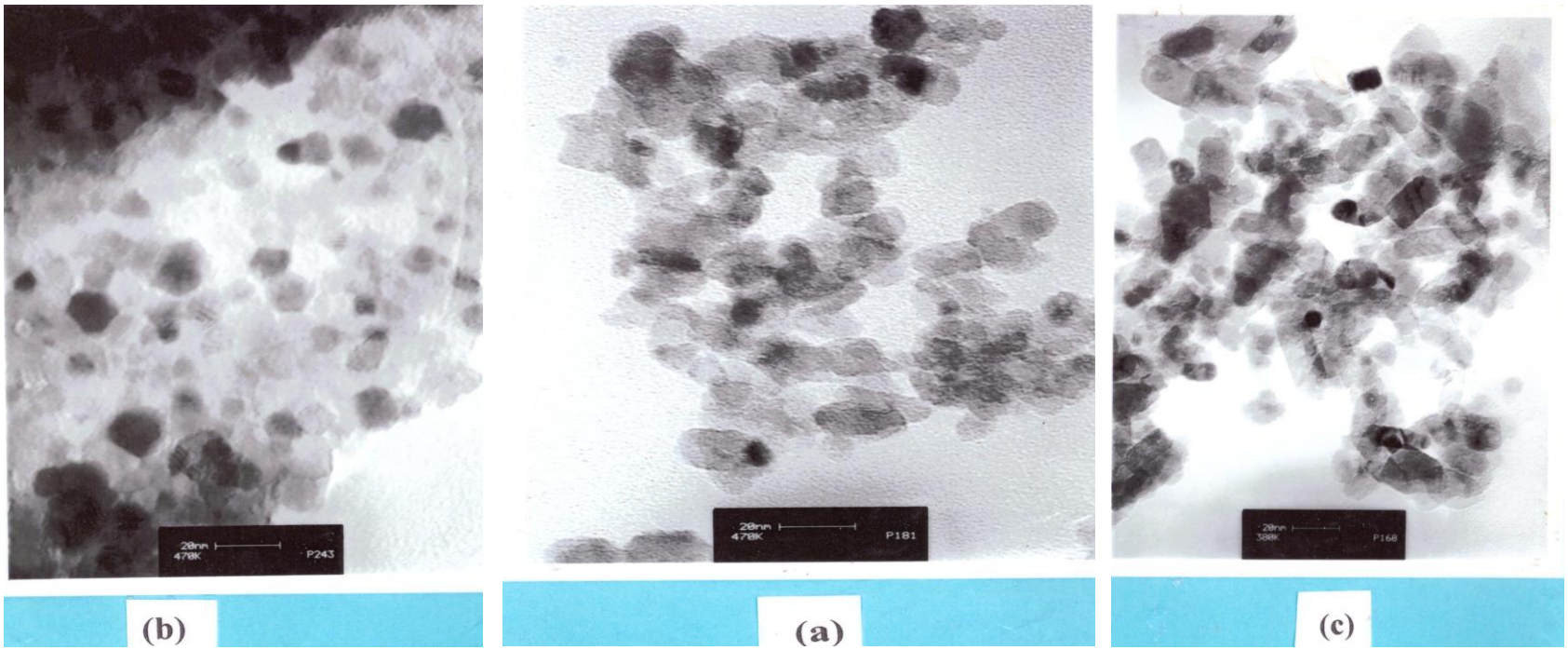

(a) Brookite phase-TEM Micrograph of Sample Ti-iso-2 annealed at 300°C

(b) TiO_2-Anatase phase nanoparticles- TEM Micrograph of Sample Ti-iso-2 annealed at 650°C

(c) TiO_2-Rutile phase nanoparticles -TEM Micrograph of Sample Ti-iso-2 annealed at 950°C, elongated, 20nm

Figure 69: TEM study of shape, annealing time effect samples Ti-iso-2

Table 17: EFFECTS OF NATURE OF TITANIUM PRECURSOR ON TiO2 NPS FORMATION, STRUCTURE, AND MORPHOLOGY

Sample Name	Major TiO_2 phase	Precursor	Temperature and time (hr) - Annealing (decomposition)	Solvent	Solution pH control (HCl / NH_4OH)	Characterization Technique		
Ti-iso-2	Amorphous, brookite, Anatase	Titanium isopropoxide	300°C – 900°C	Distilled water	0.8 ~ 1	XRD	TEM	
Ti-iso-6	Amorphous, Anatase, Rutile	Titanium isopropoxide	300°C – 900°C	Distilled water	11	XRD	TEM	
Ti-iso-pH	Anatase	Titanium isopropoxide	650°C	Distilled water	0.8; 3.5; 4.95;9; 11	XRD	TEM	
$TiCl_3$(pH9, 11)	Amorphous, Anatase	Titanium tri-chloride	200°C - 700°C	Distilled water	pH =9, 11	XRD	EDS, TEM B.E.T	RAMAN
$TiCl_3$(pH 0.8 ~ 1.63)	Amorphous, rutile	Titanium Tri-Chloride	200°C	Distilled water	pH=0.8 ~ 1.63	XRD	TEM	RAMAN
TiO_2 (acac)	Amorphous, Anatase	Titanium (IV) Acetylaetonate / Titanium (IV) Oxyacetylaceton ate (90%) Sigma Aldrich	400°C	Distilled water	pH~7	XRD	X	X
$TiOCl_2$	Anatase	Ti(IV) Oxychloride	300°C	Deionized water	pH:1; 7; 11	XRD,	HRTEM	B.E.T

Figure 70: (a): TiO_2 NPS: anatase and rutile phases synthesized by lyophilization

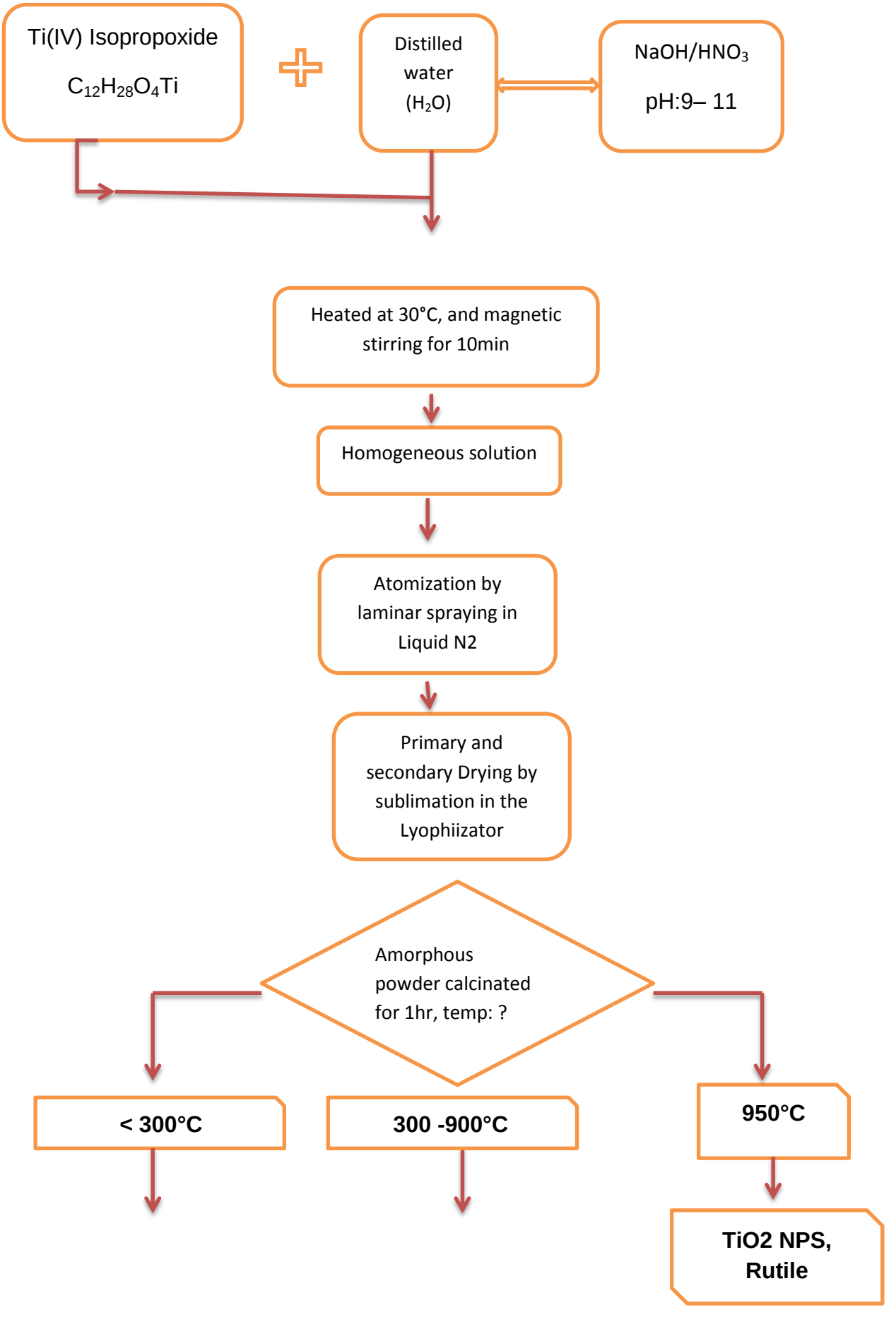

Figure 70 (b): TiO_2 NPS: Ti (IV) isopropoxide-Brookite, anatase, and rutile phases

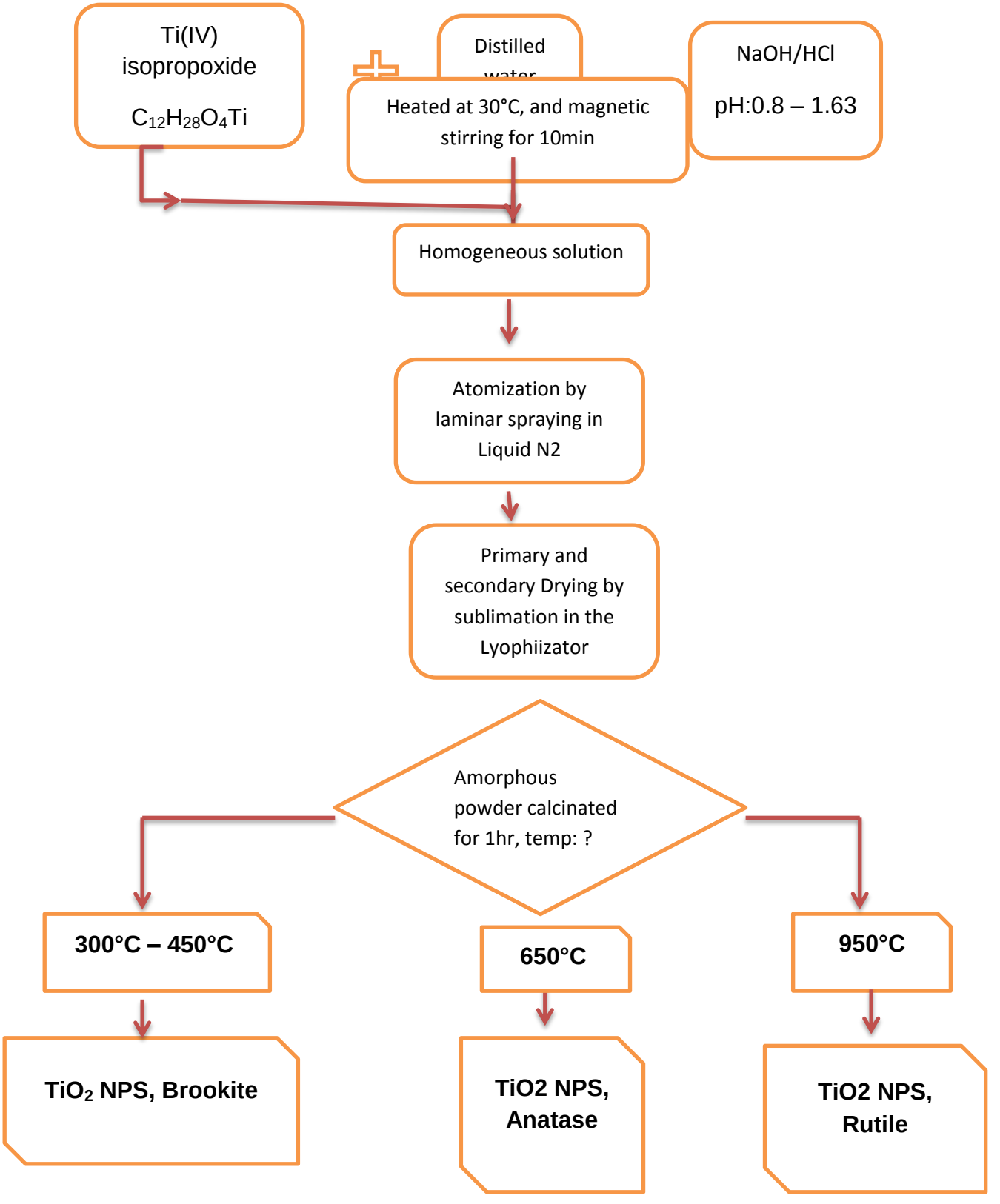

Figure 70 (c): TiO_2 NPS: P-chloro (P2) synthesized by lyophilization / diagram

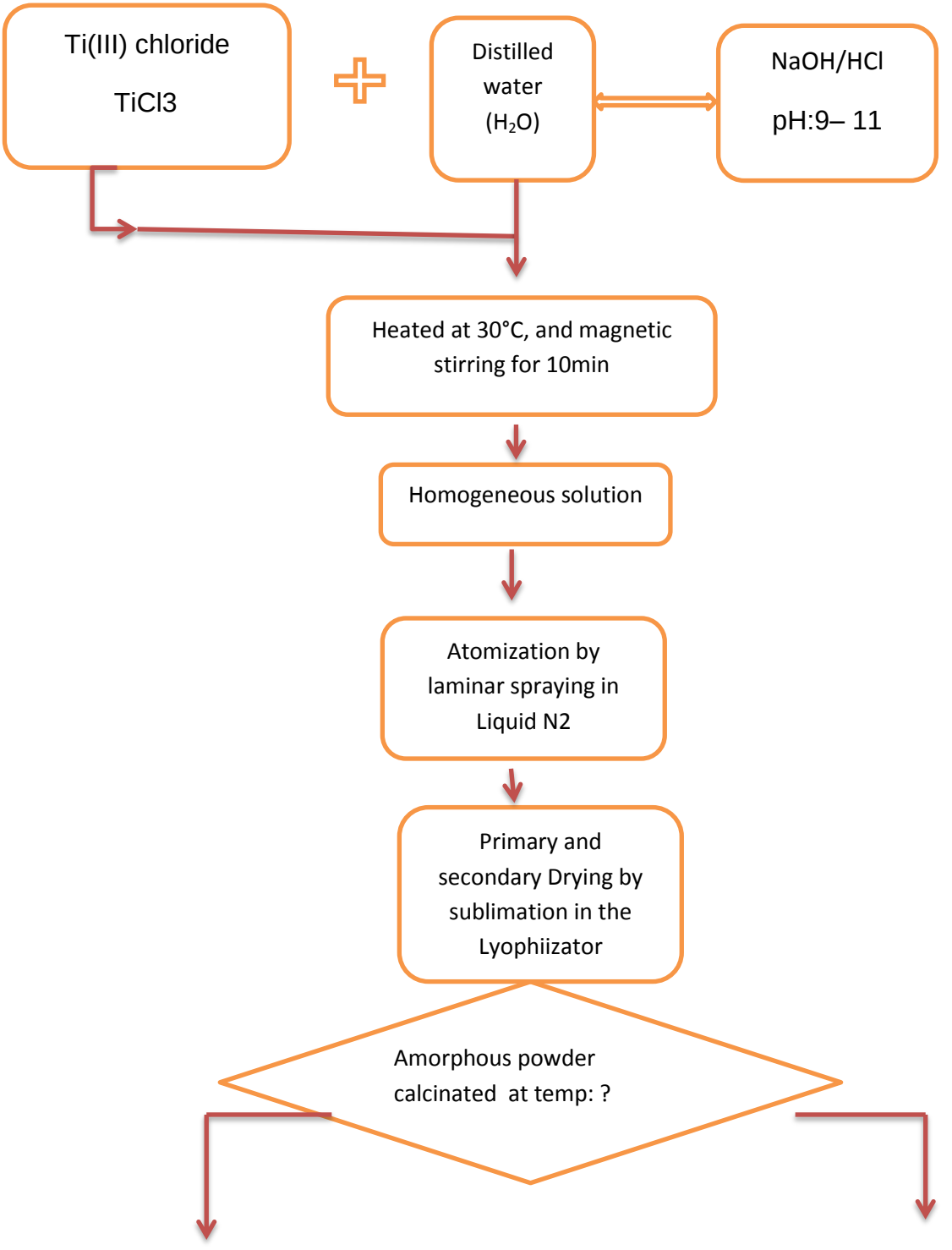

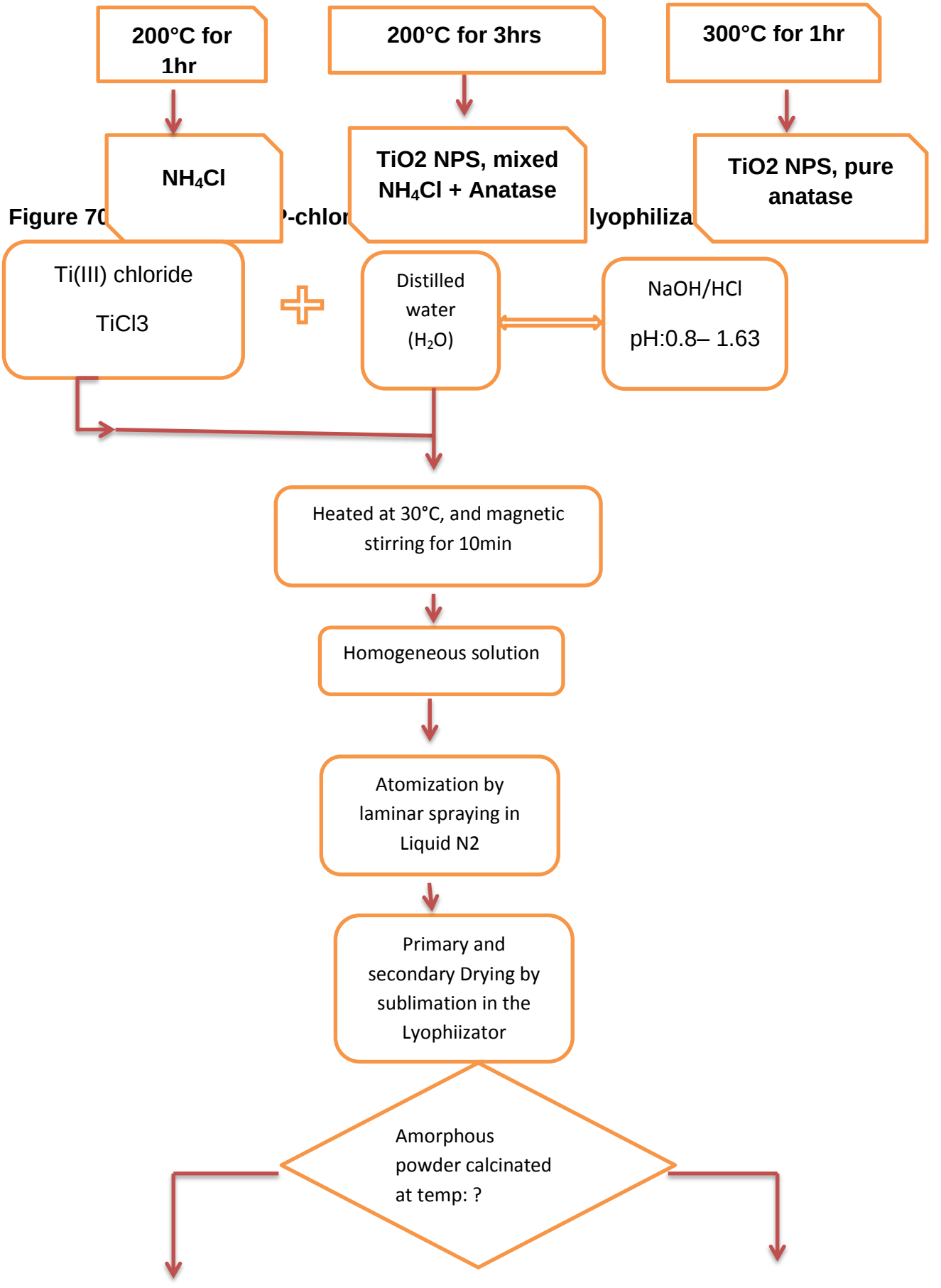

Figure 7C -chlor lyophiliza

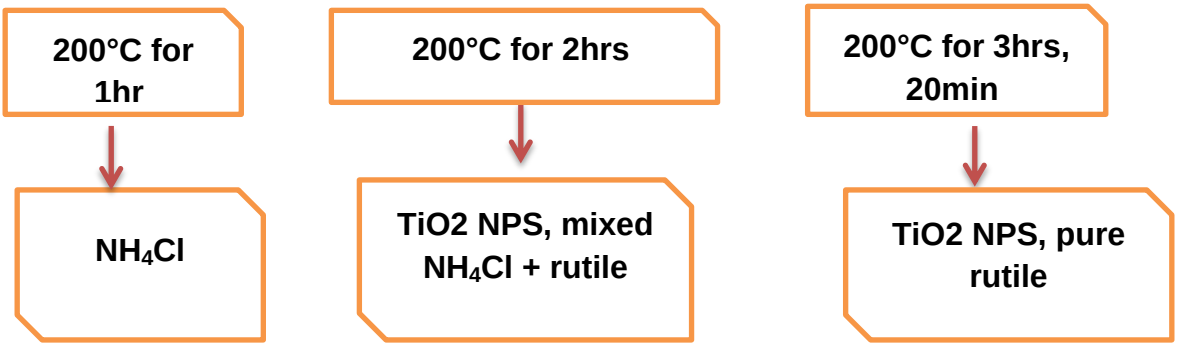

4.4.6. GAS SENSING EXPERIMENTAL RESULTS:

Application of **TiO_2** materials by Lyophilisation Technique to Gas Sensing

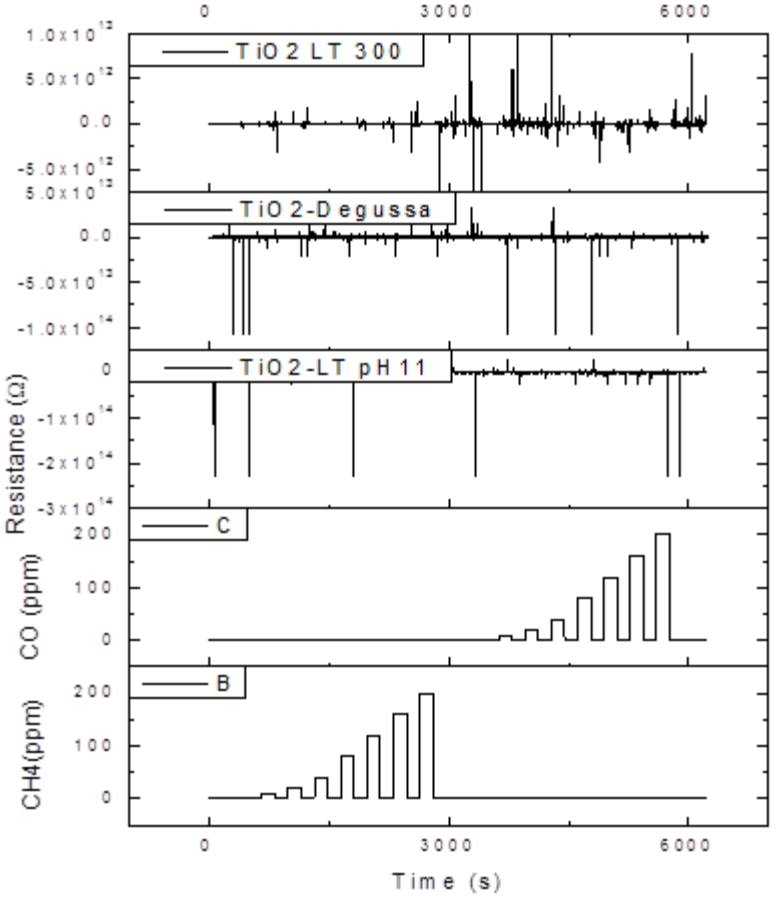

Figure 70: XRD patterns of TiCl3, pH:0.8 -1.63 annealed at 350°C for 10min, 1hr, 2.5hrs, and 6hrs

This is XRD patterns of TiCl3, pH:0.8 -1.63 annealed at 350°C for 10min, 1hr, 2.5hrs, and 6hrs versus time while under exposure to CH_4 and CO gases of varying concentrations (10, 20, 40, 80, 120, 160, and 200 ppm) at room temperature. This plot shows no response of **TiO_2** materials to any of the two gases at room temperature. This is a clear indication that one needed high temperatures to see if any response could be attained.

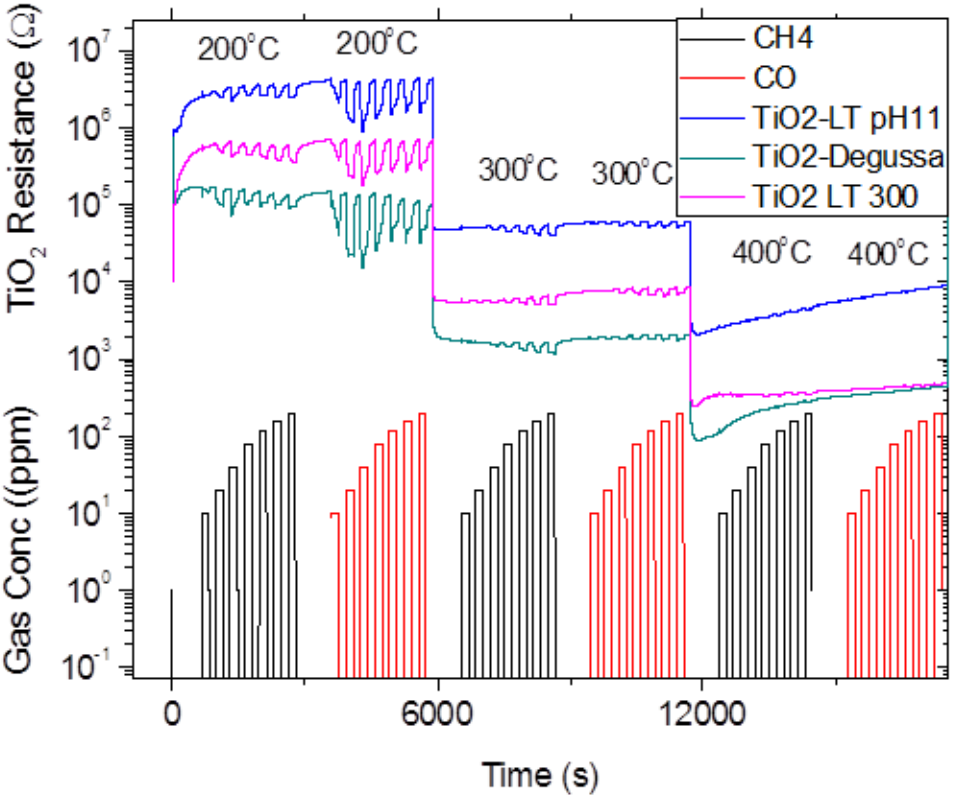

Figure 71: the plot of resistances of Degussa, TiO2 LT pH11, and TiO2 LT 300 samples versus time

This is the plot of resistances of Degussa, **TiO_2** LT pH11, and **TiO_2** LT 300 samples versus time while under exposure to CH_4 and CO gases of varying concentrations (10, 20, 40, 80, 120, 160, and 200 ppm) at a temperature of 200^{o}C, 300^{o}C, and 400^{o}C.

The plot shows first the responses of all materials to both gases are higher at 200^{o}C than at 300^{o}C and 400^{o}C. The responses decrease as the temperature of the operation increases. This means these samples would work well at temperatures lower than 200oC although the minimum temperature is yet to be determined. Room temperature sensing studies were also conducted and these are displayed in Figure 2 and will be discussed in the forthcoming sections.

Figure 5.3.3 Plot of responses to the lyophilized **TiO_2** compared to Degussa P25

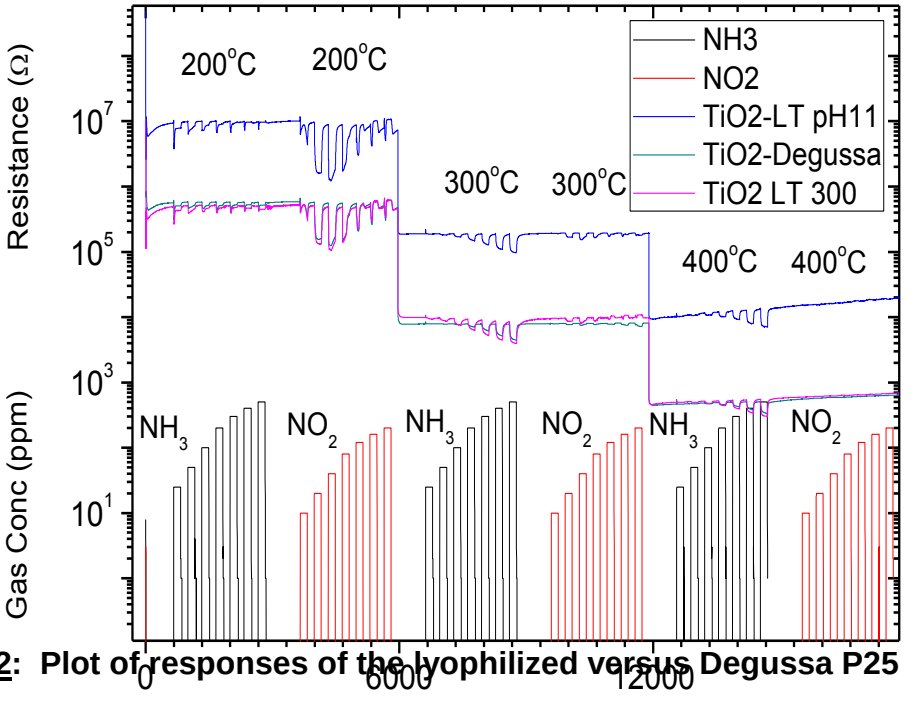

Figure 72: Plot of responses of the lyophilized versus Degussa P25

It was found that **TiO_2**-LT-pH11, Degussa^{TM} **TiO_2**, and **TiO_2**-LT300 have responses of 14%, 6%, and 4% to NO_2 respectively whereas the responses to CO were 6.5%, 14%, and 6% respectively. **TiO_2**- LT300 outperforms both Degussa^{TM} **TiO_2** and **TiO_2**-LT-pH11 on NH_3 response with a value of 3.5% where both of the competitors showed a negligible response. The influence of the synthesis parameters is proposed as an explanation of peculiar sensing characteristics, as well as the selective detection in TiO-LT-pH11 is discussed in terms of the surface area, eventual presence of the impurities in the material.

4.4.7. Antimicrobial Test Results

4.4.7.1. Culture of bacteria prepared on Petri dishes for experiments:

(**a**)

(**b**)

(c)

Figure 73: Bacterial cultures on Petri dishes: (a) E.coli, (b) S.Aureus, (c) P. V. Vulgaris

4.4.7.2. Experimental results on anti-microbial tests:

Antibacterial activity of different concentration(1.25-10mg/ml) of TD 25 on various bacterial species (E coli-K12, P Vulgarias-ATCC-49132, S aureas-MRSA-33591)

TD 25

Conc (mg	E coli(K12	P vulgaria	S aureas(MRSA-33591)
1.25	1	1.3	0.8
2.5	2	3	2
5	4	9	7
10	14	15	15.5
Antibiotic	14	13	9

Zone of inhibition (mm)

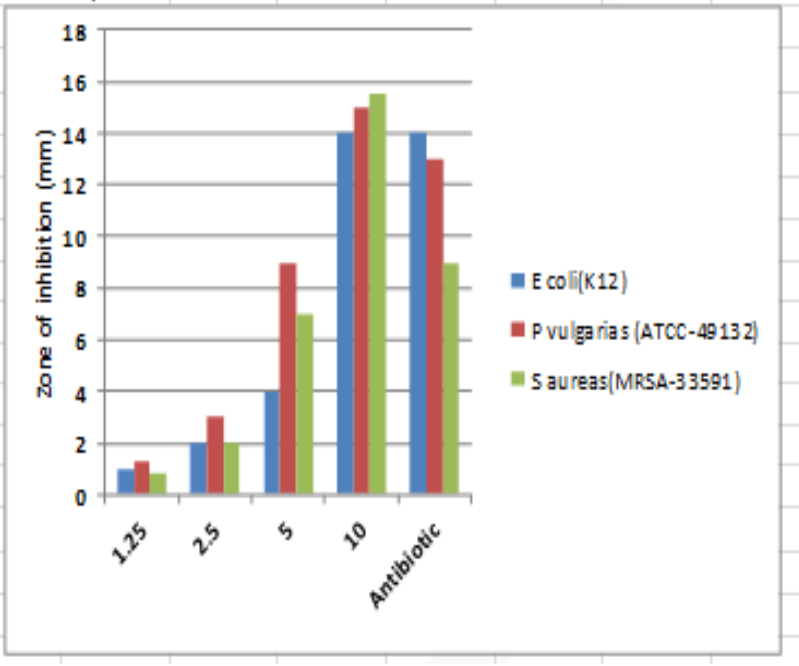

(a): Antimicrobial activity of Degussa-TiO_2, sample TD 25 on strains E.coli-k12, P.VulgarisATCC-49132, Saureas-MRSA-33591

Antibacterial activity of different concentration(1.25-10mg/ml) of LT 300 on various bacterial species (E coli-K12, P Vulgarias-

LT 300

Conc (mg	E coli(K12	P vulgaria	S aureas(MRSA-33591)
1.25	1.2	1	0.4
2.5	3	2	1
5	6	3.5	2
10	15.5	13.5	12
Antibiotic	14	13	9

Zone of inhibition (mm)

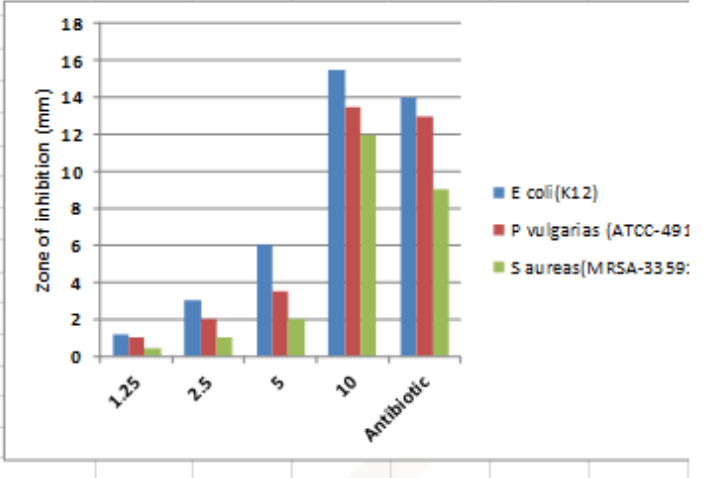

(b): Antimicrobial activity of Degussa-TiO_2, sample LT300, Lyophilized TiO_2 on

strains E.coli-k12, P.VulgarisATCC-49132, Saureas-MRSA-33591

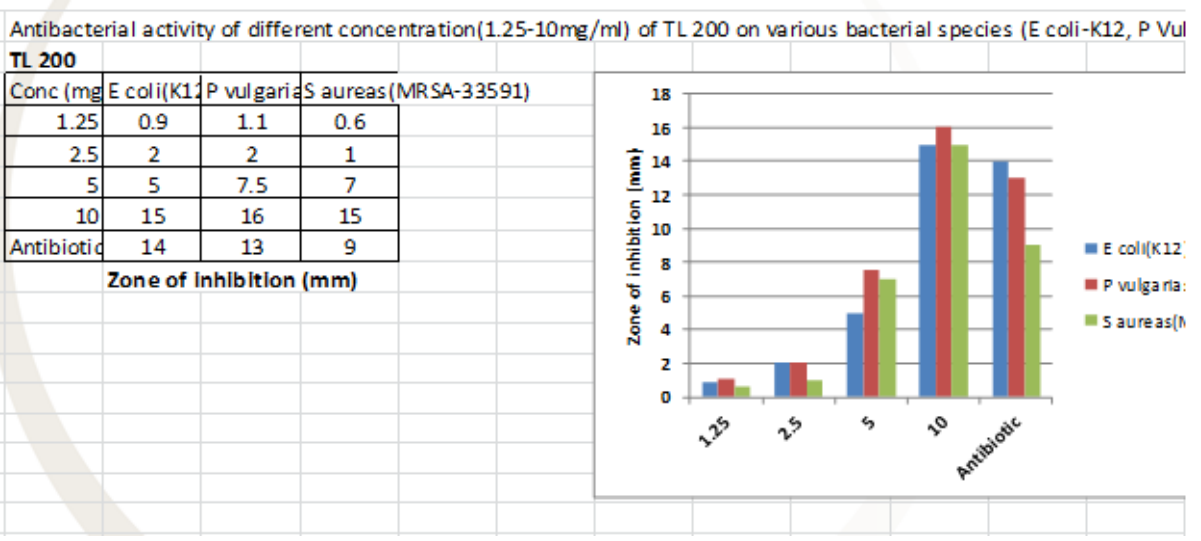

(C) Antimicrobial activity of Degussa-TiO_2, sample TL200, Lyophilized TiO_2 on strains E.coli-k12, P.VulgarisATCC-49132, Saureas-MRSA-33591

Figure 74: Antimicrobial activities of TiO_2 samples

The results of the two lyophilized samples TL 200 and TL-300 were compared to those of the (P25) Degussa **TiO_2** nanoparticles and against a standard antibiotic of known activity for each of the species: 14, 13, and 9 mm zone inhibition, respectively for E.coli-K12, P Vulgaris (ATCC-49132), and S aureus (MRSA-33591), as all samples were prepared and tested in the same conditions.

Various concentrations (1.25 – 10mg/ml of each sample were prepared and zones of inhibition measured in mm. For the concentration 10mg/ml each, the lyophilized **TiO_2** NPS, sample TL200 measured 16mm, the highest bacterial inhibition activity for the P.vulgarius pathogenic strain, P25 sample measured 15.5mm, the highest for E aureus, while TL300 measured 15.5mm, the highest for E.coli strain, commonly found in contaminated drinking water (causing diarrhea) in many parts of the world, in particular South Africa1.

These results indicate a selective antibacterial property of the lyophilized **TiO_2** NPS samples for P.vulgarius and E.coli and promise the development of a cost-effective remedy

in the treatment of contaminated drinking water and improvement of water quality in general for South Africa and many other countries.

4.4.7.3. Conclusion anti-microbial tests:

For the concentration 10mg/ml each, the lyophilized **TiO_2** NPS, sample TL200 measured 16mm, the highest bacterial inhibition activity for the P. vulgarius pathogenic strain, P25 sample measured 15.5mm, the highest for S. aureus, while TL300 measured 15.5mm, the highest for E.coli strain, commonly found in contaminated drinking water (causing diarrhoea) in many parts of the world, in particular South Africa[1]. These results indicate a selective antibacterial property of the lyophilized **TiO_2** NPS samples for P. vulgarius and E.coli.

- The results are evidence of the improvement of the efficiency of the antibacterial activity of **TiO_2** NPS by the lyophilisation synthesis method.

- This promises the development of a cost-effective remedy in the treatment of contaminated drinking water and the improvement of water quality

4.4.8. Experimental Results on Photo-catalytic activity of the lyophilized TiO_2 nanoparticles:

The results obtained are significant in that there is a net effect of the irradiation time on the degradation of the organic substance model (MB) and the effect of **TiO_2** photo-catalyst is noticeable. More importantly, the increase in the photocatalytic activity of the Lyophilized **TiO_2** samples exceeds one of the photocatalytic activity standard materials (Degussa P-25).

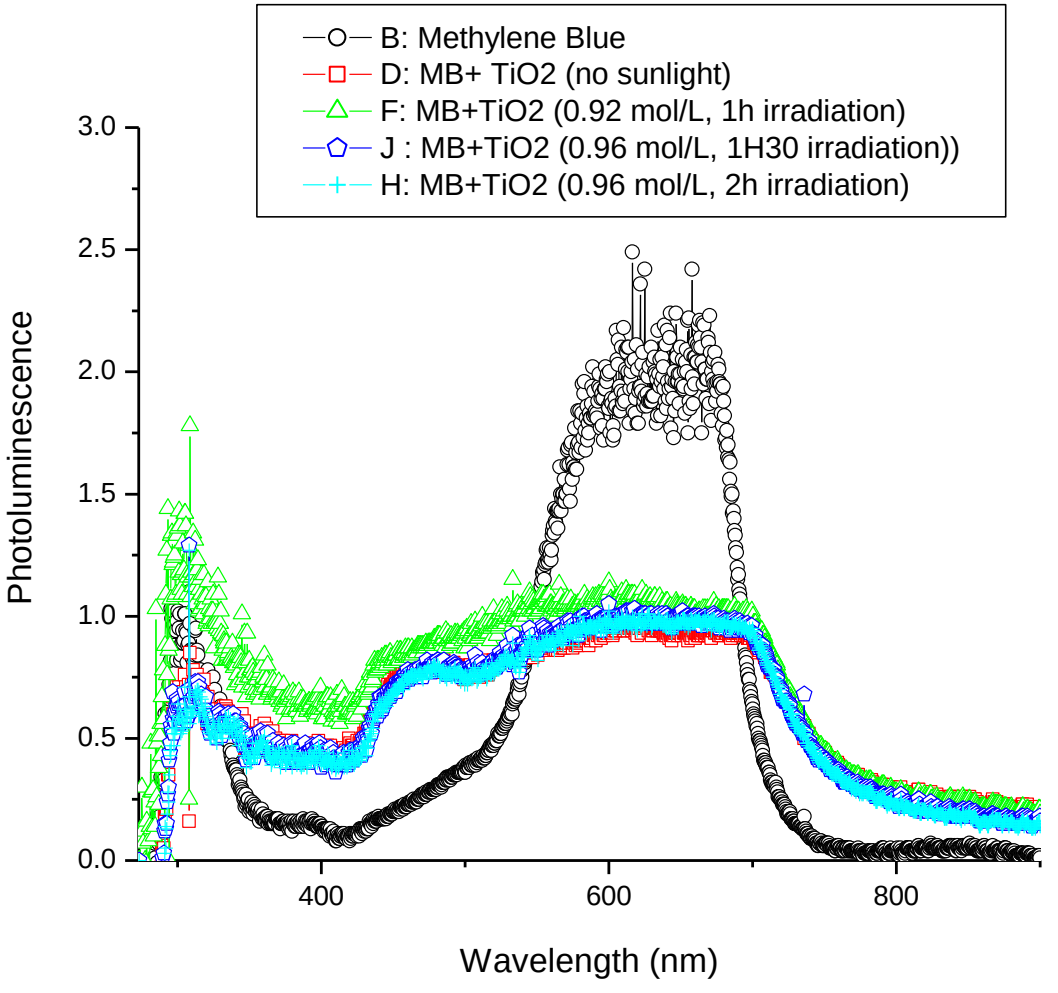

Figure 75: Photodegradation of Methylene Blue by TiO2 photocatalysts -Plot of Photoluminescence versus wavelengths

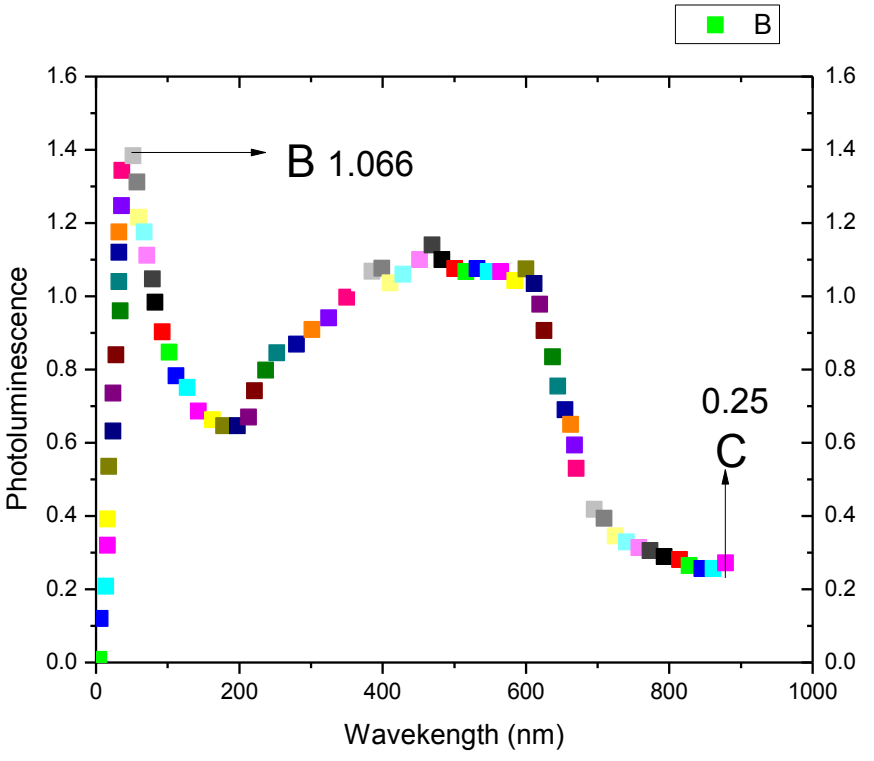

Figure 76: Photocatalytic activity of the Lyophilized TiO2

The graph demonstrates the photocatalytic activity through degradation of MB+TiO_2 (lyophilized) between point B (λ=605nm) and points C (λ=878.14nm), illumination for 60min.

In conclusion, by applying equation 9.1 to the measuring of the photocatalytic effect as mediated by the lyophilized **TiO_2** NPS in the photo-degradation efficiency, **ŋ (%)**, for the methylene blue (the test organic substance, 0.92 mol/L) to be **76.54**. The latter figure is double as compared to the photo-degradation efficiency obtained by Shodhganga et al., in the case of Degussa P25-**TiO_2** NPS.

CHAPTER 5: CONCLUSIONS AND RECOMMENDATIONS

Based on consideration of the physicochemical nature of the lyophilization Process, conclusions are drawn from technical and scientific points of view or experimental results obtained.

5.1. Technical considerations:

The properties of as-prepared TiO_2 nanoparticles were found to be by far superior compared to those prepared by conventional procedures because of very low residual porosity, the temperature of annealing is significantly lower, chemical homogeneity is achieved and the reactivity is relatively higher because of the state of the particle surface which has been maintained intact.

The achievement of the above-mentioned results requires a careful selection of titanium precursor salt, and the parametric values of the principal phases of lyophilization must be well determined.

The following principles were found to be capable of sustaining excellent chemical and crystalline homogeneity:

- To avoid separation and selective crystallization, the salts must be dissolved, mixed in the formulation, all must be endothermic /exothermic processes.
- Spraying / atomizing liquid droplets as fine as possible prevents separation during freezing, of which the rate could be limited by heating.
- While the freeze-drying is taking place, the temperature of the product has to be kept lower than the crystallization/glass temperature, especially in the case of the element that crystallizes at the lowest temperature.
- To avoid hydration of the lyophilized powder, annealing must be done without delay after the freezing-drying. In such conditions, the chemical homogeneity will be conserved.

5.2. On experimental considerations:

Temperature and pressure-induced phase transition processes in anatase Titania were investigated. It was shown that the phase transition processes in nano-anatase Titania are completely different from that of the bulk anatase in the range of 0 ~ 40Gpa. The anatase

TiO_2 maintains its crystallographic structure of the original form up to ~17 GPa, before transforming directly to baddeleyite structure.

- The optimization of the lyophilization Process and its products, has shown that the synthesis conditions account for the structural evolution of the **TiO_2** nanoparticles.
- The full control of size and size distribution, structure, and morphology of the **TiO_2** nanoparticles is dependent on control of synthesis conditions including the pH, the initial concentration of the formulation, the type of titanium precursor, and the decomposition/annealing temperature.
- For individual titanium-precursor salt or precursor solution selected, it must be treated as a special case because crystallization into single-phase anatase, brookite and rutile, and/ or phase transition, viz. from amorphous-to- brookite, amorphous-to- anatase, anatase-to-rutile, brookite –to-rutile, brookite-to-anatase, even amorphous directly to rutile (the most stable) is different depending on the synthesis conditions (pH and initial concentration) and the range of the decomposition/ annealing temperature, and duration of annealing, yet at atmospheric pressure (1atm).
- We have introduced a revision of the Williamson-Hall equation. This was necessitated by the gross underestimation of the crystallite sizes worse than the Scherrer formula. When compared to TEM crystallite sizes, we found that Scherrer sizes are also slightly less, within experimental error than the TEM sizes. The revision was accomplished through the expansion of the W-H equation into a full polynomial equation which after further binomial expansion via some trigonometric identities reduced to a cubic polynomial. The main task in this theory is to transform the β_{tot} -θ data into a plot of $\beta_{tot}^2\cos^2\theta$ against $\sin\theta$ rather than the traditional $\beta_{tot}\cos\theta$ against $\sin\theta$ plot and fit Equation 14 to this plot and extract coefficients a, b, c, and d. The coefficient is used to find the strain in the sample and coefficients b and d contain information on particle size. Although our $\beta_{tot}^2\cos^2\theta$ - $\sin\theta$ method yields strain values are surprisingly very small when compared to the more trusted Raman spectroscopy method, the new method's threshold particles are much closer to the particle sizes found from high-resolution TEM than both the Williamson-Hall and the Scherrer sizes When the Scherrer factor is added to this threshold value, the new method then also accounts for agglomerates as the particles size in the current results set range in hundreds of nanometers. It has been shown that when the current model is linearized -

$\beta_{tot}\cos^2\theta$-$\sin\theta$ method- the new strain is increased by a significant factor – about one order of magnitude higher than the $\beta_{tot}^2\cos^2\theta$-$\sin\theta$ method and coming close to the desired accuracy as in the strains obtained by Raman spectroscopy. This also forced the crystallite size to approach the values obtained by TEM imaging.

- For the concentration 10mg/ml each, the lyophilized **TiO_2** NPS, sample TL200 measured 16mm, the highest bacterial inhibition activity for the P. Vulgarius pathogenic strain, P25 sample measured 15.5mm, the highest for S. aureus, while TL300 measured 15.5mm, the highest for E.coli strain, commonly found in contaminated drinking water (causing diarrhoea) in many parts of the world, in particular South Africa. These results indicate a selective antibacterial property of the lyophilized **TiO_2** NPS samples for P. Vulgarius and E.coli.

- The results are evidence of the improvement of the efficiency of the antibacterial activity of **TiO_2** NPS by the lyophilisation synthesis method.

- This promises the development of a cost-effective remedy in the treatment of contaminated drinking water and the improvement of water quality

- By measuring the photocatalytic effect as mediated by the lyophilized **TiO_2** NPS in the photo-degradation efficiency, **ŋ (%)**, for the methylene blue (the test organic substance, 0.92 mol/L) to be **76.54**. The latter figure is double as compared to the photo-degradation efficiency obtained by Shodhganga et al., in the case of Degussa P25-**TiO_2** NPS.

Surface properties of lyophilized Titania, characterized and compared to measurement on the standard Titania-nano (Degussa-P25) for gas sensing and water purification

- The surface properties of the as-lyophilized anatase **TiO_2** nanoparticles suggest higher performance in gas sensing and water purification. Because the B.E.T surface area of the lyophilized Titania is 2.4 times higher than the B.E.T measurement, but the pore size is smaller by 37% than the commercial Degussa P25, the standard photocatalyst. This observation seems to indicate a particular behavior of the lyophilized **TiO_2** nanoparticles that tentatively was explained by interpreting the hysteresis patterns in isotherm adsorption-desorption curves. It was revealed that the lyophilized Titania was of the Hysteresis loop characteristic of mesoporous nature. Based on the literature, the mesoporous characteristic of the samples was confirmed because the measurement of the

pore sizes, all falling within <2 -50 nm) range, the values 15.907nm, 9.31 -18,83nm being respectively the diameters of pore for Degussa P25, and the lyophilized Titania respectively.

- The cause of mesoporosity would be the tensile strength effect (TSE) and the capillary condensation. Capillary condensation is a process such that the force exerted on the molecules through the pore walls causes the molecule to adsorb layer by layer. A resulting narrow gap is created by accumulated and collapsed molecules to a lower thermo-dynamical energy state.
- Further characterization is based on the classification of types of hysteresis (H1, H2, H3, and H4) which provides information on the state of agglomeration, shape of particles present, width of pores, size distribution of the particles. The classification of the adsorption process uses the graph of the amount of adsorbate (Nitrogen gas) adsorbed on the surface of adsorbents, **TiO_2** Degussa P25, lyophilized titania-nano at STP (standard pressure and temperature). The characterization of the particles of adsorbents based on the hysteresis loop has been shown by both samples responding to both gases at temperatures between 200^{o}C - 400^{o}C. The responses decrease as the temperature of the operation increased. This means these samples would work well at temperatures lower than 200^{o}C, although the minimum temperature is yet to be determined. The promising (RT) room temperature sensing studies were also conducted, but the work must be completed to be conclusive.

REFERENCES

[1] S.T. Aruna, S. Tirosh and A. Zaban, J. Mat. Chem., 2000,10,2388-2391

[2] D.F.OIlis, E.Pelizzetti and N.Sespore, Environ.Sci.Technol., 1996, 5, 1523

[3] Vesa P.S.Judin, chem.in Britain, June 1993, 504

[4] B.O'Regan and M Gratzel, Nature vol.353(1991), 737

[5] P.Kibasomba, M.J.Witcomb. A.AA.Dawe, C.Sella, O.Nemraoui, ICEM-15 Durban, 2002,1059-1060

[6] R.asahi and Taga, W.Mannstadt and A.J.Freeman, Phys.Rev.B vol.61, No.11, 2000 7.

[7] H.Tang et al, J Appl. Phys 75(4), 15 Feb. 1994

[8] R.J. Gonzalez, Phys.Rev.B, Noll, vol.55, 7014(1997)

[9] Henghong Zhang and Jillian F.Banfield, J.Phys.chem.B, 2000, 104, 3481- 3487

[10] Mono P.moret et al. Thin solid films 366(2000) 8-10

[11] Toshiaki Ohsaka et al, J.of Raman spect, vol 7, No.6,1978

[12] U. Diebold, surface science reports 48 (2003), 53-229 p.66

[13] L.S. Dubrovinsky, N.A. Dubrovinskaia, V.Swamy, J. Muscat, N.M. Harrison, R.Ahuja, B.Holm, Johansson, Nature 410 (2001) 653

[14] G.V. Samsonov, The oxide handbook. Plenum Press, New York, 1982

[15] F.A. Grant, Rev. of modern physics, vol.31, No.3, July 1959

[16] D.A Porter and K.E.Easterling, Phases transformations in metals and alloys, second edition, pl(1992).

[17] Statistical Physics, F Mandl, 2nd edition, p.228.

[18] T.Arlt, M. Bermejo and Blanco, et al., Phys. Rev. B, vol.61, No.21, 2000

[19] J.Staun Olsen, LGerward, and J.Jiang, High-Pressure Research, 2002, 25 vol.00, pp.1-5

[20] Julian Haines and J.AA.Leger, Physics B 192(1993) 233-237

[21] K.Lagarec and S.Desgreniers, solid-state commun.94, 519 (1995).

[22] J.Benard et al: L'oxydation des metaux (I), Processus f ondamentaux (1962), p372

[23] H.P.R. Frederikse, J.of appl.Phys., vol.32., No.10 (1961)

[24] J.E.Brady and J.R.Holum: The study of matter and its changes, 2nd edition ((1996), p.354

[25] R.Asahi , Y.Taga, W.Mannstadt, and A.J.Freeman, Phys.Rev.B, vol.61. No.ll(2000)

[26] Management of solid wastes: Multimedia postgraduate course in Environmental Eng., UNESCO (1996) p.35

[27] M.A.Barakat, Y.T.Chen, C.P. Huang: Removal of toxic cyanide and Cu(II) ions from water by illuminated **TiO_2** catalyst. Appl. catalysis B: Environmental 53 (2004) 13 – 20

[28] San Gi Lee, Sanghwa Lee, Ho-In Lee: Appl. catalysis A: General 207 (2001) 173 –181

[29] W.F. Zhang, Y.L He, M S Zhang, Z Yin, and Q. Chen, J.Phys.D. Appl. Phys.33(2000) 912 -916

[30] Kamina article: A gas sensor system based on conductivity measurement with segmented metal oxide films to be used in mass products: http://www-ifia.fzk.de/IFIA, retrieved 2005-4-7

[31] Tetsu Tatsuma, Koichiro Tani, Noboru Oyama, Hock-Hin Yeoh: Linamarin sensors, J. of Electroanalytical Chem.407(1996) 155-159

[32] Baheti, Ankit; Kumar, Lokesh; Bansal, Arvind kumar: Excipients used in lyophilization of small molecules. J.of Excipients and Food chemicals

[33] Henghong Zhang, R.Lee Penn, Robert J.Hamers, and J.F.Banfield, J.Phys.Chem.B, 1999, 103, 4656

[34] Hugo de Lasa, Benito Serrano, and Miguel Salaices: Photocatalytic reaction Eng. (August 2004)

[35] D. Bersani and P.P.Lottici: Appl.Phys. Lett.72(1), 1998

[36] Ignacio Martini, Jose H.Hodak, and Gregory V.Hartland: J.Phys.B(1998), 102, 9508-9517

[37] Yanqin Wang, Humin Cheng, Yanzhong Hao, Jiming MA, Weihua, Shengmin Cai, J.mater.scies 34(1999) 3721 –3729

[38] Gaelle Goutailler, Chantal Guillard, Stephane Danielle, and Liliane G.Hubert- Pfalzgraf, J.mater.Chem.2003, 13, 342-346

[39] Janne Halme: Dye-sensitized nanostructured and organic photovoltaic cells: Technical rev. and preliminary tests, February 12, 2002

[40] K.Karakulski, W.A.Morawski and J.Grzechulska, process Separation & purification Techno.14(1998) 163-173

[41] P.M Kibasomba, M.J Witcomb, O.Nemraoui, and M.Maaza: TEM characterization of lyophilized **TiO_2** Nanoparticles, Microscopy society of Southern Africa-proceedings, Vol.33-(2003)

[42] G.Hearne, J.Zhao, A.M Dawe, V.Pischedda, M.Maaza, M.K Nieuwouldt, P.Kibasomba, O.Nemraoui and D.Comins, Physical Rev.B 70, 134102(2004)

[43] Do Hun Kwon, Young Hee Jung, and Yeong Il Kim, J. of the Korean Chemical Society, 2015, Vol. 59, No. 3

[44] K. R. Narendra Pai, a G. S. Anjusree, a T. G. Deepak, a Devika Subash, a Shantikumar V. Naira and A. Sreekumaran Nair, RSC Adv., 2014,4, 36821-36827

[45] Shivaraju H.P, INTERNATIONAL, JOURNAL OF ENVIRONMENTAL SCIENCES Volume 1, No 5, 2011

[46] Guohua Chen & Wei Wang, ISSN: 0737-3937 (Print) 1532-2300

[47] Li Zhao, Jiang Chang, Wanyin Zhai, J Mater Sci: Mater Med (2009) 20:949–957, DOI 10.1007/s10856-008-3645-5

[48] Oleg A. Shlyakhtin & Young-Jei Oh, J Electroceram (2009) 23:452–461 DOI 10.1007/s10832-008-9488-0

[49] Lei ian and Haifei Zhang, Journal of chem. And Biotechno, online library 2 September 2010, Doi 10.1002/j ctb.2495

[51] National Development Plan (NDP), http://www.sanews.gov.za/south-africa/national-development- plan-unpacked, downloaded, February 23, 2016

[52] Komkrit Suttiponparnit1,2, Jingkun Jiang1†, Manoranjan Sahu1, Sirikalaya Suvachittanont2,Tawatchai Charinpanitkul3, Pratim Biswas1 Nanoscale Res Lett 2011, 6:27

[53] H. Lin a, C.P. Huang a,*, W. Li b, C. Nib, S. Ismat Shah b,c, Yao-Hsuan Tseng, Applied Catalysis B: Environmental 68 (2006) 1–11

[54] Irene E. Paulauskas and Deena R. Modeshia, Tarek T. Ali, Elsayed H. El-Mossalamy, Abdullah Y. Obaid and Sulaiman N. Basahel, Ahmed A. Al-Ghamdi, Felicity K. Sartain Platinum Metals Rev., 2013, 57, (1), 32–43•

[55] K.Joseph Antony Raj & B.Viswanathan, Indian Journal of Chemistry Vol.48A, October 2009, pp.1378 - 1382

[56] Chin S., Park E., Kim M, Bae GN, Jurng J. J.Colloid Interface Sci 2011 Oct.15; 362 (2) 470-6 doi: 10.1016/J.Jcis 2011.06.034 Epub 2011 Jul.8

[57] MAJEED A. SHAHEED and FALAH H. HUSSEIN Journal of Babylon University/Pure and Applied Sciences/ No.(1)/ Vol.(22): 2012

[58] Juan de Dios, Jose María del Campo, and David Colorado 2nd International Conference on Emerging Trends in Engineering and Technology (ICETET'2014), May 30-31, 2014 London (UK)

[59] John T. Yates (Prof), Department of Chemistry, University of Virginia, Charlottesville, VA, USA Friday, 21 October 2011 8:30, lecture room H12, Cauerstr. 11 Contact: Prof. Oliver Diwald | Institute of Particle Technology Phone: 09131/85-29404 | Mail:O.Diwald@lfg.uni-erlangen.de

[60] Olivier Rosseleaser, Mohamad Sleiman,† V. Nahuel Montesinos,§,∥,⊥ Andrey Shavorskiy, Valerie Keller, Nicolas Keller, Marta I. Litter, Hendrik Bluhm Miquel Salmeron, and Hugo Destaillats J. Phys. Chem. Lett. 2013, 4, 536−541

[61] Ulrike Diebold, Surface Science Reports 48 (2003) 53 – 229

[62] Jun-Bin Koa, Ki-Hyun Kimb, Jae-Kil Hanc and In-Cheol Kang J. Ceramic Processing Research. Vol. 11, No. 5, pp. 612~616 (2010)

[63] Bonex Wakufwa Mwakikunga, Thomas Malwela, Kenneth Thembela Hillie, Gebhu Ndlovu, DST/CSIR National Centre for Nano-Structured Materials Council for Scientific and Industrial Research, Pretoria, South Africa

[64] Chengxiang Wang, Longwei Yin *, Luyuan Zhang, Dong Xiang, and Rui Gao, Sensors 2010, 10, 2088-2106 DOI:10.3390/s100302088,

[65] Xiao Liu 1, Sitian Cheng 1, Hong Liu 1, Sha Hu 1, Daqiang Zhang 2 and Huansheng Ning 1,* Sensors 2012, 12, 9635-9665; doi:10.3390/s120709635

[66] Jing Bai and Baoxue Zhou, Chem. Rev. 2014, 114, 10131−10176, pubs.acs.org/CR

67 J. Park, J. Joo, S.G. Kwon, Y. Jang, T. Hyeon, Angewandte Chemie International Edition 46 (2007) 4630-4660

[68] M.A. El-Sayed, Accounts of Chemical Research 37 (2004) 326-333

[69] A.A.R. Watt, D. Blake, J.H. Warner, E.A. Thomsen, E.L. Tavenner, H. Rubinsztein-Dunlop, P. Meredith, Journal of Physics D: Applied Physics 38 (2005) 2006-2012.

[70] S.Ren, L.-Y. Chang S-K. Lim, J. Zhao, M. Smith, N. Zhao, V. Bulovic, M. Bawendi, S. Gradečak, Nano Letters 11 (2011) 3998-4002.

[71] W.U. Huynh, J.J. Dittmer, A.P. Alivisatos, Science 295 (2002) 2425-2427.

[72] H. Moreno-García, M.T.S. Nair, P.K. Nair, Thin Solid Films 519 (2011) 2287-2295.

[73] K. Ramanathan, M.A. Contreras, C.L. Perkins, S. Asher, F.S. Hasoon, J. Keane, D. Young, M. Romero, W. Metzger, R. Noufi, J. Ward, A. Duda, Progress in Photovoltaics: Research and Applications 11 (2003) 225-230.

[74] J. Hernández-Borja, Y.V. Vorobiev, R. Ramírez-Bon, Solar Energy Materials and Solar Cells 95 (2011) 1882-1888.

[75] S.A. McDonald, G. Konstantatos, S. Zhang, P.W. Cyr, E.J.D. Klem, L. Levina, E.H. Sargent, Natural Materials 4 (2005) 138-142.

[76] M. Bruchez Jr, M. Moronne, P. Gin, S. Weiss, A.P. Alivisatos, Science 281 (1998) 2013-2016.

[77] W.C.W. Chan, S.M. Nie, Science 281 (1998) 2016-2018.

[78] P.O. Anikeeva, J.E. Halpert, M.G. Bawendi, V. Bulović, Nano Letters 9 (2009) 2532 2536.

[79] V.L. Colvin, M.C. Schlamp, A.P. Alivisatos, Nature 360 (1994) 354-357.

[80] P.T. Guerreiro, S. Ten, N.F. Borrelli, J. Butty, G.E. Jabbour, Applied Physics Letters 71 (1997) 1595-1597.

[81] V.I. Klimov, A.A. Mikhailovsky, S. Xu, A. Malko, J.A. Hollingsworth, C.A Leatherdale, H.J. Eisler, M.G. Bawendi, Science 290 (2000) 314-317.

[82] X.F. Duan, C.M. Niu, V. Sahi, J. Chen, J.W. Parce, S. Empedocles, J.L Goldman, Nature 425 (2003) 274-278.

[83] A.L. Linsebigler, G. Lu , J. T. Yates, Chemical Reviews 95 (1995) 735-758.

[84] X. Chen, W. Shangguan, Frontiers in Energy 7 (2013) 111-118.

[85] I. Gur, N.A. Fromer, M.L. Geier, A.P.livisatos, Science 310 (2005) 462- 465

[86] C. Tura, N. Coombs, O. Dag, Chemistry of Materials 17 (2005) 573-579.

[87] Y. Zhang, Y. Chen, H. Niu, M. Gao, Small 2 (2006) 1314-1319.

[89] W. Xu, D.L. Akins, Materials Letters 58 (2004) 2623-2626. 90 L. Chen, Y.B. Chen, L.M. Wu, Journal of American Chemical Society 126 (2004) 16334-16335.

[90] Y.Zhao, X-H. Liao J.M, Hong J-J. Zhu, Materials Chemistry Physics 87 (2004) 149-153.

[91] T Ding, J-J. Zhu, Materials Science and Engineering B 100 (2003) 307- 313.

[94] V.L. Colvin, M.C. Schlamp, A.P. Alivisatos, Nature 360 (1994) 354-357.

[95] M.A. Hines, G.D. Scholes, Advanced Materials 15 (2003) 1844-1849.

[96] T. Kuzuya, S. Yamamuro, T. Hihara, K. Sumiyama, Chemistry Letters 33 (2004) 352-353.

[97] J.H. Yu J. Joo, H.M. Park, S.-I. Baik, Y.W. Kim, S.C. Kim, T. Hyeon, Journal of American Chemical Society 127 (2005) 5662-5670.

[98]. S.-H. Choi, K. An, E.-G. Kim, J.H. Yu, J.H. Kim, T. Hyeon, Advanced Functional Materials 19 (2009) 1645-1649.

[99] G. Li, C. Li, H. Tang, K. Cao, J. Chen, Materials Research Bulletin 46 (2011) 1072-1079. 31.

[100] G.Q. Xu, B. Liu, S.J. Xu, C.H. Chew, S.J. Chua, L.M. Gana, Journal of Physics and Chemistry of Solids 61 (2000) 829-836.

[101] C.B. Murray, D.J Norris, M.G. Bawendi, Journal of American Chemical Society 115 (1993) 8706-8715.

[102] Wikipedia, freeze-drying, July 18, 2015, 104

[103] S. T. Aruna, S. Tirosh and A. Zaban, Journal of materials chemistry, 31 August 2000

[105] H Zhang and J.F Banfield, J of Phys. chem B. 2000,

[106] M.Giarola. .A.Sanson, F.Monti and G.Marriotto Physical Rev.B 81, 174305 (2010)

[107] Xuang Liu, P.K.Chu, Chuanxian Ding, Mat. science and Eng.R47 (20004), 49-121

[108] V.Gombac, LRogatis, A. Gasparotto, G.Vacario, T.Montini, D.Barreca, G.Balducci, P.Fornasiero, E.Tondello, M.Graziani, Chemical Physics 339 (2007) 111-123

[109] X. Michalet, F. F. Pinaud, L. A. Bentolila, J. M. Tsay1, S. Doose, J. J. Li1, G. Sundaresan, A. M. Wu, S. S. Gambhir, and S. Weiss, Science. 2005 January 28; 307(5709): 538–544.

[110] B. Mahltig, H. Bottcher, K. Rauch, U. Dieckmannb, R. Nitsche, T. Fritz. Thin Solid Films 485 (2005) 108 – 114

[111] AWa´skowska, LGerward, J Staun Olsen, M Feliz, R Llusar, L Gracia, MMarq´ues, and J M Recio. J. Phys.: Condens. Matter 16 (2004) 53–63

[112] Sabriye Pişkin, Arzu Palantöken, and Müge Sari Yılmaz. International Conference on Emerging Trends in Engineering and Technology (ICETET'2013) Dec. 7-8, 2013 Patong Beach, Phuket (Thailand)

[114] Gopal K. Mor, Maria A. Carvalho, Ooman K. Varghese, Michael V. Pishko, Craig A. Grimes, J. Mater. Res., Vol. 19, No. 2, Feb 2004

[115] R. Asahi and Y. Taga PHYSICAL REVIEW B VOLUME 61, NUMBER 11 15 MARCH 2000-

[117 Julian Haines and J.M. Leger Physica B 192 (1993) 233-237

[118] Yenting Kuo, Clint D. Frye, Myles Ikenberry, and Kenneth J. Klabunde

[119] Kuo, Y., Frye, C. D., Ikenberry, M., & Klabunde, K. J. (2013), Catalysis Today, 199, 15-21.

[120] Uniheidelberg, catalysis group, l Seiyama, scientific communication, Analytical Chemistry, VOL. 34, NO. 1 Oct 1962

[123] Naoyoshi Taguchi, 1-2 Ikedauemachi, Nagata-ku, Kobe, Japan, Filed Apr. 7, 1970, Ser. No. 26,228

[124] V. T. Karathanos, S. A. Anglea & M. Karel, Journal of thermalanalysis volume 47, pages1451–1461(1996).

[125] H.Tang, K.Prasad, R. Sanjines, P.E.Schmid, j.of Applied Physics, 2042(1994)

[126] L.Sang-Gi, L.Sangwha, Applied catalysis A: General vol.207(1-2) pp 173 – 181 (2001)

[127] T.Verdier, M.Coutand, A.Berton and C.Rogues, Coatings 2014, 4, pp 670 – 686

[128] T. Ojha, V.Pathak, N.Drude, M.Weilerm D.Rommel, I. Lammers

[129] P. Ramminger, R. Tessadri, R. Krismer, P. Wilhartitz, International Planse Seminar, vol.4, Reutte, 2001.

APPENDICES

Appendix I:

Results in Physics 9 (2018) 628–635

Contents lists available at ScienceDirect

Results in Physics

journal homepage: www.journals.elsevier.com/results-in-physics

Strain and grain size of TiO_2 nanoparticles from TEM, Raman spectroscopy and XRD: The revisiting of the Williamson-Hall plot method

Pierre M. Kibasomba [a,b,c,d], Simon Dhlamini [c], Malik Maaza [a,d], Chuan-Pu Liu [e], Mohamed M. Rashad [f], Diaa A. Rayan [f], Bonex W. Mwakikunga [b,*]

[a] Department of Physics, Florida Research Centre, University of South Africa, Florida, South Africa
[b] DST/CSIR-National Centre for Nano-Structured Materials, PO Box 395 Pretoria, South Africa
[c] UNESCO-UNISA Africa Chair in Nanosciences/Nanotechnology, College of Graduate Studies, University of South Africa, Muckleneuk Ridge, P.O. Box 392, Pretoria, South Africa
[d] Nanosciences African Network (NANOAFNET), iThemba LABS-National Research Foundation, 1 Old Faure Road, Somerset West 7129, P.O. Box 722, Somerset West, Western Cape Province, South Africa
[e] Materials Science and Engineering, National Cheng Kung University, 1 University Rd, Tainan, Taiwan
[f] Centre for Metallurgical Research and Development Institute, (CMRDI), P.O. Box 87, Helwan, Cairo 11421, Egypt

ARTICLE INFO

Article history:
Received 9 December 2017
Received in revised form 1 March 2018
Accepted 3 March 2018
Available online 16 March 2018

Keywords:
Williamson-Hall
Scherrer
Particle
Crystallite
Strain
Size

ABSTRACT

The Williamson-Hall (W-H) equation, which has been used to obtain relative crystallite sizes and strains between samples since 1962, is revisited. A modified W-H equation is derived which takes into account the Scherrer equation, first published in 1918, (which traditionally gives more absolute crystallite size prediction) and strain prediction from Raman spectra. It is found that W-H crystallite sizes are on average 2.11 ± 0.01 times smaller than the sizes from Scherrer equation. Furthermore the strain from the W-H plots when compared to strain obtained from Raman spectral red-shifts yield factors whose values depend on the phases in the materials – whether anatase, rutile or brookite. Two main phases are identified in the annealing temperatures (350 °C–700 °C) chosen herein – anatase and brookite. A transition temperature of 550 °C has been found for nano-TiO_2 to irreversibly transform from brookite to anatase by plotting the Raman peak shifts against the annealing temperatures. The W-H underestimation on the strain in the brookite phase gives W-H/Raman factor of 3.10 ± 0.05 whereas for the anatase phase, one gets 2.46 ± 0.03. The new $\beta^2_{tot}\cos^2\theta$-$\sin\theta$ plot and when fitted with a polynomial yield less strain but much better matching with experimental TEM crystallite sizes and the agglomerates than both the traditional Williamson-Hall and the Scherrer methods. There is greater improvement in the model when linearized – that is the $\beta_{tot}\cos^2\theta$-$\sin\theta$ plot rather than the $\beta^2_{tot}\cos^2\theta$-$\sin\theta$ plot.

Introduction

Background

Comparing methods that determine particle size in nanocrystalline powders is ongoing as long as the problem of small particles remains unsolved [1]. A large chunk of research work points to the fact that the Williamson-Hall is more accurate, but over-estimate by ±35%, than the Scherrer method, worked out an improved Scherrer method on the basis of line width in the Scherrer equation and matched the calculation of W-H [2]. However, other research have shown that W-H underestimates by ±14% the particle size as compared to Scherrer, of which the correlation was confirmed with TEM [3].

The Williamson-Hall (W-H) method for crystallite size and strain analysis is still under-utilized as compared to the Scherer method, and yet it is more accurate and offers a greater benefit, the possibility of calculating, a very important material properties, in particular, structural parameter, the strain (ε), and phase composition. The W-H equation was derived in 1953 which was an improvement on the P. Scherrer (P-S) equation developed earlier before 1918 [4].

This W-H method is attributed to G.K. Williamson and his student, W.H. Hall [5]. It relies on the principle that the approximate formulae for size (Scherrer) broadening, β_L, and strain broadening, β_ε, vary quite differently with respect to Bragg angle, θ:

* Corresponding author.
E-mail address: bmwakikunga@csir.co.za (B.W. Mwakikunga).

https://doi.org/10.1016/j.rinp.2018.03.008
2211-3797/

$$\beta_L = \frac{K\lambda}{L\cos\theta}; \beta_e = C\varepsilon\tan\theta \quad (1)$$

One contribution varies as 1/cosθ and the other as tanθ. If both contributions are present then their combined effect should be determined by convolution. The simplification of Williamson and Hall is to assume the convolution is either a simple sum or sum of squares. Using the former of these then one gets:

$$\beta_{tot} = \beta_L + \beta_e = C\varepsilon\tan\theta + \frac{K\lambda}{L\cos\theta} \quad (2)$$

If one multiplies this equation by cosθ one gets:

$$\beta_{tot}\cos\theta = C\varepsilon_{W-H}\sin\theta + \frac{K\lambda}{D_{W-H}} \quad (3)$$

where $D_{W\text{-}H}$ is the grain size as determined from the Williamson-Hall plot. Comparing this to the standard equation for a straight line (m = slope; c = intercept), y = mx + c, one sees that by plotting $\beta_{tot}\cos\theta$ versus $\sin\theta$ we obtain the strain component from the slope ($C\varepsilon$) and the size component from the intercept ($K\lambda/L$) or $K\lambda/D_{W\text{-}H}$. Such a plot is known as a Williamson-Hall plot. It can be a good idea to label each data point on the Williamson-Hall plot according to the index of its reflection to see whether any pattern emerges. It has been stated [6], however, that the Williamson-Hall method, owing to its many assumptions, should not be taken too seriously in terms of its absolute values but it can be a useful method if used in the relative sense; for example a study of many powder patterns of the same chemical compound, but synthesised under different conditions, might reveal trends in the crystallite size/strain which in turn can be related to the properties of the product.

It must be noted that there have been other proposals down through history on how to calculate the crystallite size from XRD data. One of them is the Halder-Wagner (HW) method given [7,8] by

$$\left(\frac{\beta_{tot}\cos\theta}{\sin\theta}\right)^2 = \frac{K\lambda}{D_{HW}}\cdot\frac{\beta_{tot}\cos\theta}{\sin^2\theta} + 16\varepsilon_{HW}^2 \quad (4)$$

where D_{HW} and ε_{HW} are Halder-Wagner crystallite size and strain respectively. Here, when a plot of $\left(\frac{\beta_{tot}\cos\theta}{\sin\theta}\right)^2$ is made against $\frac{\beta_{tot}\cos\theta}{\sin^2\theta}$ then a straight line graph of slope $\frac{K\lambda}{D_{HW}}$ and intercept $16\varepsilon_{HW}^2$ is obtained. Here, the slopes yield the Halder-Wagner crystallite size, D_{HW}, while the intercept gives the Halder-Wagner strain, ε_{HW}. However, the Halder-Wagner method is known be somewhat limited when compared to the Williamson-Hall method. When WH and HW methods were compared to some CeO_2 sample of pre-known average crystallite size 32 nm and strain 0.4(9)%, the WH method yielded the crystallite size of 29 nm whereas the HW method gave about 28 nm. Also, the WH yielded a strain of 0.4957% whereas the HW gave a strain value of 0.07682% [9–11]. Therefore it was reported that the HW method performed poorer than the WH method.

Current derivation of the new strain-crystallite-size equation

The intent of this paper is to report on the progress from post-Scherrer and post-W-H attempt to make the W-H equation accurate and more absolute than before. We do this by scaling the W-H crystallite size ($D_{W\text{-}H}$) against the more trusted Scherrer crystallite size (D_S). If we assume a linear proportionality between $D_{W\text{-}H}$ and D_S then we can write:

$$D_{W-H} = (D_{W-H})_0 + \alpha_{W-H-S}D_S = (D_{W-H})_0 + \alpha_{W-H-S}\frac{K\lambda}{\beta_{tot}\cos\theta} \quad (5)$$

Our second argument is that if the crystallite size by the W-H is not to be trusted as stated in Ref. [6], then it is difficult to conclude that the strain obtained from the same W-H method, $\varepsilon_{W\text{-}H}$ is accurate enough. This is the second reason for the need for a revision of the W-H method.

There are other more trusted methods for obtaining strain from crystallites. These include nano-indentation [12–13], red- or blue-shift of some phonons measured by either Raman spectroscopy [15–18] or FTIR [14–15] and high pressure anvil cell coupled to optical spectroscopic systems such as UV–Vis-IR spectrophotometer [16] and high pressure XRD and Raman spectroscopy [17–24]. As for Raman spectroscopy, the relationship between red- or blue-shift ($\Delta\omega$) of the phonon peaks and the tensile strain or compressive strain, ε_R, in the nano-crystals respectively is given by [14]

$$\omega = \omega_0\left(1 - \frac{a+r+3}{2}\varepsilon_R\right) \quad (6)$$

where a and r are constants to govern the attractive, a, and repulsive, r, exponents in the potential $V(l_b)$ of each bond; here, l_b is the length of the bond. [In order to shed more light on the potential $V(l_b)$ of the bond, the potential as a function of the bond length l_b is given as an additive sum of the repulsive component (A/l_b^a) and an attractive component ($-B/l_b^r$) as $V(l_b) = (A/l_b^a) - (B/l_b^r)$]. The values of a and r are 6 and 12 for a van der Waal's bonding according to Leornad-Jones potential, 1 and 9 for ionic bonding and have a sum (a + r) of 3 for a covalent bonding [14]. The bonding in TiO_2 cannot be van der Waals nor ionic; therefore it is taken in this paper to be covalent and therefore we can express the relation between the new phonon frequency and the bulk frequency to

$$\omega = \omega_0\left(1 - \frac{3+3}{2}\varepsilon_R\right) = \omega_b(1 - 3\varepsilon_R) \quad (7)$$

Furthermore, if $\varepsilon_{W\text{-}H}$ and ε_R scale linearly with each other, then one can write:

$$\varepsilon_{W-H} = (\varepsilon_{W-H})_0 \pm \gamma\varepsilon_R \quad (8)$$

Since the traditional Williamson-Hall strain, $\varepsilon_{W\text{-}H}$, is an underestimated value, one then chooses the + rather than the − in Eq. (8). Therefore the new strain, ε', is

$$\varepsilon' = (\varepsilon_{W-H})_0 + \gamma\varepsilon_R \quad (9)$$

Then one can derive a new equation from the Williamson-Hall by substituting Eqs. (4)-(7) into Eq. (3) as follows:

$$\beta_{tot}\cos\theta = C\varepsilon'\sin\theta + \frac{K\lambda}{(D_{W-H})_0 + \alpha_{W-H-S}\frac{K\lambda}{\beta_{tot}\cos\theta}} \quad (10)$$

This means that a plot of $\beta_{tot}\cos\theta$ versus $\sin\theta$ will not give a linear plot assumed by Williamson and Hall in 1962. Indeed further analysis of Eq. (10) yields:

$$\begin{aligned}
&\beta_{tot}\cos\theta\left[(D_{W-H})_0 + \alpha_{W-H-S}\frac{K\lambda}{\beta_{tot}\cos\theta}\right] \\
&= C\varepsilon'\sin\theta\left[(D_{W-H})_0 + \alpha_{W-H-S}\frac{K\lambda}{\beta_{tot}\cos\theta}\right] \\
&\quad + K\lambda(D_{W-H})_0\beta_{tot}\cos\theta + \alpha_{W-H-S}K\lambda \\
&= (D_{W-H})_0 C\varepsilon'\sin\theta + \\
&\Rightarrow C\varepsilon'\sin\theta\alpha_{W-H-S}\frac{K\lambda}{\beta_{tot}\cos\theta}\left[(D_{W-H})_0 + \alpha_{W-H-S}\frac{K\lambda}{\beta_{tot}\cos\theta}\right] + K\lambda \\
&\Rightarrow \beta_{tot}\cos\theta(D_{W-H})_0 + \alpha_{W-H-S}\frac{K\lambda}{\beta_{tot}\cos\theta} \\
&= C\varepsilon'\sin\theta\left[(D_{W-H})_0 + \alpha_{W-H-S}\frac{K\lambda}{\beta_{tot}\cos\theta}\right] + K\lambda
\end{aligned} \quad (11)$$

or

$$\beta_{tot}^2\cos^2\theta(D_{W-H})_0 + \alpha_{W-H-S}K\lambda = C\varepsilon'\beta_{tot}\cos\theta\sin\theta\left[(D_{W-H})_0 + \alpha_{W-H-S}\frac{K\lambda}{\beta_{tot}\cos\theta}\right] + K\lambda\beta_{tot}\cos\theta \quad (11a)$$

$$\Rightarrow (D_{W-H})_0\beta_{tot}\cos\theta + \alpha_{W-H-S}K\lambda = (D_{W-H})_0C\varepsilon'\sin\theta + C\varepsilon'\alpha_{W-H-S}\frac{K\lambda\sin\theta}{\beta_{tot}\cos\theta} + K\lambda$$

$$\Rightarrow (D_{W-H})_0\beta_{tot}^2\cos^2\theta + \alpha_{W-H-S}K\lambda\beta_{tot}\cos\theta = (D_{W-H})_0C\varepsilon'\beta_{tot}\cos\theta\sin\theta + C\varepsilon'\alpha_{W-H-S}K\lambda\sin\theta + K\lambda\beta_{tot}\cos\theta$$

$$\Rightarrow (D_{W-H})_0\beta_{tot}^2\cos^2\theta + (\alpha_{W-H-S}-1)K\lambda\beta_{tot}\cos\theta = (D_{W-H})_0C\varepsilon'\beta_{tot}\cos\theta\sin\theta + C\varepsilon'\alpha_{W-H-S}K\lambda\sin\theta$$

$$\Rightarrow (D_{W-H})_0\beta_{tot}^2\cos^2\theta = (D_{W-H})_0C\varepsilon'\beta_{tot}\cos\theta\sin\theta + C\varepsilon'\alpha_{W-H-S}K\lambda\sin\theta - (\alpha_{W-H-S}-1)K\lambda\beta_{tot}\cos\theta \quad (11b)$$

If one uses the trigonometric identities of $\cos^2\theta+\sin^2\theta=1$, one gets

$$(D_{W-H})_0\beta_{tot}^2\cos^2\theta = (D_{W-H})_0C\varepsilon'\beta_{tot}(1-\sin^2\theta)^{\frac{1}{2}}\sin\theta + C\varepsilon'\alpha_{W-H-S}K\lambda\sin\theta - (\alpha_{W-H-S}-1)K\lambda\beta_{tot}(1-\sin^2\theta)^{\frac{1}{2}} \quad (12)$$

And after expanding the binomial series and neglecting the higher terms, one gets

$$(D_{W-H})_0\beta_{tot}^2\cos^2\theta = (D_{W-H})_0C\varepsilon'\beta_{tot}\left(1-\frac{1}{2}\sin^2\theta\right)\sin\theta + C\varepsilon'\alpha_{W-H-S}K\lambda\sin\theta - (\alpha_{W-H-S}-1)K\lambda\beta_{tot}\left(1-\frac{1}{2}\sin^2\theta\right) \quad (13)$$

And further simplification and re-arrangement yields

$$(D_{W-H})_0\beta_{tot}^2\cos^2\theta = -(D_{W-H})_0C\varepsilon'\beta_{tot}\frac{1}{2}\sin^3\theta + \frac{1}{2}(\alpha_{W-H-S}-1)K\lambda\beta_{tot}\sin^2\theta + [(D_{W-H})_0C\varepsilon'\beta_{tot} + C\varepsilon'\alpha_{W-H-S}K\lambda]\sin\theta - (\alpha_{W-H-S}-1)K\lambda\beta_{tot} \quad (14a)$$

$$\beta_{tot}^2\cos^2\theta = a\sin^3\theta + b\sin^2\theta + c\sin\theta + d \quad (14b)$$

The implication of this equation is that a plot of $\beta_{tot}^2\cos^2\theta$ versus $\beta_{tot}\sin\theta$ is a non-linear curve which describes a cubic polynomialy $= ax^3 + bx^2 + cx + d$ where

$$a = \frac{-\frac{1}{2}(D_{W-H})_0C\varepsilon'}{(D_{W-H})_0};\quad b = \frac{\frac{1}{2}(\alpha_{W-H-S}-1)K\lambda}{(D_{W-H})_0};\quad c = \frac{[(D_{W-H})_0C\varepsilon' + C\varepsilon'\alpha_{W-H-S}K\lambda]/\beta_{tot}}{(D_{W-H})_0};\quad d = \frac{-(\alpha_{W-H-S}-1)K\lambda}{(D_{W-H})_0}$$

or

$$a = -\frac{1}{2}C\varepsilon';\quad b = \frac{\frac{1}{2}(\alpha_{W-H-S}-1)K\lambda}{(D_{W-H})_0};\quad c = C\varepsilon' + \frac{C\varepsilon'\alpha_{W-H-S}K\lambda}{\beta_{tot}(D_{W-H})_0};\quad d = \frac{-(\alpha_{W-H-S}-1)K\lambda}{(D_{W-H})_0}$$

This means that the new strain, ε', is found from the coefficient of the $\sin^3\theta$ and the new particle size from intercept as well as from the coefficient of $\sin^2\theta$.

Therefore, the new strain is found from the intercept of the cubic polynomial as follows:-

$$\varepsilon' = \frac{-2a}{C} = -\frac{1}{2}a \quad (15)$$

And the Williamson-Hall to Scherrer parameter, α_{W-H-S}, and the threshold particle size, $(D_{W-H})_0$ are found by solving the equations for b and d simultaneously and the simplification lead to:

$$\alpha_{W-H-S} = \frac{2b}{d+2b} + \frac{1}{K\lambda} \quad (16)$$

and

$$(D_{W-H})_0 = \frac{K\lambda}{d+2b} \quad (17)$$

The main task in this theory is to transform the β_{tot}-θ data into a plot of $\beta_{tot}^2\cos^2\theta$ against $\sin\theta$ rather than the traditional $\beta_{tot}\cos\theta$ against $\sin\theta$ plot and fit Eq. (14) to this plot and extract coefficients a, b, c, and d. Coefficient a is used to find the strain in the sample and coefficients b and d contain information on particle size.

The second option is to linearize Eq. (14). This is accomplished by neglecting the higher powers of $\sin\theta$ and then reducing Eq. (14) to

$$\beta_{tot}\cos^2\theta \cong C\varepsilon'\left[1+\frac{\alpha_{W-H-S}K\lambda}{\beta_{tot}(D_{W-H})_0}\right]\sin\theta - \frac{(\alpha_{W-H-S}-1)K\lambda}{(D_{W-H})_0} \quad (18)$$

where the slope is equal to $C\varepsilon'\left[1+\frac{\alpha_{W-H-S}K\lambda}{\beta_{tot}(D_{W-H})_0}\right]$. This means that the new strain ε' is further increased by a factor of $\frac{\alpha_{W-H-S}K\lambda}{\beta_{tot}(D_{W-H})_0}$. Also the intercept which is equal to $\frac{(\alpha_{W-H-S}-1)K\lambda}{(D_{W-H})_0}$ is used to calculate the crystallite size. We will leave to the reader to find out that the strain comes close to the much trusted Raman strain and, similarly, the particle or crystallite size comes down to the values of crystallites sizes obtained from TEM imaging.

Experimental details

Two samples were used in the experiment: the first sample, Ti-iso-2-450, the lyophilized sample. We refer to it as temperature programmed synthesis TiO_2 from isopropoxide precursor at fixed pH value. The second, P-25 Degussa, the commercial TiO_2, mainly composed of anatase (99.2%).

The TiO_2 nanoparticles were synthesized by a multi-step, adapted version of the lyophilization technique. 1.0 g of titanium isopropoxide was dissolved in 150 ml of distilled water and brought to a pH of 7. The solution was sprayed "laminar regime" into liquid nitrogen in order to generate droplets rich in water (~90%). These droplets were then sublimated in a lyophiliser chamber to yield a very porous precursor. The precursor was then thermally decomposed at 450 °C in air for about 1 h to form TiO_2 nanoparticles.

For the study of the particle size and strain evolution of TiO_2, a set of samples of nanoparticles with discrete sizes was required. Samples Ti-iso-2-450, Ti-iso-550, Ti-iso-2-650, Ti-iso-2-700 and Ti-iso-900 were prepared by starting heating the amorphous titania in air for 1 h at 350 °C, 400°, 450 °C, 550 °C, 650 °C and 700 °C respectively.

The X-ray diffraction patterns of the film were measured at room temperature using the Panalytical XPERT PRO PW3050/50 diffractometer with CuKα radiation (45 kV, 400 mA, λ = 0.1540598 nm and $5° \le 2\theta \le 90°$). And the spectra were analysed with reference to Refs. [21–32]. The Auriga ZEISS Scanning electron microscope (SEM) was employed to study the morphology of the film and to estimate the thickness of oxide layers that are present.

Raman spectroscopy was carried out using a Jobin–Yvon T64000 Raman spectrograph with a 514.5 nm line from an argon ion laser. The power of the laser at the sample at the post-annealed samples was small enough (0.384 mW) in order to minimise localised heating of the sample. The T64000 was operated in single spectrograph mode, with the 1800 lines/mm grating and three objective lenses on the microscope with the following magnifications: 20×, 50× and 100×. Strain values for each samples were obtained by employing Eq. (6).

The samples were further characterized using high resolution TEM (HRTEM, JOEL-JEM 2100).

Results and discussion

Transmission electron microscopy (TEM) revealed 10–20 nm rounded and also faceted anatase nano-crystallites, Fig. 1. TEM studies of the sample Ti-iso-700 indicated an oriented-aggregation crystal growth pathways (Fig. 1).

Along this pathway, whereby small crystals grow differently from larger crystals, the small crystals aggregate in such a way that the adjacent surfaces share the same crystallographic orientation. In the process, the pair of adjacent interfaces are eliminated and the pair of nanoparticles are converted to a larger single-crystal. Due to this aggregation, the final particle size may reach large particle size up to 80 nm. Energy dispersive X-ray (EDS) measurements (not shown) conducted on these nanoparticles confirmed the TiO_2 stoichiometric composition of lyophilized anatase (sample Ti-iso-2-700) or comparison, a TEM micrograph of Degussa P25 is given in Fig. 1(b). Both spherical and faceted considerably larger particles, typically varying in size from 50 to 250 nm, have been seen compared to the sample made by the lyophilization technique.

The X-ray diffraction analysis was completed on the lyophilized samples Ti-iso-2 nanopowders, using the diffractometer with a Cu-Kα target (wavelength λ = 0.15409 nm). The experiment was ran from angle of 10° to angle of 70°, at 0.0333° step.

Fig. 2(a) summarizes the results from XRD analysis of the five annealed samples – 350, 450, 550, 650 and 700 °C. It can be observed that the (1 0 1) direction is the most preferred orientation and this direction is enhanced as the annealing temperature is raised. There are more crystallite planes which are maintained regardless of annealing temperature which indicates the polycrystallinity of the samples as well as the fact that there more than one phase in the materials.

Raman spectra of the same samples given in Fig. 2(b) reveal the preferred phonon of 150 cm^{-1} which is an indication of anatase phase. The phonon frequency (wavenumber) position is however observed to change and shift to lower wavenumbers as demonstrated by a dotted line in Fig. 2(b) showing that the annealing causes a strain in the crystallites. Since redshift is confirmed suggests that the strain is tensile in accordance with Eq. (5) in the previous sections.

Particle size and strain calculation

The average crystallite size was estimated using Scherer size and compared to the one found using Williamson-Hall method, and the strain was only estimated from the W-H method (plotting $\beta_{tot}\cos\theta$ against $\sin\theta$) as well as the Raman strain values obtained from Fig. 2(b) via Eq. (6). For some of the samples, by plotting $\beta_{tot}\cos\theta$ against $\sin\theta$, we obtain a linear profile. Observing dots spread across the linear plot of $B_s\cos\theta$ versus $\sin\theta$, the distribution is typical detail displayed by substance that accounts for elastic deformation due to thermal stress, thus an average linear profile traced through the entire range requires a characteristic data validation. For some plots that are non-linear, one often ascribes this to multiple phases in the sample. However, the reader will see that this calls for a revision of the W-H plot to take into account these non-linearities as will be discussed in the upcoming sections.

The analysis of the XRD diffractograms by the Williamson-Hall (W-H) plot ($\Gamma\cos\theta = K\lambda/D + 4\varepsilon\sin\theta$) [29] and the Debye-Scherrer (D-S) equation ($(\Gamma\cos\theta = K\lambda/D)$ [30–46] have been achieved extensively before. Here, Γ is the full-width-at-half-maximum (FWHM) of the ith peak, θ is the angle at which the ith peak is found in radians, K is a constant for a given instrument alignment which usually about 0.9, λ is the wavelength of the X-rays employed which for this case the X-ray are from Cu K_α at 1.54 Å, D_S is the Scherrer crystallite size and ε is the strain.

Fig. 3 summarizes the analyses for crystallite sizes and strain calculations from XRD and Raman spectra of the five annealed samples. In Fig. 3(a) are summarized the phonon frequency shift of the 150 cm-1, crystallite size by Scherrer and W-H methods and strains from W-H method and Raman spectra. The phonon red-shift is evidence of tensile stress. The plot demonstrates a slight increase in the phonon wavenumber after 550 °C before it continues to decrease after 600 °C. Blue shifts at an annealing temperature of 550 °C suggest a change of phase which is a non-reversible transformation from anatase to brookite [30,32,33].

The phase changes signalled by phonon position and broadenings are more evident in the amplified Fig. 3(b) where these transition temperatures can be 570 °C when phonon peak positions are used but one can identify three phases with transition temperatures 450 [from anatase to brookite] and 650 °C [from

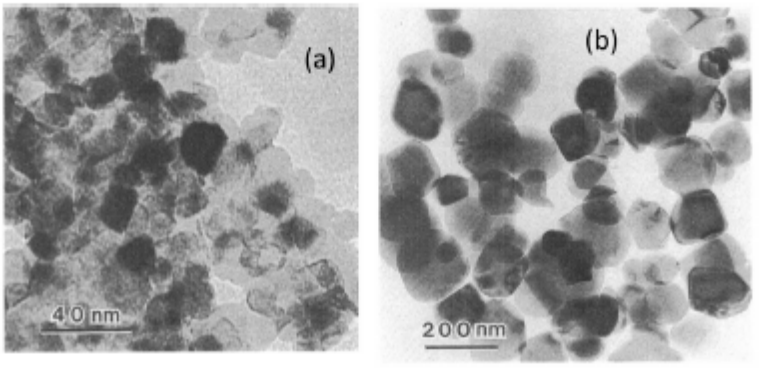

Fig. 1. (a) Lyophilized TiO_2 nanoparticles and annealed at 700 °C (b) Degussa P25 TiO_2 nanoparticles.

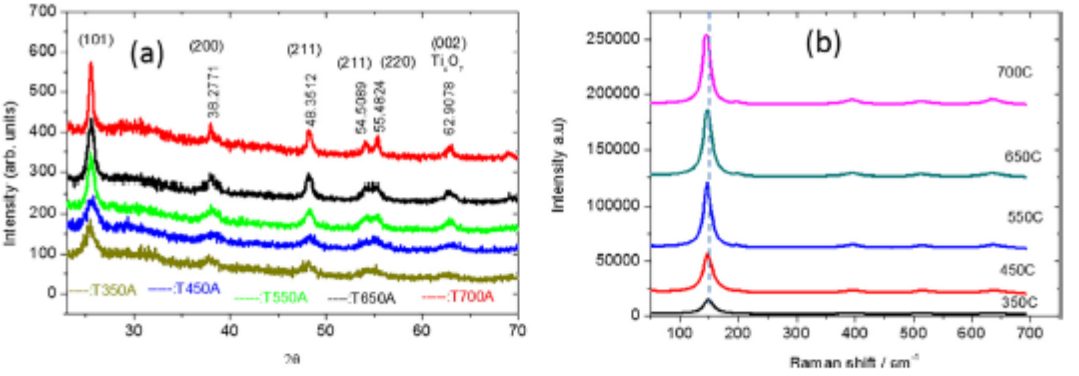

Fig. 2. (a) XRD diffractograms and (b) Raman spectra of the all lyophilized TiO_2 annealed at 350, 450, 550, 650 and 700 °C.

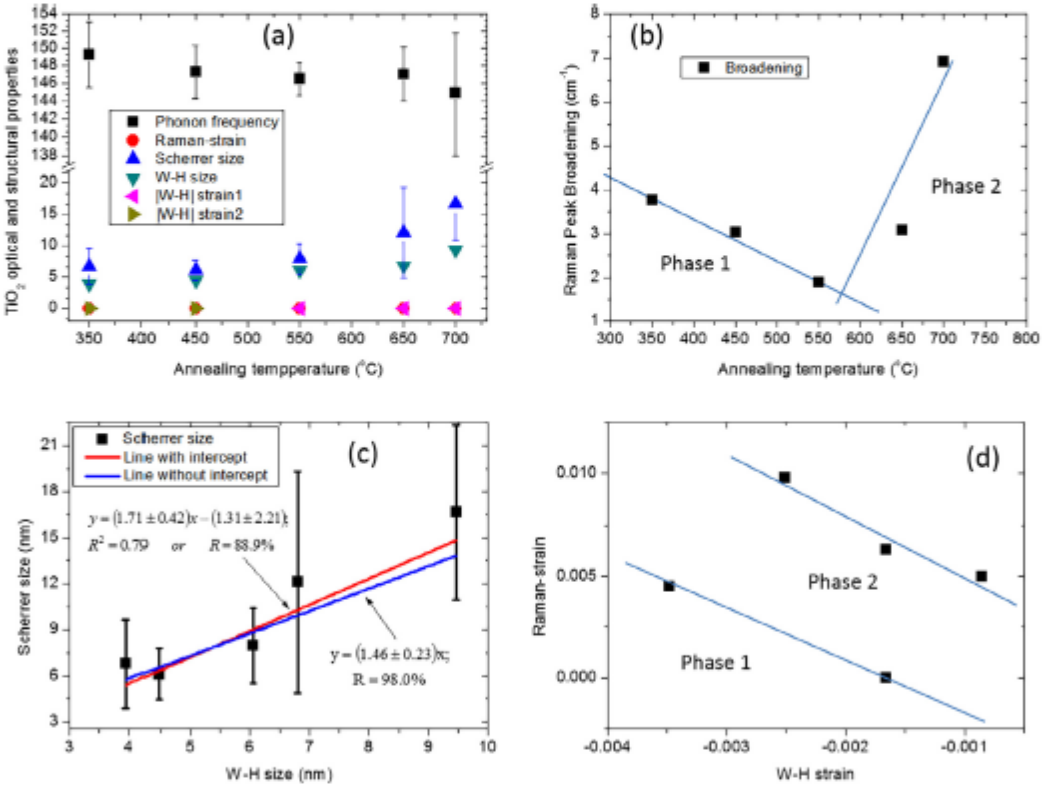

Fig. 3. (a) Williamson-Hall crystallite size (b) W-H strain/broadening versus annealing temperature with broadening-temperature plot revealing a transition temperature of 570 °C (c) Williamson-Hall crystallite size vs Scherrer crystallite size showing that Williamson-Hall plot underestimates crystallite size by 50% (d) Williamson-Hall strain vs Raman strain underestimates strain depending on whether it composite of all phases, or phase 1 only or phase 2 only by 170%, 31% and 25% respectively.

brookite to rutile] when strains calculated from W-H method as well as Raman spectra as shown by the dotted lines in Fig. 3(b). One also notes that again the strain values obtained from the W-H method are consistently less than those obtained from Raman spectral method.

The crystallite size by both methods increases with annealing temperature. However, the W-H method yields crystallite sizes consistently smaller than those obtained from the Scherrer method.

The observation that the traditional W-H method underestimates both the crystallite size and the strain value forced us to investigate the magnitude of these under-estimations. In Fig. 3 (c) we show a plot of Scherrer size, D_S, against the W-H size, $D_{W\text{-}H}$, which gives $D_S = (1.71 \pm 0.42)D_{W\text{-}H} - (1.31 \pm 2.21)$ when

intercept is considered. However, when the intercept is not considered then $D_S = (1.46 \pm 0.23)D_{W-H}$.

In Fig. 4(a) the Williamson-Hall plot shows that the TiO_2 sample annealed at 350 °C reveals non-linearity. This demonstrates that at such low temperatures, the TiO_2 has more than one phase in it as both positive and negative strains apparent from the plot which suggests non-homogeneity in the particles size as many intercepts on the y-axis are possible. At 450 °C the evidence of two distinct linear graphs emerge with two different strains. The two lines tend to point to one y-intercept which means homogeneity in particle. At 550 and 650 °C, the plot shows that the samples return to the 350 °C situation, only that there are two phases – one with positive strain and the other bearing a negative strain – are now more distinct. At 700 °C the two phases continue to exist conserving the crystallite sizes albeit with different strains.

As seen in Fig. 4(b) the modified W-H- method (plotting $\beta_{tot}^2\cos^2\theta$ against $\sin\theta$) was employed in the calculation of both new strain values and new particles sizes for the five samples annealed at different temperatures. This is accomplished by fitting the presently derived Eq. (14) or its shorthand in Eq. (15) and extracting the coefficients, a, b, c, and d in the cubic polynomial. Eqs. (15)–(17) are then employed in the calculation of the new strain, ε', the Williamson-Hall-to-Scherrer particles size parameter, α_{W-H-S}, the threshold particle size $(D_{W-H})0$ and hence the new particles size D'_{W-H}. Table 1 summarized all data discussed in this paper for the samples annealed at 350, 450, 550, 650, and 700 °C. One observes from the table, as also given in Fig. 3(a) that the W-H method gives the least particles sizes (from 1 nm to about 3 nm). This is followed by the Scherrer method which also slight underestimates the particle size and does not take into account any agglomerations. Although the new $\beta_{tot}^2\cos^2\theta$ - $\sin\theta$ method yields very small strains when compared to the more trusted Raman spectroscopy method, new method's threshold particles is much more closer to the particle sizes found from high resolution TEM than both the Williamson-Hall and the Scherrer sizes When the Scherrer factor is added to this threshold value, the new method then also accounts for agglomerates.

Further to the $(\beta_{tot}\cos\theta)^2$-$\sin\theta$ method discussed so far, it was important, in this study, to try the linear version of Eq. (14) i.e. the $\beta_{tot}\cos^2\theta$-$\sin\theta$ plot as suggested in Eq. (16). When a plot of $\beta_{tot}\cos^2\theta$ was made against $\sin\theta$, shown Fig. 4(c), and linear equations fitted to the data, the slopes and intercepts from this plot helped calculate the strains and crystallite sizes for the samples respectively. The data from such a fit are summarized in Table 2. The strains are in the order of 10-3 which one order of magnitude higher that in the cubic model or the $(\beta_{tot}\cos\theta)^2$-$\sin\theta$ method. The crystallite sizes are much higher than both the Scherrer and

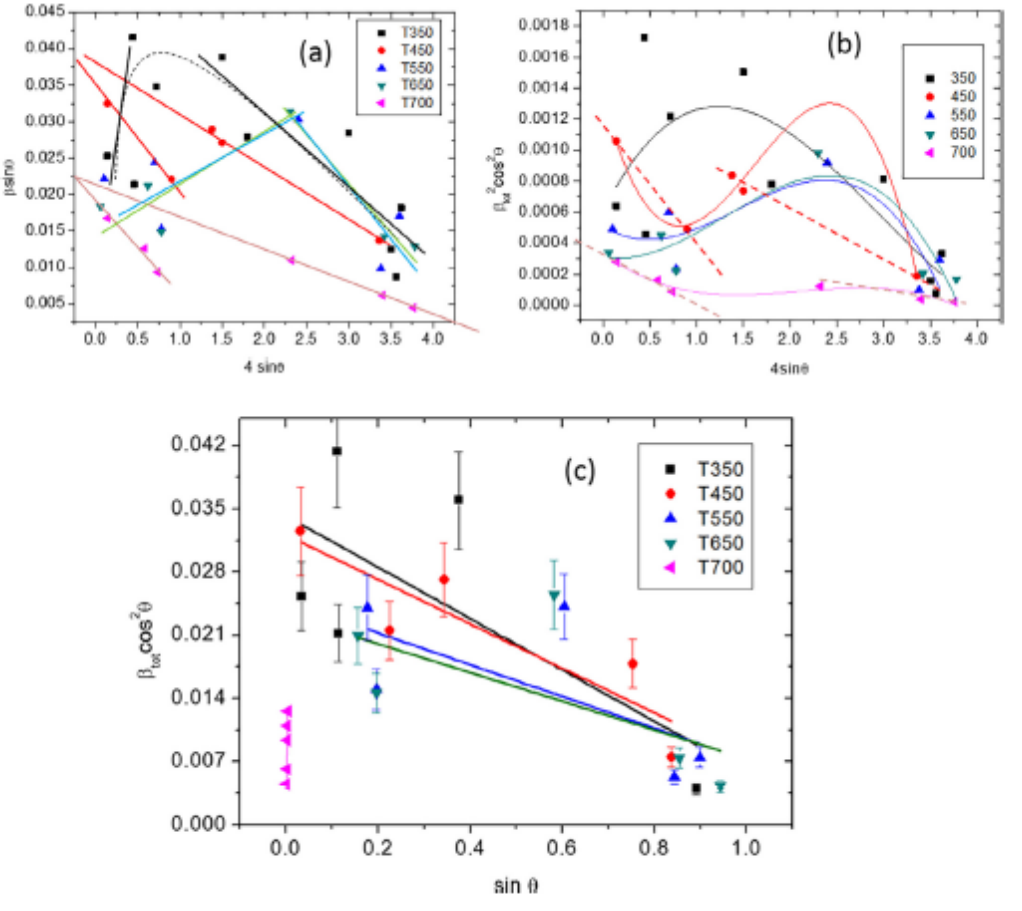

Fig. 4. (a) A Williamson-Hall plot of $\beta_{tot}\cos\theta$ against $C\sin\theta$ (where $C = 4$) calculated from XRD spectra for lyophilized TiO_2 samples annealed at 350, 450, 550, 650 and 700 °C.

Table 1
Summary of all data calculated from XRD data by Scherrer method (particle size D_S), the Williamson-Hall method (the particle size D_{W-H} and strain ε_{W-H}) the modified Williamson-Hall (the new threshold particles size $(D_{W-H})_b$ and the new particles size D'_{W-H}) and Raman spectroscopy analysis for strain ε_{Raman}.

Annealing T (°C)	D_S (nm)	D_{W-H} (nm)	ε_{W-H}	ε_{Raman}	a	a′	b	d	R^2	$(D_{W-H})_b$	D′
350	4.62 ± 1.06	2.2944	0.0493	0.153323	4.17E−04	2.09E−04	0.0075	0.00667	−0.66265	71.10752	80.85572
450	7.32 ± 5.14	2.5124	0.5907	1.837077	0.00126	6.30E−04	−0.00755	−0.02073	0.82836	43.0059	27.5607
550	5.25 ± 0.78	0.4479	0.41	1.2751	−0.00139	−6.95E−04	0.01375	0.01111	−0.51696	39.90935	50.98685
650	9.37 ± 1.28	2.6445	0.1914	0.595254	−5.68E−04	−2.84E−04	0.0067	0.00236	0.03677	97.77284	117.5435

Table 2
Summary of parameters extracted from the linearized demonstrating that a plot of $\beta_{tot}\cos^2\theta$-$\sin\theta$ method yields the new strain which are increased by a significant factor – about one order of magnitude higher than both the W-H and H-W method and the present $\beta^2_{tot}\cos^2\theta$-$\sin\theta$ method. This comes close to the desired accuracy as in the strains obtained by Raman spectroscopy. This also forced the crystallite size to approach the values obtained by HRTEM imaging.

Anneal T (°C)	D_S	Intercept	Slope	Mean grain size from TEM (nm)	ε	D_b (nm)	D′ (nm)
350	4.62	$34.22 \pm 7.56 \times 10^{-3}$	$-(28.43 \pm 1.72) \times 10^{-2}$	15	−0.00711	4.5	14.2
450	7.32	$32.1 \pm 3.83 \times 10^{-3}$	$-(24.61 \pm 0.72) \times 10^{-2}$	20	−0.00615	4.8	20.2
550	5.25	$24.77 \pm 6.82 \times 10^{-3}$	$-(1.757 \pm 1.09) \times 10^{-3}$	25	−0.00439	6.2	17.3
650	9.37	$23.22 \pm 6.84 \times 10^{-3}$	$-(1.588 \pm 1.08) \times 10^{-3}$	28	−0.00397	6.6	26.4

Williamson-Hall sizes and are in perfect agreement the HRTEM measured crystallite sizes.

Conclusion

We have introduced a revision of the Williamson-Hall equation. This was necessitated by the gross underestimation of the crystallite sizes worse than the Scherrer formula. When compared to TEM crystallite sizes, we found that Scherrer sizes are also slightly less, withn experimental error, than the TEM sizes. The revision was accomplished through the expansion of the W-H equation into a full polynomial equation which after further binomial expansion via some trigonometric identities reduced to a cubic polynomial. The main task in this theory is to transform the β_{tot}-θ data into a plot of $\beta^2_{tot}\cos^2\theta$ against $\sin\theta$ rather than the traditional $\beta_{tot}\cos\theta$ against $\sin\theta$ plot and fit Eq. (14) to this plot and extract coefficients a, b, c, and d. Coefficient a is use to find the strain in the sample and coefficients b and d contain information on particle size. Although the our $\beta^2_{tot}\cos^2\theta$-$\sin\theta$ method yields strain values are surprisingly very small when compared to the more trusted Raman spectroscopy method, new method's threshold particles is much more closer to the particle sizes found from high resolution TEM than both the Williamson-Hall and the Scherrer sizes When the Scherrer factor is added to this threshold value, the new method then also accounts for agglomerates as the particles size in the current results set range in hundreds of nanometers. It has been shown that when the current model is linearized – $\beta_{tot}\cos^2\theta$-$\sin\theta$ method- the new strain is increased by a significant factor – about one order of magnitude higher than the $\beta^2_{tot}\cos^2\theta$-$\sin\theta$ method and coming close to the desired accuracy as in the strains obtained by Raman spectroscopy. This also forced the crystallite size to approach the values obtained by TEM imaging.

Acknowledgements

The sponsorships of the South Africa-Taiwan Bilateral Programme (HGER31X) and the South Africa- Egypt Bilateral Programme (HGER40X) through the National Research Foundation (NRF) in Pretoria, South Africa are highly acknowledged.

References

[1] Gonçalves NS, Carvalho JA, Lima ZM, Sasaki JM. Size-strain study of NiO nanoparticles by X-ray powder diffraction line. Mater Lett 2012;72:36–8.
[2] Khorsand Zak A, Abd Majid WH, Abrishami ME, Yousfi Ramin. X-ray of ZnO nanoparticles by Williamson-Hall and size-strain plot methods. Solid State Sci 2011;13:251–6.
[3] Mote VD, Purushotham Y, Dole BN. Williamson-Hall analysis in estimation of lattice strain in nanometer-sized ZnO particles. J Theor Appl Phys 2012;6:6.
[4] Scherrer P. Bestimmung der Grösse und der inneren Struktur von Kolloidteilchen mittels Röntgenstrahlen. Nachr Ges Wiss Göttingen 1918;26:98–100.
[5] Williamson GK, Hall WH. X-ray line broadening from filed aluminium and wolfram. Acta Metall 1953;1:22–31.
[6] http://pd.chem.ucl.ac.uk/pdnn/peaks/sizedet.htm.
[7] Halder NC, Wagner CNJ. Separation of particle size and lattice strain in integral breadth measurements. Acta Crystallogr 1966;20:312–3.
[8] Halder NC, Wagner CNJ. analysis of the broadening of powder pattern peaks using variance, integral breadth, and fourier coefficients of the line profile. Adv X-Ray Anal 1966;9:91–102.
[9] Ida T, Shimazaki S, Hibino H, Toraya H. Diffraction peak profiles from spherical crystallites with lognormal size distribution. J Appl Cryst 2003;36:1107–15.
[10] Izumi F, Ikeda T. Implementation of the Williamson-Hall and Halder-Wagner methods in the RIETAN-FP. Adv Inst Sci Technol 2014;3:33–8.
[11] Chen KW, Jian SR, Wei PJ, Jang JSC, Lin JF. A study of the relationship between semi-circular shear bands and pop-ins induced by indentation in bulk metallic glasses. Intermetallics 2010;18:1572–7.
[12] Kumar A, Yedla N. Mechanical and structure studies of $Zr_{50}Cu_{50}$ glass matrix composites during nano-indentation-a molecular dynamics study. IOP Conf Ser: Mater Sci Eng 2015;75:012020.
[13] Kim J-J, Choi Y, Suresh S, Argon AS. Nanocrystallization during nanoindentation of a bulk amorphous metal alloy at room temperature. Science 2002;295:654–7.
[14] Gouadec G, Colomban P. Raman spectroscopy of nanomaterials: how spectra relate to disorder. Particle Size and Mechanical Properties. The open archive HAL.
[15] Beams R, Cancado LG, Novotny L. Raman characterization of defects and dopants in graphene. J Phys: Condens Matter 2015;27:083002.
[16] Ferrari AC, Basko DM. Raman spectroscopy as a versatile tool for studying the properties of graphene, Mat. Science (condensed-materials). Nat Nanotechnol 2013;8:235.
[17] Kumar S, Tiwari N, Jha SN, Chatterjee S, Bhattacharyya D, Ghosh AK. Structural and optical properties of sol–gel derived Cr-doped ZnO diluted magnetic semiconductor nanocrystals: an EXAFS study to relate the local structure. RSC Adv 2016;Issue 109, Issue in Progress doi.org/10.1039/c6ra15685a.
[18] Bera D, Qian L, Tseng T-K, Holloway PH. Quantum dots and their multimodal applications: a review. Materials 2010;3:2260–345. https://doi.org/10.3390/ma3042260.
[19] Stella C, Soundararajan N, Ramachandran K. Structural, optical, and magnetic properties of Mn and Fe-doped Co_3O_4 nanoparticles. AIP Adv 2015;5:087104.
[20] Guerbous L, Boukerika A. Nanomaterial host bands effect on the photoluminescence properties of Ce-Doped YAG Nanophosphor synthesized by Sol-Gel method. J Nanomater 2015;2015:617130–40.
[21] Dhara S, Giri PK. Size-dependent visible absorption and fast photoluminescence decay dynamics from freestanding strained silicon nanocrystals. Nanoscale Res Lett 2011;6:320.
[22] Shen G, Mao HK. High-pressure studies with X-rays using diamond anvil cells. Rep Prog Phys 2017;80:016101–101654.
[23] Lobanov SS, Prakapenka VB, Prescher C, Konôpkova Z, Liermann H-P, Crispin K, et al. Pressure, stress, and strain distribution in the double-stage diamond anvil cell. J Appl Phys 2015;118:035905.
[24] Fu X-W, Liao Z-M, Liu R, Xu J, Yu D. Size-dependent correlations between strain and phonon frequency in individual ZnO nanowires. ACS Nano 2013;7:8891–8.
[25] Fu X-W, Liao Z-M, Liu R, Lin F, Xu J, Zhu R, et al. Strain loading mode dependent bandgap deformation potential in ZnO micro/nanowires. ACS Nano 2015;9:11960–7.

[26] Gras Ch, Vrel D, Gaffet E, Bernard F. J. Alloys Comput 2001;314:240–50.
[27] Klug H, Alexander LE. X-ray diffraction procedures for polycrystalline and amorphous materials. NY: John Wiley & Sons; 1954.
[28] Hearne GR, Zhao J, Dawe AM, Pischedda V, Maaza M, Nieuwoudt MK, et al. Effect of grain size on structural transitions in anatase TiO_2: a Raman spectroscopy study at high pressure. Phys Rev B 2004;70:134102.
[29] Rehani BR, Joshi PB, Iad KN, Pratap A. Crystallite size estimation of elemental and composite silver nano-powders using XRD, principles. Indian J Pure Appl Phys 2006;44:02.
[30] Thamaphat1 K, Limsuwan P, Ngotawornchai B. Phase Characterization of TiO2 Powder by XRD and TEM. Kasetsart J (Nat Sci) 2008;42:357–61.
[31] Hadjiivanov KI, Klissurski DG. Surface chemistry of titania (anatase) and titania-supported catalysts, Surface chemistry of titania (anatase) and titania-supported catalysts. Chem Soc Rev 1996;25:61–9.
[32] Taziwa R, Meyer EL, Sideras-Haddad E, Erasmus RM, Manikandan E, Mwakikunga BW. Effect of carbon modification on the electrical, structural, and optical properties of TiO_2 electrodes and their performance in labscale dye-sensitized solar cells. Int J Photoenergy 2012;2012.
[33] Sikhwivhilu LM, Mpelane S, Mwakikunga BW, Sinha Ray S. Photoluminescence and hydrogen gas-sensing properties of titanium dioxide nanostructures synthesized by hydrothermal treatments. ACS Appl Mater Interfaces 2012;4:1656–65.
[34] Tian HH, Atzmon M. Comparison of X-ray analysis methods used to determine the grain size and strain in nanocrystalline materials. J Phil Magazine A 1999;79(8).
[35] Weibel A, Bouchet R, Boulc'h F, Knauth P. The big problem of small particles: a comparison of methods for determination of particle size in nanocrystalline anatase powders. Chem Mater 2005;17(9):2378–85.
[36] Fang F, Kennedy J, Manikandan E, Futter J, Markwitz A. Morphology and characterization of TiO2 nanoparticles synthesized by arc discharge. Chem Phys Lett 2012;521:86–90.
[37] Manikandan E, Murugan V, Kavitha G, Babu P, Maaza M. Nanoflower rod wire-like structures of dual metal (Al and Cr) doped ZnO thin films: Structural, optical and electronic properties. Mater lett 2014;131:225–8.
[38] Manikandan E, Kavitha G, Kennedy J. Epitaxial zinc oxide, graphene oxide composite thin-films by laser technique for micro-Raman and enhanced field emission study. Ceram Int 2014;40(10):16065–70.
[39] Sathyaseelan B, Manikandan E, Sivakumar K, Kennedy J, Maaza M. Enhanced visible photoluminescent and structural properties of ZnO/KIT-6 nanoporous materials for white light emitting diode (w-LED) application. J Alloy Compd 2015;651:479–82.
[40] Mwakikunga BW, Forbes A, Sideras-Haddad E, Scriba M, Manikandan E. Self assembly and properties of C: WO 3 nano-platelets and C: VO 2/V 2 O 5 triangular capsules produced by laser solution photolysis. Nanoscale Res Lett 2010;5(2):389.
[41] Sithole J, Balla Ngom MM, Khamlich D, Manikandan S, Manyala E, Saboungi N, et al. Simonkolleite nano-platelets: Synthesis and temperature effect on hydrogen gas sensing properties. Appl Surf Sci 2012;258(20):7839–43.
[42] Elayaperumal M, Krishnakumar L, Gnanasekaran K, Mani G, Rayappan John Bosco Balaguru, Ladchumananandasivam R, Maaza M. Effective Ammonia Detection Using n-ZnO/p-NiO Heterostructured Nanofibers. IEEE Sens J 2016;16(8):2477–83.
[43] Manikandan E, Moodley MK, Ray SS, Panigrahi BK, Krishnan R, Padhy N. Zinc oxide epitaxial thin film deposited over carbon on various substrate by pulsed laser deposition technique. J Nanosci Nanotechnol 2010;10(9):5602–11.
[44] Sathyaseelan B, Manikandan E, Lakshmanan V, Baskaran I, Sivakumar K. Structural, optical and morphological properties of post-growth calcined TiO2 nanopowder for opto-electronic device application: Ex-situ studies. J Alloy Compd 2016;671:486–92.
[45] Saasa V, Mokwena M, Dhonge B, Manikandan E, Kennedy J, Murmu PP, et al. Optical and structural properties of multi-wall-carbon-nanotube-modified ZnO synthesized at varying substrate temperatures for highly efficient light sensing devices. Sensors Transducers 2015;195(12):9.
[46] Manikandan A, Manikandan E, Meenatchi B, Vadivel S, Jaganathan SK, Ladchumananandasivam R, et al. Rare earth element (REE) lanthanum doped zinc oxide (La: ZnO) nanomaterials: synthesis structural optical and antibacterial studies. J Alloy Compd 2017;723:1155–61.

Appendix 2: Published paper 2

PHYSICAL REVIEW B **70**, 134102 (2004)

Effect of grain size on structural transitions in anatase TiO_2: A Raman spectroscopy study at high pressure

G. R. Hearne,* J. Zhao, A. M. Dawe, V. Pischedda, M. Maaza, M. K. Nieuwoudt, P. Kibasomba, O. Nemraoui, and J. D. Comins
School of Physics, University of the Witwatersrand, Private Bag 3, Wits 2050, Johannesburg-Gauteng, South Africa

M. J. Witcomb
Electron Microscope Unit, University of the Witwatersrand, Private Bag 3, Wits 2050, Johannesburg-Gauteng, South Africa
(Received 23 June 2004; published 12 October 2004)

Micro-Raman spectroscopy has been used to investigate the structural stability of nanoanatase (TiO_2), of ~12 nm average grain size, up to pressures of ~40 GPa in a diamond anvil cell at room temperature. This has been compared to the Raman pressure behavior of bulk anatase, which undergoes a structural transition from the tetragonal structure to the orthorhombic α-PbO_2-type intermediate near ~5 GPa before transforming to the monoclinic baddeleyite structure at an onset pressure of ~15 GPa and remains in this phase up to the highest pressure of ~35 GPa. By contrast, the nanophase anatase maintains its structural integrity up to ~18 GPa before transforming directly to the baddeleyite structure, which is stable to the highest pressure of this study. The pressure dependence of the four most prominent Raman modes is similar for both the nanophase and bulk-anatase compounds suggesting that they have similar compressibilities, all of these modes exhibiting normal stiffening behavior as the pressure rises. In a separate temperature dependent micro-Raman study to 1000 °C at ambient pressure, the most intense (E_g) mode of both the nanophase and bulk-anatase samples shows unusual stiffening behavior on heating. This mode is associated with O-Ti-O bond-bending vibrations in which O displacements are bigger than the Ti displacements. In both samples, all other prominent Raman modes exhibit anticipated softening when heated. From these temperature and pressure dependences it may be deduced that intrinsic anharmonicity and associated phonon-phonon interactions govern the temperature dependence of the intense E_g mode, whereas either or both dilatation effects or intrinsic anharmonicity determine the behavior of the other modes. The linewidth of the most intense E_g mode in nanoanatase exhibits a sharp decrease from ambient to ~2 GPa, descending to a broad minimum at ~5 GPa, in contrast to the behavior of the bulk phase. The linewidth then increases monotonically at $P > 5$ GPa similar to the behavior of the bulk solid. This unusual behavior of the linewidth in the nanophase material may be explained by the effect of internal pressure acting across the curved surface in the nanosized grains being compensated by the externally applied pressure. The average grain size of ~12 nm of the nanoanatase is less than the critical size estimated for nucleation and growth of a new structural α-PbO_2-type phase. This rationalizes how the structural transition to the α-PbO_2-type intermediate phase, which occurs in bulk anatase, has been inhibited in the nanophase material. Instead, the formation of new grain boundaries of compacted nanoparticles of anatase would be the anticipated main pressure-induced structural modification, likely representing a lower free-energy situation than if nucleation of the new α-PbO_2-type intermediate with associated anatase/α-PbO_2-type interfaces occurred. At sufficiently high pressure the free-energy gain from the volume reduction to the baddeleyite phase is shown to offset the interface energy cost involved in the nucleation and growth of this high-pressure phase and, thus, drives the direct anatase→baddeleyite structural transition. Both the nanophase and bulk-sample pressure quench from the baddeleyite to the α-PbO_2-type structure upon decompression from 35–40 GPa to ambient conditions.

DOI: 10.1103/PhysRevB.70.134102 PACS number(s): 61.46.+w, 64.70.Kb, 78.30.−j, 81.40.Vw

I. INTRODUCTION

There has been considerable previous research to understand the pressure-induced structural transitions that occur in titanium dioxide (TiO_2).[1–10] Interest has been accelerated in recent years because the structural phases of TiO_2 and related compounds HfO_2 and ZrO_2 at high pressure exhibit a high bulk modulus. These structures obtained at high pressure may be retained upon decompression to ambient conditions and thus are prime candidates for ultrahard materials, these being important for a number of industrial applications.[7,11]

Three different structural phases of TiO_2 exist in nature, viz, anatase [Fig. 1(a)], rutile, and brookite. Other structures, such as the orthorhombic α-PbO_2-type phase [Fig. 1(b)] and the monoclinic baddeleyite phase [Fig. 1(c)], may be stabilized only under high pressure from a starting material of either anatase or rutile. A single crystal of anatase, for example, undergoes the following sequence of structural transitions under high pressure:

$$\text{anatase}(I4_1/amd) \rightarrow \alpha\text{-PbO}_2\text{-type phase}(Pbcn) \rightarrow \text{baddeleyite}(P2_1/c).$$

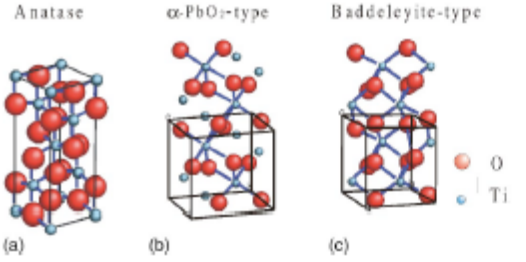

FIG. 1. Unit cells of different structural phases of TiO_2: (a) tetragonal anatase, (b) orthorhombic α-PbO_2-type phase, and (c) monoclinic baddeleyite phase.

The orthorhombic α-PbO_2-type phase is retained upon decompression to ambient conditions. Table I summarizes the main experimental results of high-pressure studies of anatase TiO_2. The differences in the transition pressures at which the structural transitions occur depend on whether the sample is single- or polycrystalline. Some of the most recent work of Arlt *et al.*[10] has shown that there may be a transition directly from the anatase to baddeleyite structure at ~13 GPa. They ascribed this to lattice defects and grain boundaries that suppress the transition of anatase to the α-PbO_2-type intermediate; however, no further details have been provided in their paper.

Nanostructured anatase TiO_2 has invoked considerable interest in recent years because it has a variety of potential applications, e.g., in photocatalysis and in photoelectrochemical solar cells.[12] The high surface-to-volume ratio in nano-particles affect the physical properties of the compound, e.g., temperature-induced microstructural evolution of nano-anatase TiO_2.[9,13–18] To the best of our knowledge there is only limited published work on the effect of the particle size of nanophase TiO_2 on the pressure-induced structural transitions,[19–21] in comparison to the wealth of research accomplished on the temperature-induced structural changes in this material.

Raman scattering is a convenient and sensitive probe widely used to characterize local structural changes and monitor structural transitions in compounds. The present work is primarily concerned with a micro-Raman investigation to ~40 GPa of nanoanatase TiO_2 of ~12 nm average grain size pressurized in a diamond anvil cell at room temperature.

II. EXPERIMENTAL

TiO_2 nanoparticles were synthesized by lyophilization. Titanium tetrachloride (99.99% Aldrich) starting salt was dissolved in distilled water to a desired concentration that determines the TiO_2 final-product particle size. Typically, 0.02 mol of dry anhydrous $TiCl_4$ was dissolved in 100 ml distilled water. The solution was flash frozen by injecting it at high pressure into liquid nitrogen through an ~80 μm nozzle with a central pin to break up the jet into a fine spray. The pulverized frozen mass was then transferred to the chamber of a Christ freeze-dryer operated at a pressure of 5 Pa where the drying operation commenced for ~24 hr. The lypohilized highly porous nanophase precursor salt was then decomposed by heating in air in the range of 300–700 °C for 3–30 min. The different structural phases of TiO_2 nanoparticles that may be stabilized (e.g., brookite, anatase, rutile) and the resultant average particle size are controlled mainly by the thermal decomposition temperature. Decomposition temperatures and the resultant structural phases that arise from the multicomponent precursor have been identified by thermal gravimetric analysis (TGA) and XRD investigations, respectively. Characterization of the nanoanatase sample was made by using both TEM as shown in Fig. 2 and by x-ray diffraction. The Scherrer formula has been used to deduce an average particle size of ~12 nm

TABLE I. Summary of the results of high-pressure studies of anatase TiO_2.

Phase transition	Anatase to α-PbO_2 type	α-PbO_2 type to baddeleyite	Anatase to baddeleyite	Method
Ohsaka *et al.* (Ref. 4)	2.6 GPa Polycrystalline			Raman spectroscopy
Haines and Leger (Ref. 7)	~7 GPa Polycrystalline	~10 GPa polycrystalline		x-ray diffraction
Lagarec and Desgreniers (Ref. 8)	4.5–7 GPa Single crystal	13–17 GPa polycrystalline		Raman spectroscopy
Arlt *et al.* (Ref. 10)	4.5 GPa Single crystal			Synchrotron x-ray diffraction
Arlt *et al.* (Ref. 10)			13 GPa Polycrystalline	Synchrotron x-ray diffraction
Swamy *et al.* (Ref. 19)			18GPa Nanophase (30–40 nm)	Synchrotron x-ray diffraction
This work			18 GPa Nanophase (~12 nm)	Raman spectroscopy
This work	5 GPa Bulk polycrystalline	12–15 GPa		Raman spectroscopy

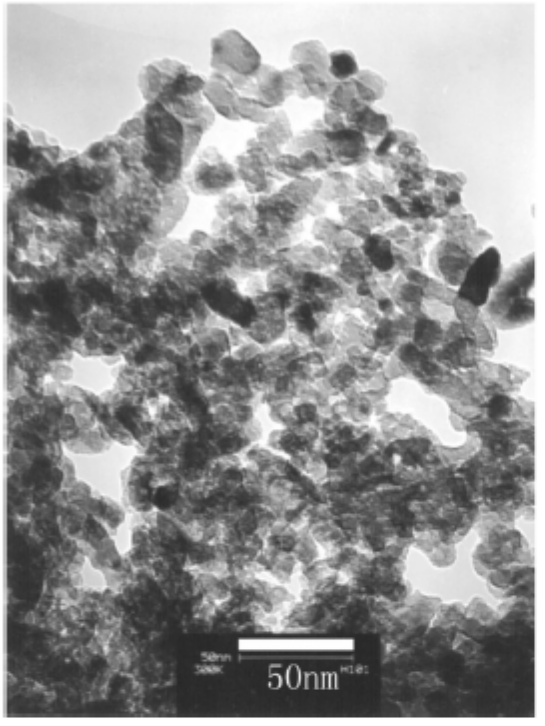

FIG. 2. Transmission electron micrograph (TEM) of as-received anatase TiO_2 nanoparticles.

from the (101) diffraction linewidth, consistent with the average value of the longest dimension of many of the irregular-shaped or platelet grains discerned in the TEM micrograph of Fig. 2. X-ray fluorescence measurements show that the sample is slightly off stoichiometry, namely, as $TiO_{1.92}$, which will give rise to some degree of Raman mode shifting and linewidth broadening[22] compared with the stoichiometric compound.

A piston-cylinder-type diamond anvil cell (DAC)[23] with anvil culets of 540 μm diam was used to generate high pressures up to ~38 GPa. After the T301 steel foil gasket had been pre-indented to ~40 μm from a starting thickness of ~250 μm, the sample was loaded into a cavity that had been spark eroded in the center of the preindentation. In one series of measurements, our new multiaperture gasket technique[24] was used to obtain Raman spectra in a single sequence of compressions of both nanophase and bulk crystalline anatase loaded into two separate cavities ($\phi \sim 100$ μm each) of the same preindented gasket. A second series of pressure measurements was performed on the nanophase sample alone. Liquid nitrogen was loaded into each sample cavity to serve as a pressure-transmitting medium by immersing the miniature DAC into a bath of the cryogen and momentarily releasing and then retightening the thrust-force screws.

Raman spectra in backscattering mode at room temperature and variable high pressures were obtained with a Jobin-Yvon T64000 spectrograph equipped with a Raman microscope, holographic gratings (1800 grooves mm^{-1}), and a liquid-nitrogen-cooled CCD detector. The 514.5 nm line of an Ar^+ laser with output power of 55 mW was used to excite the Raman scattering with the spectrograph operated in the triple-subtractive mode. Estimated laser power at the sample stage was 5 mW. The laser beam was focused onto the samples by means of an Olympus ×20 ultralong working distance objective, which results in a laser spot size of ~10 μm diam. The entrance-slit width of the premonochrometer was set at 200 μm. Under these conditions data acquisition times ranged from 30 s up to 600 s depending on the quality of the spectra. Pressure calibration within the cavity of the gasket was made in terms of the ruby R-luminescence lineshift[25] measured at the same position at which the Raman spectrum was obtained. The argon-ion laser plasma lines 516.3 nm, 516.6 nm, 517.6 nm, etc., were subsequently used for the Raman-shift calibration; these lines are removed from the Raman spectra presented in the figures of this paper.

III. RESULTS AND DISCUSSION

The pressure evolution of the Raman spectra of nanoanatase is shown in Figs. 3(a) and 3(b) whereas Raman spectra at a selected pressure of the bulk commercial sample are shown in Fig. 3(c). Under ambient conditions, the most prominent Raman bands in nanoanatase are at 146.4 cm^{-1} (E_g), 396.9 cm^{-1} (B_{1g}), 518.1 cm^{-1} (A_{1g}/B_{1g} unresolved doublet) and 641.3 cm^{-1} (E_g) where the band assignments have been indicated in brackets. These are part of six assigned Raman active modes ($A_{1g}+2B_{1g}+3E_g$) derived from factor group analysis[26] of tetragonal anatase, which belongs to the space group $D_{4h}^{19}(I4_1/amd)$. For bulk anatase the corresponding bands are at 141.3 cm^{-1}, 394.4 cm^{-1}, 516.1 cm^{-1} and 636.7 cm^{-1}. Part of the Raman peak-position shifts in the nanophase anatase may be due to deviations from stoichiometry known to affect both Raman line positions and widths.[22]

The pressure evolution of the Raman spectra of bulk anatase exhibits similar behavior to that reported in previous high-pressure studies.[8] As the pressure increases to ~5.6 GPa, several weak peaks appear at 331.0, 344.5, and 372.8 cm^{-1}, characteristic of the α-PbO_2-type phase. As pressure increases further, the intensities of these new peaks increase and they are clearly discerned at pressures of ~7.5 GPa and beyond, see Fig. 3(c). The structural transition of bulk polycrystalline anatase to the α-PbO_2-type intermediate was sluggish, as found previously,[7] coexisting with the original anatase structure up to ~15 GPa. Beyond this pressure, radically new Raman bands become apparent in the range of 225–280 cm^{-1} in addition to a prominent band at ~500 cm^{-1}; these are supposed to be characteristic of the high-pressure baddeleyite phase.[8]

The pressure evolution of the Raman spectra of the nanoanatase compound is quite different. No new peaks appear in the spectra up to ~16 GPa, which are all similar to the one at ambient pressure. Figures 3(a) and 4(a) show that the anatase phase in the nanostructured compound is stable to well beyond the transition pressure found in bulk anatase,

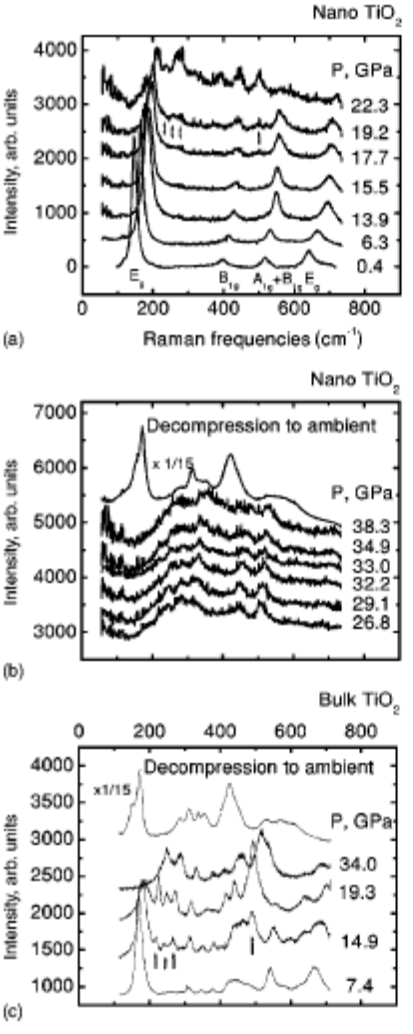

FIG. 3. Raman spectra under high pressure of nanostructured anatase (a), (b); Panel (c) is for bulk anatase. The arrows in panels (a) and (c) are to delineate new modes specific to the baddeleyite phase.

i.e., ~5 GPa. When the pressure is increased to 17.7 GPa, see Fig. 3(a), a number of new bands of low intensity are discerned at ~235 cm^{-1}, ~250 cm^{-1}, ~275 cm^{-1}, and ~500 cm^{-1}, which appear to be specific to the high-pressure baddeleyite phase[8] and which persist to the maximum applied pressure of ~38 GPa. Although, the spectra at the higher pressures, $P > 26$ GPa, have much broader bands than in the bulk sample. This may arise from one, or a combination, of the following factors: imminent pressure-induced amorphization as seen previously,[21] the effect of nonhydrostatic stress at these elevated pressures, possible changes to the morphology of the nanoparticles, fracturing of the nanoparticles to smaller subunits.

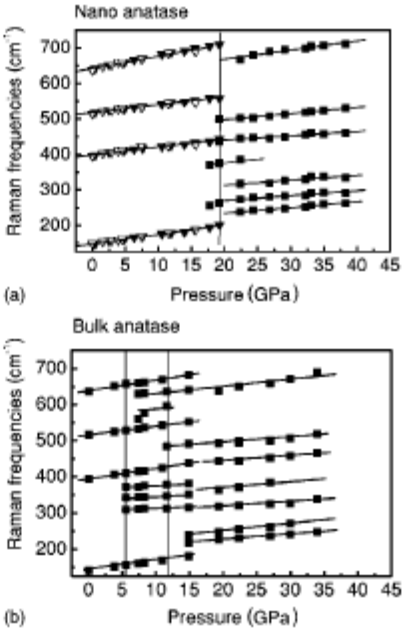

FIG. 4. Pressure dependence of frequencies of Raman active modes of (a) nanoanatase compared with that of bulk anatase in (b). Thin vertical lines show the onset pressures of structural transitions.

These results clearly demonstrate that the nanophase sample transforms directly from the anatase to baddeleyite structure at 17.7 GPa without passage via the α-PbO_2-type intermediate, consistent with a previous pressure study on nanoanatase.[21] However, when the nanophase sample is decompressed from the maximum pressure, the high-pressure baddeleyite phase is quenched to the α-PbO_2-type phase, similar to the behavior of the bulk compound [see Figs. 3(b) and 3(c)], albeit with broader Raman bands.

Raman mode frequencies of the nanophase sample as a function of pressure are shown in Fig. 4(a). The pressure dependence of the Raman frequencies ($d\nu/dP$) have been obtained by linear fits [solid curves in Fig. 4(a)] over the pressure range before and after the structural transition that occurs at ~18 GPa. The hollow and filled symbols simply delineate measurements from the two different series of measurements. The slope $d\nu/dP$ averaged over the most intense bands of nanophase anatase is 2.58 ± 0.22 cm^{-1} GPa^{-1} compared with bulk anatase in Fig. 4(b) where the slope $d\nu/dP$ average is 2.70 ± 0.13 cm^{-1} GPa^{-1}, perhaps indicating that the anatase phase in both compounds have similar compressibilities.

After the transition of nanophase anatase to the baddeleyite structure, the average $d\nu/dP$ of the high-pressure phase is 1.65 ± 0.21 cm^{-1} GPa^{-1}, suggesting that the baddeleyite phase is less compressible than the low-pressure anatase phase. This is qualitatively consistent with the compressibilities derived from the recent x-ray diffraction measurements.[10]

Figure 5(a) shows the pressure-induced changes of the linewidth of the intense E_g band of the bulk anatase com-

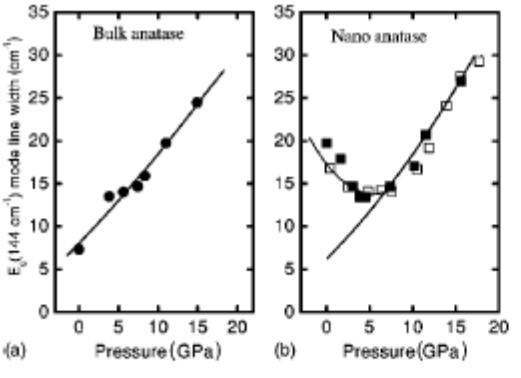

FIG. 5. Pressure dependence of the line width of the intense E_g Raman active mode (at ~144 cm^{-1} under ambient conditions) of anatase TiO_2: (a) for the bulk solid and (b) for the nanostructured material. Thin solid lines are to guide the eye.

pound; the linewidth increases from 7 cm^{-1} at ambient pressure to 25 cm^{-1} at ~15 GPa. There is an inflection at ~5 GPa perhaps attributable to the volume reduction that occurs when anatase transforms to the α-PbO_2-type phase.[7,10]

The linewidth of the intense E_g mode of nanophase anatase, by contrast, displays very different pressure behavior as shown in Fig. 5(b). The linewidth first decreases rapidly up to 1.5 GPa, reaching a broad minimum that extends up to ~5 GPa, followed by an upturn and monotonic increase as the pressure rises beyond 5 GPa. The pressure at which the broad minimum shows an upturn is close to the transition pressure of ~5 GPa where bulk anatase transforms to the α-PbO_2-type structure.

The intense E_g band (located at ~144 cm^{-1} under ambient conditions) of anatase, which arises from O-Ti-O bond-bending-type vibrations of the structure[4] has a linewidth or line shape affected by various factors. These include nonstoichiometry due to oxygen deficiencies or disorders induced by minority phases.[22,27] In addition, linewidth broadening in nanodimensioned particles may arise from the pressure effect induced by the surrounding particles or the surface stress of the particle.[28] Phonon confinement effects in nanoparticles also affect the line shape, and several authors have discussed the relation between increasing linewidth of the intense E_g mode at ~144 cm^{-1} with particle-size reduction in nanophase anatase using this idea.[15,18,29,30] In this case the correlation between the E_g linewidth and particle size has been corroborated by measurements of particle size deduced from x-ray diffraction and TEM.

To understand the unusual behavior of the E_g mode linewidth in nanophase anatase, additional Raman and XRD pressure measurements have been made up to 6.2 GPa followed by measurements upon decompression to ambient conditions. The Raman investigation shows that the change of linewidth with pressure is reversible upon pressure cycling from ambient up to 6.2 GPa and back to ambient pressure again, as shown in Fig. 6(a). The linewidth of the original as-received sample is 22.2(2) cm^{-1} compared to that of the decompressed sample, 23.8(4) cm^{-1} at ambient pressure.

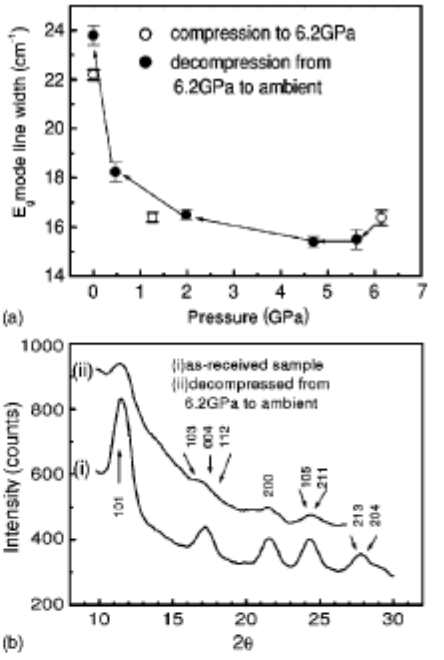

FIG. 6. (a) Detailed cyclic-pressure behavior of the intense E_g mode linewidth up to ~6 GPa. (b) XRD patterns prior and subsequent to pressure cycling.

The x-ray diffraction pattern of the sample after decompression from 6.2 GPa to ambient pressure as shown in Fig. 6(b) was obtained by using a Siemens SMART diffractometer with CCD area detector. The intensities of the x-ray pattern of the decompressed sample are weaker and broadened, but the diffraction peak positions do not show obvious differences when compared to that of the as-received sample. If the background contribution in both x-ray diffraction patterns are eliminated in Fig. 6(b), the half-width at half maximum (HWHM) of the (101) diffraction peak are 1.44(6)° for the as-received sample and 1.81(8)° for the decompressed sample. Therefore, the increase in linewidths of both the E_g Raman mode and (101) Bragg reflection after decompression to ambient pressure perhaps rules out the possibility of pressure-induced grain growth (coarsening) when the sample is pressurized to ~6 GPa. Such a grain-coarsening mechanism is expected to be irreversible and any consequent linewidth narrowing of diffraction peaks that occur should persist when the sample is decompressed to ambient conditions.

For small near-spherical particles embedded in a host matrix, viz, nanophase anatase in a nitrogen pressure-transmitting medium, we may consider the contents of the TiO_2 nanoparticle to experience an extra pressure ΔP resulting in the curvature of the nanoanatase/nitrogen interface, just as the contents of a liquid drop involve an extra pressure ΔP.

If P_i and P_e are the pressures at the interior and exterior of the nanoparticle, respectively, then the excess pressure $\Delta P = P_i - P_e$ across a curved or any planar surface is

$$\Delta P \propto f/d, \tag{1}$$

where f is the surface stress and d the linear dimension of the particle.[31,32]

The concept of surface stress f is applicable to a solid surface and is related to the surface-free energy σ, which constitutes a significant part of the total free energy of nanodimensional particles. The surface-free energy is defined as the reversible work per unit area or force per unit length of exposed edge involved in forming *new* surface material. In the case of a liquid where surface shear stresses and associated elastic strains along the surface cannot be sustained, the surface-free energy is referred to as the surface tension. However, in solid surfaces the surface area may be changed by deforming the surface *elastically*, keeping the number of surface lattice sites constant. In this case the work per unit area or force per unit length of exposed edge to change the surface area is not equal to the surface-free energy and is instead referred to as the surface stress f. If the work necessary to deform area A by increasing it by dA in the isotropic case is considered, then surface stress f is related to the surface free energy σ by[28,33]

$$f = \sigma + A\frac{d\sigma}{dA}. \tag{2}$$

In a bulk grain this extra pressure ΔP of Eq. (1) is considered to be negligible because of the dependence on the inverse linear dimensions of the grain.

Diffraction patterns at ambient conditions, with 2θ ranging from 10° to 80°, were measured on a Siemens capillary diffractometer. Data were refined using the standard analyzing programs WINCELL[34] or GSAS[35] to obtain the lattice parameters. Measurements of the lattice parameter of the NIST Si640C standard on this instrument indicated that there was a systematic error of ±0.02%, hence, lattice parameters cannot be determined to a higher precision than this. At ambient pressure the lattice parameter of the nanoanatase was found to be $a_o = 3.776 \pm 0.008$ Å and $c_o = 9.50 \pm 0.02$ Å ($V_0 = 135.5 \pm 0.7$ Å^3) and compared to the bulk sample for which $a_o = 3.785 \pm 0.002$ Å and $c_o = 9.513 \pm 0.004$ Å $V_0 = 136.3 \pm 0.4$ Å^3. This may be compared with the standard data $a_0 = 3.785$ Å and $c_0 = 9.513$ Å of bulk anatase.[36] These measurements suggest that there is possibly a slight reduction in the unit-cell volume of the nanophase material, as expected for a nanoparticle that is likely to experience an excess internal pressure across a curved boundary, as quantified in Eq. (1).

In the case of spherical particle of diameter d, the excess pressure from Eq. (1) may be written as involving surface stress

$$\Delta P = \frac{4f}{d}. \tag{3}$$

In a first approximation we equate surface tension and surface stress $\gamma = f$, although it should be recognized that f may be up to 3 times greater than this.[37,38] Using the accepted value[32] of $\gamma \sim 1.5$ Jm^{-2} we obtain from Eq. (3) an excess pressure of $\Delta P = 0.5$ GPa. The excess pressure in 12 nm diam spherical particles is then likely to be as high as $\Delta P \sim 1.5$ GPa, if it is taken into account that surface stress $f > \gamma$ should be used in Eq. (3).

Figure 5(a) shows that the linewidth of the intense E_g mode increases for a grain that is under pressure. At ambient pressure, part of the line broadening in the Raman spectrum of the nanoparticle of anatase is supposed to arise from the extra internal pressure that causes the curvature of the surface. Note also the strong pressure dependence of the linewidth up to $P \sim 1.5$ GPa in the nanophase material. As this sample is pressurized in the cavity of the gasket, the external pressure P_e rises and there is a corresponding decrease in the net pressure ΔP acting on the contents of each nanoparticle. Thus as external pressure P_e rises to compensate the internal pressure P_i, the net pressure ΔP on the nanoparticle diminishes and an associated decrease in the linewidth is expected. This proffers an explanation for the pressure dependence of the linewidth [see Fig. 6(a)] as external applied pressure rises and compensates the excess pressure ΔP internal to the particle. There is no net pressure on the contents of the nanoparticle at ~1.5 GPa, where the rapid pressure dependence of the linewidth changes drastically and the linewidth is almost at its minimum value. Any line broadening at this point is due to any one, or a combination, of the mechanisms mentioned previously, e.g., phonon confinement effects. As the applied pressure rises beyond ~1.5 GPa, the nanoparticle is then subjected to an increasing net pressure, $P_e > P_i$, from the externally applied stresses transmitted through the nitrogen medium, similar to the case of bulk anatase in Fig. 5(a). From the linewidth behavior in Figs. 5(b) and 6(a) we infer that the excess pressure in the nanoparticles is in the range of 1.5 to 5 GPa at ambient external pressure. The broad minimum may be a result of a number of factors, including a distribution of particle dimensions, some of the nanoparticles perhaps being nonspherical platelets,[39] and compaction of the grains with some consequent effect on grain boundaries or surfaces (i.e., on the f values). The broad minimum is thus supposed to represent the range of pressures required to counterbalance a range of internal pressures across a range of surface dimensions and surface stresses. Alternatively, the broad minimum may be due to fracturing of the nanoparticles to smaller subunits (with a distribution of sizes), as a result of the applied quasihydrostatic stresses in the sample cavity, and there is, consequently, an increase in excess pressure according to Eq. (1).

The behavior of the E_g-mode linewidth in the range ambient to 5 GPa is almost reversible when the external pressure is reduced to zero, [see Fig. 6(a)], albeit perhaps slightly broader in the decompression cycle. This implies that the net pressure on the particle reverts back to or in excess of ~1.5 GPa due to internal pressure P_i, which is consistent with the elastic deformation model we have proposed where a net pressure ΔP is responsible for part of the line broadening.

In situ Raman studies were also performed as a function of temperature to 1000 °C on both the nanophase and bulk anatase compounds. The temperature dependence of the Raman modes is presented here to emphasize the different effects of pressure and temperature on the modes, in particular the intense E_g mode at ~144 cm^{-1}. The Raman measurements at elevated temperatures were performed by using a

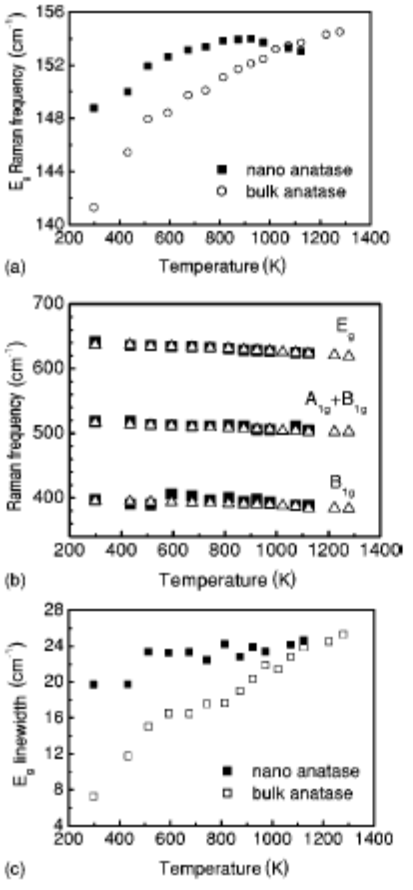

FIG. 7. (a) Temperature dependence of the intense E_g Raman mode frequencies of both nano- and bulk anatase. (b) Temperature dependence of the other Raman active mode frequencies of both nano- and bulk-anatase, solid and hollow symbols, respectively. (c) Temperature dependence of the linewidth of the intense E_g mode.

Linkham T600 high-temperature stage with the sample in an argon gas atmosphere. After the samples are stabilized at a new temperature with a drift not exceeding ±1 °C, a Raman spectrum has been collected first from the nanophase sample in a typical acquisition time of 720 s and then the much more intense spectrum from the bulk sample is collected in 7 s. This ensures that both samples have been heated for a comparable amount of time.

Figure 7(c) shows the change of the Raman linewidth of the intense E_g mode of the bulk solid is close to linear as temperature rises above 160 °C. Whereas in the nanostructured sample, the linewidth of this mode appears to be nearly constant above this temperature. In the bulk compound the linear increase in intense E_g mode linewidth is typically due to thermal expansion effects and an increasing atomic mean-square-displacement (msd), analogous to the effect of increasing disorder as the temperature rises. In the nanostructured compound, the effect of increasing temperature is similar to sintering and associated grain-coarsening effects. We suppose that both phonon confinement in nanodimensioned anatase as well as internal pressure are partly responsible for the excess linewidth of the intense E_g mode at ambient external pressure, as depicted in Fig. 5. Grain growth at high temperatures will decrease both these effects as the dimensions of each grain increases and we may expect a corresponding decrease in the linewidth. This will be counteracted by concurrent thermal effects of lattice expansion and an increased msd or thermally induced disorder leading to linewidth broadening. As a consequence of these two competing effects we may expect the linewidth to remain nearly constant.

An interesting feature of the intense E_g mode at ~144 cm^{-1} is that it exhibits hardening as the temperature rises, whereas typical softening and an associated decrease in frequency is expected as seen in the behavior of the other modes of the anatase phase, see Figs. 7(a) and 7(b).

By considering each vibrational mode ν to be a function of volume V and temperature T, the temperature dependence $d\nu/dT$ at constant pressure may be expressed as

$$\left(\frac{\partial \ln \nu}{\partial T}\right)_P = -\left(\frac{\beta}{\kappa}\right)\left(\frac{\partial \ln \nu}{\partial P}\right)_T + \left(\frac{\partial \ln \nu}{\partial T}\right)_V. \quad (4)$$

This involves similar notation to that of Peercy and Morosin[40] and Samara and Peercy,[2] where $\beta=(\partial \ln V/\partial T)_P$ is the volume thermal-expansion coefficient and $\kappa=-(\partial \ln V/\partial P)_T$ is the compressibility defined previously. This equation may be rewritten in terms of the measured pressure and temperature dependences of the Raman-active mode, viz, as

$$(\Delta\nu_T)_P = -(\Delta\nu_P)_T + (\Delta\nu_T)_V, \quad (5)$$

where the left-hand side is the *measured* change (temperature dependence) of ν on raising the temperature from 0 to T K at constant pressure of 0.01 MPa (1 bar). The first term on the right-hand side is the change in ν caused by raising the pressure—at constant temperature T—to a value P sufficient to cause the same volume change as the term on the left-hand side of (4). In accord with Eq. (4) this term may be obtained from β and the mode Gruneisen parameter

$$\gamma = \frac{1}{\kappa}\left(\frac{1}{\nu}\frac{\partial \nu}{\partial P}\right)_T,$$

which involves the *measured* pressure dependence of the mode. The second term on the right-hand side of Eq. (5) is the change in ν by raising the temperature from 0 to T K at constant volume (i.e., volume of the crystal at 0 K).

Thus Eqs. (4) and (5) serve to emphasize that the frequency shift at constant pressure has a pure volume contribution and a pure temperature contribution. Both of these contributions find their origin in the anharmonicity of the interatomic potentials, i.e., deviation from harmonic quadratic behavior. The frequency shift Δ of a particular phonon mode due to anharmonicity, to lowest order in perturbation theory, may be denoted

TABLE II. Logarithmic temperature and pressure derivatives at room temperature for the Raman modes of both nano and bulk anatase phase. These have been used to calculate the intrinsic anharmonicity $(\partial \ln \nu/\partial T)_V$ from Eq. (4).

Bulk anatase	E_g (141.3 cm^{-1})	B_{1g} (394.4 cm^{-1})	$A_{1g}+B_{1g}$ (516.1 cm^{-1})	E_g (636.7 cm^{-1})
$(\partial \ln \nu/\partial T)_P$ (10^{-5} K^{-1})	12.49±0.07	−5.5±0.1	−2.9±0.1	−3.2±0.1
$(\partial \ln \nu/\partial P)_T$ (10^{-3} GPa^{-1})	15.8±0.5	7.0±0.2	4.5±0.1	4.4±0.3
$\beta \times B \times (\partial \ln \nu/\partial P)_T$ (10^{-5} K^{-1})	7.7±0.5	3.4±0.2	2.2±0.1	2.2±0.2
$(\partial \ln \nu/\partial T)_V$ (10^{-5} K^{-1})	20.2±0.6	−2.1±0.3	−0.7±0.2	−1.0±0.3
Bulk anatase	E_g (146.4 cm^{-1})	B_{1g} (396.9 cm^{-1})	$A_{1g}+B_{1g}$ (518.1 cm^{-1})	E_g (641.3 cm^{-1})
$(\partial \ln \nu/\partial T)_P$ (10^{-5} K^{-1})	11.84±0.07	−5.1±0.2	−2.8±0.2	−3.0±0.1
$(\partial \ln \nu/\partial P)_T$ (10^{-3} GPa^{-1})	15.3±0.6	5.3±0.2	4.1±0.1	5.3±0.5
$\beta \times B \times (\partial \ln \nu/\partial P)_T$ (10^{-5} K^{-1})	7.5±0.5	2.6±0.2	2.0±0.1	2.6±0.2
$(\partial \ln \nu/\partial T)_V$ (10^{-5} K^{-1})	19.3±0.6	−2.5±0.4	−0.8±0.3	−0.4±0.3

$$\Delta = \Delta^E + (\Delta^3 + \Delta^4) = \Delta^E + \Delta^A, \tag{6}$$

where Δ^E represents the renormalized frequencies of independent harmonic oscillators in the dilatated lattice as a result of the volume change $\Delta V/V$ from thermal expansion, and this is commonly referred to as a quasiharmonic contribution. In most solids $\Delta^E < 0$, i.e., the dilatation results in softening. The frequency shifts Δ^3 and Δ^4 arise from *phonon-phonon* interactions and are from the lowest-order effects of cubic and quartic terms of the interatomic potential (see Kolk[41] pp. 75–78). The multiphonon process associated with the cubic term of the interatomic potential gives rise to a negative frequency shift Δ^3, whereas the shift Δ^4 associated with quartic anharmonicity is positive.[42] Therefore, the resultant frequency shift due to phonon-phonon interactions Δ^A may be either positive or negative depending on the relative magnitudes of the anharmonic terms in the interatomic potential.

Comparing Eqs. (4) or (5) to Eq. (6) it may be noted that the first term on the right-hand side of the equations is derived from quasiharmonic effect, i.e., frequency shift due to the volume change $-(\Delta \nu_P)_T = \Delta^E$. The second term on the right-hand side is from the intrinsic anharmonicity and associated effect of higher-order terms rather than from the quadratic of the interatomic potential, hence $(\Delta \nu_T)_V = \Delta^A$.

The temperature dependences of the phonon modes depicted in Fig. 7 may now be rationalized in terms of the pressure dependences of Fig. 4 and using Eqs. (4)–(6). The pressure dependence for each prominent anatase mode is positive $(\partial \nu/\partial P)_T > 0$ and, therefore, as part of the first term in Eq. (4) contributes a negative softening behavior to the overall temperature dependence of each mode $-(\Delta \nu_P)_T = \Delta^E < 0$. Figure 7 indicates that $(\partial \nu/\partial T)_P > 0$ for the E_g mode, and this hardening must then originate from the phonon-phonon interactions that contribute positive frequency shifts $\Delta^A > 0$ (e.g., likely quartic anharmonicity effects) that dominate the quasiharmonic effect $|\Delta^A| > |\Delta^E|$. For all the other modes, the converse may be true $|\Delta^A| < |\Delta^E|$, and the softening occurs mainly because of the dilatation, alternatively, phonon-phonon interactions are such that softening (e.g., dominant cubic anharmonicity) occurs, $\Delta^A < 0$.

Quantitative estimates of the intrinsic anharmonicity, $(\partial \ln \nu/\partial T)_V$, for each prominent anatase mode is obtained from the measured pressure and temperature dependences $(\partial \ln \nu/\partial P)_T$ and $(\partial \ln \nu/\partial T)_P$ at room temperature as obtained from linear fits to the data in Figs. 4 and 7, respectively, and by using Eq. (4). These values have been listed in Table II and may be compared with the case of rutile-type SnO_2 measured by Peercy and Morosin[40] or rutile-type TiO_2 by Samara and Peercy.[2] For the calculations in Table II, $B = 1/\kappa = 180$ GPa (Ref. 10) and $\beta = (\partial \ln V/\partial T)_P = 27.2 \times 10^{-6}$ K^{-1} at room temperature[43] have been used. It appears that the intense E_g mode, corresponding to O-Ti-O bond-bending vibrations in which the oxygen atoms undergo larger displacements than the titanium,[26] exhibits pronounced intrinsic anharmonicity compared to the other prominent modes. There is some degree of intrinsic anharmonicity in the B_{1g} mode at ~395 cm^{-1}, also corresponding to O-Ti-O bond bending, but with the titanium ion displacements being larger than that of the oxygens. Whereas the other prominent modes exceeding 500 cm^{-1}, arising from Ti-O bond-stretching-type vibrations, have appreciably less intrinsic an-

harmonicity. This perhaps provides some insight into which optical modes in the anatase structure are linked to physical properties of the compound, which are determined by anharmonic interatomic potentials, e.g., thermal expansion behavior.

We now attempt to explain why the nanostructured material transforms directly to the baddeyelite structure and why this occurs at a higher value of applied pressure compared to the behavior of the bulk compound. As the TEM micrograph shows in Fig. 2, the as-received sample consists of nanodimensional grains that often aggregate by means of the Van der Waals interaction. When the sample is pressurized the density of the sample is supposed to increase when loose grains pack together and, consequently, new interfaces or grain boundaries form.

In considering the nucleation of a new phase, e.g., spherical nuclei of the α-PbO_2-type intermediate, the minimum or critical diameter d^* for self-sustaining growth of the nucleus and the nucleation energy barrier ΔG^* in the case of homogeneous nucleation is given by[31]

$$d^* = \frac{4\gamma}{\Delta G_V - \Delta G_S}, \tag{7}$$

and

$$\Delta G^* = \frac{16\pi\gamma^3}{3(\Delta G_V - \Delta G_S)^2}. \tag{8}$$

Both equations are seen to be dependent on the interfacial energy γ that exists between interfaces of the new phase and the host matrix. ΔG_V is the free-energy reduction per unit volume due to the increase in density at the structural transition and ΔG_S is the misfit strain energy per unit volume. The two equations above are derived from minimizing the total free-energy change including the free-energy increase $A\times\gamma$ from the creation of new surface area A in the nucleation process.

To estimate d^* from Eq. (7), we use the accepted value for the surface stress value, i.e., $\gamma = f \approx 1.5$ Nm^{-1}. The reduction in free energy per unit volume due to density increase $\Delta G_V = P(\Delta V/V)$ is estimated by assuming that the structural transition would occur at $P \sim 5$ GPa and that the relative change in the unit-cell volume $\Delta V/V$ of $\sim$10 %, being similar to bulk values.[10] The estimated critical diameter is then $d^* \sim 15$ nm, for the case where the misfit strain-energy contribution has been neglected in Eq. (8). If it was to be included, then the critical diameter may be slightly larger.[31,44] It may be noted that the expression for the critical diameter (dimensions) [Eq. (7)] is true also for the case of heterogeneous nucleation, e.g., at grain boundaries where d^* is some linear dimension of the nucleus that is not necessarily spherical.[31] Also, in the case of heterogeneous nucleation, Eq. (8) would be multiplied by a shape factor $S(\theta)$, which is smaller than unity,[31] implying that shape deviation from spherical helps to lower the nucleation energy barrier ΔG^* in a heterogeneous system.

Therefore, the above estimates indicate that the α-PbO_2-type intermediate will only nucleate and grow as a stable particle if it has a diameter $d > 15$ nm, else it constitutes a cluster or embryo and collapses. Since the nanophase anatase particles have average dimensions of $d \sim 12$ nm, they are therefore smaller than d^* and may be considered to be embryonic. In the case of a nanoparticle of anatase of diameter $d < d^*$ it costs too much free energy, of order $\gamma\times d^2$, to transform to a new structural phase with α-PbO_2 surfaces of dimension d^2.

This suggests that lower-energy grain boundaries occur in the compacted nanoparticles of anatase, apparently energetically more favorable than the formation of anatase/α-PbO_2-type interfaces. Consequently, compacted nanophase anatase persists to high pressures in preference to the nucleation of a metastable α-PbO_2-type intermediate that occurs in the bulk solid. From Eq. (7) we again estimate the critical diameter for nucleation and growth of the baddeleyite phase at $\sim$15 GPa using the relative volume reduction $\Delta V/V \sim 15$ % at the anatase$\rightarrow$baddeleyite transition, typical of what has been measured in a bulk single-crystal.[10] A value for this critical diameter $d^* \sim 4$ nm is obtained if $\gamma \sim 1.5$ Nm^{-1} is used, which is similar to the value of surface stress f value used for nanoanatase and if the misfit strain energy ΔG_S is neglected. This demonstrates that the critical diameter d^* is appreciably smaller than the dimensions of the anatase nanoparticles. So nucleation and growth of the new baddeleyite phase out of the original anatase nanoparticle is plausible, consistent with the experiment observations. At sufficiently high pressures, the free-energy decrease $\Delta G_V \sim P(\Delta V/V)$ due to the density increase at the anatase $\rightarrow$baddeleyite transition is sufficient to counterbalance the increase in surface energy $\gamma\times d^2$ of the particles of the new phase that nucleate at the transition, so that nucleation and growth of the new baddeleyite phase is energetically favored. It may be noted that even though nanophase anatase does not transform to the α-PbO_2-type intermediate upon compression to the maximum pressure of this study at 35–40 GPa, the high-pressure (nanophase) baddeleyite phase back transforms to the α-PbO_2-type structure and not to the original anatase structure upon pressure release to ambient conditions. The bulk high-pressure phase behaves in a similar way under decompression.

Nanophase anatase appears to transform directly to the baddeleyite structure at an externally applied pressure of 17–18 GPa according to the Raman data of Figs. 3 and 4; note that this is higher than the transition pressure of the bulk material. One possible explanation for this is that the internal pressure distribution P_i is in the range of 1–3 GPa due to either (or both) particle-size and surface-stress distributions in the absence of external applied stresses, as inferred from the linewidth data of Fig. 5. Then at an applied pressure of $\sim$18 GPa, there is a net pressure in the range of $|\Delta P| \sim 15$–17 GPa on the distribution of nanoparticles. It is in this range that values of the externally applied pressure in the bulk compound (for which P_i is negligible) induce a transformation to the baddeleyite structure from a low-pressure precursor.

A potentially interesting subject of future pressure studies of nanostructured anatase is to check whether there are indeed critical grain sizes $d \sim 12$ nm below which compacted anatase would exhibit the formation of lower-energy grain

boundaries in preference to nucleation of new surfaces of the α-PbO_2-type intermediate, whereas at $d > 12$ nm the α-PbO_2-type intermediate does nucleate and grow. This may also be a general feature of nanostructured systems, indicating that the passage to new structural states so as to minimize free energies when P or T is changed may be quite different from the bulk.

ACKNOWLEDGMENTS

Funding for this project has been derived from the NRF-Pretoria. The assistance of our Structural Chemistry Group in the School of Chemistry and the Council for Geosciences (Pretoria-Tshwane) in obtaining some of the XRD data is also acknowledged with gratitude.

*Author to whom correspondence should be addressed. Email address: hearneg@physics.wits.ac.za

[1] M. Nicol and M. Y. Fong, J. Chem. Phys. **54**, 3167 (1971).
[2] G. A. Samara and P. S. Peercy, Phys. Rev. B **7**, 1131 (1973).
[3] Y. Hara and M. Nicol, Phys. Status Solidi B **94**, 317 (1979).
[4] T. Ohsaka, S. Yamaoka, and O. Shimomura, Solid State Commun. **30**, 345 (1979).
[5] J. F. Mammone, M. Nicol, and S. K. Sharma, J. Phys. Chem. Solids **42**, 379 (1981).
[6] H. Sato, S. Endo, M. Sugiyama, T. Kikegawa, O. Shimomura, and K. Kusaba, Science **251**, 786 (1991).
[7] J. Haines and J. M. Leger, Physica B **192**, 233 (1993).
[8] K. Lagarec and S. Desgreniers, Solid State Commun. **94**, 519 (1995).
[9] J. K. Dewhurst and J. E. Lowther, Phys. Rev. B **54**, R3673 (1996).
[10] T. Arlt, M. Beermejo, M. A. Blanco, L. Gerward, J. Z. Jiang, J. S. Olsen, and J. M. Recio, Phys. Rev. B **61**, 14414 (2000).
[11] L. S. Dubrovinsky, N. A. Dubrovinskaia, V. Swamy, J. Muscat, N. M. Harrison, R. Ahuja, *et al.*, Nature (London) **410**, 653 (2001).
[12] T. E. Mallouk, Nature (London) **353**, 698 (1991).
[13] X.-Z. Ding, X.-H. Liu, and Y.-Z. He, J. Mater. Sci. Lett. **15**, 1789 (1996).
[14] A. A. Gribb and J. F. Banfield, Am. Mineral. **82**, 717 (1997).
[15] Y. Ilda, M. Furukawa, T. Aoki, and T. Sakai, Appl. Spectrosc. **52**, 673 (1998).
[16] R. L. Penn and J. F. Banfield, Am. Mineral. **84**, 871 (1999).
[17] H. Zhang and J. F. Banfield, J. Mater. Res. **15**, 437 (2000).
[18] W. F. Zhang, Y. L. He, M. S. Zhang, Z. Yin, and Q. Chen, J. Phys. D **33**, 912 (2000).
[19] J. S. Olsen, L. Gerward, and J. Z. Jiang, J. Phys. Chem. Solids **60**, 229 (1999); V. Swamy, L. S. Dubrovinsky, N. A. Dubrovinskaia, A. S. Simionovici, M. Drakopoulos, V. Dmitriev, and H. P. Weber, Solid State Commun. **125**, 111 (2003).
[20] Z. Wang, S. K. Saxena, V. Pischedda, H. P. Liermann, and C. S. Zha, J. Phys.: Condens. Matter **13**, 8317 (2001).
[21] Z. Wang and S. K. Saxena, Solid State Commun. **118**, 75 (2001).
[22] J. C. Parker and R. W. Siegel, Appl. Phys. Lett. **A66**, 943 (1990).
[23] Y. Machavariani, M. P. Pasternak, G. R. Hearne, and G. K. Rozenberg, Rev. Sci. Instrum. **69**, 1423 (1998).
[24] J. Zhao, G. Hearne, M. Maaza, M. K. Nieuwoudt, and J. D. Comins, Rev. Sci. Instrum. **71**, 4509 (2001).
[25] H. K. Mao, P. M. Bell, J. W. Shaner, and D. J. Steinberg, J. Appl. Phys. **49**, 3276 (1978).
[26] T. Ohsaka, F. Izumi, and Y. Fujiki, J. Raman Spectrosc. **7**, 321 (1978).
[27] J. C. Parker and R. W. Siegel, J. Mater. Res. **5**, 1246 (1990).
[28] J. S. Vermaak, C. W. Mays, and D. Kuhlmann-Wilsdorf, Surf. Sci. **12**, 128 (1968).
[29] D. Bersani, P. P. Lottici, and X.-Z. Ding, Appl. Phys. Lett. **72**, 73 (1998).
[30] M. Ivanda, S. Music, M. Gotic, A. Turkovic, A. M. Tonejc, and O. Gamulin, J. Mol. Struct. **480–481**, 641 (1999).
[31] D. A. Porter and K. E. Easterling, *Phase Transformations in Metals and Alloys* (Chapman & Hall, London, 1992).
[32] H. Zhang and J. F. Banfield, J. Mater. Chem. **8**, 2073 (1998).
[33] J. W. Cahn, Acta Metall. **28**, 1333 (1980).
[34] CCP14 website, http://www.ccp14.ac.uk/
[35] A. C. Larson and R. B. v. Dreele, Los Alamos National Laboratory, Report LAUR 86-748 (1994).
[36] C. J. Howard, T. M. Sabine, and F. Dickson, Acta Crystallogr., Sect. B: Struct. Sci. **B47**, 462 (1991).
[37] R. C. Cammamarata, Prog. Surf. Sci. **46**, 1 (1994).
[38] H. Ibach, Surf. Sci. Rep. **29**, 193 (1997).
[39] Consider a faceted nanoparticle with an equilibrium shape of a square plate with thickness $2x_1$ and width $2x_2$. If the surface stresses of the broad faces and edges are f_1 and f_2, respectively, then the excess pressure across the broad face is $\Delta P = 2f_2/x_2$, whereas the excess pressure across the edge is $\Delta P = f_1/x_1 + f_2/x_2$. These expressions are similar to the case of a spherical particle, and are derived by considering forces in equilibrium at each of the faces. The force exerted by the exposed perimeter of the broad face $4(2x_2)f_2$ must balance the force due to the excess pressure on that face $\Delta P\ (4x_2^2)$, and similarly for the edge faces of the faceted particle.
[40] P. S. Peercy and B. Morosin, Phys. Rev. B **7**, 2779 (1973).
[41] B. Kolk, *Studies of Dynamical Properties of Solids with the Mossbauer Effect* (Elsevier, Amsterdam, 1984).
[42] A. A. Maradudin and A. E. Fein, Phys. Rev. **128**, 2589 (1962).
[43] M. Horn, C. F. Schwerdtfeger, and E. P. Meagher, Z. Kristallogr. **136**, 273 (1972).
[44] J. Z. Jiang, J. S. Olsen, L. Gerward, and S. Morup, Europhys. Lett. **44**, 620 (1998).

Appendix 3: literature survey on the methods of synthesis of nanostructured nanoparticles

Introduction

Nano-sized particles are commonly synthesized by Laser or plasma is driven gas-phase reactions, evaporation-condensation mechanisms, sol-gel methods, or other wet chemical routes such as Inverse micelle preparation of inorganic clusters. However, the primary difficulty that we encounter in our endeavor to obtain high-performance nanostructured materials using a given synthesis method is its versatility. This implies the adaptability of the method in terms of synthesis conditions to produce materials with specifications such as size, structure (phase), and morphology (shape) having required properties for given applications. Before employing a selected synthetic method, we must be able to identify the effects of all variables at each step of synthesis involving the precursor to the end-nanostructured product. Let us emphasize, our exclusive interest with the physical properties of the nanostructured materials as designed and produced by the synthetic methods. In this survey we are not looking at the performance but on the mechanisms and the physical properties (size, phase, and shape) of the nanostructured materials by the synthesis methods.

In short, the present study of the synthesis methods follows a descriptive approach by considering mainly the mechanisms of formation of the nanostructured materials based on initial conditions of preparation i.e. reactions of Titanium precursors and other reactants used. Moreover, subjecting the end-products of the processes to techniques of analysis, description, and classification which constitute the basis of nanoscience is essential as well. The relevant techniques allow us to evaluation the nanostructured materials formed and processed in terms of size of particles, the level of agglomeration, amorphousness, or, sometimes crystallinity, whether or not metastable crystallographic phase with large poly-dispersity in size and shape.

3.2 The Mechanisms of the commonly used Synthesis methods

3.2.1 The Sol-Gel Method: According to G.C. Righini, and A. Chiappini (2014), also Esposito S.(2019), the summary of the Sol-Gel method is depicted in the figure that follows:

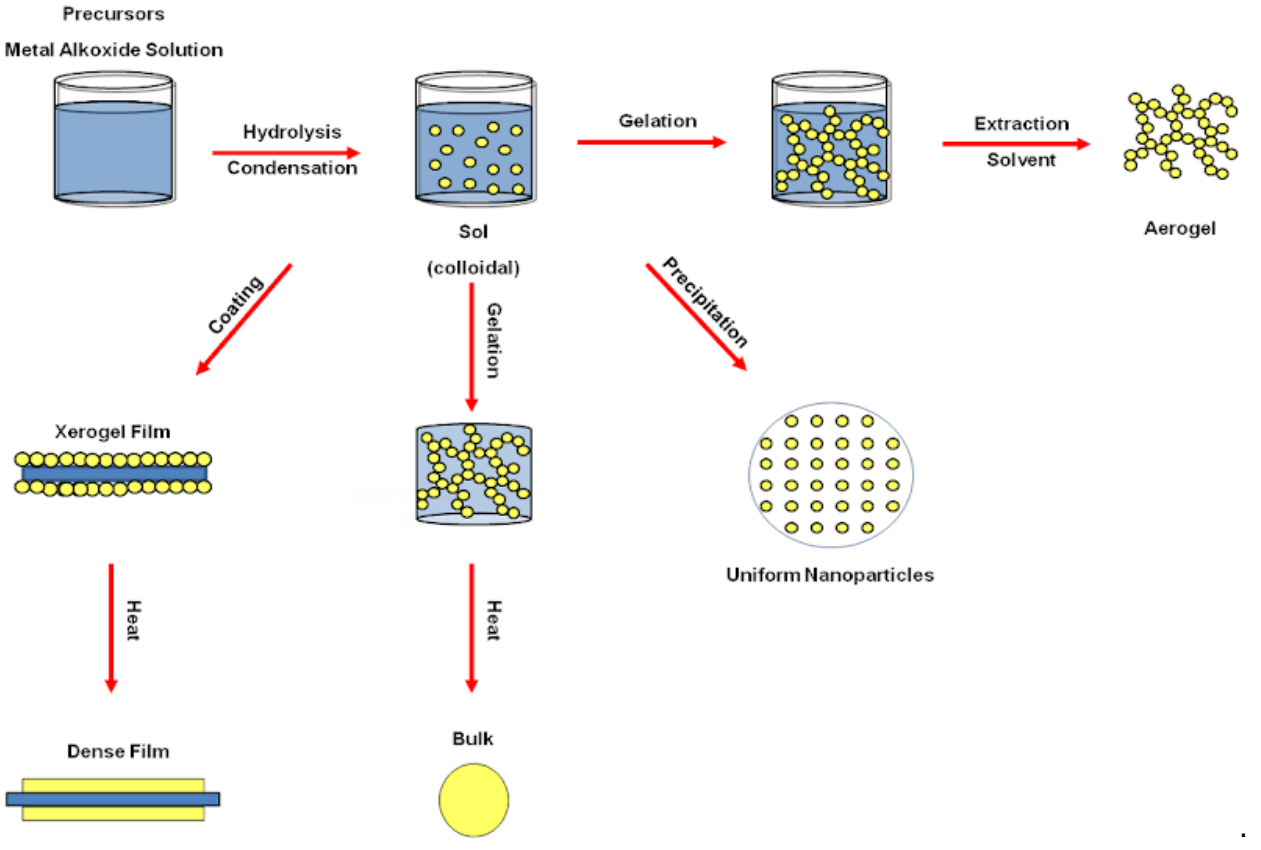

Pookmanee and S. Phanichphant (2009) have described the So-Gel Mechanism more specifically for the synthesis of **TiO_2** nanoparticles.

3.2.2 Inverse Micelles:

K. Taek Lim and Ha Soo Hwang (2004) reported the synthesis of **TiO_2** nanoparticles, anatase phase, sized ~ 13nm by using the inverse Micelles synthesis method, of which we summarize the mechanism as follows:

The formation of **TiO_2** Nanoparticles is a result of a long process that takes place in high-pressure equipment in five steps including:

1) The preparation of a single phased solution from alkoxide precursor dissolved in water, of which the water-to-alkoxide ratio is controlled,

2) The addition of a certain amount of surfactant serving as a stabilizing agent and to control the size and morphology of the particles.

3) Controlling temperature at 25°C and CO_2 atmosphere pressure with a syringe pump at 276 bars.

4) Circling over and over and stirring for 24hrs the reaction mixtures across the "remote cell" while lowering CO_2 pressure to 64.3bars at the same time maintaining the temperature at 25°C, and slowly escaping vapor-phased CO_2.

5) Rinsing with ethanol the amorphous **TiO_2** material obtained in step 4, following with its drying at 105°C for 1 day.

6) Annealing the product at 500°C for 3hrs to end-resulting in **TiO_2** Nanoparticles of about 13nm size.

3.2.3 Laser Ablation synthesis Method:

Singh A et al., 2016, describes a typical set-up that is used to make **TiO_2** nanoparticles by Laser ablation.

The set-up includes 1) A nanosecond 85W fiber laser beam source and the lens that focuses it on the target, 2) the immersed metal (titanium)-target in a bath of deionized water (DIW), a test vessel, 4) computerized XY scanner, connected to the laser beam. The laser ablation is processed when the laser beam is irradiated from the top and fixed perpendicularly to the plane of the target. It is recommended that one should try to obtain the maximum fluency possible, by varying the power of the laser affecting the spot

diameter. Sadrolhosseini A.R. (2016) describes the beginning of the ablation of the metal target at the moment that the sorption of laser beam energy takes place. The laser beam interacts with the metal target resulting in the production of the heat and the photoionization of the metal target. The metal nanoparticles are then freed from the metal plate with varying phases depending on the absorbed energy.

3.2.4 Biological Synthesis (Dr. Raghad DH.Abdul Jalill et al., 2016)

M. Sundrarajan and S.Gowri (2011) give a step-by-step description of the process of making **TiO_2** nanoparticles, involving seven following steps:

1) The reaction of a certain amount of titanium precursor, for example, 0.4M of titanium tetra-isopropoxide, and ethanolic leaf extract.

2) Stirring at 50°C continuously for the reactants out four hours.

3) Centrifuge the mixture at speed of 10000 rpm for 15 minutes,

4) Washing the obtained **TiO_2** nanoparticles with ethanol

5) Repeating the stirring and once more centrifuge at 5000 rpm for 10 minutes.

6) Isolate **TiO_2** nanoparticles from the mixture,

7) Dry, grind and anneal in the furnace the product obtained in step 6 at 500C for about 3hours.

3.2.5 Electro-Chemical Synthesis Method.

Anandgaonker P.et al. (2014) describes the synthesis process of making metal oxides nanoparticles via the electrochemical method (for narrow size distribution, particle size control done by current density variation 10nA/cm^2 to 14mA/cm^2) based on the figure below:

The mechanism explained in the following steps:

1. Oxidation of bulk titanium metal sheet taking place at anode, whereas the Platinum sheet serving as a cathode. The two electrodes are separated by a gap of about 1.1cm filled with electrolyte including the tetra-propyl of ammonium bromide (TPAB) in acetonitrile-tetrahydrofuran (in the ratio 4 to 1). The migration from the anode and the reduction at the cathode leads to the formation of either metal powder or metal oxide in the “zero oxidation state”. The effect of ammonium stabilizer is the stopping of the formation of agglomeration.
2. Application of current density leading to the formation of titanium clusters (> 95%), stabilized by the tetra-propyl of ammonium bromide. The electrolysis in a Nitrogen atmosphere favors the formation of Titanium oxide Nanoparticles.
3. The Decantation is performed because of the insolubility of titanium material in the “solvent mixture “
4. Washing several times with tetra Hydrofuran the decanted “solid product”, still containing propyl ammonium Bromide.
5. Drying the product under vacuum desiccators and calcinate it at 550°C

3.2.6 Freeze-Drying synthesis Method:

Narendra K.R et al (2014) made nanoparticles of **TiO_2** using lyophilization of polyester (polymer) and **TiO_2** precursor (Ti(IV) isopropoxide).

3.2.7 Microemulsion – Heat treated Method

Zori M.H (2010) made**TiO_2** nanoparticles using the Microemulsion method and described the mechanism of the synthesis.